Open Research Online

The Open University's repository of research publications
and other research outputs

Characterization of Inelastic Strain in Type 316H Austenitic Stainless Steel using Electron Backscatter Diffraction

Thesis

How to cite:

Unnikrishnan, Rahul (2019). Characterization of Inelastic Strain in Type 316H Austenitic Stainless Steel using Electron Backscatter Diffraction. PhD thesis The Open University.

For guidance on citations see FAQs.

© 2018 The Author

https://creativecommons.org/licenses/by-nc-nd/4.0/

Version: Version of Record

Link(s) to article on publisher's website:
http://dx.doi.org/doi:10.21954/ou.ro.0000ee46

Copyright and Moral Rights for the articles on this site are retained by the individual authors and/or other copyright owners. For more information on Open Research Online's data policy on reuse of materials please consult the policies page.

oro.open.ac.uk

Characterization of inelastic strain in type 316H austenitic stainless steel using electron backscatter diffraction

By

Rahul Unnikrishnan

Faculty of Science, Technology, Engineering & Mathematics

School of Engineering & Innovation

This dissertation is submitted for the degree of
Doctor of Philosophy

May 2019

ABSTRACT

Type 316H austenitic stainless steel is widely used in the UK's advanced gas-cooled reactors, for example in boiler components, due to its good corrosion, creep and fatigue properties at temperatures around 550ºC. The influence of service conditions such as the type of loading, strain rate, load and temperature histories and the environment have to be considered in assessing the remaining safe lifetime of plant operating at high temperature, so that fatigue and creep-fatigue damage can be quantified to ensure that the material will still be able to withstand the required future loads in the creep-fatigue-damaged condition.

Electron backscatter diffraction (EBSD), which can measure crystallographic orientations in polycrystalline materials, has been used to quantify and map inelastic strains in materials in terms of metrics derived from the local orientation changes or by calculating the geometrically necessary dislocation densities. This thesis explores the potential of EBSD for characterizing localised inelastic strain from lattice orientation measurements during uniaxial stress relaxation and cyclic loading.

The study was conducted on ex-service Type 316H austenitic stainless steels, through a series of monotonic tests under tensile primary load, secondary stress relaxation and under low cycle fatigue/creep-fatigue conditions. The EBSD metrics termed kernel average misorientation (KAM), grain orientation spread (GOS), low-angle boundary fraction (LABF) and deformed grain fraction (DGF) all showed a linear variation with inelastic strain accumulation in both tensile and cyclic tests. In contrast the proportion of twin boundaries reduced with increasing inelastic strains. This study demonstrated that the development of misorientation depends on the temperature and precipitate

distribution. The misorientation developed in solution annealed material was much lower than that in ex-service material. Near grain boundaries, the local misorientations were found to increase with increasing stress relaxation and cavities were identified from secondary electron images. A misorientation-based strain assessment method considering the deformed grain fraction was found to be more consistent than using mean misorientation values as this reduced the scatter associated with inhomogeneities in grain size. After tensile deformation at different strains and cyclic deformation at different strain ranges, a good correlation was found between the behaviour of different EBSD metrics and the measured mean microhardness. However, hardness measurements did not clearly detect the inelastic strain developed during stress relaxation and cyclic strain accumulation (i.e. the strain accumulated over different numbers of cycles). Scanning transmission electron microscopy showed the dislocations in tensile samples after stress relaxation to form homogeneous diffuse cell structures, and clear cell structures were also evident after cyclic deformation. The cell structures elongated to veins with further cyclic strain accumulation.

Local misorientation maps were used to study the inelastic deformation around a reheat crack in an ex-service component. The EBSD misorientation maps showed good correlation with microhardness maps. Local misorientation maps showed strain accumulation along grain boundaries. Comparison with Small Angle Neutron Scattering (SANS) cavitation measurements showed that the areas with more cavities had higher local misorientations. Although stress concentration at grain boundaries is well documented, such a relationship between high local misorientation and cavitation has never been seen before in austenitic materials subject to stress relaxation.

ACKNOWLEDGEMENTS

Firstly, I would like to express my sincere gratitude to my supervisors Dr Shirley M Northover, Prof. P John Bouchard and Dr Hedieh Jazaeri for the continuous support of my PhD study and related research, for their patience, motivation, and immense knowledge. Their guidance helped me in all the time of research and writing of this thesis. I could not have imagined having better supervisors for my PhD study.

I acknowledge the financial support from EDF energy, UK and the Open University. I would like to thank Dr David Dean, Mr Mike Spindler, Mr Jacob Knight and Dr Sarah Spindler of EDF Energy for their useful discussions in shaping the research project. My special gratitude to Dr Richard Moat for the helpful discussions. I am also grateful to Dr Thomas Simm, Swansea University for help with EBSD analysis using MTEX.

I would like to thank Mr. Damian Flack and Mr. Peter Ledgard for their help with the specimen machining, Mr. Gordon Imlach for his assistance in using SEM, Dr Igor Kraev for his assistance in using TEM and Dr Felicity Williams for her assistance in metallography. My special thanks to Mr Stan Hiller for his assistance with the mechanical testing. I would also like to thank Mrs. Olivia Acquah and Mrs. Donna for their assistance with the administrative works throughout the PhD.

Thanks to all my colleagues during this period, Jino, Shanmukha, Anas, Yadu, Avishek, Paheli, Beverly, Yeli, Ellies, Abdullah, Sanjoo, Gerardo, Jeferson, Rodolpho, Xinfang, Johannas, Mushfique and other friends and their family for their friendship and support during my stay. Special thanks to Anas for help with MATLAB codes.

Acknowledgement

I would like say a heartfelt thanks to my beloved parents Mr.Unnikrishnan Nair and Mrs. Bindu R Nair, my sister, Arundhathy, my grandparents and Mr. Harikumar Nair and family for their love, support, and sacrifices.

Last but not the least, my sincerest appreciation is reserved for my wife Lakshmi for her unconditional love.

PREFACE

This thesis is submitted for the degree of Doctor of Philosophy of The Open University, United Kingdom. The research described herein was conducted in the School of Engineering & Innovation, Faculty of Science, Technology, Engineering and Mathematics between January 2015 and April 2018 under the supervision of Dr Shirley M. Northover, Prof. P. John Bouchard and Dr Hedieh Jazaeri.

This work is original to the best of my knowledge, except where reference is made to the work of others. This work has not been submitted in whole or part for any other degree at any other university. Part of this work has been published in an academic journal and presented at conferences as listed below:

- Unnikrishnan R, Northover S M, Jazaeri H, Bouchard P J, (2016), "Investigating plastic deformation around a reheat-crack in a 316H austenitic stainless steel weldment by misorientation mapping". Procedia Structural Integrity 2, 3501-3507
- EBSD analysis of strain-controlled high temperature low cycle fatigue deformation in service-aged type 316H austenitic stainless steel, 4th International ECCC Creep & Fracture Conference, 10th-14th September 2017, Düsseldorf, Germany (Poster presentation)
- An EBSD misorientation study of inelastic strains during high temperature low cycle fatigue deformation of type 316H austenitic stainless steel, Electron Backscatter Diffraction Meeting, 4th-5th April 2017, University of Oxford, United Kingdom. (Oral presentation)

- An EBSD misorientation approach to quantify inelastic strain during creep-fatigue of type 316H austenitic stainless steels, Oxford Instruments EBSD Symposium, 2nd-3rd November 2016, Stockholm, Sweden (Oral presentation)
- An EBSD misorientation approach to investigate the grain strain distribution around a reheat crack in 316H austenitic stainless steel, 21st European Conference on Fracture, 20th-24th June 2016, Catania, Italy (Oral presentation)
- 7th International conference on Creep, Fatigue and Creep-Fatigue Interaction, 19th-22nd January 2016, Indira Gandhi Centre for Atomic Research, Kalpakam, Chennai, India (Poster presentation)
- A lattice misorientation approach to quantify inelastic strains during creep-fatigue deformation of 316H austenitic stainless steel, BSSM Postgraduate Experimental Mechanics Conference, 19th -20th November 2015, University of Southampton, United Kingdom (Oral presentation)
- Condition monitoring of structural components in nuclear power plants by electron backscatter diffraction, Universities Nuclear Technology Forum, 31st March - 2nd April 2015, The Open University, Milton Keynes, United Kingdom (Oral presentation)

TABLE OF CONTENTS

LIST OF ABBREVIATIONS

AGR	Advanced gas cooled reactor
AFC	Area fraction of cavities
CCD	Charge coupled device
C-F	Creep fatigue
DGF	Deformed grain fraction
DIC	Digital image correlation
DPPA	Diffraction peak profile analysis
DSA	Dynamic strain ageing
E	Young’s modulus
EBSD	Electron backscatter diffraction
ECCI	Electron channelling contrast imaging
ECD	Equivalent circle diameter
EDM	Electro-discharge machining
EDS	Energy dispersive spectroscopy
f.c.c	Face centred cubic
GAM	Grain average misorientation
GB	Grain boundary
GBF	Grain boundary fraction
GBS	Grain boundary sliding
GND	Geometrically necessary dislocation

GOS/AMIS	Grain orientation spread/ Average intragrain misorientation
HAGB	High angle grain boundary
HAZ	Heat affected zone
HTLCF	High temperature low cycle fatigue
IAP	Instron AlignPro
JSMS	Society of material science, Japan
KAM	Kernel average misorientation
LABF	Low angle boundary fraction
LAMF	Low angle misorientation fraction
LAGB	Low angle grain boundary
LCF	Low cycle fatigue
LVDT	Linear variable displacement transducer
m.u.d	multiples of the uniform density
ND	Normal direction
NDT	Non-destructive testing
OIM	Orientation imaging microscopy
OM	Optical microscopy
PLC	Portevin Le-Chatelier
RD	Rolling direction
SANS	Small angle neutron scattering
SEM	Scanning electron microscopy
SSD	Statistically stored dislocation

STEM	Scanning transmission electron microscopy
TBF	Twin boundary fraction
TD	Transverse direction
TEM	Transmission electron microscopy
TTP	Time temperature precipitation
TTT	Time temperature transformation
W	Cumulative inelastic strain energy
$\sum\varepsilon_{ie}$	Cumulative inelastic strain
$\sum\varepsilon_{t}$	Cumulative tensile strain
$\sum\varepsilon_{c}$	Cumulative tensile strain
Δw	Inelastic strain energy per cycle
ε_e	Elastic strain
ε_p	Plastic strain

CHAPTER 1

INTRODUCTION

1.1. Background

In this era of global warming and climatic changes, affordable and clean energy is very important for sustainable development. Nuclear power makes a significant contribution to clean energy reducing greenhouse gas emissions and at the same time meeting the increasing energy demands of a growing world [1]. Almost 19% UK's electricity is generated from nuclear energy. The Advanced Gas-Cooled Reactor (AGR) is a second-generation reactor developed from Magnox reactor technology in the UK to improve thermal efficiency. Most of the AGRs have executed their original design life and are approaching decommissioning from 2023 [2]–[4]. The main focus of the nuclear industry in many countries is on continuing to operate their existing power plants, rather than building new ones, due to the economic benefits this offers. The Chernobyl disaster (in 1986), which is considered the world's worst nuclear power plant accident has raised international concern about reactor safety despite the economic attractiveness of nuclear power. In order to extend the life of ageing power plants the most important requirement is to demonstrate the safe and efficient operation of their reactors [5].

Figure 1.1 shows a schematic of an AGR. A total of 14 AGRs currently operate at 6 sites in the UK. The carbon dioxide circulates through the core, reaching a temperature of 650°C, and then past steam generator tubes outside it, but still inside the concrete and steel pressure vessel. Control rods penetrate the moderator and a secondary shutdown system involves injecting nitrogen to the coolant [6]. The main criterion for continued plant operation is that the plants must remain safe to the satisfaction of the regulators but

they must also be economically viable to meet the requirements of the utility companies and other stakeholders [5]. Regulators require Periodic Safety Reviews (PSR) of old power plants as they were not built to the same standards as modern ones. The actual working life of a plant depends on various factors such as:

- changes in the operating conditions compared with those assumed in the design,
- the findings from maintenance inspections,
- the results of test programmes and
- the outcome of safety assessments [5].

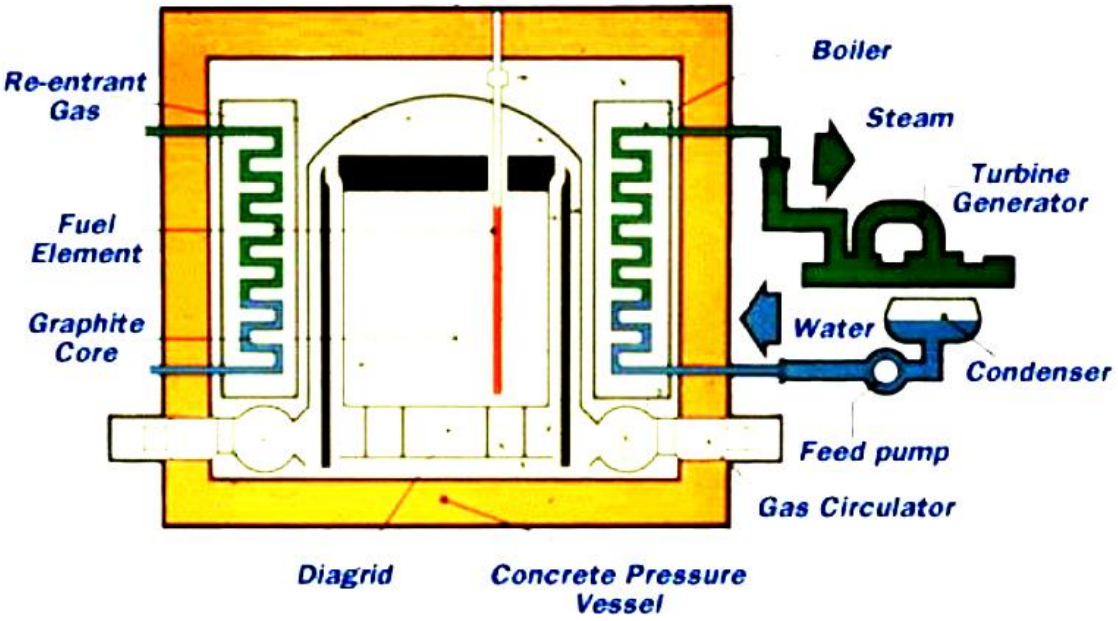

Figure 1. 1 Schematic of Advanced Gas-Cooled Reactor [7].

Type 316H austenitic stainless steel is widely used in the UK's advanced gas cooled reactors, for example in boiler components, due to its good corrosion, creep and fatigue properties at temperatures of around 550^{o}C [8], [9], [18], [19], [10]–[17]. The influence of service exposures such as the type of loading, strain, strain rate, temperature, etc. has to be considered in the life assessment of a high temperature material and so the creep damage has to be studied in detail to ensure that the material can still withstand the applied

load in a creep damaged condition [20]. Creep deformation of polycrystalline materials at elevated temperature can lead to the nucleation, growth and coalescence of intergranular voids to form micro-cracks along the grain boundaries [20].

The electron backscatter diffraction (EBSD) technique using a scanning electron microscope (SEM) has recently emerged as a powerful method for material characterization. It gives microstructural level information along with the lattice orientation in the material. Recently many research studies have been conducted using this technique to find correlations between the inelastic strains in materials with the lattice misorientation at high spatial resolution. It can be used for precise measurements of plastic strain and creep strain in bulk samples [21], [22], [31], [32], [23]–[30]. The Society of Material Science, Japan had issued a guideline for EBSD measurement (JSMS, 2016), which focused on misorientation assessment for creep damage evaluation in Type 316 austenitic stainless steel. The main application of this method is to estimating inelastic strains in nuclear structural component whose prior deformation history is unknown. This thesis offers an opportunity to provide data for an EBSD-based damage measurement method in the R5 procedure which has been developed within the UK power generation industry to assess the integrity of nuclear and conventional plant operating at high temperatures.

1.2. Purpose of this study

Githinji et al [11] proposed a misorientation-based approach to quantifying plastic and creep strain in ex-service and solution annealed type 316H stainless steel. This approach was based exclusively on constant load creep studies. However, the relationship between crystallographic misorientations and inelastic strain is not well studied under conditions of stress relaxation or creep-fatigue which are more relevant to real plant conditions. To

be useful in predicting a plant's remaining safe operating time, a more reliable method of measuring the plastic and creep strains under different conditions of operation is needed [11].

1.3. Structure of thesis

This thesis consists of 9 chapters that address different topics relevant to the research objectives.

Chapter 2 reviews the available literature relevant to this thesis. The topics discussed include precipitation, plastic deformation, creep deformation and fatigue in 316 austenitic stainless steels, reheat cracking, creep strain/damage monitoring techniques and EBSD for assessing strain in metallic materials.

Chapter 3 briefly explains the experimental methods and the measurement settings used in this thesis. This chapter is divided into four sections: mechanical tests, microstructural and dislocation characterization, strain measurement from lattice curvature measurement and other techniques for measuring dislocation density.

Chapter 4 introduces the 316H austenitic stainless steel materials used in this study including their service history, the as-received microstructure and chemical composition, grain sizes, precipitation, microstructure after re-solution heat treatment and thermal aging, dislocation structures and mechanical properties.

The influence of temperature, precipitates and grain size on the development of strain-induced lattice misorientation during uniaxial deformation is covered in Chapter 5. This chapter gives details of the material studied, the tests conducted, the measurements made and the data analysis of the results from these tests.

Chapters 6 and 7 cover the effect of cyclic deformation on lattice misorientation development. These chapters describe the cyclic tests conducted, the EBSD measurements done and the effect of different cyclic deformation parameters on misorientations developed. Chapter 6 focusses on the effect of strain range, dwell, strain rate and microstructure on EBSD metrics whereas Chapter 7 covers how cyclic strain accumulation affects the EBSD metrics of interest.

Chapter 8 presents an overall discussion of the thesis and reports EBSD studies around a reheat crack in a structural component.

Chapter 9 draws together conclusions of the thesis and sets out suggestions for future work.

CHAPTER 2

LITERATURE REVIEW

2.1. Introduction

The primary aim of this thesis is to investigate the potential of EBSD to characterize the inelastic strain developed during uniaxial stress relaxation and low cycle fatigue/creep-fatigue deformation of Type 316H austenitic stainless steel. This chapter starts with a literature review of the alloying elements, precipitates, and deformation (plastic, creep and fatigue/creep-fatigue) of austenitic stainless steels. It then reviews different methods of monitoring creep strain and damage. This chapter also reviews EBSD studies done so far to understand plastic/cyclic/creep deformation in different metals and alloys and ends with a summary identifying the limitations of the literature.

2.2. Type 316H Austenitic stainless steel

Austenitic stainless steels are used for high temperature components due to their excellent creep and oxidation properties. Austenitic stainless steels containing chromium and nickel are generally given a 300 series classification [33]. Type 316 steel contains 2–4% (wt%) molybdenum, to improve general corrosion resistance, (particularly pitting corrosion) [34]. Type 316H steel is the high temperature version of 316 steel with 17% chromium, 12% nickel, 2.5% molybdenum and a carbon content of 0.04 to 0.08% to give enhanced creep properties. This steel is always solution heat treated followed by quenching to get a fully austenitic structure [35].

The austenite phase provides high ductility and toughness, no impact transition at cryogenic temperatures and a low stacking fault energy. The alloying elements lead to high work-hardening rates; so, the strengthening method for austenitic stainless steels is work-hardening rather than heat treatment. Austenitic stainless steels, owing to their face-

centred cubic (*f.c.c.)* structure, are suitable for use at elevated temperatures (especially above 550 ºC) since they do not lose their strength as quickly as other ferrous phases, and so are used where good creep properties are required at temperatures above 550ºC [36][37].

The composition of type 316H austenitic steels was designed to give good creep properties. The role of the major alloying elements is:

Chromium is the most important alloying element in stainless steels. It increases corrosion and oxidation resistance at high temperatures by forming a passive oxide (Cr_2O_3) surface layer [36]. It forms a substitutional solid solution in austenite. The Cr content is governed by that needed to give a passive film (~17%) and the Ni content follows from that [36]. Chromium is a strong ferrite stabilizer, so a combination of austenite stabilizing elements such as Ni, Mn, N, C, etc. is always added to maintain an austenitic microstructure at room temperature. As a rule of thumb, around 17% Cr and 11% Ni is required to stabilize austenite at room temperature. The effect of chromium on precipitation is reviewed in the next section.

Nickel is another substitutional element. Ni acts as an austenite stabilizer and increases the toughness, ductility, weldability and general corrosion resistance of stainless steel [36][37]. A high nickel content in the matrix can make the thermal expansion coefficient of the alloy closer to that of the oxide layer, reducing the risk of oxide rupture and increasing the corrosion resistance at high temperatures [36], [38]. Nickel usually dissolves in carbides, partially substituting for chromium; whereas it is a major constituent in some other types of precipitates, like the G phase [39]. The addition of Ni increases the stacking fault energy (SFE) [40]. The SFE affects the motion of dislocations;

raising the SFE aids the activation of cross slip and so promotes strain hardening during deformation. More details regarding SFE are given in section 2.2.2.

Carbon atoms occupy interstitial sites within the *f.c.c* structure of austenitic stainless steel, providing solid solution strengthening [37]. Carbon is a major austenite stabilising element but its use is limited by its low solubility in austenite. Carbon forms $M_{23}C_6$ (M=Cr, Fe, Mo, V, W in different proportions) chromium rich carbides on grain boundaries, leading to chromium depletion in the austenite matrix (called sensitisation) and consequently lowering the material's intergranular corrosion resistance [41]. Type 316L stainless steels have carbon content less than 0.03wt% and 316H has carbon content between 0.04 and 0.1wt% [36].

Nitrogen is another interstitial solute and a strong austenite stabilizer. The solid solution strengthening effect of N is more pronounced than C, and N also enhances the strain hardening effect. Nitrogen reduces the tendency to form compounds with chromium by lowering the diffusion of C and hence is considered as beneficial in austenite [36]. Nitrogen's limited solubility can be increased by the addition of manganese [37]. Its addition is also beneficial for creep strength, by promoting the precipitation of nitrides and carbonitrides [40]. The addition of nitrogen also increases the creep-fatigue life of 316L steels. This could be for two reasons:

(i) Nitrogen inhibits cross-slip and the climb of dislocations, promoting the planar slip mode in cyclic deformation. The dislocation structure in 316L steels is reported to change from cells to planar with the addition of nitrogen. It is reported that a planar structure is more resistant to fatigue damage than a cell structure [42].

(ii) Stress relaxation has been found to be lower in 316LN steel than in 316, reducing the plastic deformation occurring during the hold time, which eventually reduced cavitation [43] .

Manganese is an austenite former and sometimes used as a replacement for nickel; however, such an alloy exhibits less corrosion resistance [40]. Mn increases nitrogen's solubility in austenite without forming nitrides and hence enhances nitrogen's solid solution strengthening effect. The addition of manganese has some disadvantages such as weakening the passive film and increasing the risk of pitting corrosion at manganese sulphide inclusions [40].

Silicon, which is a ferrite stabilizer, improves the oxidation resistance of the stainless steel by forming a dense silicon oxide layer on the surface [40]. Silicon also prevents carburisation and nitridation of austenitic steels at high temperatures by forming an oxide layer [36].

Molybdenum is a strong ferrite former and necessitates the addition of more austenite stabilizers to keep the austenitic structure [37]. It enhances the corrosion resistance of stainless steel, especially against pitting corrosion [40]. Molybdenum improves creep strength by solid solution hardening and by facilitating carbide precipitation [36]. However, it promotes sigma phase and Laves phase formation during long-term aging [38].

Vanadium forms more stable carbides than chromium and improves the creep resistance around 550^{o}C [36].

Copper enhances the corrosion resistance of stainless steel in certain acids and promotes the austenitic structure [44]. In high temperature grades, copper has been recently shown to form precipitates during long term aging at high temperatures (above 400^{o}C),

improving the creep strength [40]. Copper also helps increase stacking fault energy (see section 2.4 for more details on SFE) [40].

2.2.1. Precipitation in austenitic stainless steel

Creep-resistant 316H austenitic stainless steel contains many alloying elements in a supersaturated solid solution in the austenite phase. The precipitates play an important role in enhancing its creep properties. In austenitic stainless steel, precipitation results from the decreasing solubility of the alloying elements in the austenite when it is cooled down. Before using the alloy, it is solution annealed at a suitable temperature; usually following by rapid cooling to form a supersaturated solid solution [37], [45], [46]. When the alloy is in service at high temperatures, it ages, the supersaturated elements diffuse and react to form precipitates. Crystallographic defects within the matrix structure are preferential nucleation sites for second phase precipitates [37].

Grain boundaries and grain corners are the most favoured nucleation sites because of their high energy, their ability to accommodate the structural mismatch between precipitate and matrix and also their high density of vacancies which facilitates the diffusion of solute atoms [37], [40], [46]. Twin boundaries are the next most preferential nucleation sites. Precipitation first occurs at incoherent twin boundaries and then in coherent twin boundaries [47]. Within the grains, the slip bands which are associated with a high density of tangled dislocations are preferential sites for precipitate nucleation [40]. Other crystallographic defects such as vacancies and dislocations can also be sites of precipitate nucleation [37]. The type, morphology, size, distribution and stability of the precipitates are the factors dominating the creep behaviour of the alloy. The temperature-time precipitation (TTP) diagram of an annealed Type 316 stainless steel (see Figure 2.1) shows the precipitation as time proceeds.

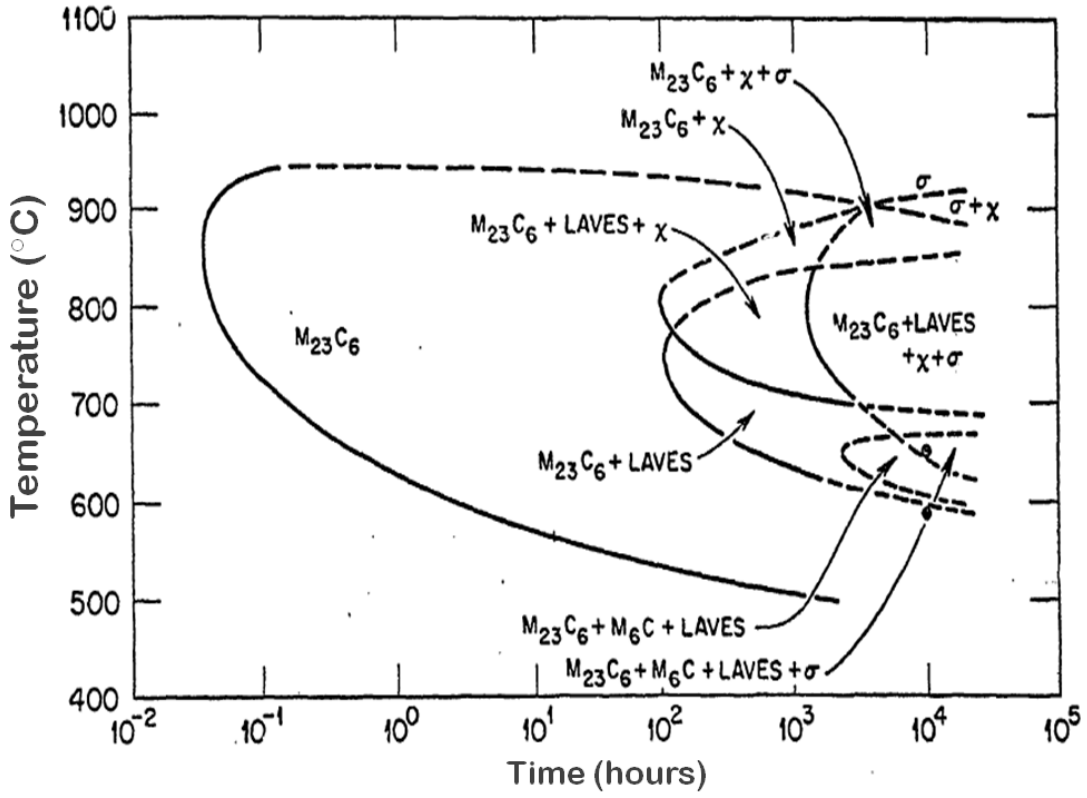

Figure 2.1 Time-temperature-precipitation diagram of 316 stainless steel solution treated at 1260ºC for 1.5hour and water quenched [38].

$M_{23}C_6$ is a general notation for precipitates with the structure of $Cr_{23}C_6$ (which in steels is usually in reality a mixed carbide). Fe, Mo, V, W and Ni can all partially substitute for Cr (M=Cr, Fe, Mo, V, W) [36]. $M_{23}C_6$ has an *f.c.c* structure with a lattice parameter varying between 10.57 and 10.68 Å [36]. The precipitation of $M_{23}C_6$ is accelerated above 550ºC and usually starts on grain boundaries and incoherent twin boundaries where diffusion is much more rapid than in the bulk material. As aging advances, $M_{23}C_6$ can precipitate on other sites like coherent twin boundaries, within the grains on dislocations and around other particles, like residual carbides/nitrides. Some alloying elements can markedly affect the precipitation of $M_{23}C_6$ carbide. Elements like molybdenum and nickel enhance it by decreasing the solubility of carbon in austenite, whereas nitrogen, which increases the carbon solubility, reduces $M_{23}C_6$ precipitation. To improve both corrosion

and creep properties it is desirable that $M_{23}C_6$ carbides precipitate as fine intragranular particles instead of chain-shape ones on grain boundaries [46]. Planar $M_{23}C_6$ precipitates are less damaging to creep-fatigue properties than triangular ones [40].

M_6C, called eta carbide in the literature, is another type of *f.c.c* carbide (a_0=10.62-11.28 Å) which usually forms after long-term aging [36]. M can be varying combinations of elements like chromium, iron, molybdenum, nickel, niobium and silicon. This phase forms on similar sites to $M_{23}C_6$ and with similar morphologies [46].

Laves phase is an intermetallic phase formed by iron and elements such as Mo, Nb and Ti with a hexagonal unit cell (a_0=4.73 Å, c_0=7.72 Å) which depends on a close match of the atomic sizes of its constituent elements [38]. Laves phase is known to be generally stable at temperatures above 815 ºC [38].

Sigma phase is a well-known intermetallic phase with a tetragonal crystal structure (a_0=8.828-8.832 Å, c_o=4.579-4.599 Å) forming in Fe-Cr alloying systems [38]. In highly alloyed austenitic stainless steels other elements such as Mo, Ni, Mn and Si may dissolve in sigma phase, replacing iron and chromium atoms. Sigma phases were reported to precipitate along grain boundaries, twin boundaries and on MnS inclusions [48]. The precipitation of sigma phase embrittles the alloy, especially when it forms continuously on grain boundaries. However, its dispersed intragranular form, slightly improves the creep properties [40]. Sigma phases were reported to be absent in 316 steel thermally aged at 575ºC for 5 years [48].

χ-phase precipitates at grain boundaries and intragranularly at dislocations at temperatures above 750ºC [37]. χ phase has a *b.c.c* structure with a lattice parameter between 8.807 and 8.878 Å [37].

Zhu et al [48] reported the precipitation sequence for Type 316H austenitic stainless steel thermally aged at around 550^{o}C as dense intra-granular carbides, intra-granular laves phase particles, large grain boundary $M_{23}C_6$ carbides and a few grain boundary laves phase particles [48].

2.2.2. Plastic deformation in austenitic stainless steel

Plasticity is one of the major characteristics of metals that has led to their technological importance. The major mechanism of plastic deformation in polycrystalline materials is the movement and generation of dislocations on the crystal planes under the influence of an applied stress [49][50]. The stress required to move dislocations increases during plastic flow (this is known as work/strain hardening) as the dislocations are hindered by obstacles such as solute atoms, precipitates, dislocations and grain boundaries [51]. The assessment of plastic damage can be done through macroscopic measurement of scalar quantities such as the strain, strain rate etc. The term '**damage**' is used in this thesis to represent inelastic strain accumulated in the material (plastic and/or creep strains) after deformation.

There are two main types of dislocation movement. ***Glide*** occurs when a dislocation moves in the surface which contains both its line and Burgers vector. Glide is a conservative dislocation motion involving local atomic displacements that proceed through switching one or few interatomic bonds at a time [49] and is reversible. The glide of many dislocations results in slip. Climb is (a non-conservative motion) when a dislocation moves out of the glide plane and is not reversible [49]. Climb involves the diffusion of point effects and hence is strongly dependent on temperature [52] [49]. Plastic deformation can be described as the successive sliding of one plane of atoms over

another on so called slip planes. The slip planes are normally the planes in a crystal with the highest density of atoms and the slip directions are the directions where the atoms are most closely packed. Hence the plastic deformation of metals varies with their crystal structure. The shear stress acting to move a dislocation is given by

$$\tau = \frac{F}{A}\cos\Phi\cos\lambda \quad (2.1)$$

Where F$\cos\lambda$ is the force component in the slip direction, λ being the angle between the applied force, F, and the slip direction (see Figure 2.2). The area of the slip plane is A/$\cos\Phi$, where Φ is the angle between applied force and the normal to the slip plane. A minimum value of shear stress, usually called the critical resolved shear stress (τ_c), is required to initiate slip. The quantity $\cos\Phi\cos\lambda$ is known as the *Schmid factor* [50].

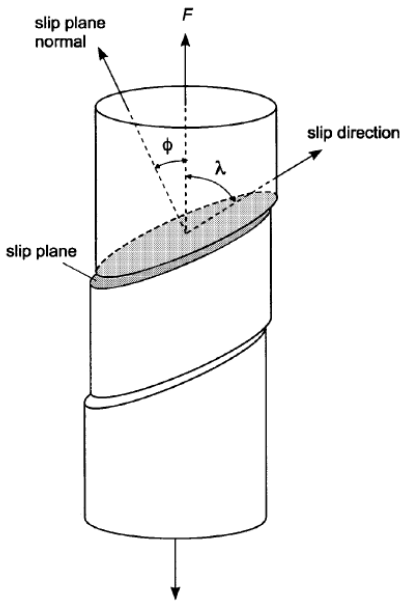

Figure 2.2 Illustration of geometry of slip in crystalline material.[50]

Austenitic stainless steel has a face centred cubic (*f.c.c*) structure and plastic deformation occurs due to the twelve {111}<110> slip systems ({Slip plane}<Slip direction>) [53]. Dislocations leave their glide plane by cross-slip or climb [49]. In *f.c.c.* systems, dislocations are often confined to one set of {111} planes in which they dissociate into

Shockley partials by a planar dissociation [54]. If the stacking fault energy (SFE) is high, dislocations remain undissociated and cross-slip can occur freely. Austenitic stainless steel has a low SFE [55] so cross-slip is more difficult at room temperature as the dislocations have to constrict to change slip planes [55]. The region corresponding to the stacking fault can be clearly seen by the characteristic fringe (////) pattern (see Figure 2.3). The SFE determines the width of the faulted region between two partial dislocations present in the *fcc* matrix. Wide stacking faults (i.e. lower SFE) between partials impede the motion of dislocations and reduce the activation of cross slip [55]. A lower SFE results in a larger faulted region, and therefore a lower tendency for the material to work harden. SFE increases with increasing temperature [56].

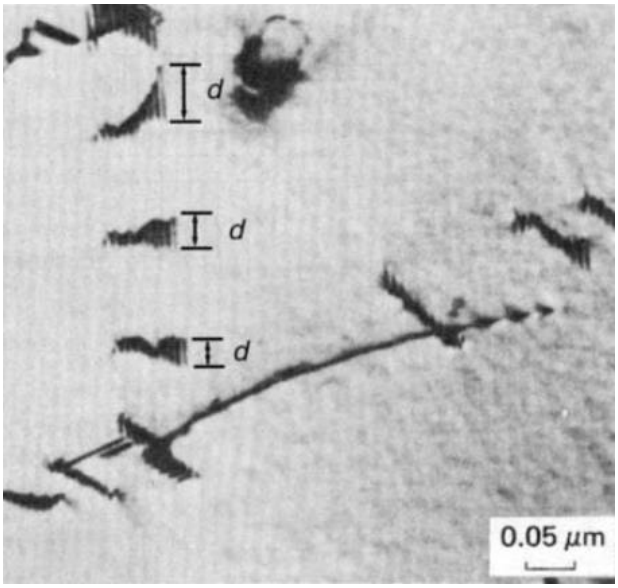

Figure 2.3 Dislocations in AISI 304 stainless steel splitting into partials bounded by short stacking-fault region. Partials' spacing is marked as d [55].

A twin is a region of the crystal where the lattice orientation is a mirror image of the orientation of the rest of the crystal. The formation of a twin can be described as a lattice shear (see Figure 2.4). Twins can form during crystal growth (annealing twins) or by deformation (mechanical/deformation twins) [51]. Twinning is characterized by one specific plane (the 'mirror', 'coherent twin' or 'twinning' plane K_1) and one specific

direction (the shear direction η_1). For *f.c.c* materials the K_1 plane is {111} and η_1 is <11-2> [57]. In *f.c.c.* metals, perfect twin boundaries are characterised by a misorientation of 60° about the <111> axis and have 1 in every 3 lattice sites coinciding. They are described as Σ3 coincident site lattice (CSL) boundaries where Σ represents the reciprocal density of coincident sites [58]. It has been reported that fatigue cracks predominantly nucleate at the {111}/ Σ 3 boundaries in strain controlled high cycle fatigue tests on an annealed austenitic stainless steel at room temperature [59]. But the propagation rate of fatigue cracks was lower for the specimens of 304 stainless steel with a higher fraction (73 %) of low- Σ boundaries including Σ 3 boundaries (58 %) than for the specimen with a lower fraction (53 %) of low- Σ boundaries including Σ 3 boundaries (39 %) [60].

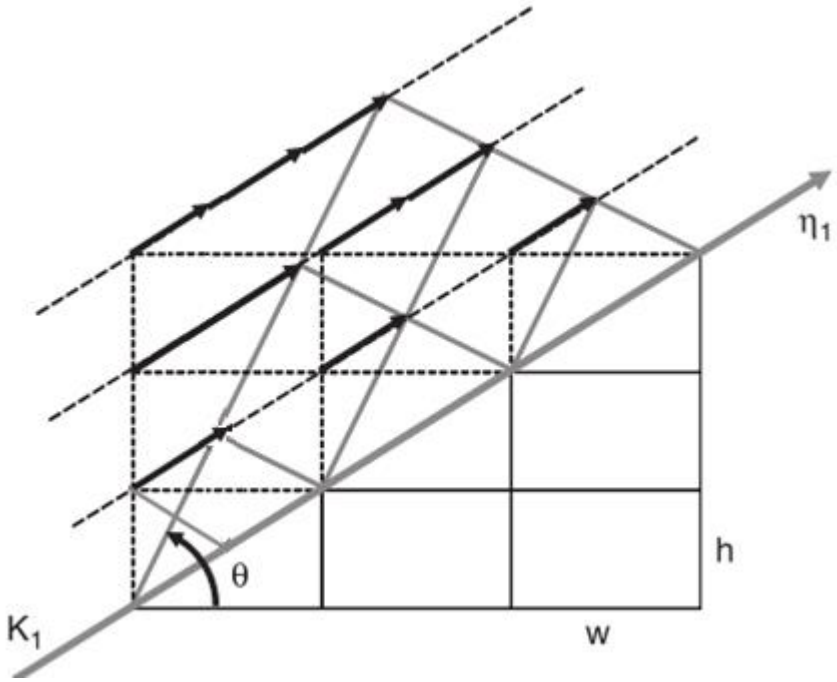

Figure 2.4 Formation of a twin by shearing over parallel atom planes. K_1 is the twinning plane and η_1 is the shear direction. The value of 'h' is 'a' and 'w' is 'a$\sqrt{2}$' where 'a' is the lattice parameter.

2.3. Creep deformation in austenitic stainless steel

Time dependent deformation in material at elevated temperature is called creep. Generally, significant creep occurs at homologous temperatures above 0.5 (the homologous temperature is the ratio, using the absolute scale, between the test temperature and the material's melting temperature), but this critical value can be increased by adding suitable alloying elements whose atoms take substitutional or interstitial locations depending on their size. Creep strength can be improved by the addition of finely dispersed particles of a second phase. The precipitates should be stable to high temperature, preferably above the recrystallization temperature, for good creep resistance [45], [53], [61], [62].

Figure 2.5 shows a typical constant load creep curve. The creep curve is characterised by four main regimes, defined according to their creep rates. These are instantaneous strain (during initial loading), primary creep (decreasing creep rate due to increasing strain hardening from the mobile dislocations introduced on loading), secondary creep (equilibrium between strain-hardening and recovery processes, producing a steady-state creep rate) and tertiary creep (accelerating creep rate due to metallurgical changes such as the formation of cavities, coarsening of precipitates and re-crystallisation) [51], [61], [63]. The minimum creep rate is an important design parameter in the design of alloys since secondary creep occupies a large proportion of material's service-life. During primary creep in 316H steel, the density of mobile dislocations increases with the applied stress [64] [65] and so does the primary creep rate.

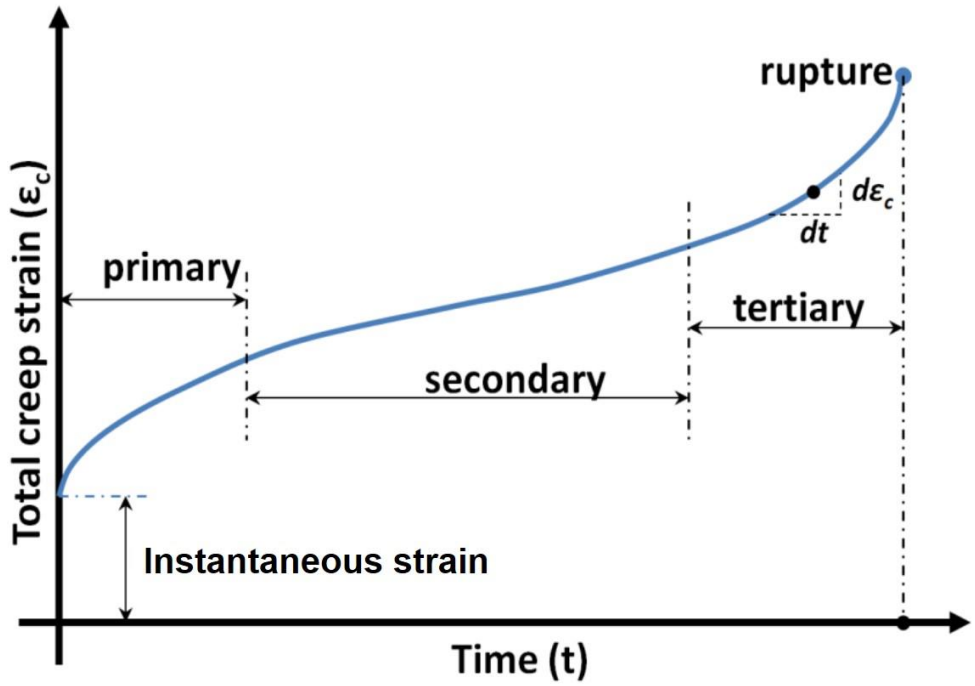

Figure 2.5 Typical constant load creep curve (schematic) [11].

2.3.1. Dislocation structures formed during creep

Dislocation climb is enhanced by the increased atomic diffusion rates at elevated temperatures. Climb allows dislocations to change their slip planes and bypass obstacles. The dislocations' improved mobility through climb and cross-slip, allows them to annihilate by interactions between oppositely signed dislocations or to rearrange to form low-energy configurations such as low angle boundaries. A low angle boundary is essentially an array of dislocations which separate regions of a crystal differing in orientation by less than approximately 15° [50]. During recovery the tangles and networks of interlocked dislocations are gradually released and rearranged, thus reducing their density, leading to the formation of 3D dislocation networks (although we only see a 2D projection in TEM images) [11] [66] [43].

2.3.2. Deformation Mechanism Maps

Ashby et al [64] represented all the possible deformation mechanisms of a material in a stress-temperature space. The various regions of the map show the different dominant deformation mechanisms for those stress-temperature conditions. The deformation maps of a 316 stainless steel at two different grain size are shown in Figure 2.6 and Figure 2.7. The strength of stainless steel depends on its service history. However, the deformation maps describe the deformation mechanisms of the steel as determined in one state only, which is usually the bar-stock in the as received condition. An alternative way to represent creep data is as a map with strain-rate and stress as the axes (see Figure 2.8).

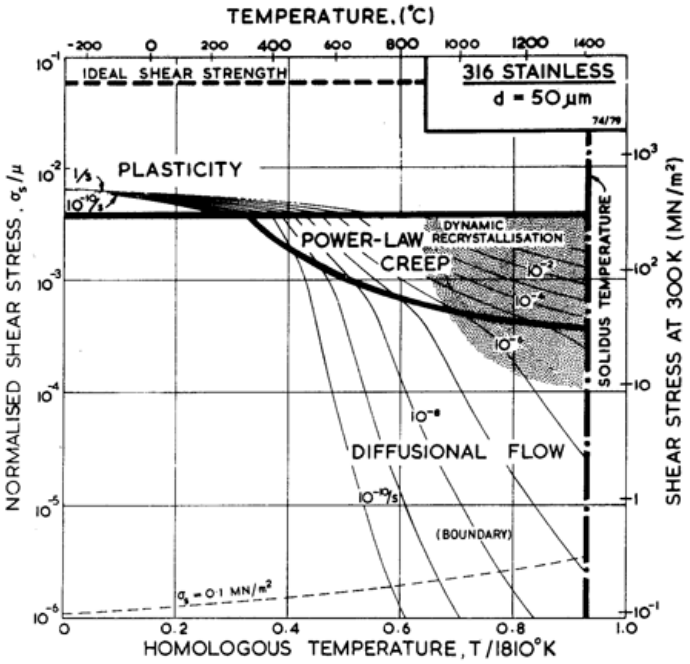

Figure 2.6 A deformation map for type 316 stainless steel of grain size 50μm [64].

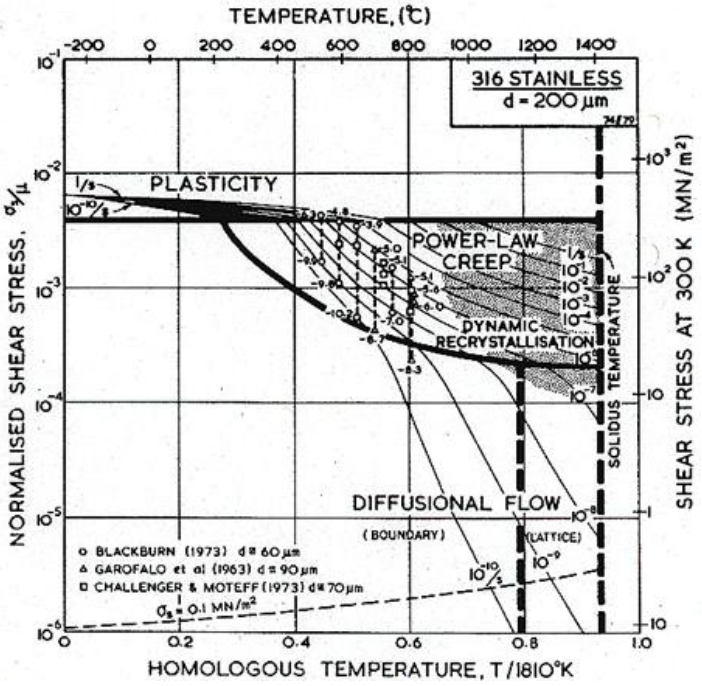

Figure 2.7 A deformation map for type 316 stainless steel of grain size 200μm, showing data [64].

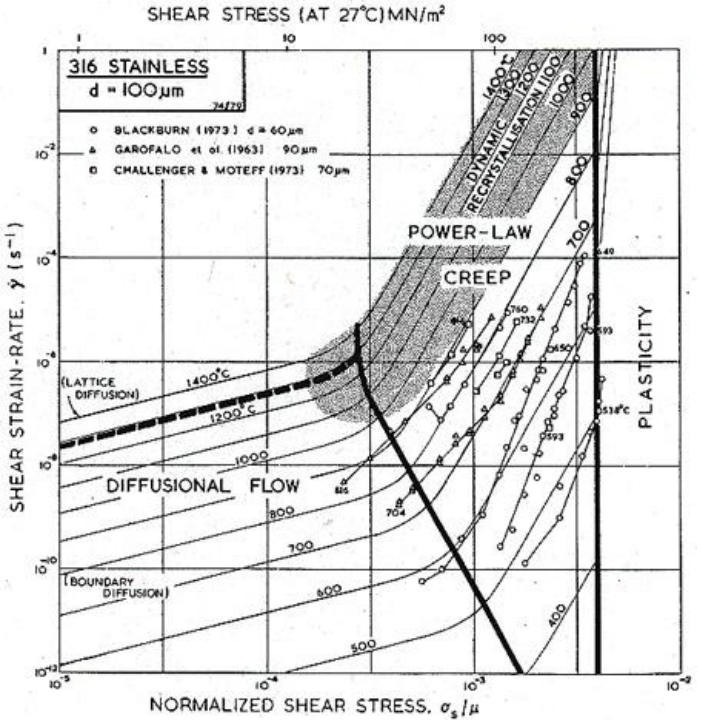

Figure 2.8 A strain-rate/stress map for type 316 stainless steel of grain size 100μm, showing data [64].

2.3.3. Microstructural changes due to creep

Creep deformation in metals is generally accompanied by the following structural changes:

Slip involving the movement of dislocations on certain crystallographic planes [52][55]

New slip systems may become active when metals are deformed at elevated temperature and in high temperature creep slip occurs over short distances on many different slip planes. This arises by the operation of many dislocation sources which at room temperature would be inhibited by the repulsion between dislocations from adjacent loops. At high temperatures the loops can climb and annihilate and a steady stream of new dislocations form from multiple sources.

Formation of sub-grain boundaries as a result of dislocation climb and rearrangement[52][55]

Creep deformation is inhomogeneous and may result in lattice bending, particularly close to the grain boundaries [11]. Lattice bending arises because locally more dislocations of one particular sign will be formed. Since dislocation climb can occur at high temperatures, the dislocations may arrange themselves into a low-angle grain boundary to minimize their total line and strain energies [50]. Sometimes with increasing dislocation density, the dislocations arrange to diffuse cell walls form rather than low angle grain boundary [11]. The dislocation density increases during primary creep up to a certain level and remains constant throughout the steady state creep. Large sub-grains are produced by creep at high temperature under a low stress or creep rate.

Grain boundary sliding (GBS) [52][55]

Grain-boundary sliding is a shear process which occurs at elevated temperatures in polycrystalline metals. It is promoted by increasing the temperature. GBS can be accommodated in three ways: elastic accommodation, diffusional flow or plastic flow. When GBS cannot be accommodated in any of these three ways, voids form and grow at grain boundaries [67].

2.3.4. Mechanisms of creep deformation

Diffusion creep

Diffusion creep occurs by the transport of vacancies through the crystal or along the grain boundaries. The deformation is achieved by the preferential formation of vacancies on those grain boundaries under tension and absorption of vacancies at boundaries under compression. Both vacancy formation and vacancy migration are thermally activated processes. When bulk diffusion of vacancies is dominant, this type of deformation is called Nabarro or Nabarro-Herring creep. At lower temperatures where grain boundary diffusion is dominant it is called Coble creep [51].

Dislocation creep

Thermally activated dislocation glide will be the predominant mechanism of creep deformation at stress levels above those indicated for diffusion creep on deformation mechanism maps. The creep rate depends on the obstacles in the material such as precipitates, solute atoms and other dislocations [53]. The climb of edge dislocations over obstacles is the rate-controlling step [68]. Depending on the temperature and stress, four different sub- classes of dislocation creep mechanisms can be found: glide and bulk diffusion-controlled climb; glide and pipe diffusion-controlled climb; Harper–Dorn creep and power law breakdown which are all well explained in the literature [53][51].

Grain boundary sliding

During grain boundary sliding (GBS) two grains slide over each other due to resolved shear stresses. Grains more or less keep their aspect ratios after extensive GBS in contrast to the mechanism of dislocation glide where grains are extended in the direction of deformation. At low strain rates, GBS may become more important than dislocation glide. GBS alone would result immediately in the formation of cavities between the grains where grains are sliding apart and an overlap of material where they come together. Hence GBS can influence the initiation of intergranular fracture even when it does not contribute significantly to steady state creep [51].

2.3.5. Stress relaxation in metals

Stress relaxation tests, where the strain is held constant and the stress decreases, help to determine creep strain rates in a considerably shorter time than constant load creep tests that take weeks to months. These tests allow sampling of a wide range of stresses and strain rates with a very small plastic strain. Here, the elastic strain (ε_e) is transferred to plastic strain (ε_p); the total strain (ε_T) remains constant.

$$\varepsilon_T = \varepsilon_e + \varepsilon_p = C \quad (2.2)$$

As the test proceeds, elastic stresses relax thereby replacing elastic strain by plastic strain, through a creep deformation process, which depends on the applied stress.

Substituting Hooke's law

$$\sigma = E\varepsilon_e \ (2.3)$$

where E is Young's modulus and σ is the stress, into equation 3 and differentiating with respect to time,

$$\frac{d\varepsilon_p}{dt} = -\frac{1}{E}\frac{d\sigma}{dt} \quad (2.4)$$

relates the stress rate during the stress relaxation test to the plastic or creep strain rate. Stress relaxation tests are also referred to as self-programmed variable-stress creep tests [69]–[71].

The maximum elastic strain is given by,

$$\varepsilon_{e(max)} = \frac{\sigma_y}{E} \quad (2.5)$$

The stress relaxation behaviour during simulated age-forming (SAF) of Al-Zn-Cu alloy at 120, 160 and 200ºC was divided in to 3 stages (see Figure 2.9). Stage I was the high stress stage, Stage II the medium stress transition stage and Stage III the low stress equilibrium stage [72]. The deformation activation energy and the stress exponent suggested that the mechanisms of stress relaxation are dislocation creep in stages I and II, and Coble creep (diffusion process of vacancy transfer along grain boundaries) in stage III [72].

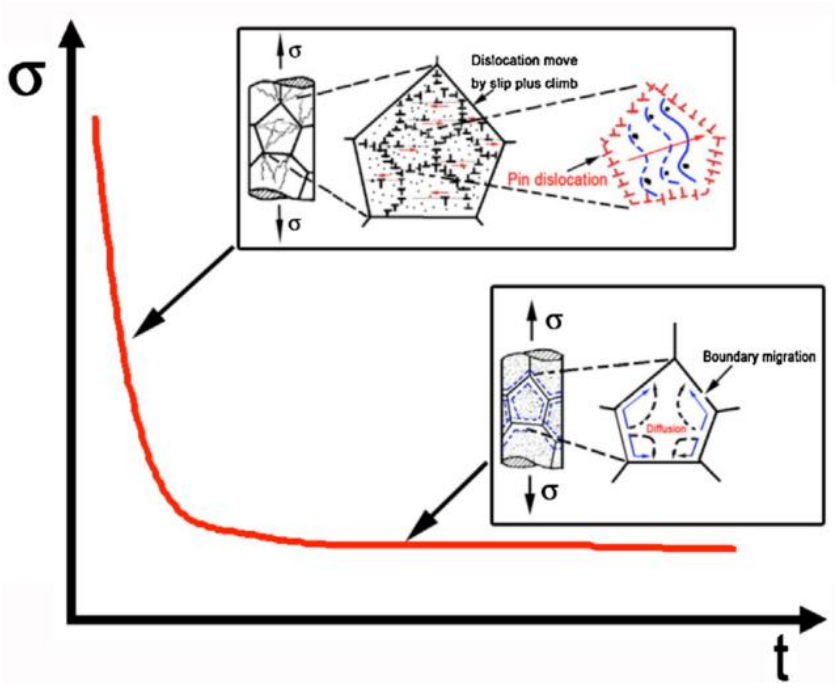

Figure 2.9 Schematic mechanism diagram for the Al–Zn–Mg–Cu alloy in stress relaxation [72]

2.3.6. Dynamic strain ageing in austenitic stainless steels

Dynamic strain aging (DSA) is a hardening mechanism affecting many materials, which manifests itself by “jerky” or serrated plastic flows and inhomogeneous yielding. These instabilities are referred to as the Portevin Le-Chatelier (PLC) effect [51], [73], [74], and arise from temperature dependent strain localisation within a specific range of strains and strain rates, as a consequence of DSA [2]. The PLC effect increases the flow stress, ultimate tensile strength and the work hardening rate. It also decreases the ductility of metals with corresponding decreases in elongation, the effective gauge cross-sectional area, the strain rate sensitivity coefficient and the fracture toughness [75]. DSA has been reported in austenitic stainless steels over a temperature range of 273ºC to 800ºC [76]. Generally the deformation of stainless steels is independent of the strain rate at room temperature, whereas at higher temperatures, the strain rate has a significant effect on the flow stress [53], [77]. In binary Al-Li alloys the serrations were not affected by precipitation [78].

DSA occurs as a result of interaction between the moving dislocations/defects and diffusing solute atoms (e.g. C, N, Cr) during deformation. The mobile dislocations act as carriers of the plastic strain and move among the obstacles formed by other defects in the bulk material [75]. The serrations may be attributed to a repeated locking and unlocking of dislocations from their solute atmospheres [79], leading to heterogeneous deformation with an alternating increase/decrease in plasticity, despite monotonic straining [74]. The maximum temperature at which serrations are seen is when the characteristic rearrangement time of the solute clouds around the moving dislocations becomes short enough to keep up with the dislocations’ changing positions, so that the dislocations can no longer break away from them. The dislocations then "drag along" their clouds in thermal equilibrium [80].

Teresa et al [81] classified the tensile curves into major 2 types. Type A serrations separated by smooth curve segments as seen in curve a in Figure 2.10 are caused by Luders bands that nucleate at one specimen grip and propagate smoothly in succession, one at a time to the other grip. Periodic serrations start, after an initial strain, due to the jerky propagation of the bands. As the bands move irregularly, when the bands reach areas of high local stress, the overall stress has to rise to continue deformation. Further deformation leads to a smooth distribution of bands (curve b in Figure 2.10, e.g. 316H at 550^{o}C, 0.025%/s, see Figure 5.1). Once, smooth bands are formed, any following new bands will also be smooth resulting in curve c of Figure 2.10. Local heterogeneities (e.g. severe notches) already present in the material or any introduced during deformation (e.g. by a long load suppression or load relaxation during band propagation; strain gradient associated with the Luders band front can been related to dislocation motion and strain hardening behaviour [82]) may lead to irregular serrations or alternating serrations (Type B) in the flow curve (curve f and d respectively in Figure 2.10). A smooth curve is obtained when solute moves rapidly to dislocations. i.e. when there is little or no heterogeneity or localization (curve e in Figure 2.10).

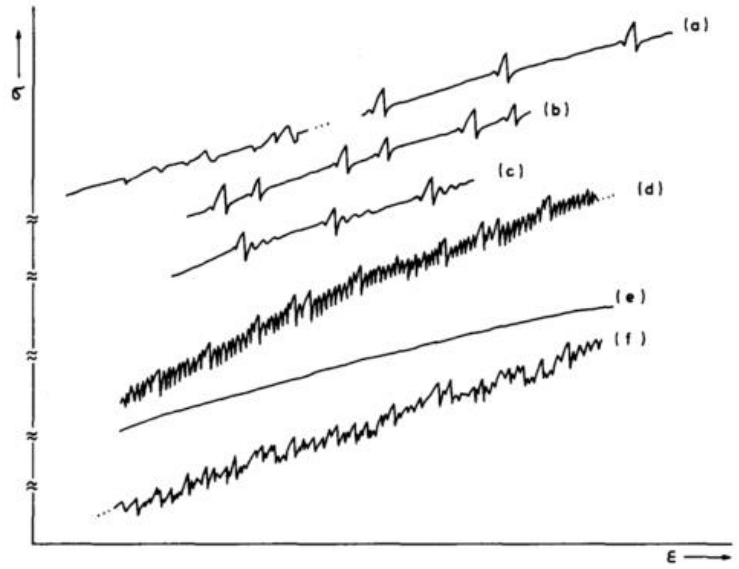

Figure 2.10 Types of tensile curves demonstrating DSA under different conditions: (a) 'normal' type A serrations, (b) alternating type A serrations, (c) transition to type B serrations, (d) type B serrations, (e) non-serrated curve, (f) irregular serrations due to heterogeneities [81].

2.4. Fatigue and Creep-fatigue deformation in austenitic stainless steel

When pure metals are subjected to cyclic plastic strains, they may soften or harden depending on their initial microstructure [83]. When well-annealed *f.c.c* single crystals oriented for single slip were subjected to fully reversed cyclic strains, rapid hardening was observed for first few cycles followed by saturation. The dislocation density increased during the tensile part of the cycles and reduced during the compressive part due to the interaction and annihilation of dislocations during the compressive part [84]. If a pre-strained material is stressed in the direction opposite to the pre-strain direction, a lower yield strength is often obtained. This is called the Bauschinger effect [85].

The relationship between the macroscopic slip mode and the type of dislocation structure (e.g. tangles, persistent slip bands, cell etc.) formed during cyclic deformation of polycrystalline *f.c.c* metals and alloys was first described by Feltner and Laird [83], [86]. Wavy slip lines indicate that cross slip can occur easily and that the cyclic stress-strain

behaviour is likely to be independent of strain history. In the planar slip mode, cross slip is difficult and the material's cyclic behaviour is dependent of its previous cyclic stress-strain history [87][88]. At room temperature, crack initiation in fatigue occurs by the motion of dislocations back and forth along slip planes, gradually resulting in the formation of extrusions and intrusions on the surface. Eventually a crack develops at one of these discontinuities which then grows along the slip plane (stage I in Figure 2.11) before propagating perpendicular to the maximum principal stress axis (stage II) [62]. In polycrystalline commercial alloys, grain boundaries, precipitates, impurities and texture all affect the fatigue deformation. The damage (measured in terms of the inelastic strain accumulation) caused by variable loading of materials is cumulative and is usually manifested only in the final stages by macroscopic crack propagation and final fracture [89].

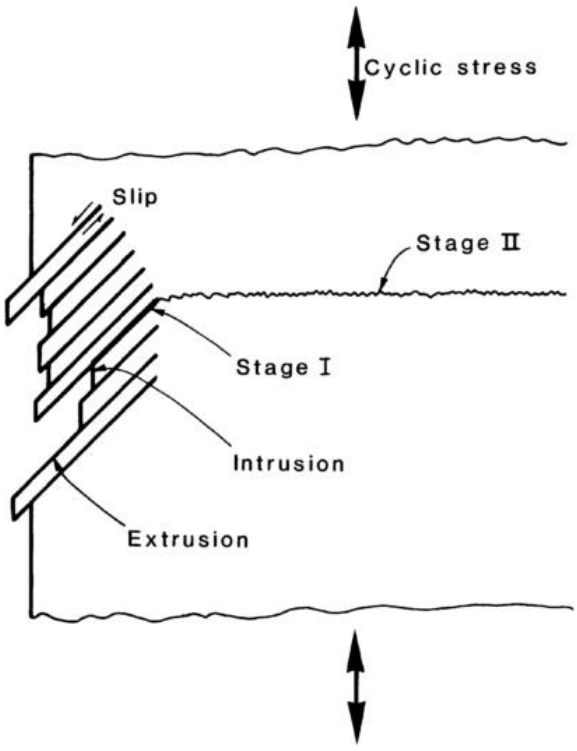

Figure 2.11 Mechanism of fatigue crack initiation and growth [62]

It should be expected that fatigue properties are also affected by the temperature. The effect of a high temperature on the mechanical properties can be associated with transformations of the material structure due to diffusion processes, enhanced thermal activation of processes other than diffusion (eg: climb), aging, dislocation restructuring (softening), and recrystallization [90]. Intergranular cracking can be observed after fatigue [62]. In this case, the stage I region was reduced and can be eliminated altogether if a grain boundary acts as a crack starter.

In cyclic tests at any given plastic strain amplitude, *f.c.c*. materials with a low SFE and showing planar slip exhibit more reversible slip and better fatigue resistance than *f.c.c*, materials with a high SFE and a wavy slip mode [91].

At temperatures below 250ºC, 316H austenitic stainless steels subjected to cyclic deformation show rapid hardening followed by softening until a saturation peak stress is attained [92]. Above 250ºC, the softening is gradually replaced by a more pronounced cyclic hardening and an increase in the saturation peak stress. The strain hardening can be attributed to the generation of dislocations and their mutual interaction as well as the interaction of interstitial solute atoms with the dislocations which generate the plastic and creep strains. The softening could be associated with rearrangement of the dislocations and micro-crack generation [93]. The saturation stress stage continues (or the stress slightly decreases with the number of cycles) up to failure [92]. Planar arrays of dislocations were reported after cyclically deforming 316H austenitic stainless steel at temperatures in which a minimum in the saturation peak stress occurs (between room temperature and 250ºC). Cell substructures were observed between 250 and 850ºC [92].

2.4.1. Factors affecting the fatigue/creep-fatigue endurance of 316SS

Hold time/Dwell time: Considering the creep-fatigue interaction during cyclic deformation with a hold period at either the peak tensile strain or the peak compressive strain, different parameters characterising the stress relaxation behaviour near half-life can be defined as shown schematically in Figure 2.12.

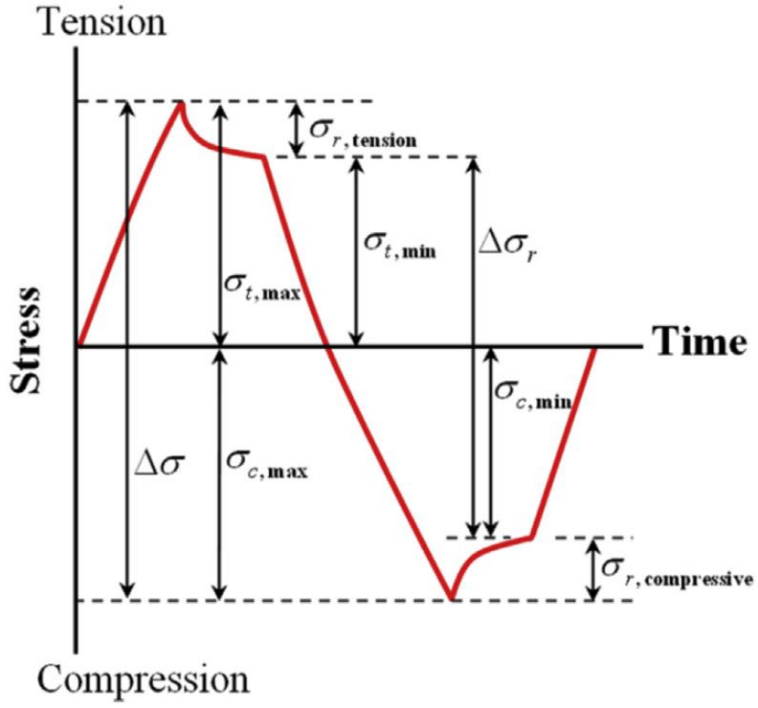

Figure 2.12 Definition of the different characteristic stress values observed in hold-time tests [94].

The shape of the relaxation curve depends both on the strain range and the temperature [94]. Stresses are found to relax more at higher temperatures or higher strain ranges. However, when the hold period is extremely long, the degree of stress relaxation becomes almost constant [94].

When plotted on a log-log scale, the number of cycles to failure at 600^{o}C, at a given strain range, decreases linearly with increasing hold period, except in the case of extremely long hold periods (~900min). However at 593^{o}C, a total strain range of 2% and a hold period

of 24hr, the of number of cycles to failure, N_f was higher than that with a hold period of 10hr, due to aging of the materials during the long-hold testing [94]. In comparison to continuous cycling, the reduction in fatigue life on introducing dwell times may be due to the interaction between the steady advancing fatigue crack and the creep damage formed during the periods of stress relaxation [95]. Stress relaxation during hold was attributed to the (enhanced) recovery of the dislocation structure that may favour the development of a cell-subgrain structure [96]. The reduction in fatigue life (compared to continuous cycling) is greater at lower strain ranges than higher strain ranges. At a given strain range, the number of cycles to failure, N_f in symmetrical hold (both tensile and compressive hold) testing is higher than that in the tension hold testing for a given hold period which indicates that in creep fatigue testing of 316 SS the tensile hold produces more damage than the compressive hold. The effect of a tensile hold on the value of N_f becomes more obvious at higher temperatures [94].

Cycle time (C_t): When c_t is very short (<6s for a total strain range of ±1%) or long (>10min for a total strain range of ±1%), the value of N_f is independent of c_t for continuous cycling at 600^{o}C at a strain rate of $6.7x10^{-3}s^{-1}$ [97]. Consistent behaviour was observed for tension-hold-only and symmetrical hold testing, in that on a log-log plot the value of N_f decreased linearly with increasing c_t. For a given cycle time, the value of N_f in the symmetrical hold testing is generally higher than that in the tensile hold only testing [97].

Strain range: Figure 2.13 shows the relationship between the plastic strain range ($\Delta\varepsilon_p$) and number of cycles to failure (N_f) in creep damage testing at 593 and 693^{o}C with different tensile hold periods. It's clear from the literature that at a given $\Delta\varepsilon_p$ the value of N_f decreases with increasing hold period.

At a given hold period, the relationship between $\Delta\varepsilon_p$ and N_f is identical to the Coffin-Manson relationship [94]

$$\frac{\Delta\varepsilon_p}{2} = A(2N_f)^c \quad (2.6)$$

Where A and c are the fatigue ductility coefficient and the fatigue ductility exponent respectively. The values of A with a positive sign and c with a negative sign increase as the tensile hold period increases. Hence, the $\Delta\varepsilon_p - N_f$ curve becomes steeper at longer hold periods.

The curves in Figure 2.13 provide a method of extrapolating the results from short hold period tests at high plastic strain ranges to much lower plastic strain ranges. If experiments are carried out to determine the $\Delta\varepsilon_p - N_f$ curves at different temperatures, the values of A and c can be fitted with respect to hold time and temperature. A model, which can be considered as the modification of Coffin-Manson equation, can be developed to predict the value of N_f at a given $\Delta\varepsilon_p$ [94].

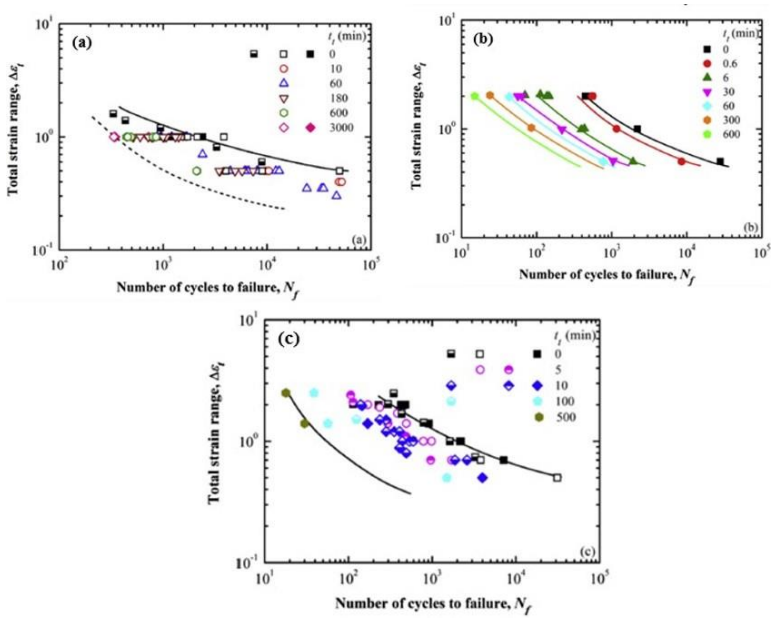

Figure 2.13 The effect of total strain range, $\Delta\varepsilon_t$, on the number of cycles to failure, N_f, of 316 steels with different hold periods at (a) 550 °C, (b) 593 °C, and (c) 600°C. [94].

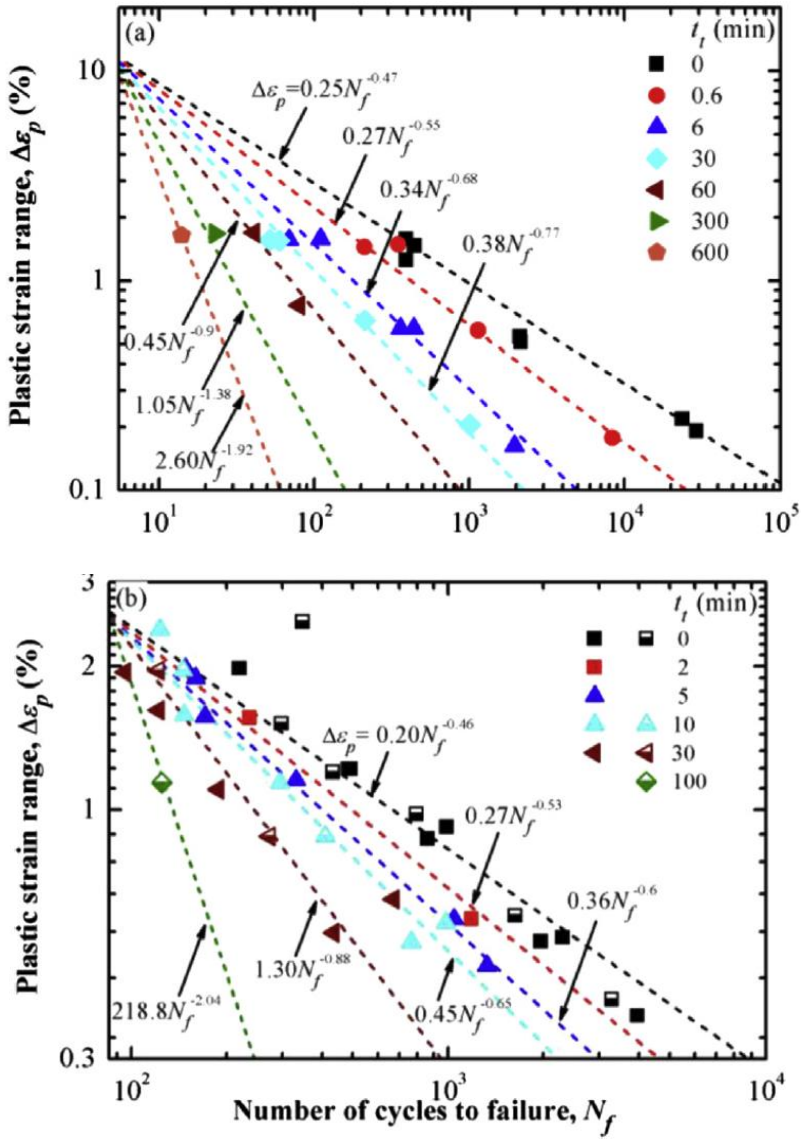

Figure 2.14 Relationship between the plastic strain range $\Delta\varepsilon_p$, and the number of cycles to failure N_f, with different tensile hold periods at (a) 593°C, and (b) 600°C. The solid symbol and lower half-filled symbol respectively denote the materials of type 316 and 316L stainless steel [94].

Cyclic frequency/ Strain rate: Comparison of metallographic and fractographic studies of low cycle fatigue and thermomechanical fatigue tests of 316 austenitic steel with and without dwell periods showed that the proportion of intergranular cracking increased as the frequency was reduced from 0.01 Hz to 0.001 Hz. Furthermore, transgranular fatigue failure dominated at high frequencies whereas intergranular, time-dependent failure

predominated at low frequencies and low imposed mechanical strain amplitudes. Both transgranular and interganular failure was observed at intermediate frequencies and strain amplitudes [96].

Prior Deformation: Investigation of the effects of prior deformation on creep behaviour is essential as most components used in power-generating plants enter service in a pre-strained condition, e.g. welded components. Most studies conducted on 316 stainless steels, indicate that pre-straining reduces the initial creep loading strain but has a variable effect on the creep rupture strains and minimum creep rates. Generally, prior deformation increases the number density of dislocations which limit the movement of dislocations in the subsequent creep loading [98]. At elevated temperatures, carbide precipitation pins the dislocations introduced during the pre-straining, further limiting their movement and hence reducing creep rates [99].

2.4.2. Calculation of creep-fatigue damage

The term '**Damage**' is generally used to indicate deterioration of material properties. As mentioned earlier in this chapter, accumulated inelastic strain is referred to as damage in this thesis. However, the literature uses the term damage in different senses as briefly reviewed below. Fatigue/ creep-fatigue damage (from stress-strain test data) is mainly calculated in the literature by three methods.

- Cumulative inelastic strain energy [96], [100] (used mainly for fatigue deformation and defined by the area under the stress strain curve, see section 6.2.3 for more details)
- Cumulative inelastic strain (used for creep, fatigue and creep-fatigue loading see section 6.2.3)

- Time fraction to failure (explained later in this section which is used in RCC-MR codes) or number of cycles to failure (for fatigue/ creep-fatigue loading)

Creep-fatigue tests can be analysed using R5 [101]–[104] procedure methods that account for cyclic fatigue and creep deformation, where the results can be compared with the R5 creep fatigue initiation diagram, and other test data available for the material [101].

The total creep-fatigue damage, D is considered as the linear sum of damage due to fatigue (D_f) and creep (D_c). Crack initiation is considered to occur when D=1 [101]. The process of fatigue damage is considered as two stages. The first corresponds to the formation of a defect size, a_i = 0.02mm. The second stage is the growth of this defect to a specified depth, a_0.

D_f and D_c[1] can be used to define the co-ordinate axes of the 'Damage Diagram' shown in Figure 2.15. A crack initiation envelope can be plotted defining the locus of the points where $D_f+D_c = 1$. If $D < 1$, then crack initiation is avoided [101].

[1] Where D_c is defined as ductility exhaustion ratio of cumulative creep strain to the rupture strain including the effects of multiaxial loading in R5 procedure [101].

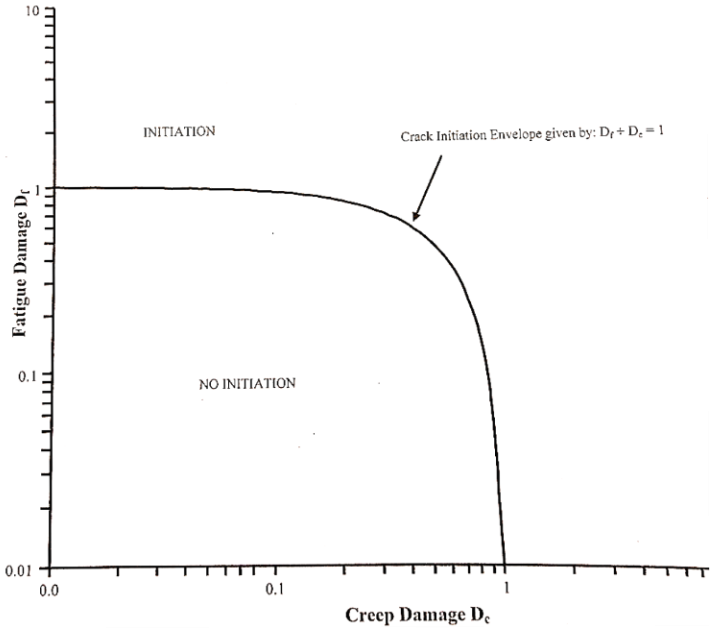

Figure 2.15 Creep-fatigue damage interaction diagram [101].

The RCC-MR codes [101] calculates overall damage in a creep-fatigue deformation as,

$$D_t = D_c + D_f = \sum \frac{t_h}{t_r} + \sum \frac{N}{N_f} \quad (2.7)$$

The creep damage term (D_c) is the fraction of the total amount of the hold time, t_h so far (i.e. up to the N^{th} cycle) to the rupture time, t_r (obtained from a pure creep test at the same stress as during the hold period). The fatigue damage term (D_f), is the current number of cycles (N) for the fatigue tests with hold periods at a given strain amplitude as a fraction of the to the number of cycles to failure (N_f) for continuous cyclic tests at the same strain amplitude.

This empirical model based on cumulative damage assumes that the life of specimens is governed by the separate accumulation of fatigue and creep damages and gives conservative estimates of remaining life.

Hormozi et al [93] developed a new model for the overall damage caused in cyclic and creep fatigue deformation, which used a hysteresis energy damage parameter for the

fatigue damage calculation. This showed good agreement with experimental results for low cycle tests and creep-fatigue tests at 650^{o}C.

The total damage was calculated in this model as

$$D_t = D_c + D_f = \int_0^{t_h} \frac{dt}{t_r} + \text{hysteresis energy damage} \quad (2.8)$$

The hysteresis energy damage is calculated as a function of the average of the inelastic strain energy density for the number of cycles after which the damage initiated.

2.5. Reheat cracking and cavitation in 316H steel

Reheat cracking has been found to occur in type 316H stainless steel steam headers during service at around 550^{o}C after about 10,000-20,000 h of operation [105]. Intergranular cracks, resulting from the coalescence of cavities nucleated around intergranular particles, were observed in the HAZ between 1 to 5mm away from the fusion line of 316H steel welds [106]. Welding thermal cycles introduce local plastic strains in the joint HAZ owing to mechanical constraint. Thermal expansions and contractions are accommodated by elastic deformation beyond the HAZ and hence the base metal is unaffected. But severe thermal gradients closer to the weld region induce more plastic deformation and hence hardening. TEM studies of the HAZ of 316H showed a very high dislocation density with well-defined dislocation cells [106]. Towards the weld region, the hardness and dislocation density can reduce due to partial recovery at the welding temperature [106][107]. The increase of hardness in the weld HAZ may also be due to the strain induced nucleation of intergranular and intragranular $M_{23}C_6$ carbide precipitates which may increase temper embrittlement. These microstructural features are more predominant in aged material [38], [106].

Twin boundaries and low angle grain boundaries are found to be resistant to cracking in austenitic stainless steels [108][109]. Studies of cracking in the coarse-grained heat-affected zone of T23 (2.25Cr–1.6W) steel showed that only random high-angle boundaries played a crucial role in intergranular cracking. Cavities and small cracks were preferentially initiated from high angle grain boundaries. Grain boundaries with misorientation angles less than 15^{o} were found in this study to be more resistant to cracking [110].

Cavity nucleation and growth are significant in the creep-damage dominant condition under creep-fatigue loading [111]. Ueno et al [111] investigated creep-fatigue loading of 304 stainless steel under creep-damage-dominated conditions. The courses of cavity and precipitate nucleation and growth and of microcrack initiation were studied. Cavities were observed at 2% life cycle in regions adjacent to precipitates such as carbides Their results showed that beyond 20% total life, the cavities nucleated along grain boundaries at sites nearly perpendicular to the loading direction and that they continued to grow up to the end of life. Cavities which were not at boundaries perpendicular to the loading direction stopped growing. The area fraction of cavities (AFC) increased with increasing life fraction. At 100% life cycle, grain boundary separation was seen at cavities and some interfaces between precipitates and grains also separated [111].

2.6. Creep strain/damage characterisation techniques

Characterising the creep strain (or damage in terms of inelastic strain) of high temperature structural components power plants is very important in order to guard against failure. The available techniques can be broadly classified into three groups: metallurgical methods, microscopic techniques and methods based on physical properties.

2.6.1. Metallurgical based methods

These are deployed during a planned site overhaul as a part of a pre-planned inspection schedule.

Replica metallography: This is a non-destructive testing (NDT) technique, generally used during plant maintenance. It involves replicating the microstructure of a metallographically prepared surface onto a film, which is then subjected to microstructural evaluation. It can quantitatively and qualitatively monitor the growth of cavities [112].

2.6.2. Macroscopic techniques

These measure the creep damage through examining macroscopic scalar quantities

Dimensional effects: Maharaj et al [113] obtained a high degree of correlation between changes in the outer diameter of a superalloy tube with creep damage, but for accuracy the results had to be corrected for oxide growth and temperature [104].

Extensometer: In laboratory tests, uniaxial creep strain is frequently measured by using cylindrical bar test pieces on which ridges have been machined to identify the gauge length over which strain is to be measured. Mechanical extensometers, fitted to these ridges, are used to transfer their displacements during creep to a location outside the high-temperature furnace, where they can be accurately measured by low cost transducers at ambient temperatures. The measured displacements are then used to compute the variation of strain with time [114].

LVDT transducer: The linear variable differential transducer (LVDT) consists of a hollow pipe which contains a number of axially spaced cylindrical coils (see Figure 2.16). The output voltage of the coil varies with respect to the shaft position. When the central primary coil is energised with alternating current, voltages are induced in the secondaries.

The coils are connected in series opposition so that the two voltages are in antiphase in the secondary circuit and the net output is the difference between these two voltages. The LVDT transducer is attached to a frame that is fixed at the top and the bottom of the test specimen; the strain is measured between these two points. LVDT transducers can measure large deformations in a repeatable way even at high temperatures, but they are not suitable in dynamic loading because of their large mass [115].

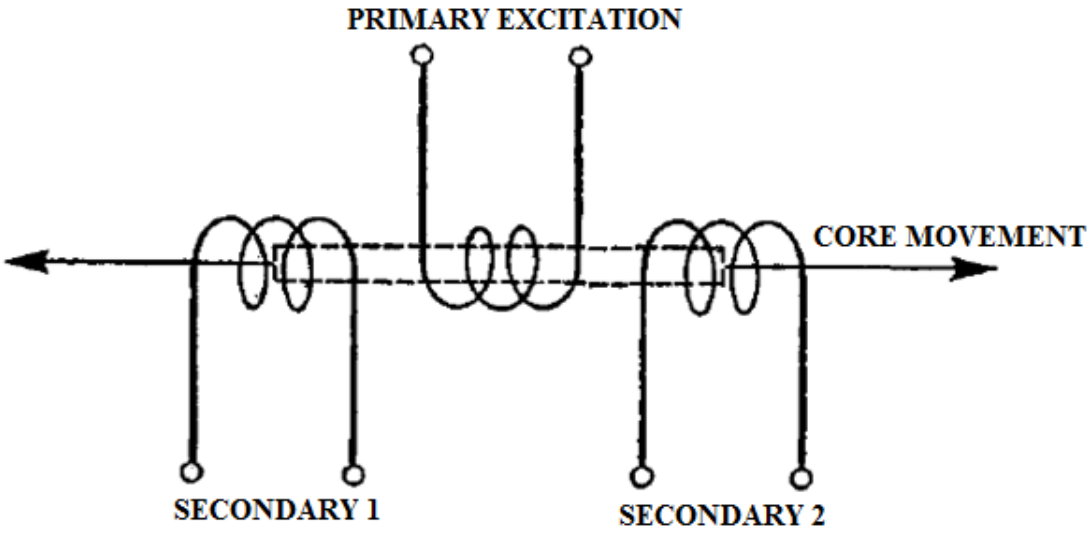

Figure 2.16 Schematic of LVDT [115].

High temperature capacitive strain gauges: these can measure strain at high temperature and have long term stability. The strain is measured as a function of the difference in capacitance between two plate areas [116].

Hardness measurements: hardness is a measure of a material's resistance to deformation. In many steels hardness values have also been found to be proportional to the square root of the dislocation density [117][118]. Hardness measurements are used to find areas of softening during creep. Although there is a high degree of scatter in hardness data, hardness testing can be used as a predictive approach to estimate remaining life [119]. The main reason that hardness measurements carried out in industrial environments

are often affected by large errors is that the presence of a thin soft surface layer, generally produced by decarburisation during the steelmaking heat treatment, can produce highly misleading results unless the surface is prepared by material removal. Another reason is the high sensitivity of this technique to local microstructural variations, resulting in large point to point variation in the same specimen and poor reproducibility, especially when the load applied to the indenter is low. This is a major issue in monitoring welds, especially at the narrow heat affected zones where most failures occurs. The point to point scatter might lead to inaccurate estimations of properties. Therefore hardness measurements are only used to get a qualitative indication of whether a component has experienced excessive temperatures during service [112].

Digital Image Correlation (DIC): DIC is based on using sophisticated computational algorithms that track the patterns (usually made by depositing paint or metallic coatings) in digital images of the test surfaces, taken before and after a loading event that produces surface deformations to calculate the strain distribution on the surface [8].

2.6.3. Techniques based on physical properties

The signals/data obtained from most of the NDT techniques mentioned above are only affected by creep in its early stages and most of these methods are generally used to detect volumetric creep, Few of them can detect localised creep, which frequently causes the failure of welded components [112].

Ultrasonic testing: Ultrasonic absorption increases with increasing creep strain in measurements made in Cr-Mo-V low-alloyed steel. This has been attributed to the altered dislocation structure that increases the dislocation damping [62], [112].

Acoustic emission: This technique quantifies creep damage using the sound waves that are emitted during an object's deformation. With proper validation this can be used to identify a flaw's location, type and criticality [120].

X-ray Diffraction Peak Profiling: X-ray peaks shift with elastic strain and broaden with plastic strain. The broadening of the diffraction peaks is due to the reduction of periodicity in the lattice, which is related to the density of dislocations and other lattice imperfections. Imperfections/dislocations cause the peaks to broaden, become asymmetric and move from the Bragg position [121]. More details about X-ray peak broadening are given in Chapter 3.

Small Angle Neutron Scattering: Neutrons can be used to study the microstructural features in a material. Grain boundaries, dislocations, precipitates or voids scatter an incident neutron beam. The advantages of neutron scattering over conventional X-rays are a simplified data analysis, due to the absence of multiple Bragg scattering if neutrons of longer wavelength (order of magnitude of 1 nm) are used, and the ability to inspect thicker sections. Small Angle Neutron Scattering (SANS) is used to study precipitates and cavities, which are the main sources of scattering in creep damaged structural components [112], [122], [123].

EBSD: Electron backscatter diffraction (EBSD) is a scanning electron microscope (SEM) based electron diffraction technique allowing automated mapping of crystal orientations at ~50nm spatial resolution (material dependent) from bulk samples. Several researchers have attempted to measure the degrees of elastic and inelastic strain by using EBSD utilizing either changes in the diffraction pattern geometry or changes in the local orientation [22], [25], [27], [29], [32], [124]–[126].

2.7. Electron Backscatter Diffraction

EBSD is the most widely used tool for the determination of microtexture in metallic materials [124]. EBSD has been widely adopted among metallurgists due to the wide availability of SEMs, the ease of sample preparation from the bulk, the speed of its data acquisition, and its access to complementary information about the microstructure on a submicron scale [127].

2.7.1. EBSD working principle

The basic working principles of EBSD have been described in the literature [31], [51], [124], [125], [127]. The major component of an EBSD detector is the phosphor screen which captures the backscattered electron diffraction pattern and transmits it to a camera [125] which usually consists of a charge-couple device (CCD). A computer and dedicated software is used for pattern indexing, analysis and output (see Figure 2.19) [125].

EBSD patterns are generated by backscatter diffraction of a stationary beam of high energy electrons from a volume of crystal material approximately 10nm deep [112]. The backscattered diffraction or Kikuchi patterns are regular arrangement of parallel bands or lines on a steep continuous background (see Figure 2.17).

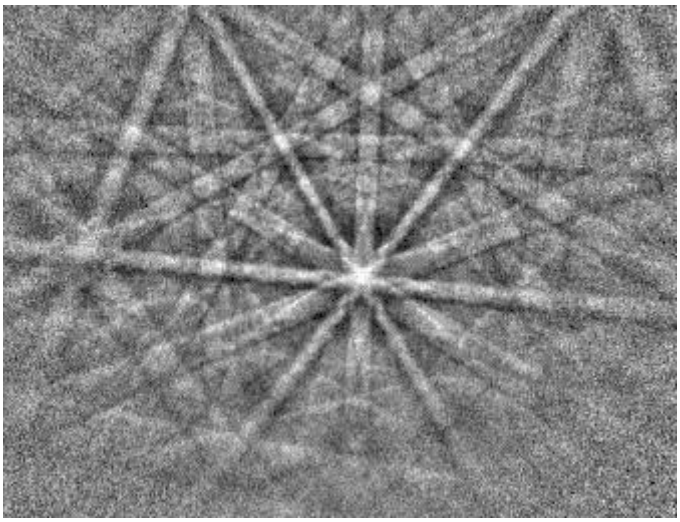

Figure 2.17 Backscatter Kikuchi pattern from Type 316H austenitic stainless steel at 20keV, acquired using a Zeiss Supra 55VP FEG SEM with a NordlysF detector.

When an electron beam falls on a crystalline material, it is scattered in all directions but the scattered intensity is not uniform. For EBSD in SEM, diffraction occurs from the interaction of primary "backscattered" electrons with (planes of) atoms close to the specimen surface. Those electrons that arrive close to the Bragg angle, θ_B for a set of lattice planes will undergo elastic scattering to give a strong, diffracted beam. The separation of these lines (the width of the diffracted bands) is related to the interplanar spacing ($\boldsymbol{d_{hkl}}$) according to Bragg's law:

$$2 \cdot d_{hkl} \cdot \sin \theta_B = n \cdot \lambda \qquad (2.9)$$

Where n is the order of diffraction and λ is the wavelength of the incident electron beam.

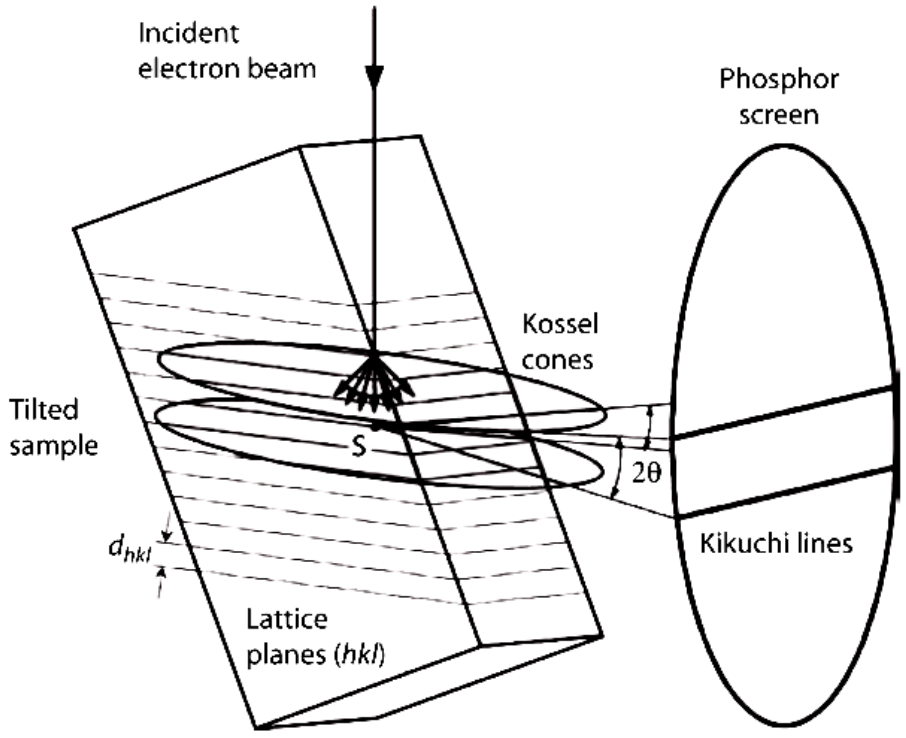

Figure 2.18 Formation of backscattered Kikuchi patterns by EBSD in SEM [124].

The envelope of the diffracted electrons from one set of planes is the surface of two cones (Kossel cones, see Figure 2.18). For SEM electron energies, the Bragg angle, θ_B is usually

very small. So the apex angle (180- $2\theta_B$) of the cone is close to 180^o, i.e. the cones are almost flat and hence their projection on the screen becomes a pair of straight lines [124].

The intersection of bands corresponds to a zone axis (or pole) and the major zone axes may be recognized by the symmetry of the intersection of several bands. The Kikuchi lines are directly linked to the arrangement of reflecting planes in the crystal and hence they show the orientation in the crystal. The crystallographic orientation is determined in three steps (see Figure 2.19) [124]:

- Identifying the positions of the lines
- Indexing the pattern, by determining the crystallographic indices of each Kikuchi band and pole.
- Determining the relative position of bands and poles with respect to an external reference frame i.e. Rolling direction (RD), Normal direction (ND) and Transverse direction (TD) (see Figure 2.19).

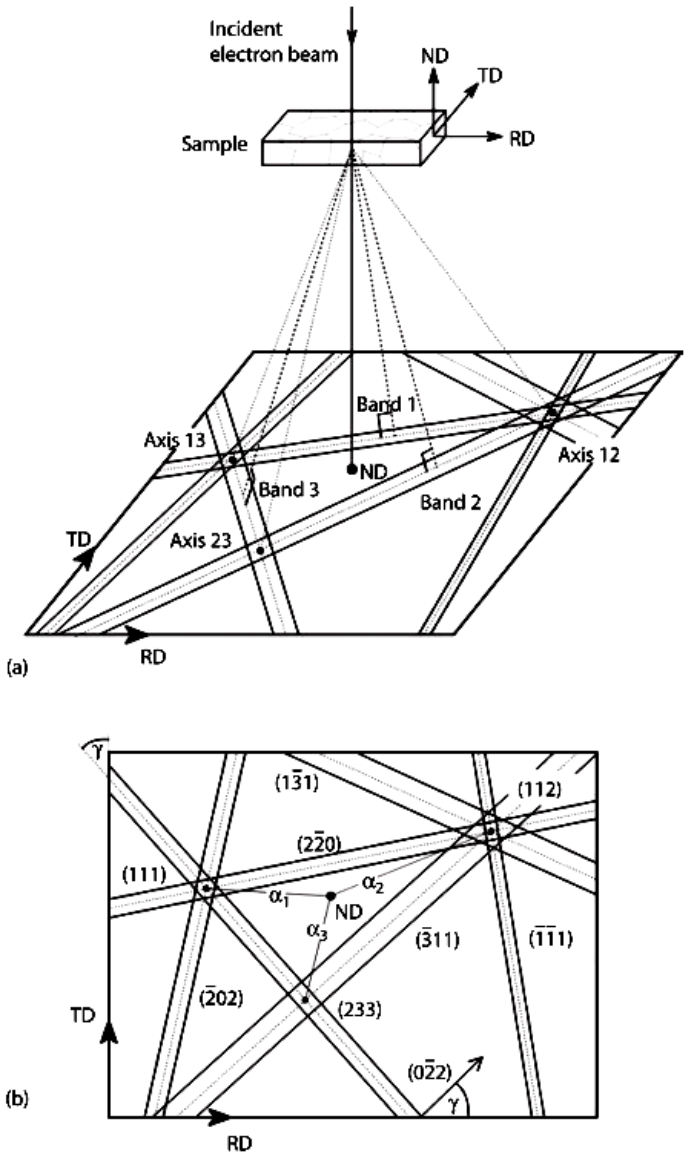

Figure 2.19 Diagrams illustrating determination of crystallographic orientation of a TEM Kikuchi pattern (a) Correlation between the reference frame and Kikuchi pattern and (b) Indexed Kikuchi pattern drawn to scale [124].

Very high angular resolutions of up to 0.1^o can be achieved in EBSD by using little binning (i.e. not combining groups of adjacent pixels in the diffraction pattern into "super pixels", to increase the sensitivity of the CCD camera [124] during pattern acquisition) and using a small bin size in the Hough transform accumulator array [128]. Tilting the specimen by angle of 60-70^o allows more of the diffracted electrons to escape towards the detector.

2.7.2. Effect of strain on EBSD patterns

In structural materials local strain concentrations near microstructural features such as inclusions, precipitates and grain boundaries need to be studied in detail to understand the deformation process and failure. The presence of strain in the crystal lattice affects EBSD patterns [127][31]. As classically defined, each grain has a single orientation but within a real grain the orientation can vary in a continuous or discontinuous manner. This is called as 'orientation perturbation'. The perturbations close to interfaces and deformed structures echo the distribution of strain [124].

Elastic strain

Uniaxial elastic strain of a single crystal produces a change in one of the cell parameters and results in a shift in the pattern in one of the zone axis directions along with a change in the separation of the diffraction lines (see Figure 2.20) [31]. However, the maximum elastic strains achieved in most real materials are very small (for example 0.117% for 316H at 550^{o}C) and it is difficult to measure such small shifts (of only one or two pixels) in the zone axis positions in the diffraction patterns. If the crystal bends during elastic deformation, the pattern quality will be further degraded [31].

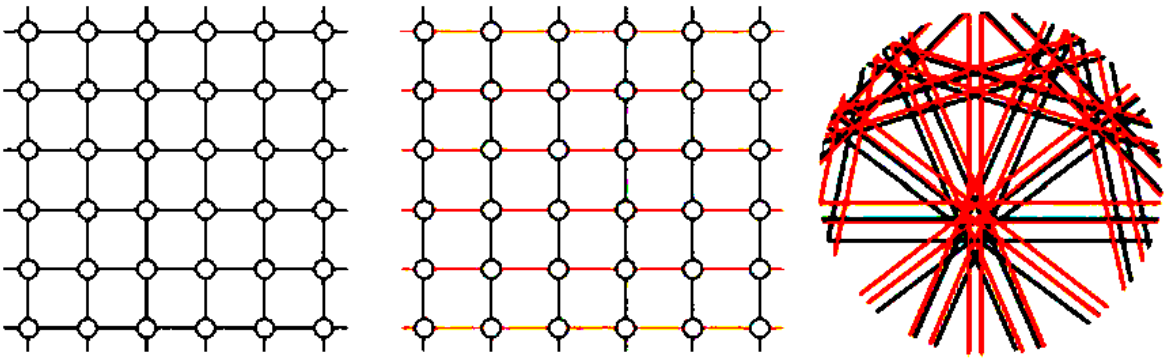

Figure 2.20 A crystal lattice strained 11% uniaxially in the horizontal direction and a schematic overlay of the patterns with (red) and without strains (black) [31].

Plastic strain

Plastic strain also degrades the sharpness or image quality of Kikuchi patterns. The distortions due to plastic strain are incorporated in the crystal lattice by the formation of dislocations. The dislocations formed within a particular volume can be divided in to two classes [31]:

i. **Statistically Stored Dislocations (SSDs)**, are those in the material which contribute significantly to the dislocation density but whose Burgers vectors sum to a net zero. The diffraction patterns from this volume are degraded due to local perturbations of the diffracting lattice planes leading to incoherent scattering (see Figure 2.21).

ii. **Geometrically Necessary Dislocations (GNDs)**, with a non-zero Burgers vector sum represent the excess dislocations stored within a Burger's circuit and contribute to a change in the crystallographic orientation i.e. a lattice curvature. The quality of patterns from this diffraction volume will be degraded as they are each a superposition of many patterns due to lattice bending.

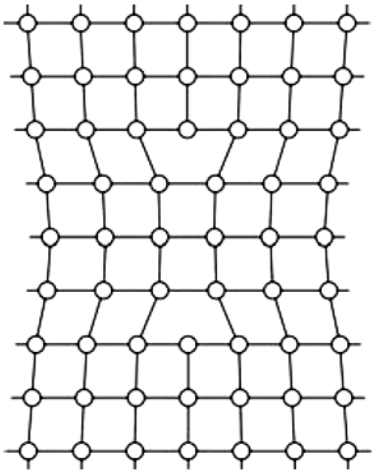

Figure 2.21 Diagram showing the local disturbance in the crystal lattice due to two opposing edge dislocations with a net zero Burgers vector [31].

2.8. Previous studies on EBSD and inelastic strains

EBSD can be used to map or quantify inelastic strains in terms of the local orientation change, local misorientation (misorientation, as used here, being the difference in orientation between pixels), average misorientation, or by calculating the geometrically necessary dislocation densities [127]. All these metrics are calculated from the orientations derived from the EBSD pattern. The intragranular misorientations in a polycrystal can be mapped using different EBSD metrics which will be explained later. The accommodation of strain by lattice rotations can be visualised in so called 'grain boundary' maps [129][31].

2.8.1. EBSD and plastic deformation

Many studies have been conducted on polycrystalline materials to study the effect of plastic deformation on EBSD metrics at both ambient and high temperatures [11], [27], [136], [137], [28], [32], [130]–[135]. EBSD metrics GOS, GAM, KAM, LABF (see Chapter 3 for details regarding the EBSD metrics) monotonically increased with plastic strain in tension and compression for 316 austenitic stainless steels [32][11][137]. Githinji et al [11] reported the variation of KAM_a with plastic strain to be insensitive to the temperature or strain rate. Comparison of solution annealed 316H specimens deformed to a true strain of 0.098 at different strain rates revealed that the proportion of grains with AMIS $<1.5^o$ (see section 3.4.3) increased as the strain rate was reduced but for strain rates above $10^{-6}s^{-1}$ there was a little difference in the variation of KAM with plastic strain. In that study the variation of KAM with plastic strain was reported to be sensitive to grain size. Shanmukha et al [137] suggested GOS_a to be more sensitive to strain at higher plastic strains as KAM and LABF only consider misorientations between 0.15-2^o and 2-

15^o respectively; but at higher strains the density of high angle misorientations $>15^o$ which are not taken in to consideration tends to increase.

2.8.2. EBSD and creep deformation

Many studies have demonstrated the capability of EBSD to measure creep strains during uniaxial load controlled deformation [11], [25], [28], [29], [118], [130], [138]–[141]. Round robin studies by Kamaya et al [142] concluded that area averaged intragrain misorientation (GOS_a in this thesis) is the best EBSD metric for measuring creep damage in terms of inelastic strain. The scatter in KAM_a was assumed to be due to errors associated with crystal orientation measurements [142]. The Society of Materials Science, Japan has issued guidelines for material damage evaluation (in terms of plastic/creep strain) using EBSD [142]. Studies by Githinji et al [11] on 316H austenitic steel showed DGF which is derived from GOS_a to be a better metric to measure creep damage. DGF which only consider the fraction of grains with GOS_a above a certain threshold value was found to be the metric least sensitive to local deformation associated with precipitates and precipitate-dislocation interactions [11].

2.8.3. EBSD and cyclic deformation

Longer holding times at peak tensile strain reduced the creep-fatigue life of nickel-based alloy 230 [143]. Creep-fatigue tests of 9Cr-1Mo-steel showed a significant reduction in the deformation rate when a holding time of 30 minutes was introduced. The hardness values and GAM increased with increasing deformation and with the number of cycles. Some of the dislocations introduced by fatigue deformation were recovered by stress relaxation. The creep deformation during stress holding resulted in a lowering of GAM which is the KAM averaged for a grain (see Chapter 3 for details regarding EBSD metrics) [144].

Fujiyama et al [140] found that in SUS304HTB austenitic stainless steel KAM_{ave} and GOS_{ave} (See Chapter 3 for details regarding EBSD metrics) increased with time fraction (or cycle fraction) for creep and creep-fatigue, whereas in Mod.9.Cr.Steel, a tempered martensitic stainless steel, both metrics decreased. Their KAM-based approach showed a good relationship with macroscopic strains for both creep and creep-fatigue conditions. The change of KAM distribution with damage accumulation was more extensive in creep-fatigue tests than in creep tests.

Claire et al [145] used the metrics KAM and GOS to study fatigue damage in Fe-3Si steel for different total strain ranges from 0.3% to 1%. The area fraction of KAM>0.5^{o} was constant up to a total strain range of 0.7% and then increasd linearly with further increase in the strain range. The number of grains with GOS>1^{o} (DGF(1)) was also found to increase with increasing strain range in this study. Another study by Vogt et al [146] in low-carbon steel suggested that cyclic strain is accommodated by easy glide of dislocations which rapidly arrange into cells, and higher KAM values were found at the locations of cell structures for different strain amplitudes.

Creep-fatigue tests on a Ni-Cr-W-Mo based alloy, found interior intergranular cracks only on random high angle GBs with cellular precipitates and not on random high angle GBs without cellular precipitates [143]. This confirmed the deleterious effect of GB cellular precipitates on the mechanical properties of the material. As the total strain range increased, the deformation was concentrated to GBs since the test temperature (850^{o}C) was higher than the material's equicohesive temperature and the GBs became weaker regions than the grain interiors.

2.8.4. EBSD to study local damage around weldments and cracks

Measurements of the strain distributions around welds and heat affected zones of ex-service materials is very important, to check if weld repairs are necessary. Numerous studies have proved EBSD to be an effective tool for characterizing the microstructure and strain distributions in weldments and the heat affected zone (HAZ) [11],[32], [133], [153]–[162], [136], [163], [139], [147]–[152].

Creep cavitation is an important degradation mechanism in stainless steels. Reheat cracks in austenitic stainless steels result from cavity nucleation in the HAZ grain boundaries, followed by cavity growth and linkage to form micro- and macro- intergranular cracks in the HAZ [122]. Cracks develop because, during post weld heat treatment, the grain interiors precipitation harden, which prevents plastic deformation there [105][122]. Cavitation also occurs in the coarse-grained zones of welded joints that are weakened by intergranular precipitations (AlN, Mo, Nb, V carbides) and segregated impurities during high temperature service in the presence of significant residual stresses. These residual stresses are created by localized stress caused by the geometry and thermal history of the material [105][164]. The cavitation damage is accelerated by the severe triaxial stress fields created by constrained weld geometries [16].

Fujiyama et al [152] showed that EBSD can be an effective tool for studying the local creep damage process in high chromium heat resistant steel weldments. That study identified a close relationship between maps of hardness and of KAM. The KAM values around creep voids increased due to strain induced misorientation changes. Githinji et al [11] studied the intragranular misorientations across a weldment in service aged 316H steel. The maximum misorientations were observed at the fusion boundary at the top,

middle and bottom of the weld. The strain was quantified from the misorientations, based on calibration curves from isothermal monotonic creep tests.

2.9. Summary and limitations of the literature

The phenomena of plastic, fatigue and creep deformation in austenitic stainless steels have been much studied including the effects of alloying elements and precipitates on their mechanical properties. The different factors affecting the fatigue life of austenitic stainless steels have also been studied in detail. EBSD has been shown to be a useful tool to study plastic and creep deformation in metals by characterizing local deformation. Most of the published literature shows GOS and KAM to give good correlations with plastic/creep strain. The Japanese Materials Research Society are already using an EBSD standard for certain creep strain measurements.

The following limitations were found in the literature on 316H austenitic stainless steels reviewed here in seeking to establish a reliable method for using EBSD measurements in life assessment of stainless steel power plant components subject to creep-fatigue:

- Very limited information is available on misorientation development during high temperature plastic deformation and uniaxial stress relaxation on type 316H austenitic stainless steels.
- Very limited literature is available on the effects of strain range, dwell and temperature and of microstructural changes on misorientation development on 316H austenitic stainless steel.
- Although much research has been done in quantifying creep strain using EBSD, only a limited number of studies have been reported on the evolution of intragranular misorientations during cyclic strain accumulation.

- Although creep cavitation due to the accumulation of creep strain is suggested as the major reason for reheat cracking in type 316H stainless steels, only limited information is available about dislocation accumulation around cavities. Most of the studies were done to quantify the cavities, but none of the methods associated these with EBSD misorientations.

CHAPTER 3

EXPERIMENTAL TECHNIQUES

3.1. Introduction

This chapter discusses in detail the experimental techniques used in this study. Mechanical tests were performed to deform the material of interest (the material is introduced in chapter 4) in a controlled manner to investigate postulated correlations between EBSD-based misorientation metrics and the strain introduced. Hardness testing and X-ray diffraction peak profiling were also used to characterise the strain developed, for comparison with the EBSD metrics. Section 3.2 describes the uniaxial and cyclic tests conducted and the hardness measurements made. The conditions under which the mechanical tests were performed are described in terms of the material, standards, specimen geometries, strain, strain control, strain range, strain rate, hold time, temperature, temperature control and data analysis.

In section 3.3 the characterization tools used for microstructural assessment are covered. These include scanning electron microscopy (SEM), energy dispersive spectroscopy (EDS), scanning transmission electron microscopy (STEM), STEM-EDS and X-ray diffraction. The discussion focuses on the operating conditions and the sample preparation required.

Section 3.4 discusses the EBSD strain measurement technique used in the current study. This section explores the working principle of EBSD, the operating conditions, the measurement parameters used and the data analysis methods.

Section 3.5 discusses other methods to which the EBSD results can be compared to validate the newly developed strain measurement method, followed by a discussion of the limitations of the experimental tests in section 3.6. A summary of the key points discussed is given in section 3.7.

3.2. Mechanical testing

3.2.1. Uniaxial tensile tests

Uniaxial tensile tests were performed at room temperature (~21^{o}C) and high temperature (550^{o}C and 640^{o}C) to understand and quantify the stress-strain properties of the material of interest under controlled deformation conditions. The tests were conducted according to BS EN ISO 6892-1:2016 [165] (for room temperature) and BS EN 6892-2 :2011 [166] (for elevated temperature) for all test conditions.

The tests were carried out in an Instron 8862 machine with a load capacity of 100kN and fitted with a single screw electromechanical actuator, capable of very slow strain rate tests (see Figure 3.1). The test machine was controlled through built-in Instron Bluehill software and tests were performed under strain control with strain rates 0.025%/s and 0.0025%/s both at room and elevated temperatures.

The strain was monitored and controlled externally through an Instron high temperature extensometer (Instron 2632-054) interfaced with Instron's controllers and mounted on to the specimen gauge length using vitreous silica rods (see Figure 3.1). The extensometer gauge length was 12.5mm and it was fitted with chisel-ended alumina rods which transmitted the mechanical displacement of the rods to the strain gauge in the extensometer body with a maximum travel of 2.5mm. The strain was monitored by means

of this conversion of mechanical movements to electrical signals. The extensometer was calibrated before every test to improve the accuracy of the strain measurements.

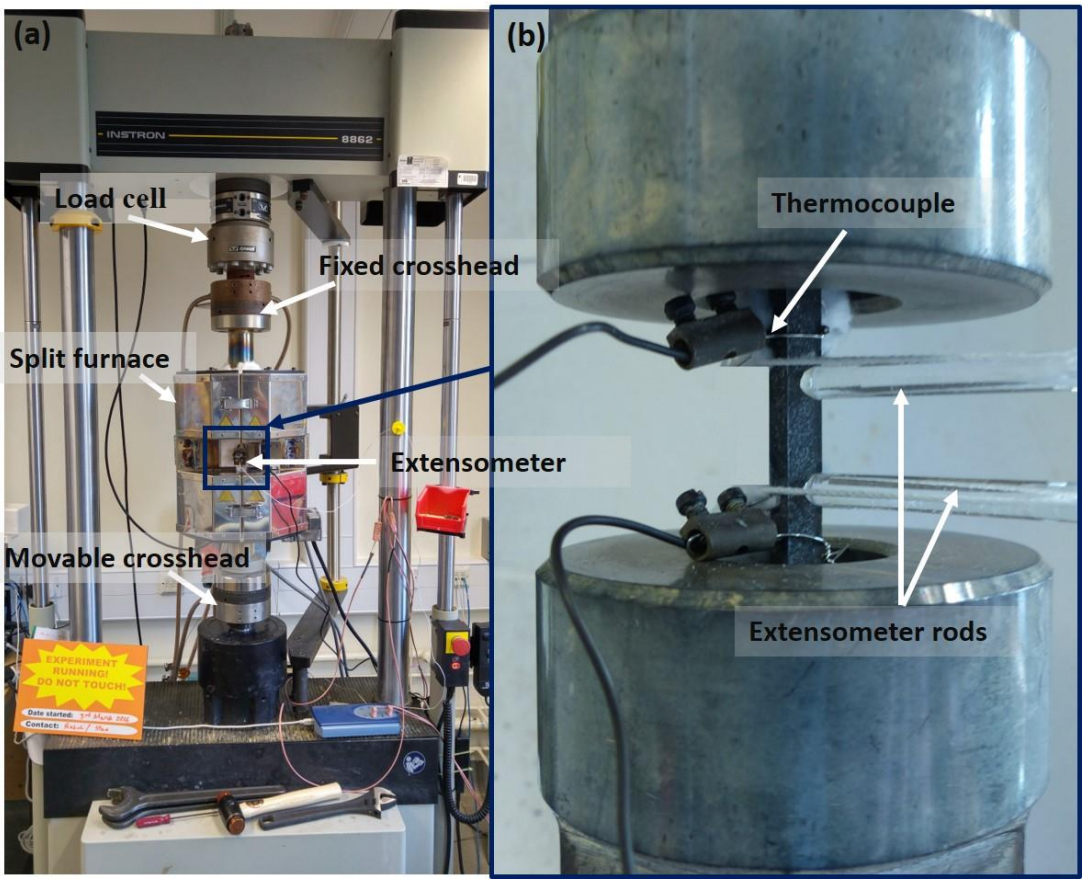

Figure 3.1 Photographs of (a) Instron 8862 machine fitted with split furnace, (b) Instron 2632-054 high temperature extensometer and thermocouples mounted on the tensile test specimen.

A split furnace with a side window was used for the high temperature tests. A Eurotherm 3216 controller was used to monitor the temperature of the furnace. The three temperature zones of the furnace were manually adjusted to give a uniform temperature along the specimen gauge length. The specimen temperature was monitored by calibrated type-N thermocouples attached directly to two locations within the specimen gauge length through special clamps (see Figure 3.1). Once the uniform temperature was achieved, the specimens were held for 1 hour to allow temperature homogenisation before deformation.

The temperature was maintained with a variation of ±3ºC through careful setting of temperature in each zone and proper insulation. At the end of test, the specimens were unloaded and allowed to cool in the air to room temperature.

The specimens tested in each condition were extracted from adjacent locations in source materials to get repeatable results, as there was noted to be a slight change in properties between various locations in the component from which the material was extracted (details in Chapter 4). The data were continuously recorded (every 1s) by the software during the test; that is the test time, cross head extension, load and strain. The true strain (ε) was computed from the nominal strain (e) by the equation

$$\varepsilon = \ln(e + 1). \qquad (3.1)$$

Tensile tests were conducted on material from the outer, middle and inner radii of the as-received steam header to study the radial variation in mechanical properties (more details of material are given in Chapter 4). Tests were also conducted on re-solution treated and thermally aged material (see Chapter 4). Some of the tests were maintained at constant total strain hold for 24 hours (by monitoring the extensometer strain) at different initial strain levels to study the effect of initial strain on stress relaxation. Details of all uniaxial tensile tests and stress relaxation tests are given in Chapter 5.

Specimen design

Limited ex-service material for the experimental work was provided by the industrial sponsor, and through thickness variation in properties was noted that further restricted the tests. The property variations across the material are reported in Chapter 4. The number of experimental deformation parameters explored had to be restricted to get maximum results from locations having the same properties. This was the reason for choosing a small cyclic test specimen size and flat tensile specimens.

In the interest of getting a maximum number of test specimens from the available material, while adhering to BS standards, flat specimens were prepared for the tensile tests, using wire electro-discharge machining (EDM). The specimen design is shown in Figure 3.2. The specimens were held securely using in-house manufactured holders [137]. The dimensions of the test specimens were measured using a Vernier calliper before testing.

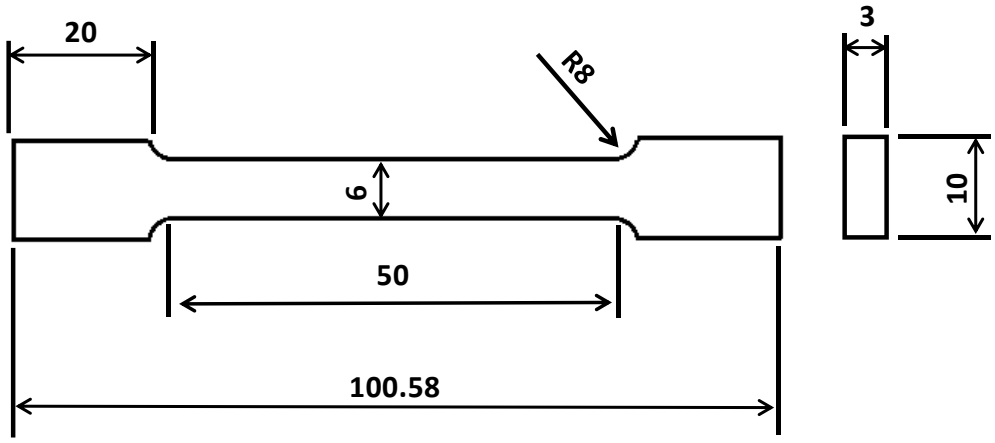

Figure 3.2 Schematic diagram of uniaxial tensile test specimen. Dimensions in mm.

3.2.2. Cyclic tests

Strain-controlled symmetric cyclic tests were also carried out using the Instron 8862 machine described in section 3.2.1. The alignment of the machine was very important for the cyclic deformation tests, to avoid buckling the specimen during compression and to ensure a uniform load distribution along the gauge volume. The test rig was aligned following the ASTM E1012-14 standard [167]. Alignment was done using a test specimen with 8 strain gauges parallel (within a tolerance of ±2 degrees) to the loading direction attached to the gauge length and using Instron AlignPro (IAP) fixture equipment and software. The IAP software helps the user manually correct for concentric and angular misalignment, when the sample is preloaded to between 50-100N. The calibrated type N-thermocouples and extensometer were carefully attached to all cylindrical cyclic

test specimen gauge length (with 2 thermocouples at each end of gauge length) with the help of clamping devices and ceramic rods as shown in Figure 3.3.

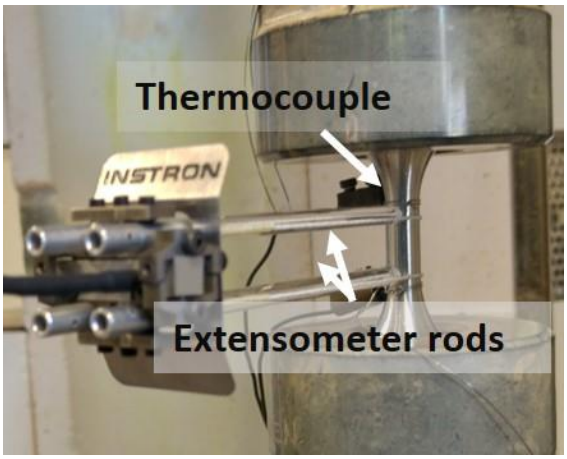

Figure 3.3 Photograph of thermocouples and extensometer mounted on a cyclic test specimen.

Tests were conducted both at room temperature and elevated temperatures by varying different parameters such as the total strain range, the hold time at peak tensile strain and the different numbers of cycles. In all cases, the first quarter cycle was in tension, and the cyclic loops were symmetric. Tests were conducted on ex-service material, re-solution heat treated material and thermally aged steel.

Specimen design

The detailed specimen design is shown in Figure 3.4 and a photograph in Figure 3.5. The specimens for cyclic testing were designed in such a way to get the maximum number from the limited material available (as mentioned in section 3.2.1. Uniaxial tensile tests) but each having enough cross-sectional area to avoid buckling. The specimens were designed to minimise the effect of backlash (a threaded design and shoulders to hold in locknuts). But a few tests were still affected by backlash caused by the thread tolerances in the lock nut and test sample. Despite this the specimen design was kept the same due to the limited availability of material.

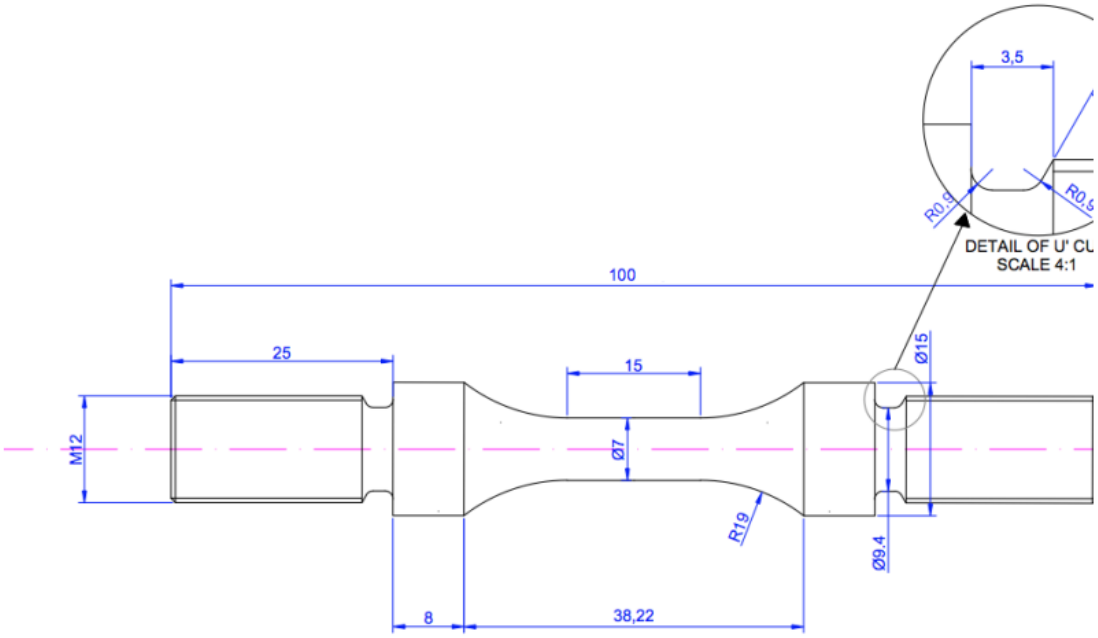

Figure 3.4 Schematic diagram of a cyclic test specimen. Dimensions in mm.

Figure 3.5 Photograph of a cyclic tested specimen.

3.3. Microstructure characterization

3.3.1. Optical Microscopy

Optical microscopy (OM) is the primary means for scientists and engineers to examine the microstructure of materials at low magnifications. In the present study, a Leica DMI 5000M reflected light microscope fitted with a Leica DFC280 digital camera was used for capturing and processing optical images through the Leica Application Suite software.

This is an inverted microscope and so only the sample surface facing the objective lens needs be perfectly flat. The microscope was operated in the bright field (BF) mode where the polished surface appears bright and surface irregularities such as grain boundaries, precipitates, inclusions, slip bands, pit etc. appear dark as their reflected light is not directed back to the objective. The micrographs were captured at the lowest possible magnification to get overall information about the grain structure in a large field of view.

Sample preparation

The samples for optical microscopy were prepared using conventional metallographic procedures of grinding on successive grades of emery papers followed by polishing using successively finer diamond suspensions. The last stage was an electrolytic etching at 6V potential for 5 seconds using an electrolyte comprising 10% oxalic acid.

3.3.2. SEM

A scanning electron microscope is one of the most versatile instruments available for microstructure characterisation at high resolution. Imaging is mainly done in secondary electron and backscatter electron modes. The former gives more detailed topographical contrast and the latter gives contrast predominantly based on composition. The working principle of SEM is explained elsewhere [168]. The three-dimensional appearance of structures in the secondary electron imaging mode is due to the large depth of field of the equipment.

In the present work, a Zeiss Supra 55VP FEG SEM operated at 5KeV with a 30µm objective aperture was used in the secondary electron imaging and backscatter electron imaging modes for microstructural examination of etched samples, to study the grain boundaries, precipitates and cavities in different steels.

Sample preparation

Sample preparation for SEM imaging and EBSD followed the same procedure. The samples were cut from the test specimen using wire EDM, which produces little plastic deformation [169]. The EBSD samples of tensile and creep-fatigue tests were studied on a cross-section parallel to the deformation axis (see Figure 3.5).

SEM samples were prepared using conventional metallographic procedures of grinding on successive grades of emery papers followed by polishing using successively finer diamond suspensions. The final stage of sample preparation was electro polishing at room temperature for 60 seconds at 22V potential using Struers A21 electrolyte, to produce a specimen free from preparation-induced surface deformation. To study the precipitate size distribution, the final preparatory stage after diamond suspension polishing involved etching by Murakami's reagent (10gK3Fe(CN)6,10g KOH, 100ml water) for 60 seconds. This polishing method, starting with coarse emery papers and finishing with electropolishing, removes all the EDM affected layers from the material.

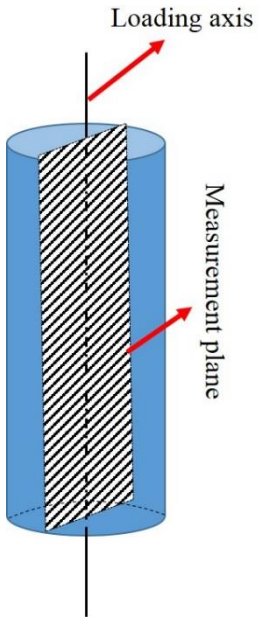

Figure 3.6 Schematic drawing showing the plane on which strains were studied, parallel to the loading direction in the cylindrical cyclic specimens.

3.3.3. Energy Dispersive X-ray Spectroscopy (EDS)

Chemical analysis is performed in an SEM by measuring the energy and intensity distribution of the X-rays generated by the interaction of electrons with the material. The EDS detector used in the current study was an X-Max 50mm^2 (Oxford Instruments) attached to the Zeiss Supra 55VP FEGSEM. The measurements were conducted using spot mode on the bulk material as well as on many features like intra- and inter-granular precipitates. An accelerating voltage of 20KeV, a 30µm objective aperture and a working distance of 8.5mm were used in the high current mode. The spectrum was recorded and analysed using Aztec software. The limited energy resolution of EDS leads to overlap problems when peaks are less than 50KeV apart, so EDS is only used for semi-quantitative assessment of the local chemical composition [168]. The sample preparation for EDS was the same as that for SEM.

3.3.4. Scanning Transmission Electron Microscopy (STEM)

A scanning transmission electron microscope was used in high-angle annular dark-field imaging mode (STEM-HAADF) to characterize dislocations in the current study, because the standard invisibility criteria for dislocation contrast in TEM don't apply for STEM [170] . The working principle of STEM can be found elsewhere [171].

In the present study, a JEOL JEM 2100 transmission electron microscope with a LaB6 emitter was used at an operating voltage of 200keV and the images were acquired using STEM dark field detector operated in HAADF mode.

Sample preparation

The sample preparation for STEM studies used the following procedures:

Sectioning: 0.25mm thick slices were machined from the deformed specimens by wire EDM.

Grinding: This was carried out using a Gatan Model 623 disc grinder and involved fixing the EDM slices onto a specimen mount, using a low melting point wax, and grinding sequentially, using 40μm, 15μm and 5μm grit SiC paper, lubricated with water. This was followed by re-melting the wax, turning over the slices, re-affixing, and grinding their other side until a thickness of about 100μm was achieved. It was not advisable to produce a very thin slice as the preparation-induced deformation could spread throughout the thickness, distorting the original dislocation structures.

Punching: A Gatan Disc Punch model-659 was used to produce 3mm diameter discs from the sectioned slices, to fit into the standard TEM specimen holders.

Electropolishing: was performed on a Metalthin Mk4 machine designed to direct jets of cooled electrolyte at both sides of the sample while maintaining a potential difference between it and a platinum electrode. The electropolishing was carried out at -50±5°C

using a potential difference of 20V and an electrolyte of 5% perchloric acid in methanol. The process was terminated when a hole was detected in the sample. The samples were then carefully washed in cooled methanol. The electropolishing solution was handled with utmost care due to its corrosive, irritant and inflammable nature.

3.4. Electron Backscatter Diffraction (EBSD) characterization

EBSD was used to measure grain size. A misorientation between neighbouring pixels greater than 15^{o} was defined as evidence of a grain boundary and the grain size was obtained directly from the Channel 5 EBSD software. MATLAB codes were also used to calculate the ASTM grain size number from the EBSD data. Details of the EBSD data acquisition are given later in this section.

EBSD was also used to study the crystallographic misorientations associated with the inelastic strains in Type 316H austenitic stainless steel deformed under strain control, with the aim of developing an EBSD-based damage assessment method. Plastic strain also degrades the sharpness or image quality of Kikuchi patterns. The basic principles of EBSD and the different strain measurement approaches have been described in Chapter 2. This section will describe the EBSD data acquisition and analysis procedures used.

3.4.1. Sample extraction and preparation

The samples for EBSD were extracted from an axial diametrical plane of the deformed gauge length by EDM and prepared as described in 3.3.2. SEM. The EBSD analysis was performed by examining the axial plane parallel to loading direction.

3.4.2. EBSD acquisition settings

The EBSD measurements were carried using a Zeiss Supra 55VP FEG SEM with a NordlysF detector. Oxford Instruments Aztec software was used to perform automated EBSD measurements to study the microstructural changes during deformation.

From the Aztec database, the austenite phase (Iron fcc) was used for pattern indexing. The following parameters were used for the EBSD measurements: sample tilt of 70^{o}, accelerating Voltage: 20kV, aperture size of 120μm, working distance of 15 ±0.1mm, step size of 1μm, Hough resolution of 120 and camera binning 4x4.

From each sample EBSD measurements were made over at least 3 areas consisting of at least 150 grains. Mean values were obtained through post-processing the data. For studies on the reheat crack, a larger step size of 2μm was used, to examine a larger area.

3.4.3. EBSD data analysis

Using EBSD, misorientations in a polycrystal can be mapped or quantified in terms of the relative orientation change, local misorientation, average misorientation, or by calculation of geometrically necessary dislocation densities [127]. All these metrics are calculated from the orientations derived from the EBSD patterns. The different EBSD metrics will be explained later.

HKL Channel-5 software was used for the EBSD data post processing. The EBSD data collected from each point in a map is its phase, its orientation with respect to the specimen coordinate system and a measure of the pattern quality. The orientation data in this study were used to infer the presence of inelastic strain. No clean-up procedure was used in order to maintain the quality of the data. MTEX (v4.4.0), which is a free MATLAB toolbox for analysing and modelling crystallographic textures using EBSD, was also used for data analysis [172]. MATLAB codes can be developed and used to analyse EBSD data using MTEX. Such a flexibly is not available in commercial EBSD analysis software.

The accommodation of strain by lattice rotations can be visualised in grain boundary maps. Figure 3.7 shows misorientations in the range $2 < \theta < 15°$, identified by the

EBSD software as “low angle grain boundaries (LAGBs)” in red and high angle grain boundaries (HAGBs, >15^{o}) in black. The regions of high concentrations of low angle grain misorientations indicate the area of higher GND density. Orientation Imaging Microscopy (OIM) measurements allow users to define the ‘grain boundaries’ that they want to plot in the maps [31].

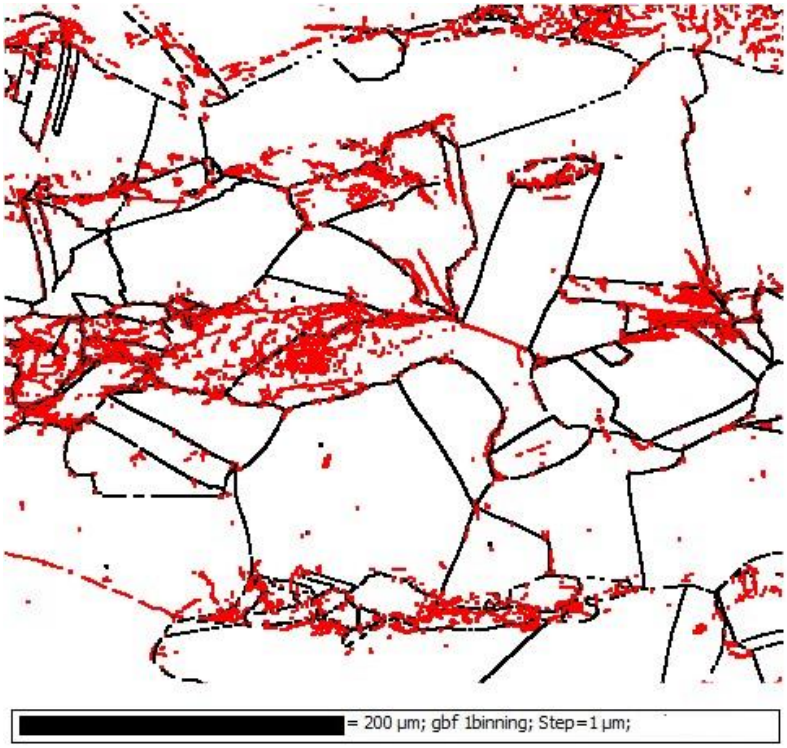

Figure 3.7 Grain boundaries in a sample of ex-service type 316H austenitic stainless steel; red misorientation 2-15^{o}, black misorientation>15^{o} (98.9% indexing rate and no clean-up).

There are two ways of characterizing local misorientation.

- Based on the whole grain (Section 3.4.3.1)
- Based on individual measurement points or on a kernel (Section 3.4.3.2)

Grain based methods

In this method, every measurement point within one grain is assigned the same local misorientation value and the values differ from grain to grain.

Grain Orientation Spread or Average Intragrain Misorientation (GOS, AMIS)

GOS (also called AMIS) is used to characterize the distribution of low angle misorientations in a grain [173]. To calculate GOS; first, the average orientation of a grain is calculated, then the misorientation between this average orientation and the orientation of each individual measurement point within the grain is calculated. The GOS for a grain is then the mean deviation between the orientation of each point in the grain and the average orientation of the grain (see Figure 3.8).

In this study, GOS_a ($AMIS_a$) is the mean GOS value for all the grains in 3 EBSD maps (giving a total of roughly 150 grains measured) for each deformation condition.

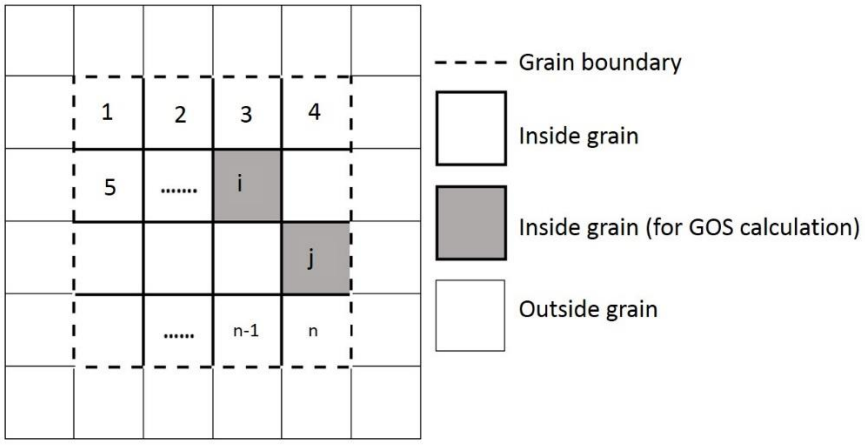

Figure 3.8 Schematic calculation of GOS

$$GOS = \frac{\sum_{i=1}^{n}(q_m - q_i)}{n} \qquad (3.2)$$

q_i = Crystal orientation at point i

q_m = Average orientation of the grain

Deformed Grain Fraction (DGF)

The calculation of DGF is based on the grain statistical data obtained in the computation of $AMIS_a$ (GOS_a) [11]. The DGF is evaluated using the equation [11]:

$$DGF = \frac{m_d}{m_a} \qquad (3.3)$$

where m_d is the total number of grains with misorientation greater than a defined grain deformation threshold and m_a is the total number of grains in an orientation map [11]. In this thesis the threshold values were taken as 0.5 and 1°. In calculating DGF, grains in the map smaller than an equivalent circle diameter (ECD) of 11µm were excluded. This was mainly to avoid including spurious grains arising from incorrectly indexed points (since no data cleaning was performed) [11], [174]. This non- indexing is mostly due to patterns overlapping particularly at grain boundaries, the presence of phases not selected for indexing, the presence of an amorphous contamination layer and/or severe deformation which inhibits coherent diffraction [11].

Kernel scale method

These methods are based on the surroundings, or kernel, around individual measurement points. A kernel is a set of points within an area of prescribed size surrounding the point of interest. Square grids kernels are usually defined as 3x3, 5x5 etc sets of points. Here, each point has its own individual value of local misorientation irrespective of which grain it's in (it is not quite 'irrespective' of grain boundaries as orientations greater than 15° are excluded).

Kernel Average Misorientation (KAM)

For calculation of KAM, the arithmetic mean of the scalar misorientation between pixels in a kernel is calculated and mapped (see Figure 3.9) [127]. The effect of the grain boundary is removed by excluding misorientations greater than a threshold (misorientation above 15° is defined as a grain boundary). The grain boundary edges are preserved as KAM focuses on the central point of the kernel [31]. In this study, KAM

was computed using a 3x3 kernel for all misorientations in the range 0°-2°. KAM depends on step size used for EBSD measurements [11]. The KAM data were binned using a 0.01° class width giving 200 classes between 0-2°. of The KAM distributions were fitted by lognormal functions using OriginPro (v8) software [175].

The KAM distributions gave a better log normal fit with smaller binning (see Figure 3.10 and Table 3.1). The function equations are given in Table 3.1. A schematic of a lognormal distribution is shown in Figure 3.11. Lognormal fitting was used to calculate the average KAM value for each EBSD map. The relative frequency of KAM is obtained directly from the HKL Channel5 software.

$p_{l,m}$: misorientation between points l and m

$$KAM_i = \frac{p_{i,2}+p_{i,3}+p_{i,5}+p_{i,7}+p_{i,8}}{5} \qquad (3.4)$$

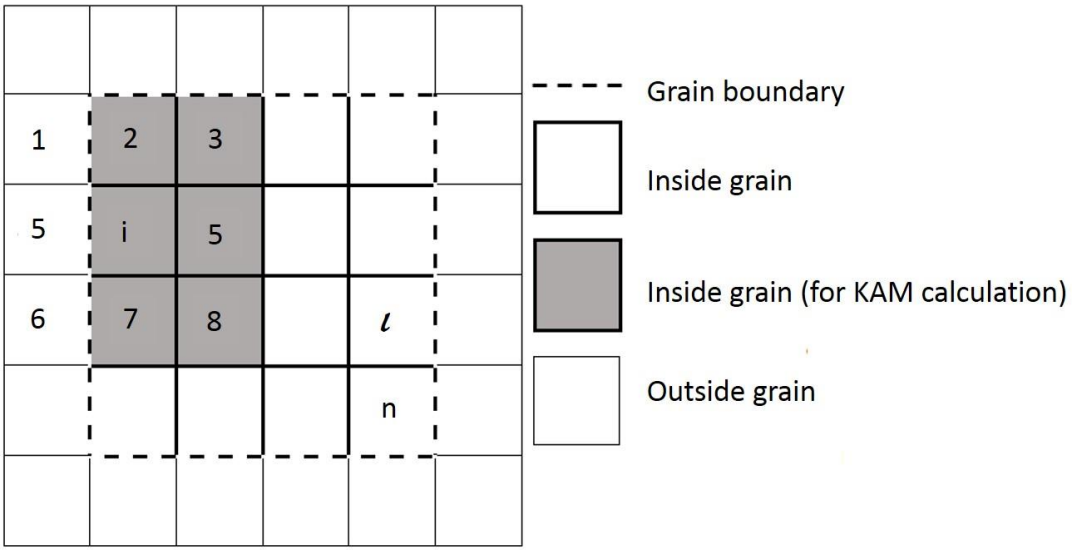

Figure 3.9 Schematic illustration of calculation by KAM.

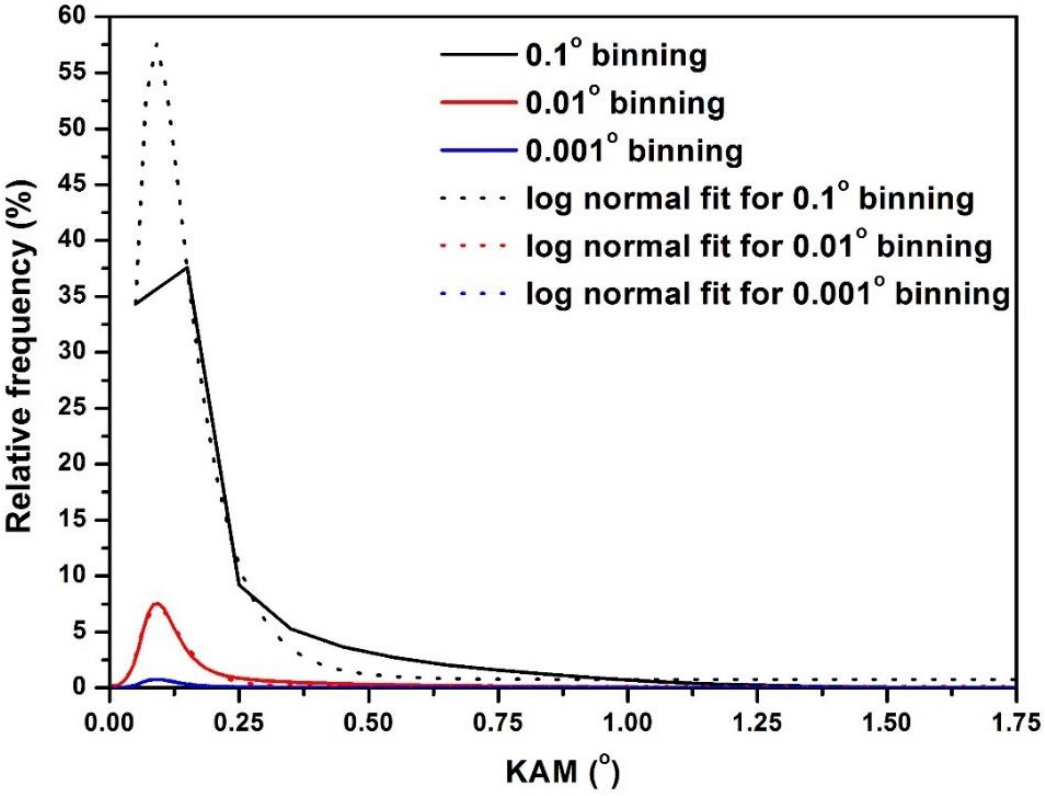

Figure 3.10 Lognormal distribution fits of KAM data as a function of bin width for a sample of ex-service type 316H austenitic stainless steel. KAM is in degrees.

Table 3.1 Typical lognormal distribution parameters for KAM data of as received ex-service stainless steel binned at different intervals. Parameters explained in Figure 3.11.

Binning	Model	Lognormal fitting		
	Function equation	y = y0 + A/(sqrt(2* π)*w*x)*exp(-(ln(x/xc))^2/(2*w^2))		
	Reduced Chi-Sqr	1.17658	0.0267	2.74E-04
	Adj. R-Square	0.98958	0.9844	0.98406
			Value	Standard Error
0.1°	Frequency	y0*	0.74383	0.26855
	Frequency	xc	0.12114	0.00305
	Frequency	w	0.55877	0.02232
	Frequency	A	8.25554	0.32122
0.01°	Frequency	y0	0.12057	0.01237
	Frequency	xc	0.10824	6.19E-04
	Frequency	w	0.42855	0.00532
	Frequency	A	0.75766	0.00803
0.001°	Frequency	y0	0.01219	3.97E-04
	Frequency	xc	0.10808	1.97E-04
	Frequency	w	0.42661	0.00169
	Frequency	A	0.07565	2.56E-04
*y0 = offset, xc = center, w = log standard deviation, A = Area, PI=3.143				

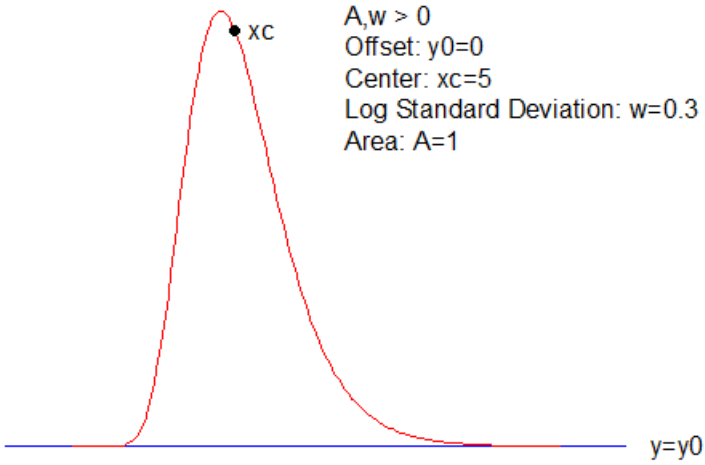

Figure 3.11 A schematic of a lognormal distribution fitting [175]

The KAM lognormal value was found to be almost constant on further binning beyond 0.01°. So 0.01° was used in this thesis. KAM was found to build up faster in a fine grained 316H material than in coarse grained material [11] and hence it can be used only to compare materials of a similar grain size.

Other EBSD metrics

Grain Boundary Fractions (GBF)

In OIM, 'grain boundaries' are defined as regions where the misorientations between neighbouring points are above a certain value. There are two types of grain boundaries defined based on local misorientations; that is HAGBs and LAGBs as explained earlier in this section (see Figure 3.7). HAGBs arise from discrete orientation differences between grains and LAGBs evolve as an array of lattice dislocations which display local strain gradients (in terms of GND) and hence can be used to assess the extent of plastic deformation [50][159].

Twin Boundary Fractions (TBF)

A misorientation of 60° about the <111> axis is a perfect twin boundary. Using the HKL software, a twin boundary is usually identified allowing a tolerance of 8.66° (from the Brandon criterion [176]) thereby including all near-twin boundaries. The twin boundary fraction is then calculated as the length fraction of the identified twin boundaries to the total length of all HAGBs (boundaries with misorientation >15°) in a map.

Low Angle Misorientation Fraction or Low Angle Boundary Fraction (LAMF, LABF)

The low angle misorientation fraction was based on misorientation assessment between a measurement point and its neighbour to the right and the one directly below it in an orientation map with a square grid of points. The total number of misorientations was therefore double the number of measurement points in a map less the points with zero solution. In the HKL Channel-5 software the minimum grain boundary angle was set to 2° using the general preferences component and the software set to detect all misorientations >2° (a misorientation of 2° is generally considered as the lower limit of a subgrain boundary [11] and the upper limit as 15°, misorientation <2° is considered in calculation of KAM) in the orientation data, using the grain boundary component. The detected misorientation data were exported into an excel spreadsheet where LABF was computed as follows:

$$\text{LABF} = \frac{N(\theta_{2-15})}{N(\theta_{>2})} \quad (3.5)$$

where $N(\theta_{2-15})$ is the number of misorientations with angles between 2°-15° and $N(\theta_{>2})$ is the total number of misorientations in the orientation map with angles >2°. LABF has been found to be insensitive to the loading direction as it showed little variation measured on planes parallel and normal to loading direction (after plastic deformation) [11]. However, the correlation between LABF and the applied strain can only be used for

assessing strain in materials of comparable average grain size with the calibration material (misorientations were found to build faster in a fine grained 316H material compared to coarse grained material during plastic deformation [11]).

Apart from the LABF, the area under the Low Angle Boundary Fraction frequency distribution (LABFA) was also calculated for strain analysis. LABF and LABFA both vary with the step size used for the EBSD measurements [11]. Hence maintaining the same step size for EBSD acquisition is very important.

3.5. Hardness measurements

Like some EBSD metrics, hardness values are known to be proportional to the square root of dislocation density [177], but a direct correspondence between two methods is limited due to the difference in their spatial resolutions and the different extent of the strain fields analysed. Nano-hardness measurements were also done to compare with EBSD measurements of a similar spatial resolution (in an area of 400μm^2, indents spaced 20μm apart).

The macro-hardness measurements were taken using Vickers hardness testing, which uses a square based diamond pyramid indenter with 136^o between its opposite facets. The measurement was done according to BS EN ISO 6507-1:2005 [178] on a Struers Duramin-A 300 machine using a maximum force of 5kgf for 10s and an indent spacing of 0.5mm on the surface. Macro-hardness measurements were used to get an idea of the hardness in the bulk material.

The macro-hardness is expressed in terms of Vickers hardness number by:

$$HV = \frac{2P\sin(\omega/2)}{L^2} = \frac{1.854P}{L^2} \qquad (3.10)$$

where P is the applied load in kg, ω is the angle between indenter's opposite facets and L is the average length in mm of indentation diagonals. The indent spacing's were all >3L to avoid overlap of the indentation deformation fields [178].

An MTS Nano Indenter XP fitted with a diamond indenter and controlled by TestWorks-4 software was used for nano-hardness measurements. The BS EN ISO 14577-1:2015 [179] standard was followed for nano-hardness measurements. A maximum force of 50kN for 15 seconds was used with an indent spacing of 20µm. The nano-hardness in terms of N/mm^2 is given by:

$$H_n = \frac{F_{max}}{A_p} \ , \ A_p = 24.5h_c^2 \qquad (3.11)$$

where F_{max} is the maximum applied force in N, h_c is the unloaded indentation depth, and A_p is the projected area in mm^2 of the contact between the indenter and the sample. This was comparable with EBSD measurements taken at 1µm and 2µm step size. The specimen preparation for the hardness measurements was the same as that for EBSD.

3.6. X-ray peak profiling

The study of X-ray diffraction peaks is useful in studying the microstructure of crystalline materials. Diffraction peak profile analysis is an indirect statistical method to characterize information regarding the phase, sub-grain size, dislocation density and other defect densities in the material.

When a monochromatic x-ray beam is incident upon a crystalline material, a diffraction pattern is produced. The peaks in this pattern correspond to diffraction from different crystallographic planes and from the positions of these peaks it is possible to identify the crystal structure. The position of the peaks can also provide information on elastic strain in the metal. This is done by measuring how far a peak has moved from the un-deformed position and from this the elastic strain and stress in a sample can be calculated. The peak

shape is influenced by ‘crystallite size’, ‘strain’ and ‘faulting’. Dislocations make a significant contribution to strain and size broadening in plastically deformed materials [121]. In this study, measurements of peak broadening were used to qualitatively assess the inelastic strain developed in uniaxial deformation and cyclic deformation on selected test samples.

A D5000 x-ray diffractometer (Siemens, UK) operating in reflection mode was used for the measurements. Cu-Kα radiation was used in Bragg-Bretano geometry [180]. The samples were scanned, in 0.02^o steps, between 2θ angles of 5^o and 120^o, to obtain 3 FCC peaks: 111, 200 and 220. An annealed 316 sample was used as the instrumental standard.

The same specimens were used for EBSD and X-ray measurements with the samples prepared as already described for EBSD. The x-ray measurements were done on surfaces parallel to the loading direction (the same plane as the EBSD measurements).

3.7. Summary

The procedures for all the mechanical tests have been described along with the international standards followed. The sample preparation procedures for EBSD and STEM were explained in detail. Optical and electron microscopic microstructural examinations of the material have also been explained in detail. The EBSD data analysis methods for strain measurements were also described. Other experimental techniques used to support the EBSD results were also briefly explained.

CHAPTER 4

CHARACTERIZATION OF THE INITIAL MATERIAL

4.1. Introduction

The material studied in this work is type 316H austenitic stainless steel supplied in the form of an ex-service steam header by EDF energy. In this chapter the samples of materials used are described in terms of their location in the header, heat treatment, chemical composition, microstructure, dislocation structure, precipitate size distribution and mechanical properties. Details are given of grain size calculations, based on EBSD OIM, and the examination of the microstructures and dislocation structures of differently heat treated material samples, prior to deformation, using SEM and STEM-HAADF. The local chemical composition of the material is presented as determined using EDS in both SEM and STEM. The chapter concludes with a summary of the key findings from these studies.

4.2. Materials

The different material samples used in this study are summarized in Figure 4.1 described in following sections.

4.2.1. 316H austenitic stainless steel

The material used in this study was from a steam header nozzle (part of a superheater used to convert saturated or wet steam into dry steam in a power plant). The header was made from AISI Type 316H austenitic stainless steel (EDF Energy reference 2B2/1 cast 69431). It had been in service for 90,930 hours at a mean temperature of 516°C and under an internal steam pressure of around 16MPa. The component's internal diameter and

thickness were 304.8mm and 63.5mm respectively, as shown in the diagram of Figure 4.2. The header had been removed from service in the year 2000 following discovery of a reheat crack near the nozzle weld. The composition of the service-aged material, as provided by EDF energy, is given in Table 4.1. Specimens for mechanical tests were extracted from the marked blocks HRA2a shown in Figure 4.2 which were far from the nozzle and the reheat crack.

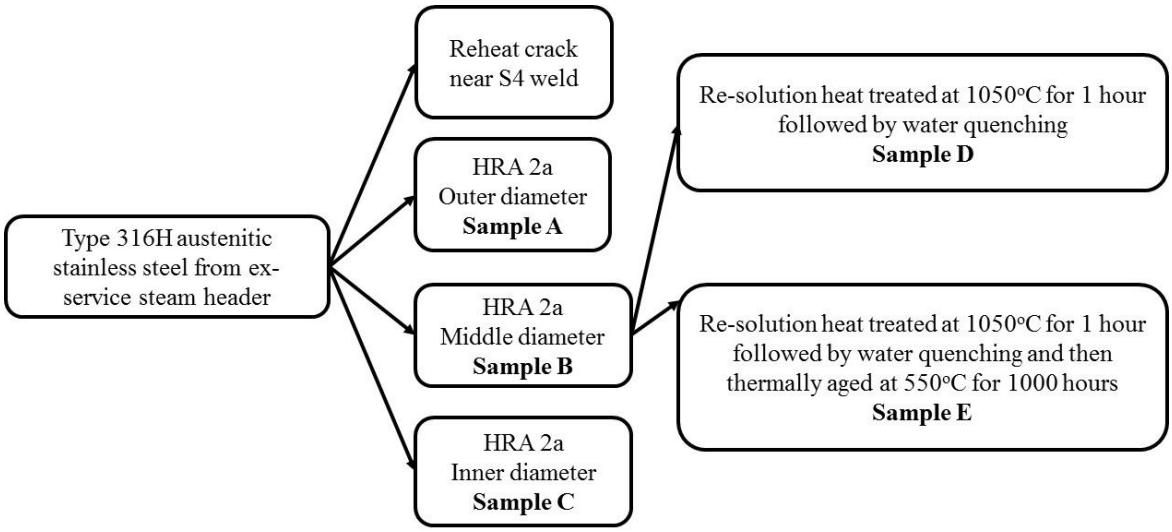

Figure 4.1 Summary of Type 316H austenitic stainless steel samples studied

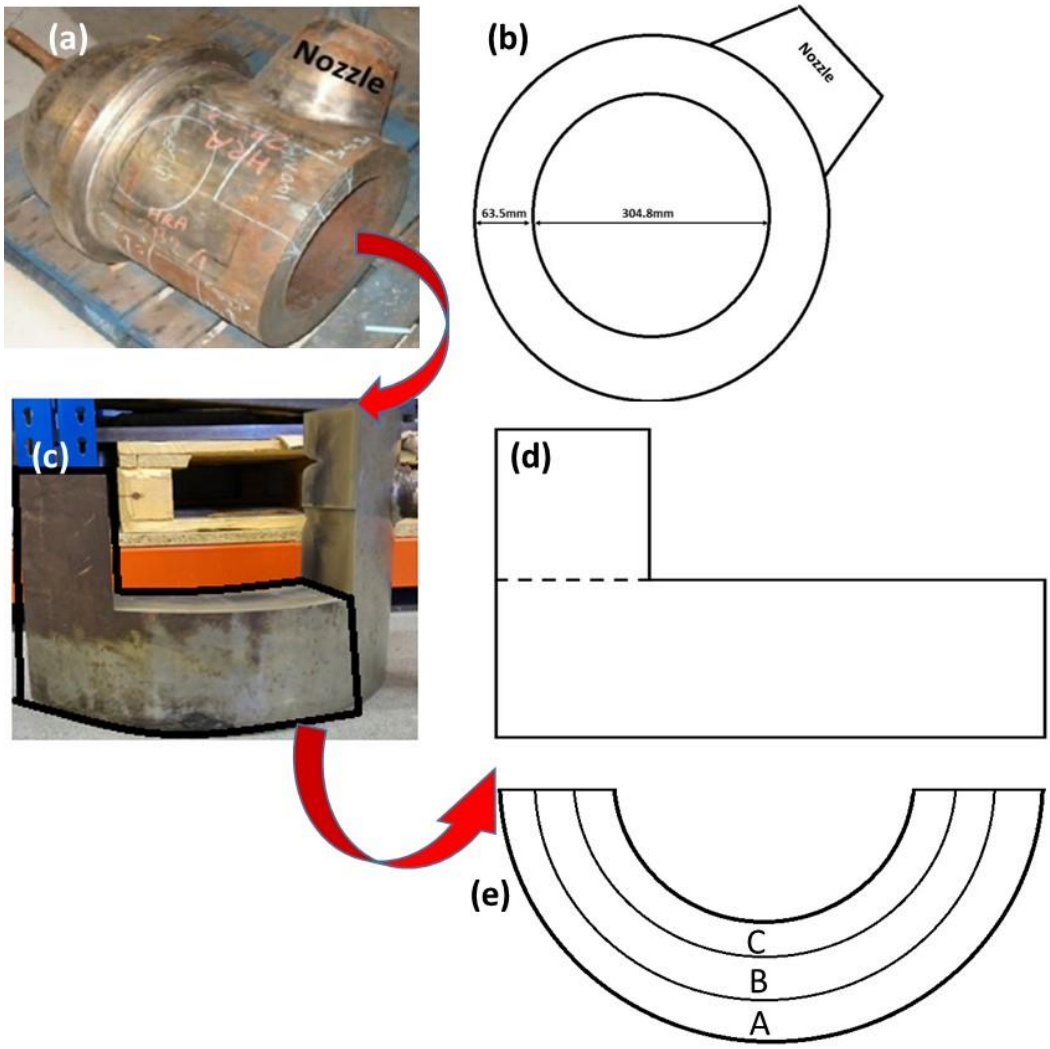

Figure 4.2 Photograph of (a) ex-service 316H austenitic stainless steel steam header provided by EDF Energy, (b) schematic showing the dimensions of header (c) steam header section used for the current study and (d, e) schematic diagram of the section showing the positions of material A, B and C.

Studies were also conducted sample B material which had been re-solution heat treated, at 1050^{o}C for one hour followed by water quenching, to dissolve all the precipitates and relieve stresses and strains. This material was denoted as "Sample D" and was used to study the influence of prior deformation and precipitates on subsequent deformation. Some of Sample D was then thermally aged at 550^{o}C for 1000 hours to produce "Sample E" which was used to study the effect of precipitation without prior stresses and strains.

Table 4.1. Overall chemical composition (weight %) of service-aged Type 316H stainless steel header [11].

C	Si	Mn	P	S	Cr	Ni	Mo	Al	Cu
0.066	0.42	1.00	0.029	0.015	17.82	11.81	2.33	0.003	0.23
Sn	V	W	Co	Pb	B	N	Nb	Ti	Fe
0.016	0.031	0.068	0.093	0.003	0.0051	0.096	0.007	0.004	Bal.

4.2.2. Ex-service 316H austenitic stainless steel weldments

Welding is used to join structural power plant components operating at high temperature. In this study, a misorientation-based approach (see section 3.4.3) was used to study deformation in the regions close to the reheat crack around the nozzle of the steam header provided by EDF Energy (see Figure 4.3). The service history of the weldment is the same as that of the ex-service material mentioned in section 4.2.1.

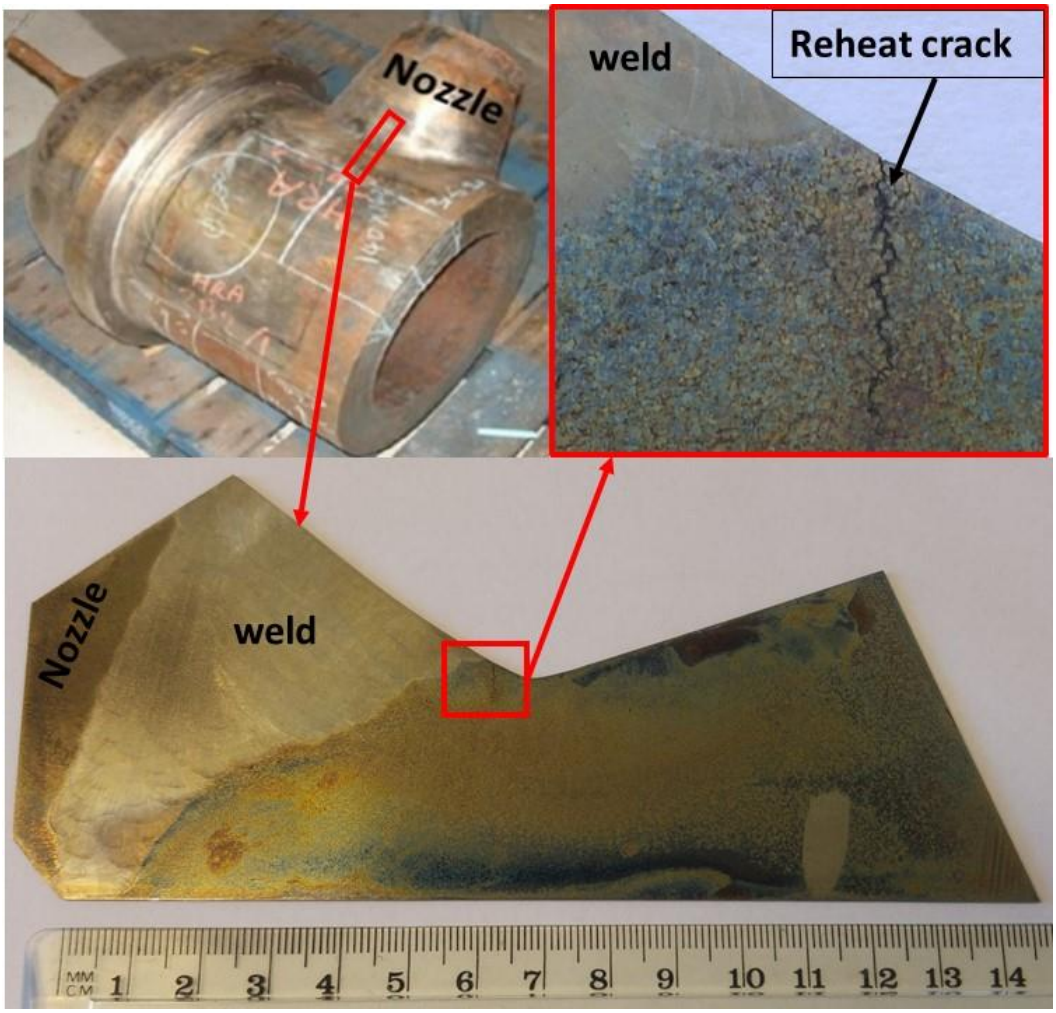

Figure 4.3 Photograph of a reheat crack near the weld in the ex-service 316H austenitic stainless steel steam header (HRA 2B2/1 cast 69431). The macrograph of weld was obtained by boiling the weldment in a solution of 50% HCl in water at 70^{o}C [147].

4.3. Material Characterization

An initial characterization of the parent material for testing was carried out in terms of its, grain size, micro-texture and local chemical composition.

4.3.1. Characterization of Microstructures

The microstructures were characterized using a Leica DMI 5000M reflected light optical microscope fitted with a Leica DFC280 digital camera and a Zeiss Supra 55VP FEGSEM. The details of the optical microscope and SEM have already been given in chapter 3. The optical microscope was used only to get a larger field of view of the microstructure. Low

magnification optical microstructures of the different material samples A, B, C, D and E used in this study are shown in Figure 4.4 and Figure 4.5. Detailed microstructural studies were carried out using SEM and EBSD.

Although there were slight differences in the mechanical properties and micro-textures (measured using EBSD, explained later in section 4.3) between material A, B and C, there was no obvious difference in the optical microstructure of these materials. The SEM microstructure of ex-service material (material sample A) showed extensive intra- and inter-granular precipitates (see Figure 4.6), the inter-granular precipitates being larger. The intra-granular precipitates were not uniformly distributed within the grains. EDS analysis of the intra- and intergranular precipitates showed higher chromium concentrations than in areas without precipitates (see Figure 4.7-Figure 4.9). Molybdenum peaks were also apparently present in the EDS spectra but as there is an overlap between S Kα and Mo Lα, molybdenum and sulphur could not reliably be distinguished. The predominant carbides reported in type 316H material are $M_{23}C_6$ (M = Cr, Fe, Mo) [15]. Higher counts of carbon, chromium and molybdenum in the EDS spectrum leads the assumption that the carbides are $M_{23}C_6$. $M_{23}C_6$ can form on grain boundaries, inclusion interfaces twin boundaries and inside austenite grains [181].

The microstructure of Material sample D was completely different from Material A, B and C, showing almost no precipitation (see Figure 4.10), but there were precipitates of nanometre size in this material. These precipitates are reported to be $M_{23}C_6$ carbides as irregular and coherent blocks at grain boundaries [46].

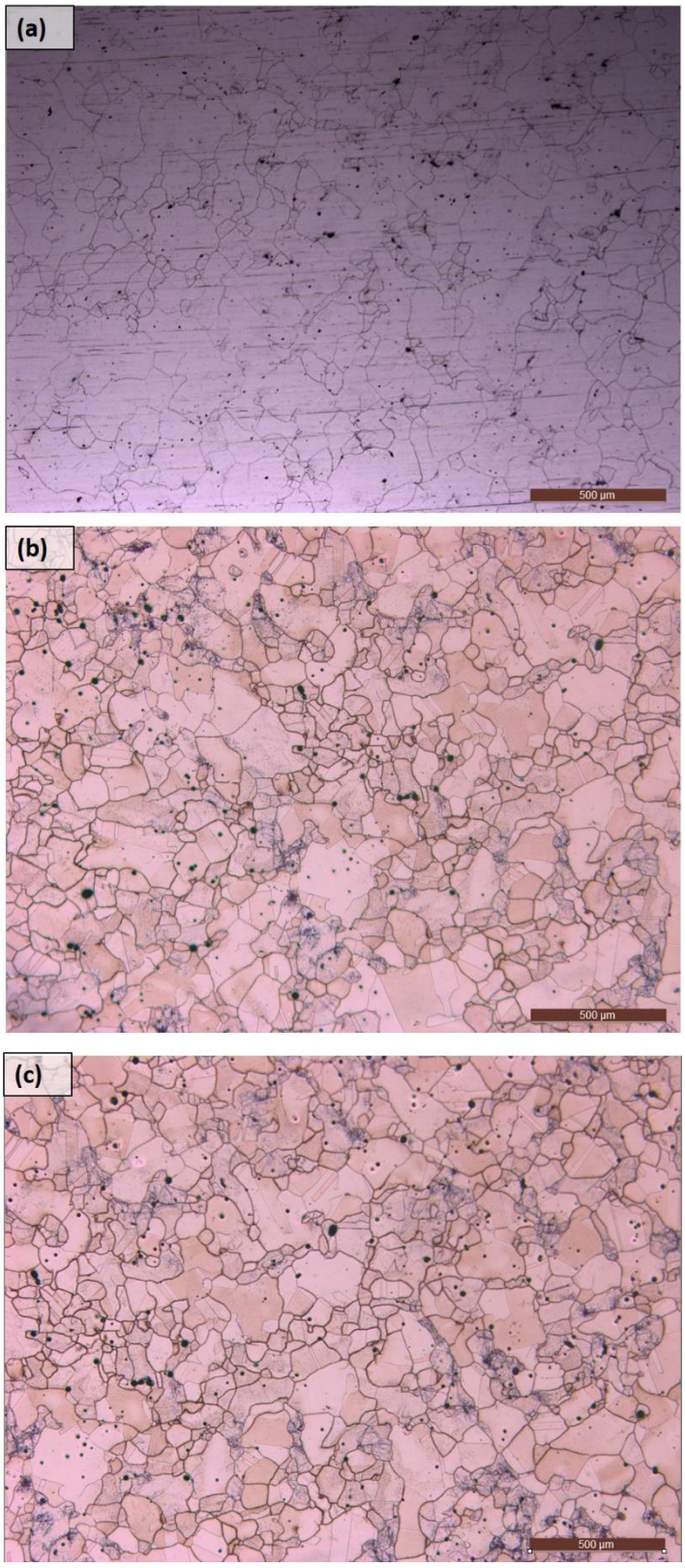

Figure 4.4 Optical microstructure of (a) ex-service sample material, (b) ex-service sample material B, (c) ex-service sample material C.

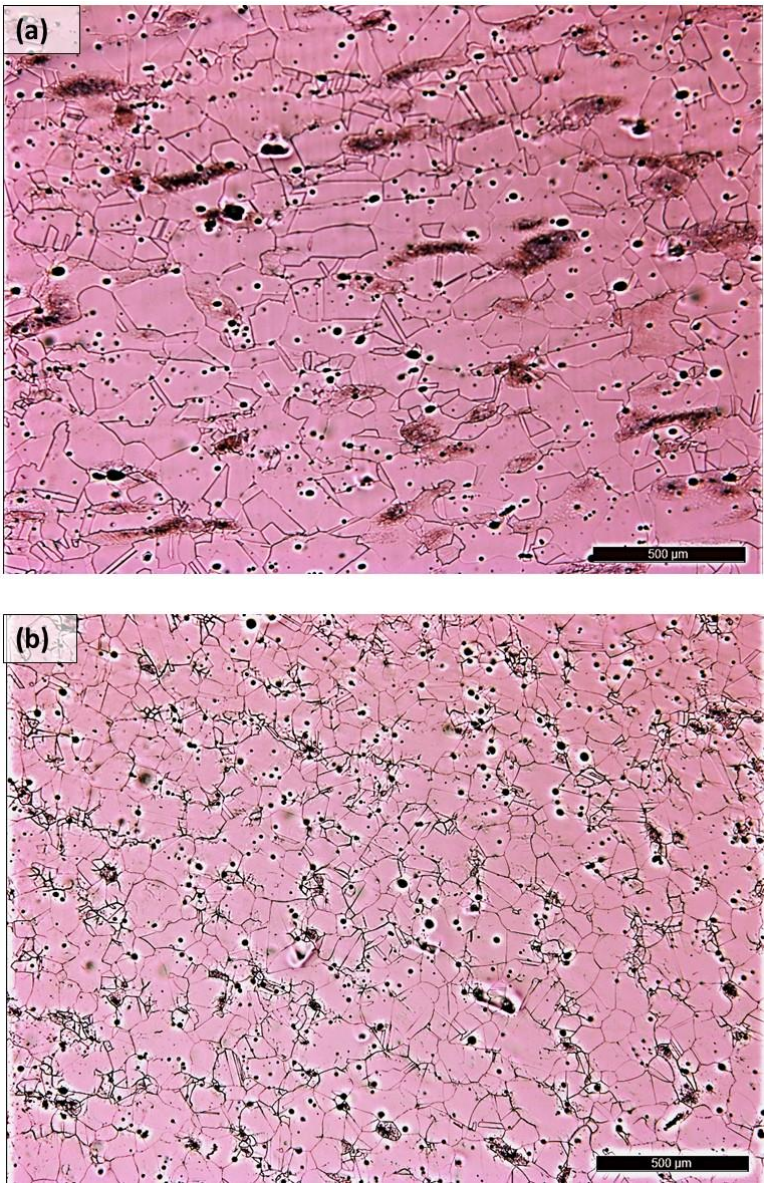

Figure 4.5 Optical microstructure of (a) solution annealed sample material D and (b) thermally aged sample material E.

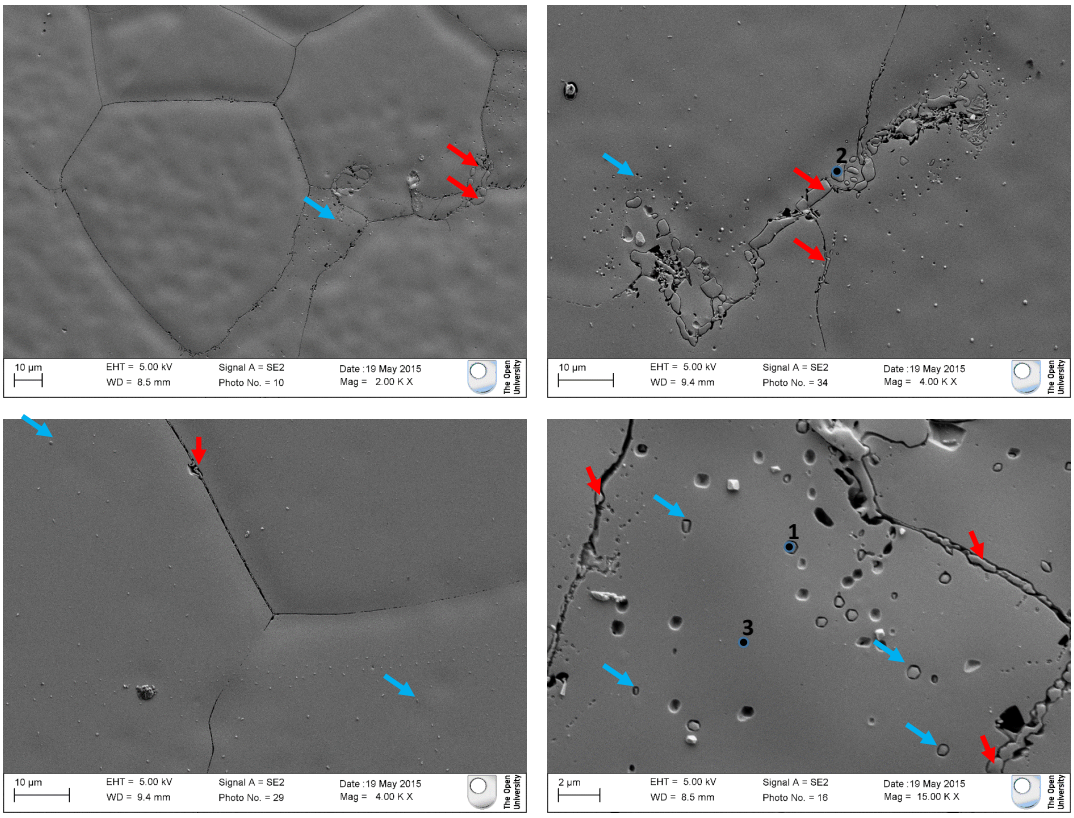

Figure 4.6 SEM micrographs of ex-service material (Sample material A) with inter- and intra-granular precipitates. Intra-granular precipitates are marked by blue arrows and inter-granular precipitates by red arrows.

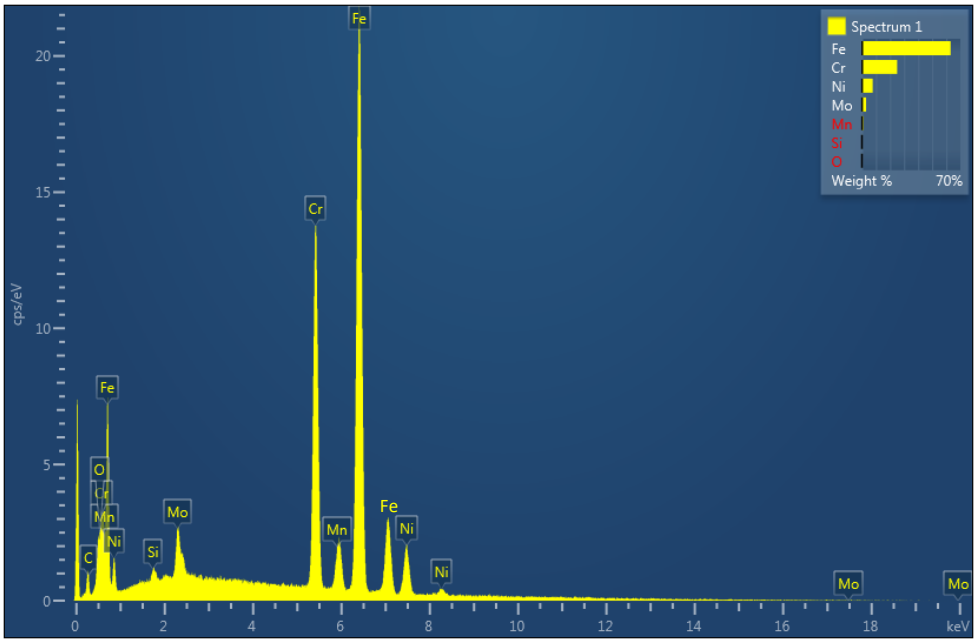

Figure 4.7 EDS spectra of inter-granular precipitate in sample material A (location 1 in Figure 4.6). X-ray energies/keV on x-axis and counts per second/eV on y-axis.

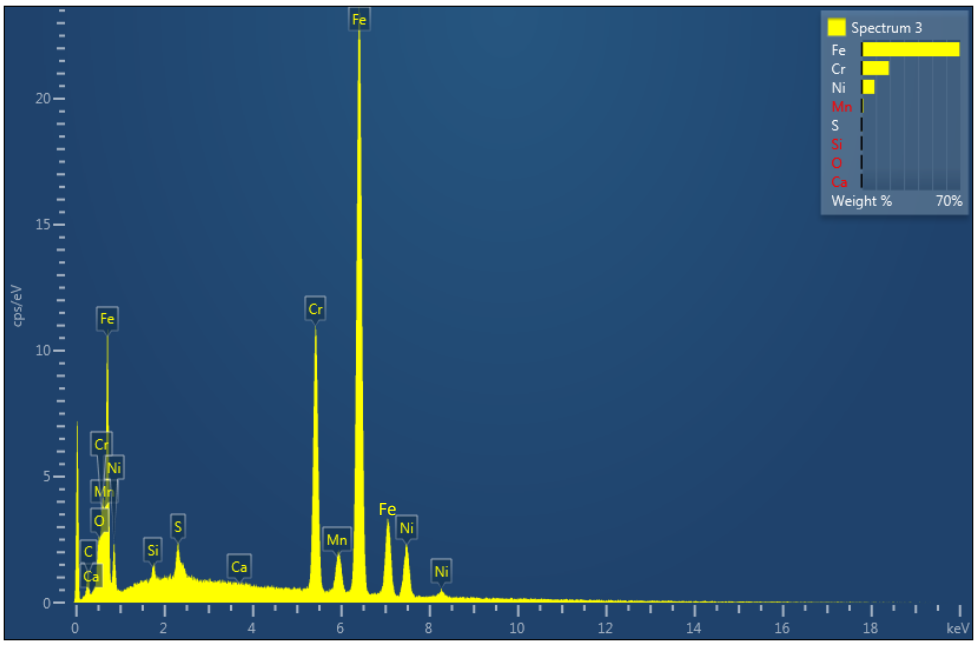

Figure 4.8 EDS spectrum of intra-granular precipitate in sample Material A (location 2 in Figure 4.6). X-ray energies/keV on x-axis and counts per second/eV on y-axis.

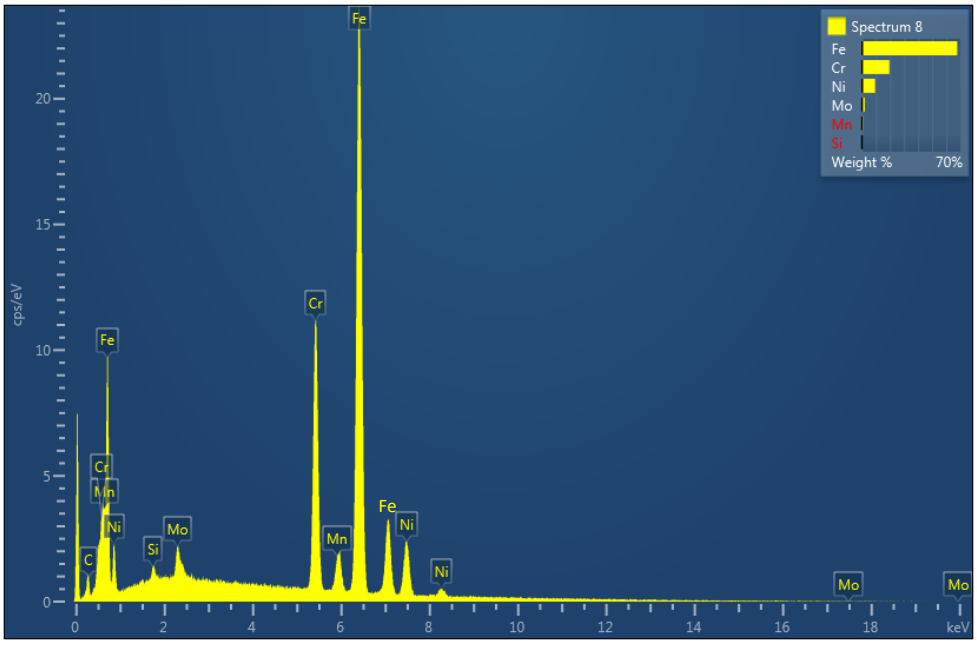

Figure 4.9 EDS spectrum of austenite matrix in sample Material A (location 3 in Figure 4.6). X-ray energies/keV on x-axis and counts per second/eV on y-axis.

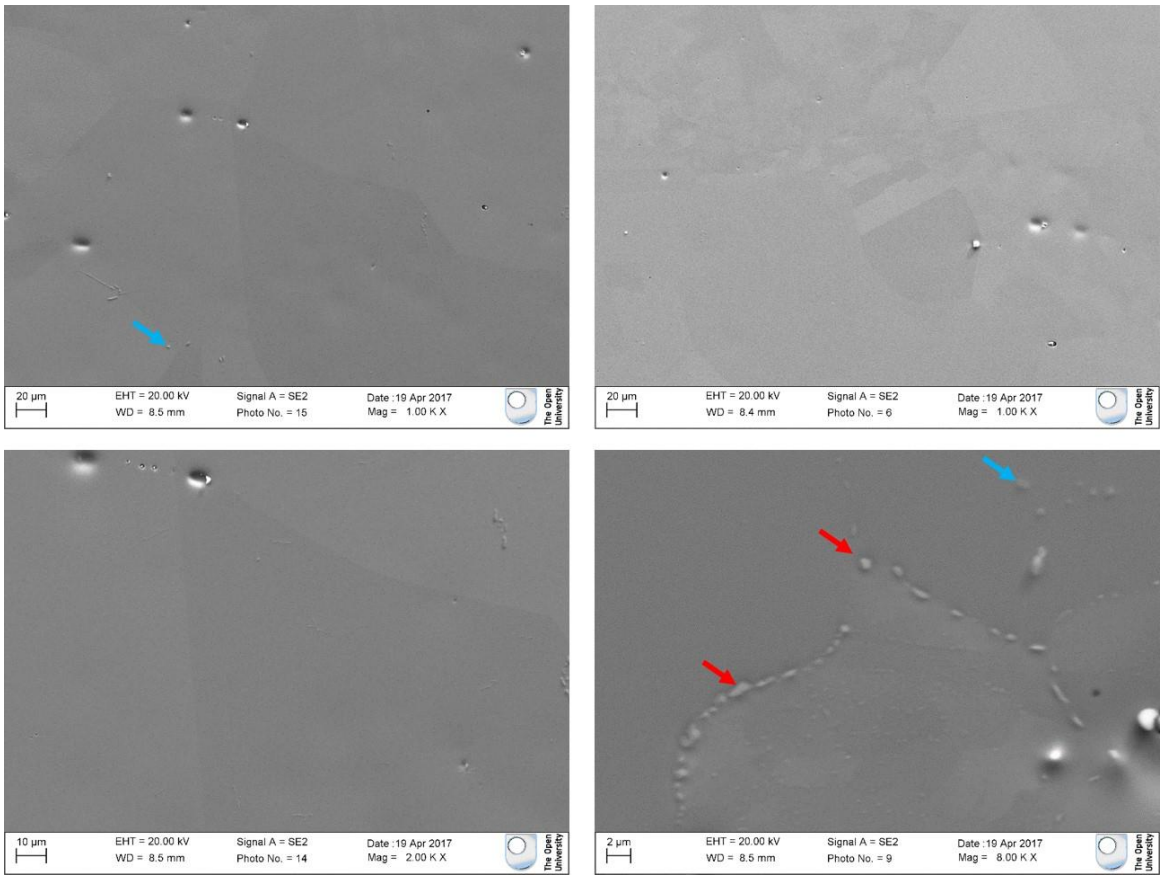

Figure 4.10 SEM micrographs of re-solution heat treated steel with inter- and intra-granular precipitates (sample Material sample D). Intra-granular precipitates are marked by blue arrows and inter-granular precipitates by red arrows.

The solution annealing heat treatment did not eliminate all the precipitates in ex-service material (see Figure 4.10). Similar observations were reported by Stoter [46]. Very few intra- and inter-granular precipitates were visible in sample E (see Figure 4.11) and the precipitates were much finer than in sample A.

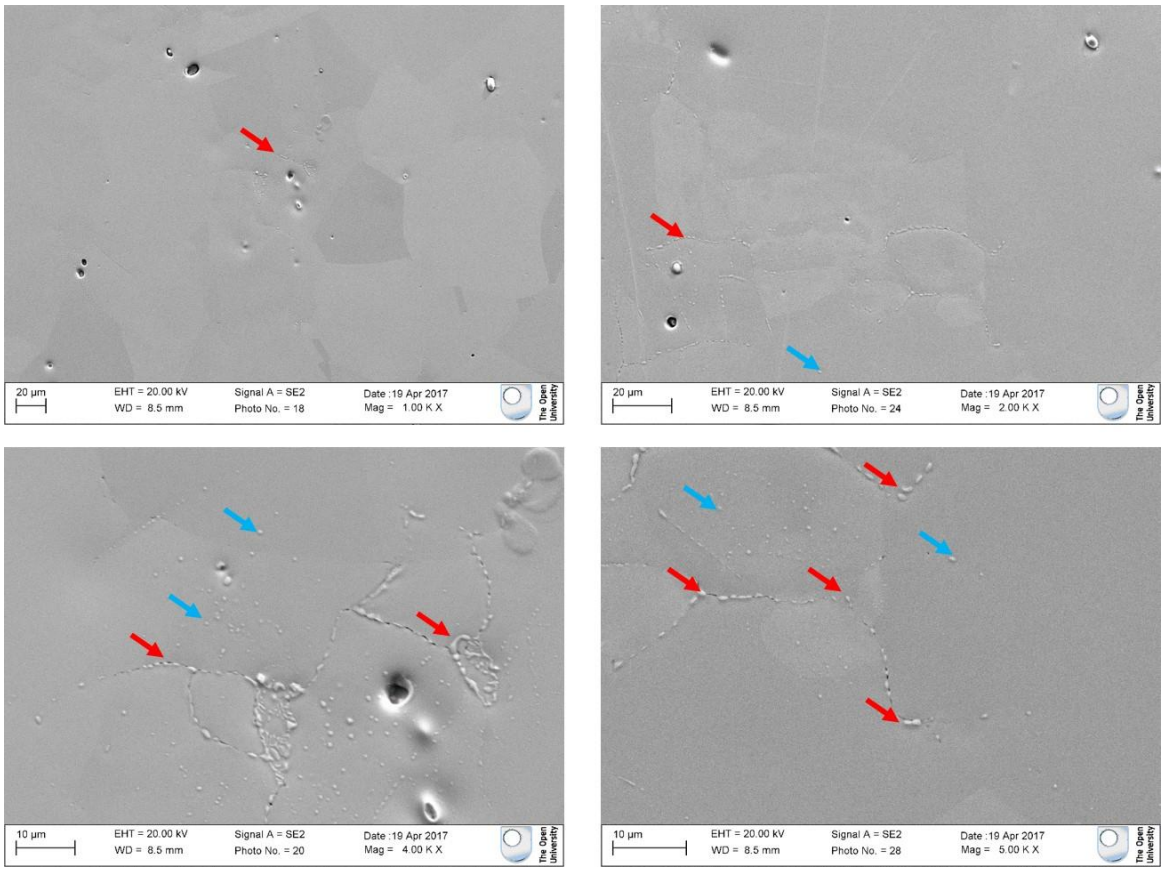

Figure 4.11 SEM micrographs of thermally aged steel with inter- and intra-granular precipitates (sample Material E). Intra-granular precipitates are marked by blue arrows and inter-granular precipitates by red arrows.

The size distributions of the precipitates in ex-service (samples A, B and C), solution annealed (Sample D) and thermally aged (Sample E) material studied in this thesis are shown in Figure 4.12. Precipitates of average diameter 0.1 to 2.8µm were studied (over an area of 2 mm^2) using SEM backscatter images at a magnification of 20000X. At least 1500 precipitates were measured for each ex-service material (samples A, B and C) and at least 500 in each of the solution annealed (sample D) and thermally aged (sample E) materials. The number density of precipitates between 0.7µm and 1.8µm was slightly higher for sample material C (see Figure 4.12 (c)) than in sample materials A and B (for ex-service material, see Figure 4.12 (a),(b)). This could be due either to temperature variations across the thickness of ex-service component during its service or to the manufacturing method. There were fewest precipitates in the solution annealed material

(sample material C, see Figure 4.12(d)), followed by the thermally aged material (sample material E, see Figure 4.12 (e)).

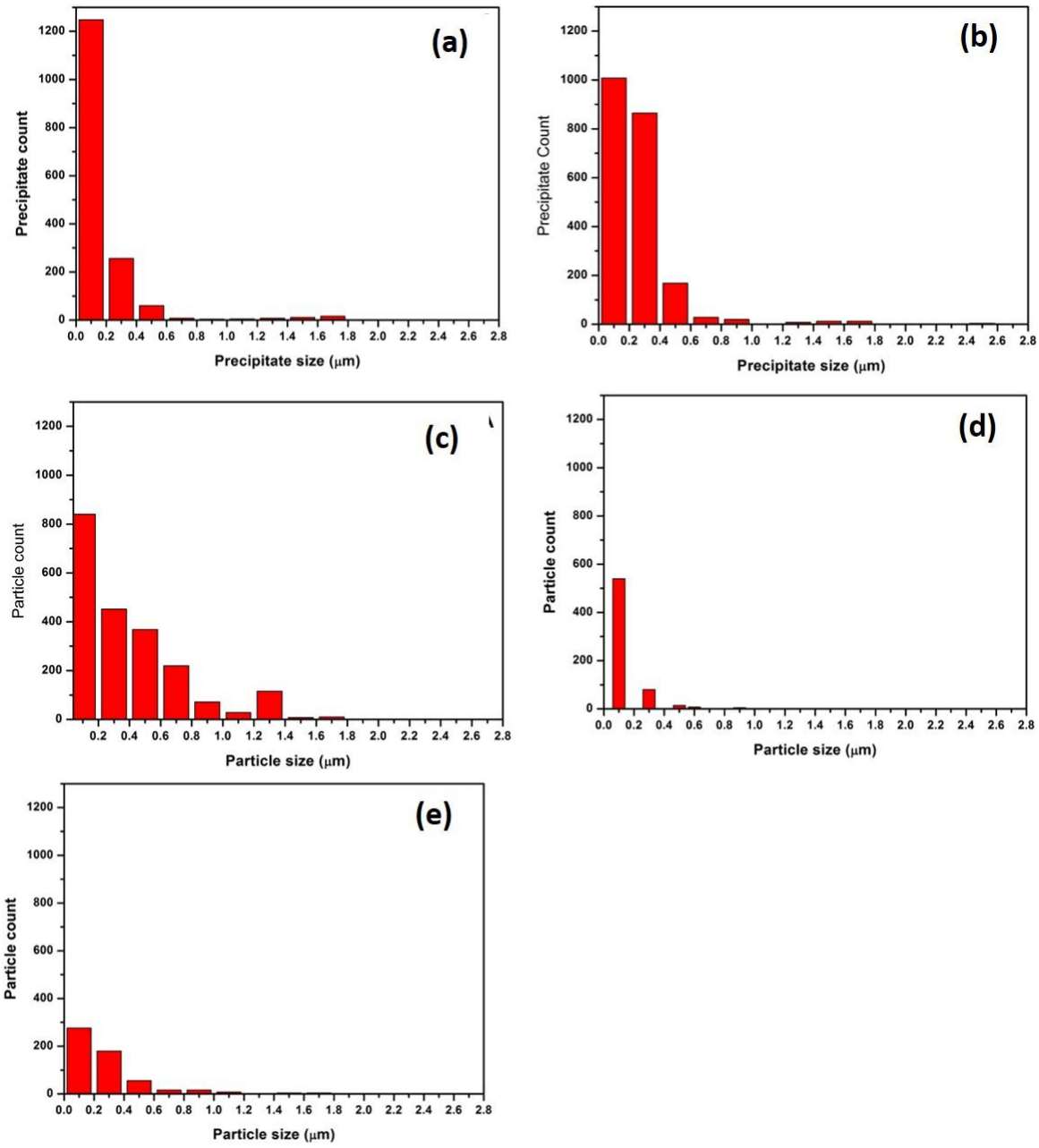

Figure 4.12 Size distribution of precipitates in (a) ex-service sample material A, (b) ex-service sample material B, (c) ex-service sample material C, (d) solution annealed sample material D and (e) thermally aged sample material E.

4.3.2. Characterization of dislocation structures

Plastic strain is usually accommodated in crystals by slip, twinning or phase transformation. When the crystal undergoes slip, the lattice defects tend to accumulate along the slip planes. These line defects are called dislocations. The movement of dislocation involves rearrangement of the atomic bonds around it. At high temperatures, the dislocations tend to rearrange into energetically favourable cells as the deformation proceeds. It is well known that once a dislocation cell structure is established in cold deformation, any further increase in strain leads to a decrease in the cell size [182]. The dislocation structure is closely related to the crystallographic misorientation of adjacent cells. If there are areas of dislocations with a net non-zero Burgers vector (GNDs) , they can create lattice curvature leading to change in crystallographic orientation [31]. Dislocation structures significantly affect plastic deformation so it is important to characterize these structures to understand the relationship between the dislocation structures present and the material's deformation.

In the current study, a JEOL 2100 STEM in HAADF mode was used to characterize dislocation structures in the ex-service, re-solution heat treated and thermally aged materials. Images were taken using the STEM dark field detectors. Details of the TEM are given in Chapter 3. The statistical representativeness of TEM images in describing a bulk material is always a concern. Hence the commonest dislocation structures in all of the TEM foils studied for each condition are presented assuming they are representative of the bulk material.

Dislocation structures in the ex-service material (sample material A) consisted of individual dislocations and dislocation tangles (see Figure 4.13*)*. A high density of intra-granular precipitates seemed to favour the formation of dislocation tangles. Dislocation

pinning was observed around the randomly placed intragranular precipitates and there was also evidence of dislocation bowing and looping.

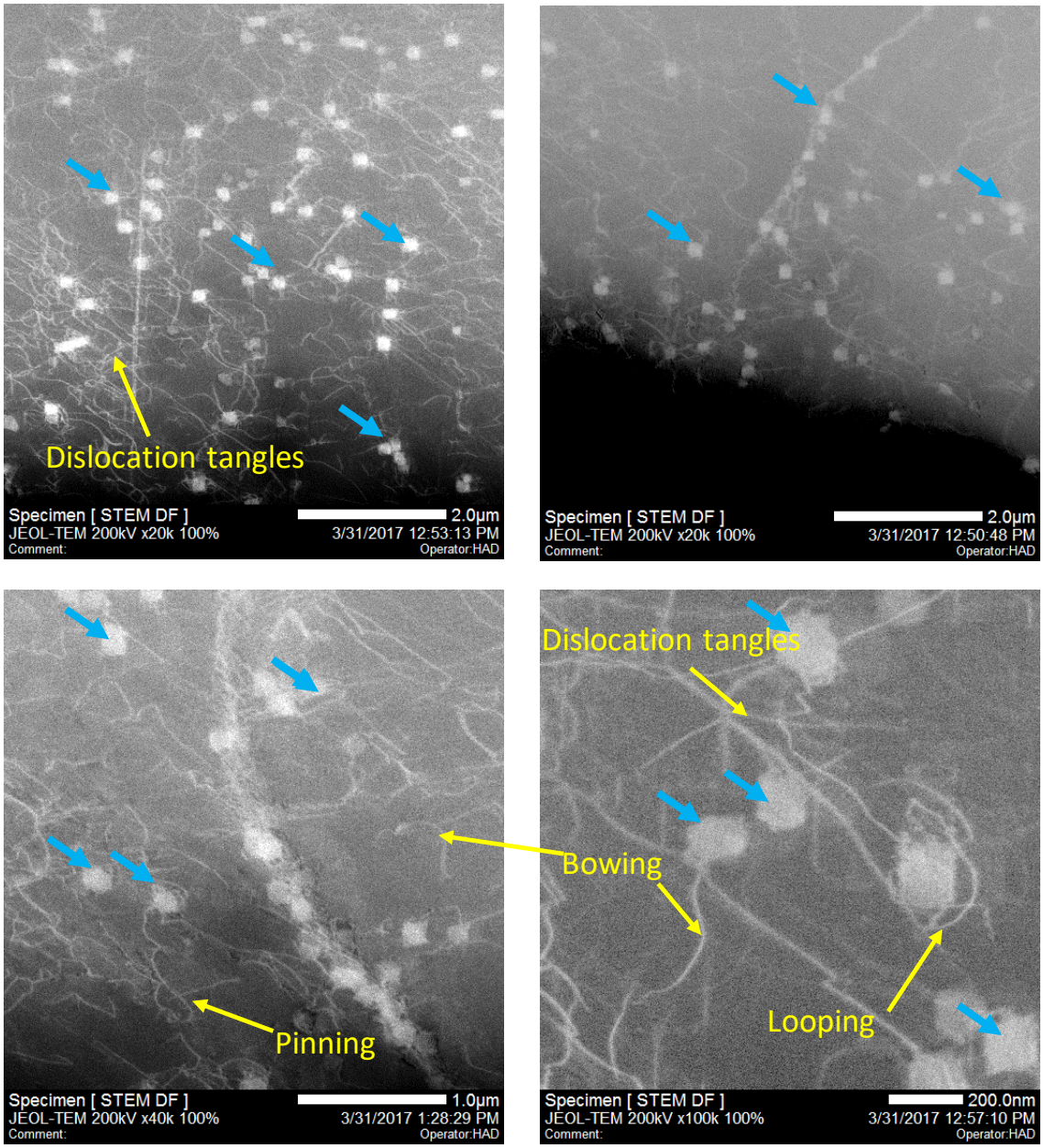

Figure 4.13 STEM HAADF images of ex-service type 316H material (sample material A) showing dislocation pinning, bowing, looping and tangles around precipitates. Intragranular precipitates are marked by blue arrows.

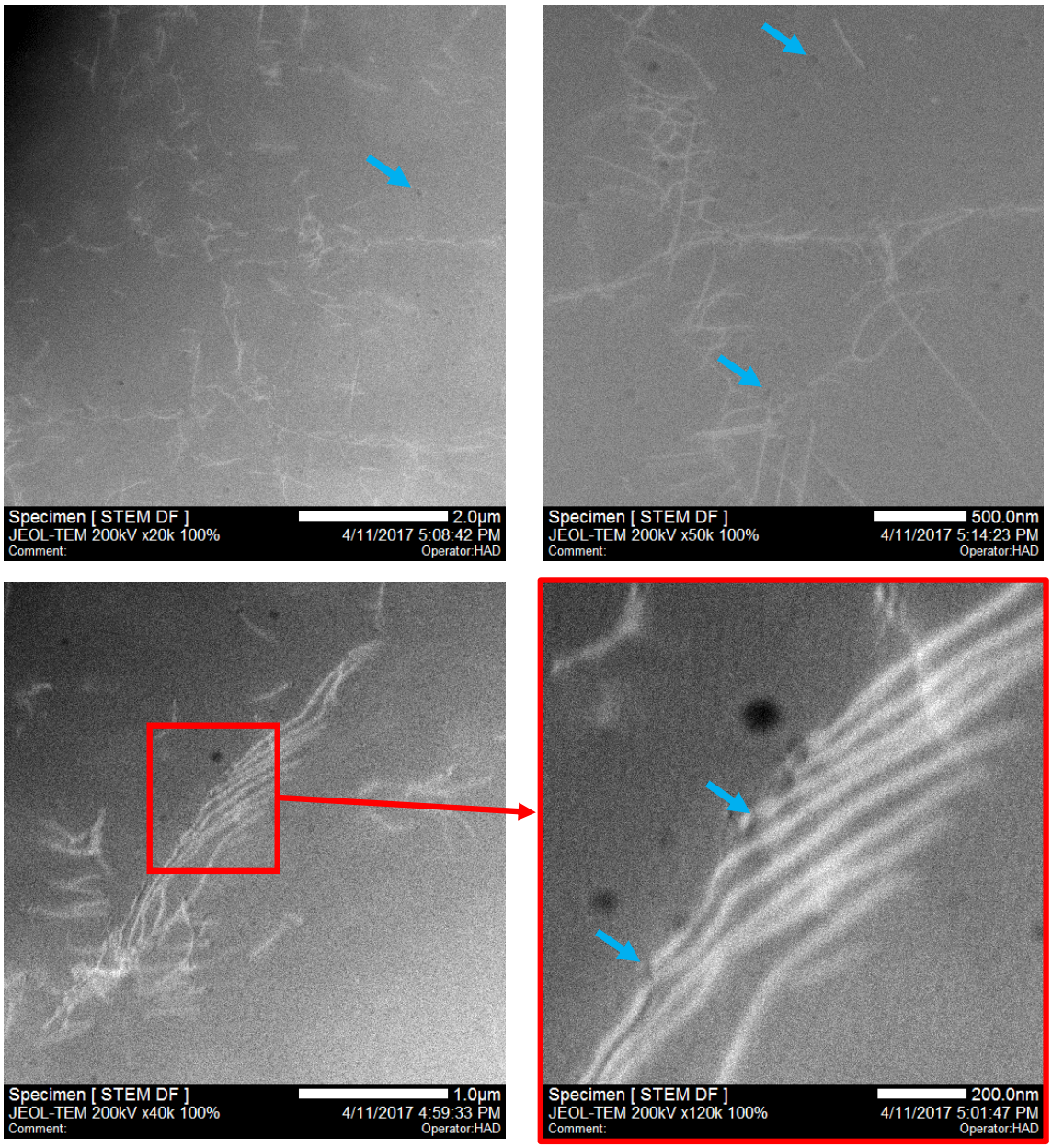

Figure 4.14 STEM HAADF images of solution heat treated type 316H austenitic stainless steel (material D). Intra-granular precipitates are marked by blue arrows.

There were far fewer individual dislocations visible in sample material D (see Figure 4.14) and fewer precipitates of nanometre size (blue arrows). TEM EDS showed a Cr concentration at these precipitates. There was some evidence of dislocation bowing.

STEM microstructures of thermally aged material (sample E) are shown in Figure 4.15. There were areas with and without dislocations in the TEM foils observed. Inter-granular nano-precipitates were present. $M_{23}C_6$ precipitates were reported to nucleate along

dislocations within 10 hours at 550ºC [38] and more precipitates were found at areas of higher dislocation density in the material.

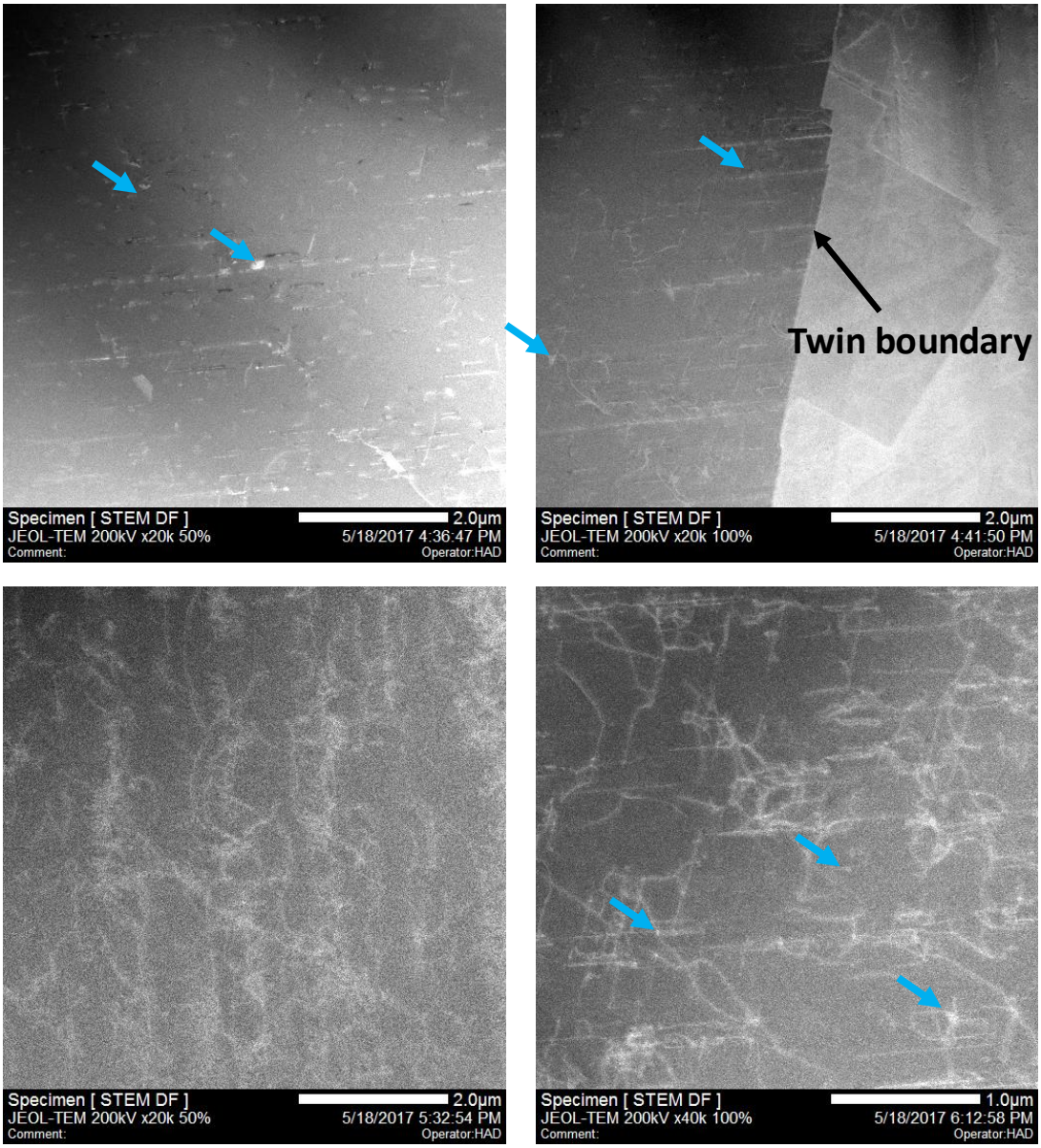

Figure 4.15 STEM HAADF images of thermally aged type 316H material (material E) showing dislocations, precipitates and twin boundaries. Intra-granular precipitates are marked by blue arrows.

It is clear from the current results that the STEM microstructures of ex-service, re-solution heat treated and thermally aged materials are very different; the ex-service material contained larger intra-granular precipitates and dense dislocation structures whereas the solution annealed material had very few precipitates and dislocations. There were more

precipitates in thermally aged material than in solution annealed material. Similar results were obtained after precipitate analysis using SEM (see Figure 4.12).

4.3.4. Grain size

Grain size measurements were carried out both relying on the EBSD software and using the linear intercept method described in ASTM standard E112-13 [183]. In orientation imaging microscopy, a grain is defined by an algorithm that groups pixels lying within a tolerance orientation angle as one. The grain boundary is defined by an orientation difference between adjacent pixels of > 15^{o}. The grain area is determined by counting the number of pixels in a grain multiplied by the product of the square of the step size and a factor depending on the shape of the grid used. The factor is one for a square grid and $(1/2)\sqrt{3}$ for a hexagonal grid [127].

The EBSD grain boundary maps were also used to calculate the grain size using the linear intercept method, as EBSD revealed the grains better than optical microscopy. This is because in EBSD the grain boundaries are defined by the misorientation between neighbouring pixels, whereas conventional metallographic methods may not properly reveal all grain boundaries by optical microscopy, because of the variable chemical etching of different boundaries. Three EBSD maps, each of an area approximately $0.8*0.8mm^2$, and with a minimum of around 500 grains were used for grain size measurement. Only maps with indexing rates >96% and containing at least 150 grains were used for grain size calculation. Only grains with ECD>11µm were considered, to reduce errors associated with mis-indexing in the ECD grain size calculations.

The measurement of grain size using OIM was based on the ECD (Equivalent circle diameter[129]) method. The ECD grain size was calculated using:

$$\zeta = \sqrt{\frac{4A}{\pi}} \quad (4.1)$$

where ζ is the grain size in microns and A is the grain area, given by the total number of measurement points per grain multiplied by the square of the step size [184]. The Channel5 software automatically calculates the grain area and the ECD grain size of each grain [185].

MTEX [172], a free MATLAB toolbox for EBSD measurement, was used for grain size measurement using the mean linear intercept (MLI) method. MATLAB codes were developed to superimpose straight lines of known length (L) in random directions on the grain boundary maps and to count the number of intercepts (N). Since the automatic algorithm counts twin boundaries, the intercepts were manually counted to exclude twin boundaries. The spacing between the lines were fixed to get at least 40 intercepts from each map (see Figure 4.16). The mean linear intercept grain size in the x direction (L_x) was the calculated by:

$$L_x = \frac{R_x s P_x}{N_x} \quad (4.2)$$

where R_x is the number of rows scanned in x direction, N_x is the number of complete boundaries intercepted, P_x is the number of pixels in the x direction and s is the distance between pixels. The procedure was repeated in the y direction and the mean linear intercept in both x and y directions was taken as the mean linear grain size for that orientation map. The mean grain sizes obtained by both the methods are reported in Table 4.2. The high scatter in the mean grain size values calculated using the ECD method can be attributed to the very wide distribution of grain sizes up to 300µm and the peak in frequency at lower values (see Figure 4.17).

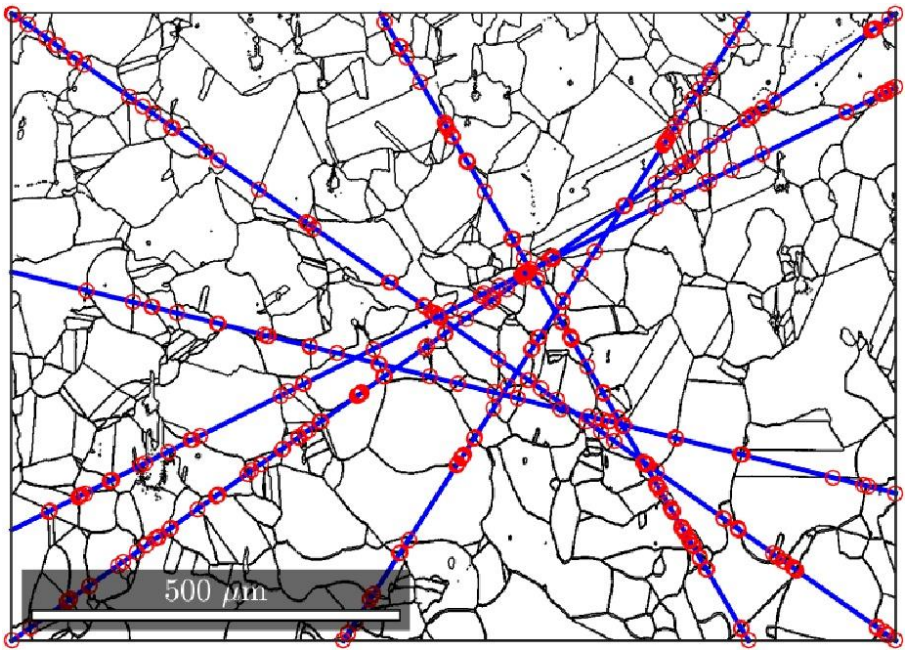

Figure 4.16 EBSD grain boundary maps showing random superimposed lines for MLI grain size determination. Red circles mark the intersections of vertical lines with the grain boundaries.

Table 4.2 Mean and standard deviation of grain size (in μm) of the Type 316H austenitic stainless steel studied, derived using EBSD grain boundary maps.

Method	Material A	Material B	Material C	Material D	Material E
MLI-EBSD	78±8	76±7	76±6	85±9	84±8
ECD-EBSD	29±21	32±30	36±30	45±38	42±31

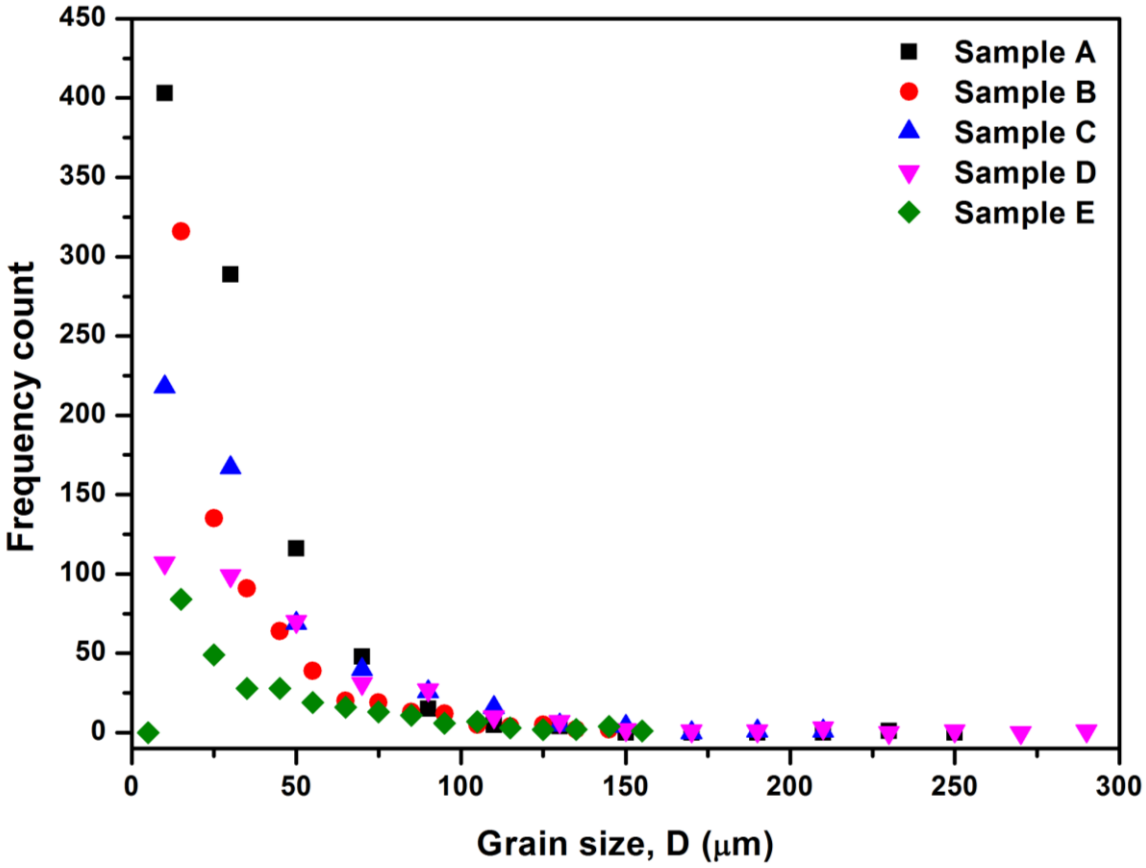

Figure 4.17 EBSD-ECD grain size (D) distribution of type 316H austenitic stainless steels used in the study.

4.3.5. Texture analysis

The crystallographic orientations of a polycrystalline material refers to the orientation of the grains' crystal lattices with respect to an external fixed coordinate system. The tendency to have a preferred pattern in orientation is called texture. Many material properties (Young's Modulus, Poisson's ratio, strength, ductility, toughness, thermal expansion, etc.) are texture dependent [124]. The most common way of representing micro texture is using a pole figure. In a pole figure, the numbers of grains having specific crystallographic directions oriented along each real space direction are projected onto a sphere containing it. Commonly a stereographic projection is used to display the distribution for each specific direction in 2D [124]. The {111}, {101} and {100} pole figures of different materials used in this study are shown in Figure 4.18 and Figure 4.19.

The pole figure is normalized and pole figure densities are expressed in multiples of the uniform density (m.u.d.). There was only a weak texture evident in all the materials used for the study (see Figure 4.18, Figure 4.19).

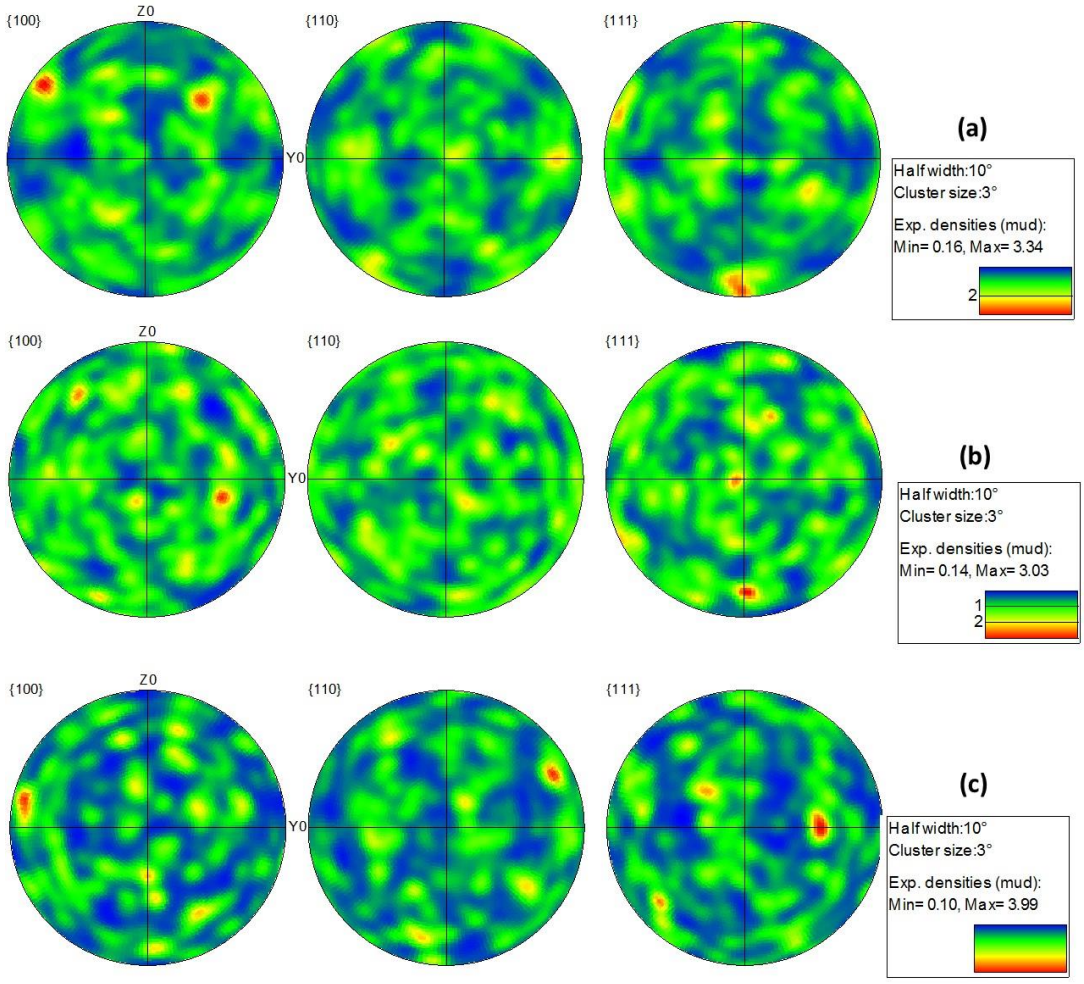

Figure 4.18 Pole figures plots of undeformed service-aged Type 316H stainless steel (a) material A, (b) material B and (c) material C.

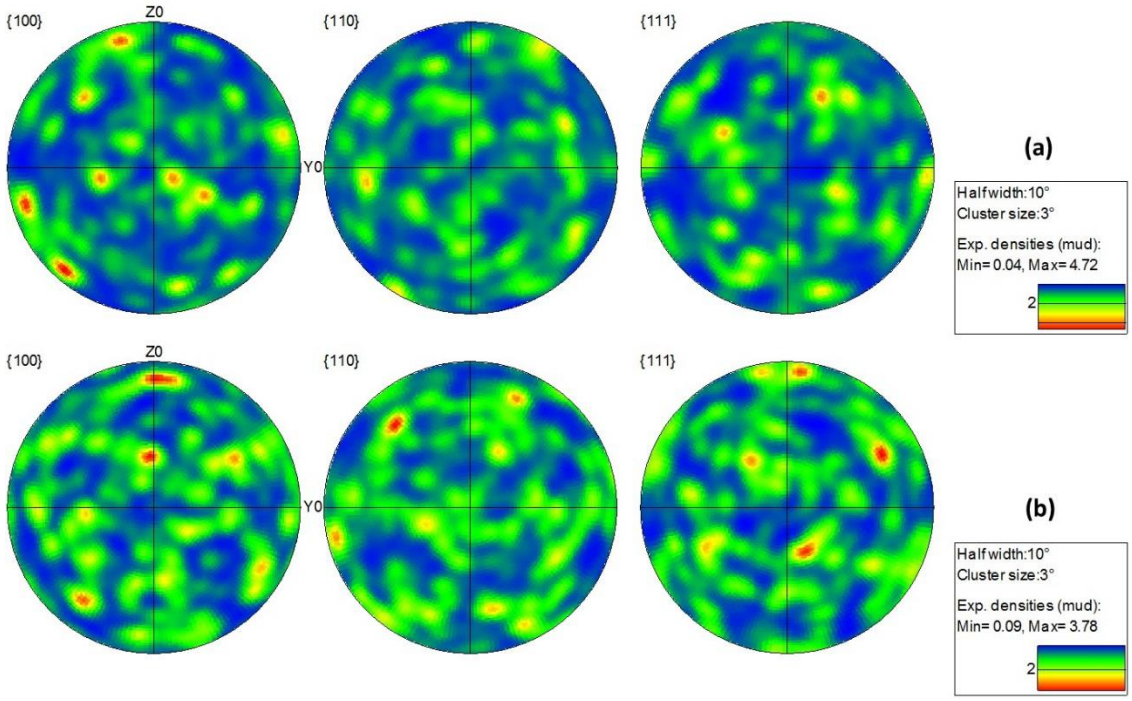

Figure 4.19 Pole figures plots of (a) solution annealed type 316H stainless steel (material D) and (d) thermally aged type 316H austenitic stainless steel (material E).

4.3.6. Tensile Properties

High temperature tensile tests were conducted on samples of the material extracted from the different locations (sample materials A, B and C in Figure 4.2) of the steam header where cyclic and stress relaxation tests were also conducted. Tensile tests at different temperatures (23 and 550ºC) and strain rates (0.025 and 0.0025%/s) were conducted on ex-service sample materials A, B, C, re-solution heat treated (sample material D), and thermally aged materials (sample material E). Details of the tensile test results are given in Chapter 5.

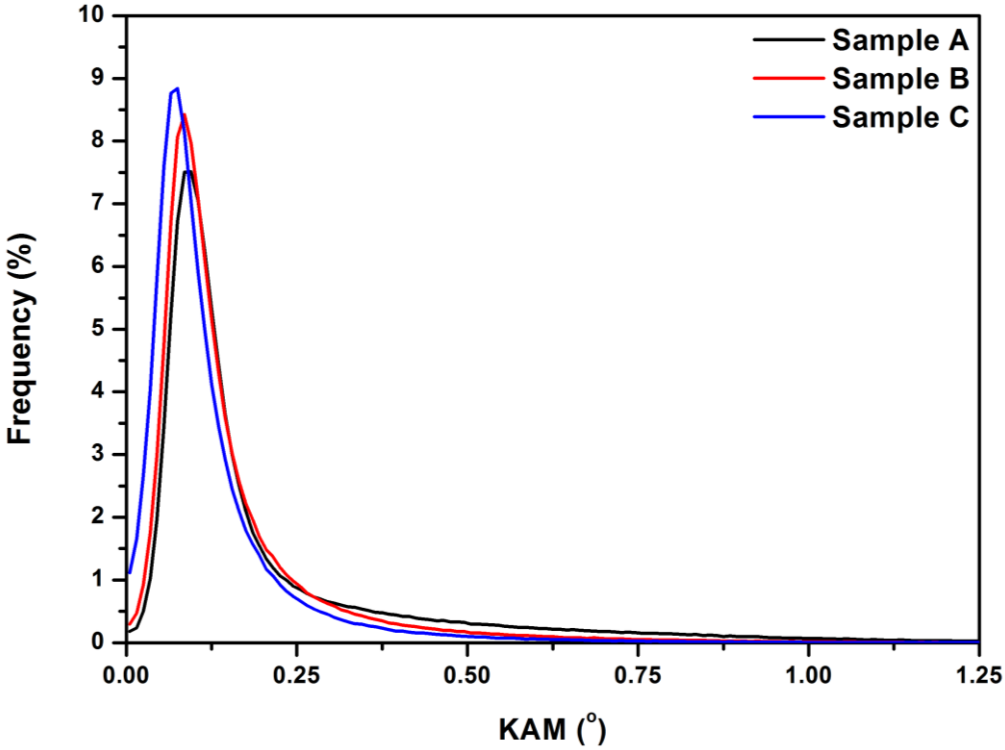

Figure 4.20 Kernel average misorientation distribution at different locations of the type 316H steel steam header used for the study.

The corresponding KAM distributions (see Figure 4.20) also showed the highest KAM values for sample material A, which is from the outer location of the header and the lowest for sample material C which is from the inner location. This clearly shows that there was more deformation in the outer part of the header during its manufacture or service although the grain sizes of sample materials A, B and C were almost the same. Details of the grain size measurements are given in section 4.3.2. This clearly indicates a through thickness heterogeneity across the header.

The 0.2% and 1% proof stresses were calculated for samples of the materials under each different deformation condition by finding the intersections of the true stress-strain curve with lines parallel to their linear (elastic) region but offset by 0.2% and 1%, respectively. The 0.2% and 1% proof stresses of sample materials A, B, C, D and E are given in Table

4.3. All the stress-strain curves showed evidence of dynamic strain ageing (DSA) [73] as discussed in Chapter 5.

Table 4.3 Proof stress in MPa of Type 316H austenitic stainless steel samples studied. All tests carried out at a strain rate of 0.025%/s unless otherwise mentioned.

Temp. (°C)	Material A	Material B	Material C	Material D	Material E	Material E (0.0025%/s)
23	285[1], 319[2]	--	--	212, 247	--	--
550	168, 193	163, 190	143, 179	106, 128	146, 167	159, 185
640	--	106, 128	--	--	--	--
Key: [1]0.2% proof stress, [2]1% proof stress						

4.4. Summary

The average grain size of re-solution treated and thermally aged material was slightly higher than that of ex-service material. Ex-service material had intra- and inter-granular precipitates and a complex dislocation structure. The dislocation densities in solution annealed and thermally aged materials were lower than in ex-service material. The size distribution of precipitates in ex-service, solution annealed and thermally aged material were studied. The precipitates were smaller in solution annealed and thermally aged material than in ex-service material. The precipitates were found to nucleate near dislocations in thermally aged material. The tensile properties were found to vary with radial location in the ex-service header.

CHAPTER 5

MISORIENTATION DEVELOPMENT UNDER UNIAXIAL LOADING

5.1. Introduction

The influence of plastic strain on misorientation development under uniaxial loading has already been reported for this material [11]. However little information is available about the development of misorientation during uniaxial stress relaxation. In this chapter, the evolution of lattice misorientations after strain controlled plastic deformation at room temperature (23^{o}C) and elevated temperatures (550, 640^{o}C) are reported. Tensile tests were conducted on ex-service (sample material B), solution annealed (sample material D) and thermally aged (sample material E). The tensile test and EBSD results from sample materials B and D were compared to see the effect of grain size and precipitates on misorientation development. Experiments with a constant strain hold of 24 hours were also conducted on ex-service materials after 2, 5, 10 and 15% prior engineering plastic strain, to see the effect of stress relaxation (i.e. displacement control) on misorientation development. The chapter compares the results from EBSD with those from techniques like hardness measurement, examination of the microstructures, using SEM, and of the dislocation structures, using TEM, and then concludes with a summary of the key findings.

5.2. Influence of temperature, strain rate and microstructure on misorientation development (in ex-service, re-solution heat treated and thermally aged steel materials)

5.2.1. Tensile tests

The effects of temperature and carbide precipitation on misorientation development was investigated through tensile tests conducted at both room temperature and 550^{o}C on ex-service (material B), solution annealed (material D) and thermally aged (material E) material. Based on the MLI method, the average grain size of Material B was 76±7 µm, Material D was 85±9 µm and Material E was 84±8 µm, showing the grain sizes to be comparable. The tensile tests were conducted as described in Chapter 3. Room temperature (RT) tensile tests were conducted on Materials B and D to study the effect of carbide precipitates on misorientation development. Details of the size distributions of the carbides are reported in chapter 4 (section 4.3.1). The conditions under which the tensile tests were conducted are given in Table 5.1 Investigations were also carried out at two strain rates (0.025, 0.0025%/s) on material B (Sample IDs 550B5%0.025 and 550B5%0.0025) at 550^{o}C to study the effect of strain rate on misorientation development at high temperature.

Table 5.1. Tensile test conditions for Type 316H stainless steel to study the effect of precipitate and grain size on misorientation development.

Steels	Engineering Strain (%)	True Strain (mm/mm)	Temperature (^{o}C)	Sample ID
B	5	0.04879	23	RTB5%0.025*
B	5	0.04879	550	550B5%0.025
B	5	0.04879	550	550B5%0.0025
B	15	0.13976	550	550B15%0.025
D	5	0.04879	23	RTD5%0.025
D	5	0.04879	550	550D5%0.025
D	5	0.04879	640	640D5%0.025
E	15	0.13976	550	550E15%0.025

*RTB5%0.025 (Red for temperature in degree Celsius/room temperature, Black for type of steel as mentioned in Chapter 4, Brown for Engineering strain and Green for strain rate.

5.2.2. EBSD measurements

The EBSD measurements were carried out on deformed materials as described in Chapter 3. The misorientations developed were studied as a function of inelastic strain (plastic strain in this case) using the different EBSD metrics discussed in Chapter 4. The tests have already been described in Table 5.1. Misorientations were assessed both at the local scale (KAM, LABFA) and at longer range (GOS_a, DGF(0.5), DGF(1), TBF).

5.2.3. Mechanical test results

The true stress-strain curves obtained from the mechanical tests are shown in Figure 5.1. All the stress-strain curves at elevated temperatures showed serrations (see Figure 5.1) due to DSA (see section 2.3.5 in Chapter 2). At the same strain, the stresses were lower for solution annealed materials (RTD5%0.025, 550D5%0.025) than for ex-service material (RTB5%0.025, 550B5%0.025), which shows the hardening effect of precipitates on plastic deformation.

The yield stress of the ex-service material was lower at high temperature compared to RT as expected (see Figure 5.1, RTB5%0.025, 550B5%0.025 and 640B5%0.025). The effect of DSA on the stress-strain curve was more significant at a lower strain rate e.g comparing (550B5%0.0025) to 550B5%0.025 (see Figure 5.2), but the flow stress remained unchanged with lower strain rates.

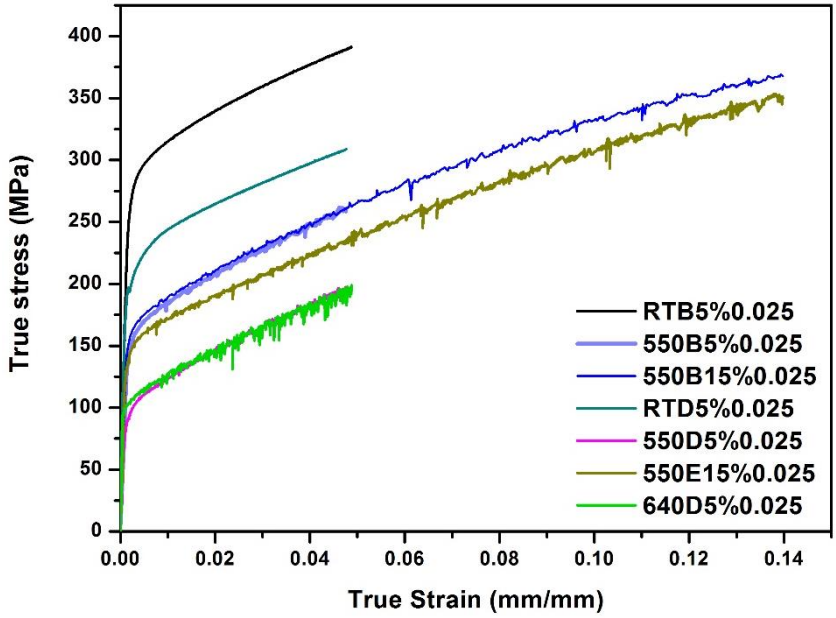

Figure 5.1 Stress-strain curves for Type-316H steel deformed as in Table 5.1 at a strain rate of 0.025%/s.

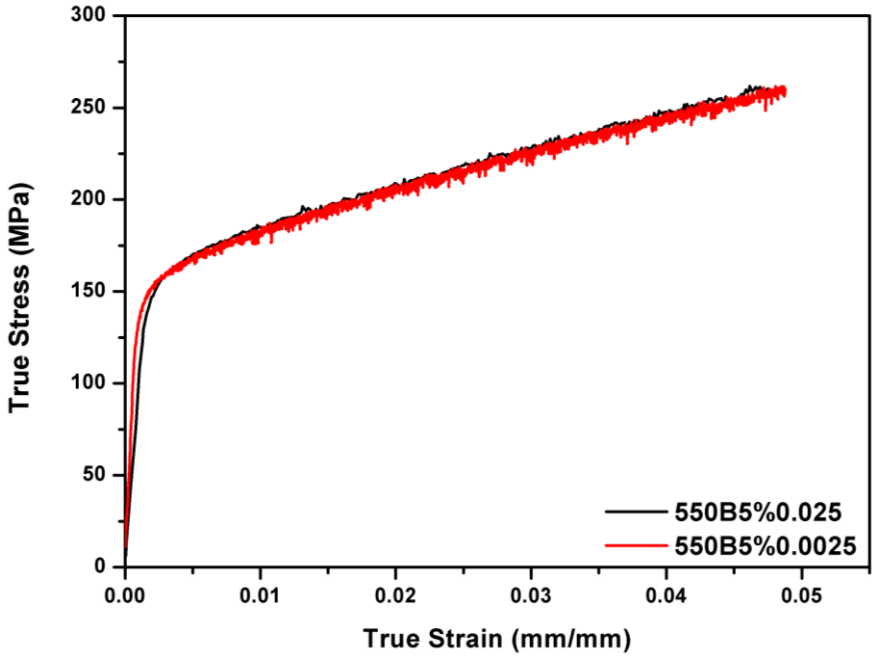

Figure 5.2. Stress-strain curves for ex-service type-316H steel (material B) deformed at a strain rate of 0.025 and 0.0025%/s.

5.2.4. EBSD results

The EBSD metrics showed little difference when the strain rate was reduced from 0.025%/s to 0.0025%/s except for TBF and LABFA (see Figure 5.3). Figure 5.3 shows the effect of strain rate on the EBSD metrics. KAM_a lognormal, GOSa, DGF(1) and DGF(0.5) were found to be insensitive to strain rate when the strain rate was reduced from 0.025%/s to 0.0025%/s. TBF_a was found to increase with a reduction in strain rate (See Figure 5.3).

For the same strain, the EBSD metrics, except for LABFA, were found to be generally insensitive to the deformation temperature (see Figure 5.4) for solution annealed material. A direct comparison of the results at room and high temperatures is difficult as there are almost no precipitates in solution annealed material at room temperature whereas precipitation would have already started at 550 and 640^{o}C. There was a systematic small reduction in KAM_a lognormal and DGF(0.5) with increasing deformation temperature from room temperature to 640^{o}C. But for ex-service material (Material B) the EBSD metrics except for TBF were higher after deformation at 550^{o}C (see Figure 5.5) than for the same strain at RT.

The misorientation built up was lower, and the TBF metric consistently higher, in the absence of precipitates (see Figure 5.6). Figure 5.7 clearly shows the effect of precipitates on local misorientation development. The misorientation built up was slightly higher in ex-service material (Material B) than in thermally aged material (Material E) (See Figure 5.8). This can be attributed to the effect of the precipitates. The precipitates in Material B

are very stable and are larger than in the other conditions as the material was in service for almost 10 years.

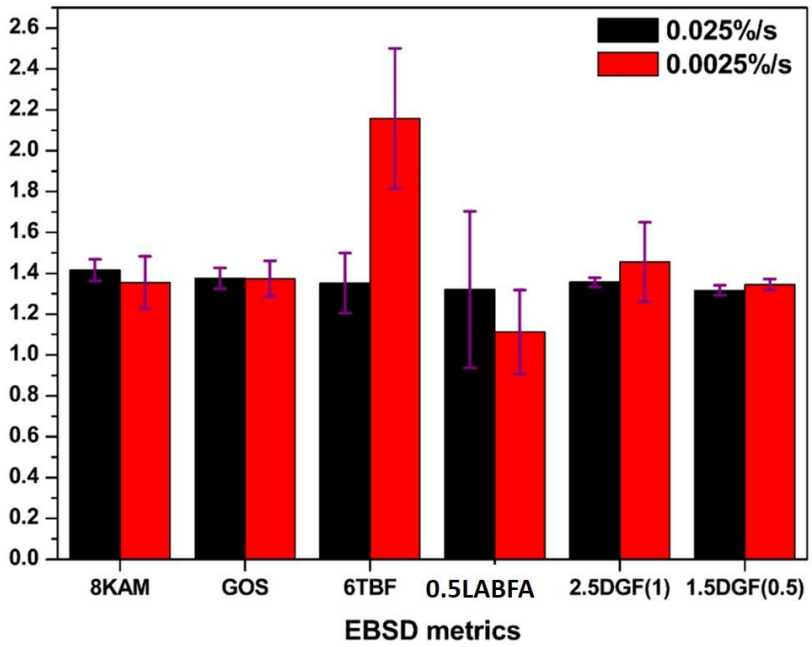

Figure 5.3. Variations of KAM_a lognormal, GOS_a, TBF, LABFA, DGF(1) and DGF(0.5) with strain rate for ex-service Type 316H stainless steel deformed to 5% strain at 550°C. KAM is multiplied by 8, TBF by 6, LABFA by 0.5, DGF(1) by 2.5 and DGF(0.5) by 1.5 to represent all EBSD metrics in same plot.

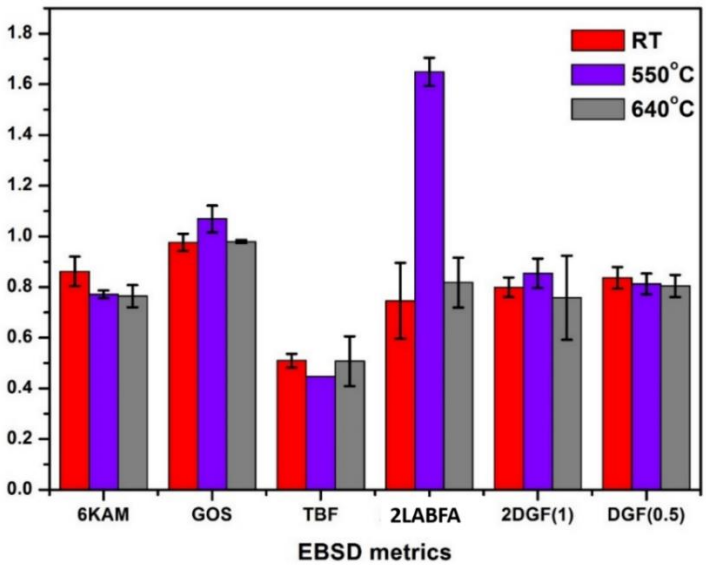

Figure 5.4 Variations of KAM_a lognormal, GOS_a, TBF, LABFA, DGF(1) and DGF(0.5) with temperature for solution annealed Type 316H stainless steel deformed to 5% strain at RT, 550°C and 640°C. KAM is multiplied by 6, LABFA by 2 and DGF(1) by 2 to represent all EBSD metrics in same plot.

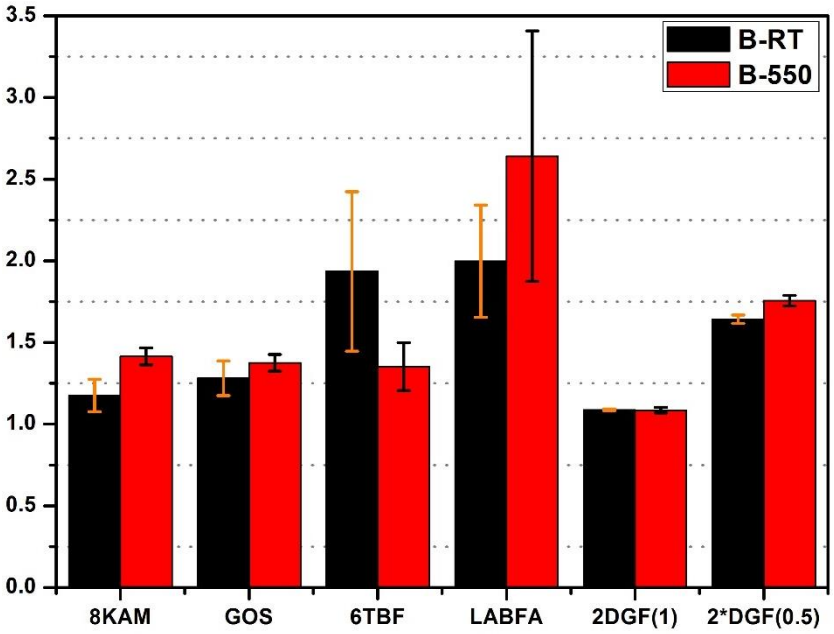

Figure 5.5 Variations of KAM_a lognormal, GOS_a, TBF, LABFA, DGF(1) and DGF(0.5) with temperature for ex-service Type 316H stainless steel deformed to 5% strain at RT and 550°C. KAM is multiplied by 8, TBF by 6, DGF(1) by 2 and DGF(0.5) by 2 to represent all EBSD metrics in same plot.

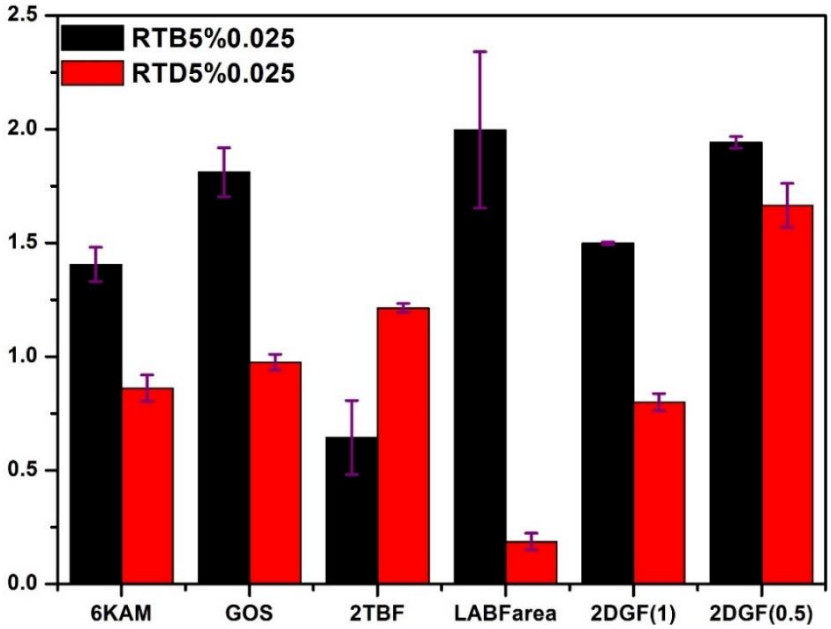

Figure 5.6. Variations of KAM_a lognormal, GOS_a, TBF, LABFA, DGF(1) and DGF(0.5) with precipitates (ex-service in black and solution annealed material in red) for Type 316H stainless steel deformed to true strain 0.13976 (5% engineering strain) at room temperature at a strain rate of 0.025%/s. KAM is multiplied by 6, TBF by 2, DGF(1) by 2 and DGF(0.5) by 2 to represent all EBSD metrics in same plot.

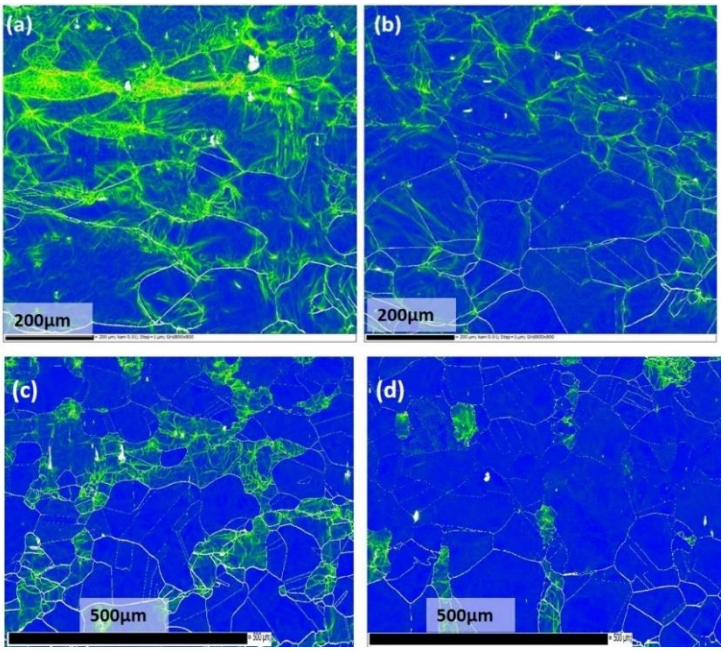

Figure 5.7. EBSD KAM maps of (a) ex-service and (b) solution annealed type 316H steel both deformed to true strain 0.049 (5% engineering strain) (c) as-received ex-service material (material B) and (d) solution annealed undeformed material (material D). Rainbow colours from blue to red shows minimum to maximum inelastic strain. The scale bar on the bottom of map is 200µm.

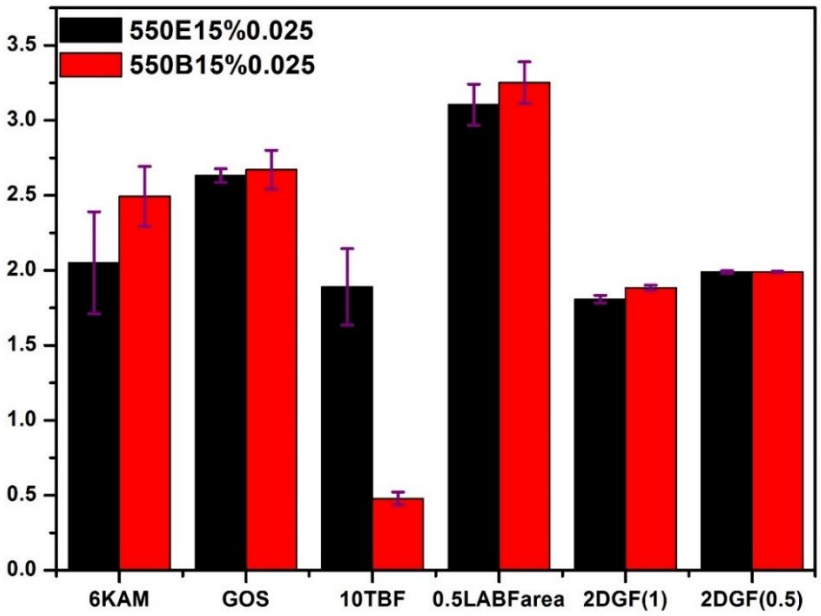

Figure 5.8. Variations of KAM_a lognormal, GOS_a, TBF, LABFA, DGF(1) and DGF(0.5) with precipitates (Ex-service and thermally aged) for Type 316H stainless steel deformed to true strain 0.140 (15% engineering strain) at 550°C at a strain rate of 0.025%/s. KAM is multiplied by 6, TBF by 10, LABFA by 0.5, DGF(1) by 2 and DGF(0.5) by 2 to represent all EBSD metrics in same plot.

5.2.5. Discussion

Flow behaviour and dynamic strain ageing

The flow behaviours (yield stress, ultimate stress) of ex-service material differed at room temperature and 550^{o}C. (see Figure 5.1). The flow behaviour (yield stress, ultimate stress) was different in the absence of precipitates (compare ex-service and solution annealed material at room temperature in Figure 5.1). The microstructures of ex-service, solution annealed, and thermally aged material was presented in chapter 4 (see Figure 4.6-Figure 4.11). The flow behaviour differed in the values of the flow stress (yield stress, ultimate stress), and in the rate of strain hardening. Strain hardening is related to the dislocation density in a material. The intragranular precipitates also influence the strain hardening because an additional stress is required for a dislocation to cut through a precipitate [50]. The flow stress is proportional to the square root of dislocation density [186]. Githinji et al [11] also reported similar observations for ex-service 316H: the flow stresses of solution annealed material were lower than for ex-service 316H. The lower flow stress of solution annealed material compared with the ex-service material at room temperature can be attributed to both the lack of precipitates and to lower strain hardening. The spikes/serrations in the flow curves at high temperature can be attributed to DSA which arises due to the locking and unlocking of dislocations by surrounding solute atmospheres (see Chapter 2). The serrations observed at 0.0025%/s were more evident than at a strain rate of 0.025%/s (see Figure 5.2). Similar serrations were reported on ex-service 316H material at a strain rate of 0.003%/s [11], arising from the repeated unlocking and passage of deformation bands.

Sensitivity of EBSD metrics to microstructure and loading conditions

The sensitivity of EBSD metrics to the effects of deformation temperature (RT, 550 and 640^{o}C), strain rate (0.025, 0.0025%/s) and microstructure (ex-service, solution annealed and thermally aged) has been studied. At a true strain of 0.04879, the room temperature

flow stresses for the ex-service (material B, RTB5%0.025) and solution annealed material (material D, RTD5%0.025) were significantly higher than those at 550°C (see Figure 5.1, 550B5%0.025, 550D5%0.025). This could be due to differences in the deformation mechanisms at these two temperatures. Increased thermal activation at 550^{o}C facilitates the processes of dislocation climb over obstacles and cross-slip. This reduces the pile-up of dislocations at barriers and so reduces the back stresses generated along the slip planes. Consequently, the stress needed to achieve a given deformation is lower at 550°C than at 24°C. In solution annealed material, the EBSD metrics showed little effect of deformation temperature (see Figure 5.4). In ex-service material, the EBSD metrics KAM_a lognormal, GOS_a, LABFA and DGF(0.5) at the same strain were found to increase slightly with increasing temperature (RT to 550^{o}C) (see Figure 5.5) TBF was lower at 550^{o}C than at RT for the same strain.

The effect of temperature on EBSD metrics was more consistent in ex-service material than in solution annealed material (compare Figure 5.4 and Figure 5.5). This shows the importance of precipitates in strain hardening. The higher density of precipitates in ex-service material might have been acting as dislocation barriers whereas at elevated temperatures dislocation climb and cross-slip can occur to overcome the precipitates. The absence of precipitates reduced the strain hardening rate of the solution annealed material deformed at room temperature, thereby reducing the flow stress (see Figure 5.1, RTB5%0.025, RTD5%0.025). Local and grain scale misorientations were consistently higher in the absence of precipitates (see Figure 5.6) except for TBF.

The strain rate independence of EBSD metrics has been reported previously for 316H steel by Githinji et al [11] and for 2.25%Cr-1%Mo steel by Fukuoka et al [187]. Similar results were obtained in this study (see Figure 5.3). The LABFA metric was found to be

marginally lower after deformation at a strain rate of 0.0025%/s than at 0.025%/s. This suggests that as the strain rate is reduced the number of GNDs is reducing which is consistent with the observations of Githinji et al [11] on 316H ex-service material. LABFA does not consider misorientation < 2^o and this could be the reason for the scatter in LABFA (see Figure 5.3-Figure 5.6).

The TBF was higher for a material deformed at a strain rate of 0.0025%/s than at 0.025%/s (see Figure 5.3). The TBF will be highest in undeformed material due to the tendency of austenitic stainless steel to develop annealing twins [188]. During deformation, the twin boundaries may block dislocation motion [189][190] resulting in dislocation pile-ups and/or absorptions. These interactions may introduce lattice rotation at the twin boundaries resulting in their losing their near-twin orientation [191]. At a lower strain rate (0.0025%/s compared to 0.025%/s) the dislocation density will be lower. So, the higher fraction of twin boundaries can again be attributed to lower dislocation accumulation.

Studying the effect of grain size alone in this material is very difficult as heat treatments done to change the grain size might affect the precipitation as well. But studies by Githinji et al [11] on similar material showed that grain size had little effect on the long-range misorientation build-up, whereas the build-up was faster on a local scale in fine grained material.

5.3. The influence of plastic strain and stress relaxation on misorientation development

5.3.1. Mechanical tests

This section addresses the effects of uniaxial tensile strain (plastic strain) and the inelastic strains developed during stress relaxation at constant total strain on misorientation

development. Tests were conducted on ex-service material (material B) at 550ºC. To ensure that specimens had similar chemical compositions and properties, the test materials were extracted from adjacent locations in the ex-service component (location B in Figure 4.2**).** Details of the test conditions are given in Table 5.2. To study the effect of plastic strain on misorientation development, tests were conducted at engineering strains of 2, 5, 10 and 15% at a strain rate of 0.025%/s. The same tests were then repeated but with the specimens held at constant total strain at the peak strain for 24 hours, to study the effect of stress relaxation in uniaxial loading. The strain was held constant by monitoring the strain in the specimen gauge length using a high temperature extensometer. The uniaxial sample design and loading conditions were described in chapter 3. Due to the limited availability of test machines, no experiments could be conducted with longer dwells.

Table 5.2 Tensile test conditions for Type 316H stainless steel, studying the effect of plastic strain and stress relaxation on misorientation development.

Steels	Engineering strain (%)	Hold time (hour)	True strain (mm/mm)	Temperature (ºC)	Sample ID
B	2	--	0.0198	550	550B2%0.025
B	5	--	0.0488	550	550B5%0.025
B	10	--	0.095	550	550B10%0.025
B	15	--	0.1398	550	550B15%0.025
B	2	24	--	550	550B2%0.025H24*
B	5	24	--	550	550B5%0.025H24
B	10	24	--	550	550B10%0.025H24
B	15	24	--	550	550B15%0.025H24

*550B**2%**0.025H24 (Red for temperature in degrees Celsius, Black for type of steel as mentioned in Chapter 4, Brown for Engineering strain, Green for strain rate and Blue for hold time in hours. EBSD measurements followed the same procedures as described in section 5.2.2. EBSD measurements

5.3.3. Mechanical test results

The tensile stress-strain curves at 550^{o}C are shown in Figure 5.9. The stress-strain curve with 24 hour dwell and the stress relaxation with time when the material was held at constant strain is shown in Figure 5.10. The effect of hold time is more evident at higher strains. The stress relaxed is calculated as the difference between the stress at peak strain and the stress after a 24 hour hold. The stress relaxed after tensile hold is reported in Table 5.3. The higher the strain, the more the stress relaxed. The inelastic strain developed during dwell (constant strain hold) is calculated as stress relaxed divided by Youngs modulus. The Youngs modulus of material B was calculated from tensile test (550B5%0.025) as 135GPa. The calculated inelastic strains are given in Table 5.3. Also the stress drops rapidly in the early stage of relaxation (see Figure 5.10). Similar results were reported for 316L steel [192][193].

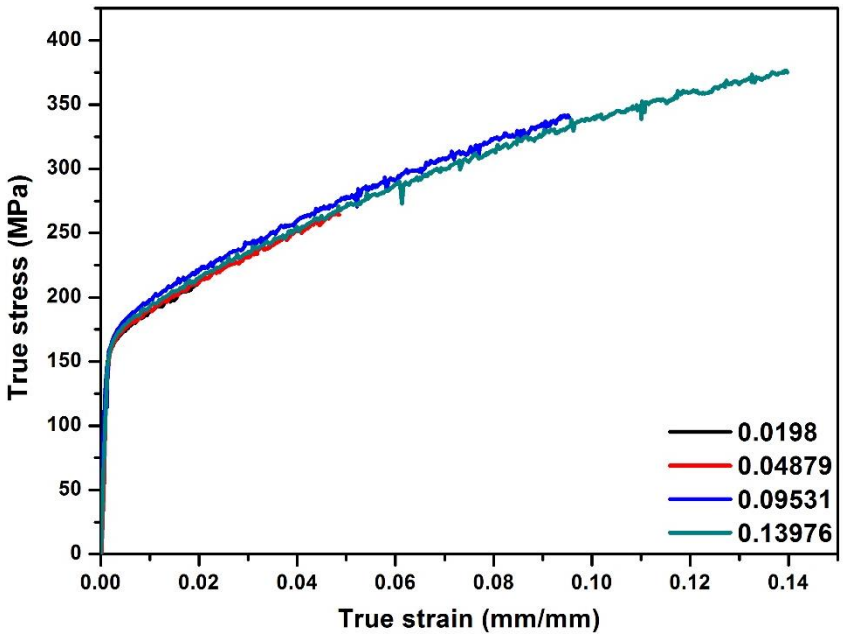

Figure 5.9. True stress-strain curves for ex-service Type 316H austenitic stainless steel deformed to different strains (temperature=550^{o}C, strain rate=0.025%/s)

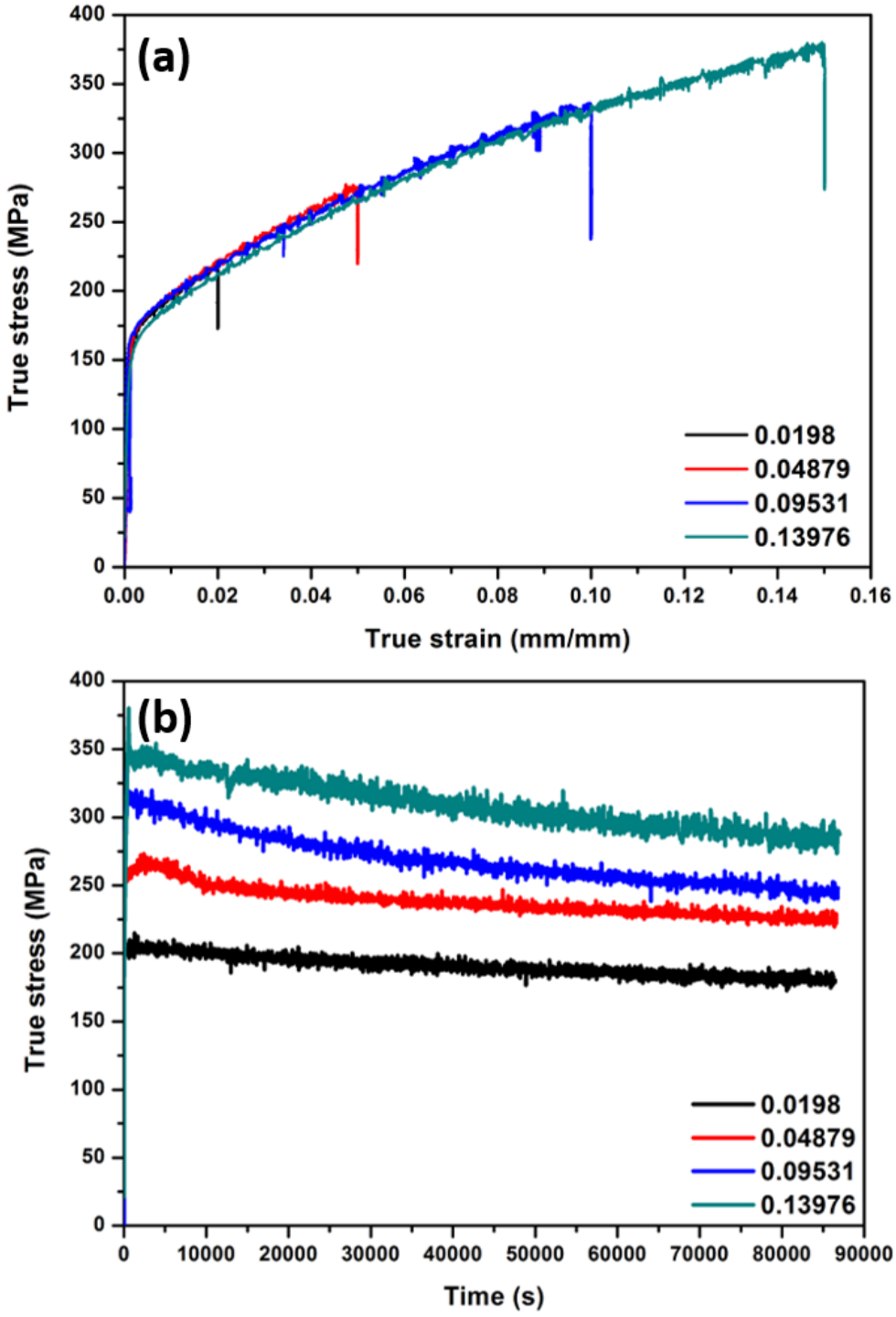

Figure 5.10 (a) True stress-true strain curve and (b) Stress relaxation curves for ex-service Type 316H austenitic stainless steel uniaxially loaded to different strains (temperature=550^{o}C, strain rate=0.025%/s) and then held at constant total strain for 24 hour.

Table 5.3 Peak stress, final stress, stress relaxed and estimated inelastic strain after stress relaxation for 24 hours where tensile samples of service aged Type 316H stainless steel have been uniaxially loaded to different levels of plastic strain.

Sample ID	True Strain (mm/mm)	True stress (MPa)			Estimated inelastic (creep) strain, $\Delta\sigma/E^*$ (mm/mm)
		Maximum at peak strain	After 24h dwell	Difference ($\Delta\sigma$)	
550B2%0.025H24	0.0198	216.1	180.1	35.97	2.665E-04
550B5%0.025H24	0.04879	275	222.1	52.9	3.915E-04
550B10%0.025H24	0.0953	335.3	247.9	87.3	6.467E-04
550B15%0.025H24	0.13976	378.2	274.7	103.5	7.663E-04

**E= Youngs Modulus=135GPa*

5.3.4. EBSD results

The accumulation of misorientation as a function of inelastic strain under uniaxial deformation followed by stress relaxation was quantified using KAM_a lognormal, GOS_a, DGF(1), DGF(0.5), TBF_a and LABFA metrics. The standard error of each EBSD metric was calculated as the scatter in the mean metric values from 3 EBSD maps collected from different locations of the sample. The results are shown in Figure 5.11, Figure 5.12, Figure 5.13, and Figure 5.14.

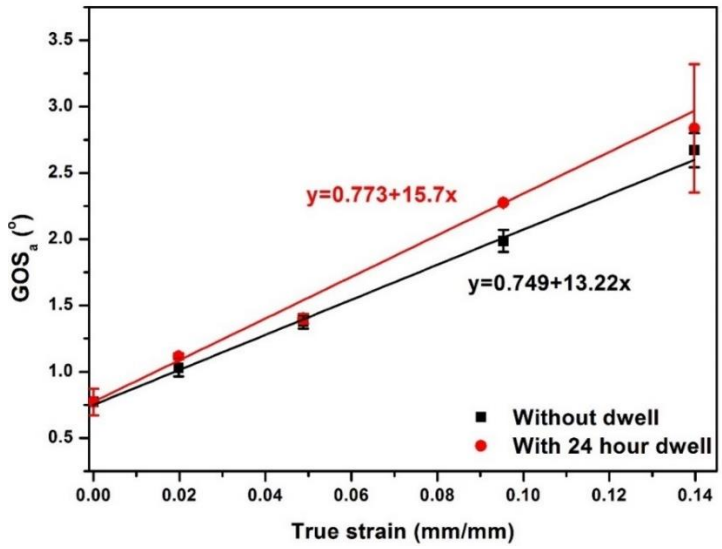

Figure 5.11 Variations of GOS_a, with strain for ex-service Type 316H stainless steel deformed to different strains followed by constant total strain hold for 24 hour. (Temperature=550°C, strain rate= 0.025%/s). There are no theoretical assumptions behind using a linear fit.

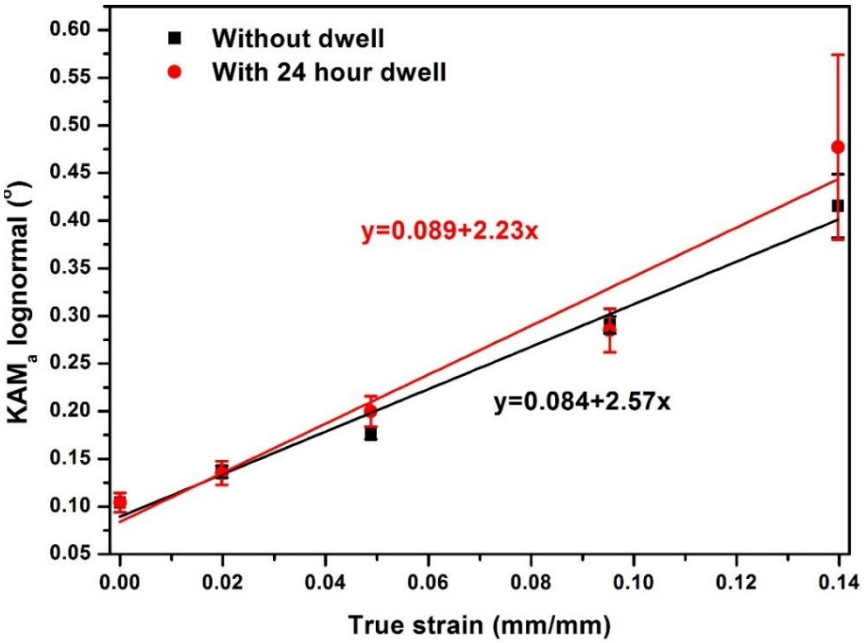

Figure 5.12 Variations of KAM_a lognormal, with strain for ex-service Type 316H stainless steel deformed to different strains followed by constant total strain hold for 24 hour. (temperature=550°C, strain rate= 0.025%/s). There are no theoretical assumptions behind using a linear fit.

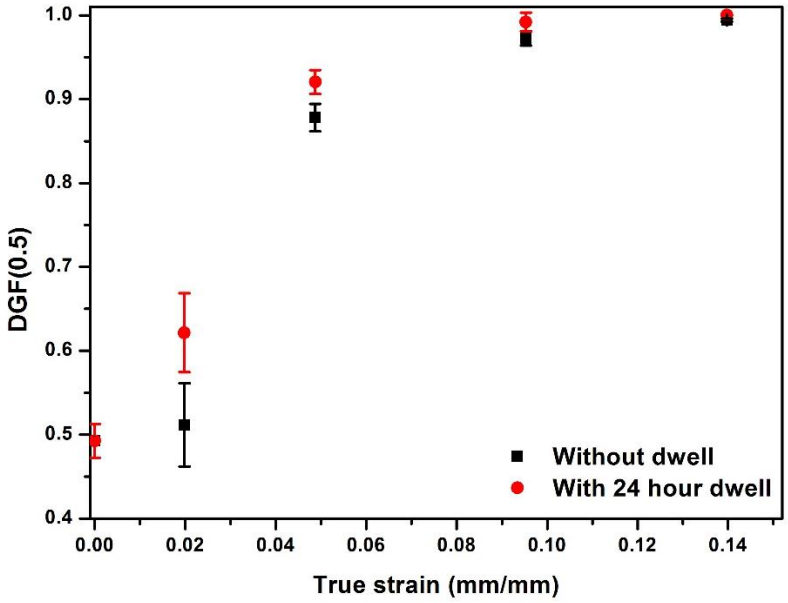

Figure 5.13 Variations of DGF(0.5), with strain for ex-service Type 316H stainless steel deformed to different strains followed by constant total strain hold for 24 hour. (temperature=550°C, strain rate= 0.025%/s)

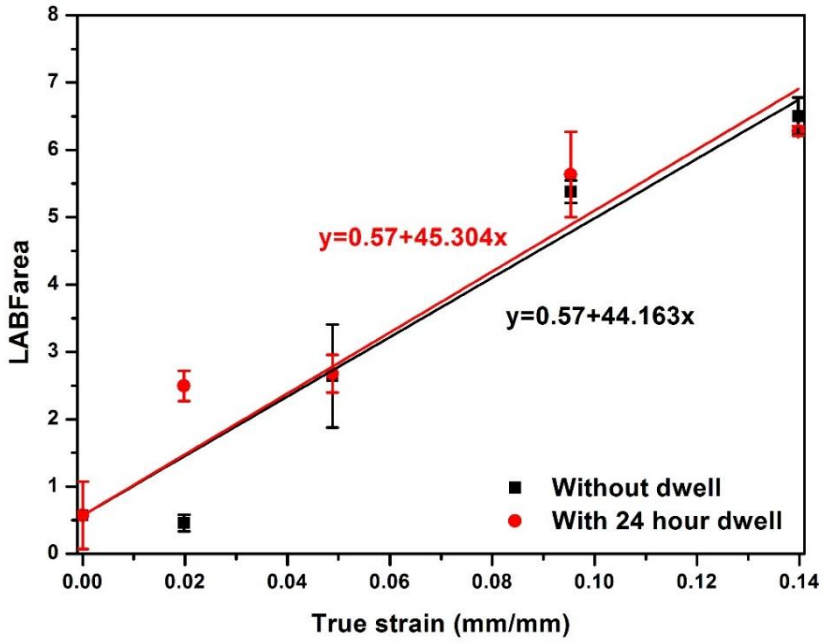

Figure 5.14 Variations of LABFarea (LABFA) with strain for ex-service Type 316H stainless steel deformed to different strains followed by constant total strain hold for 24 hour. (temperature=550°C, strain rate= 0.025%/s). There are no theoretical assumptions behind using a linear fit.

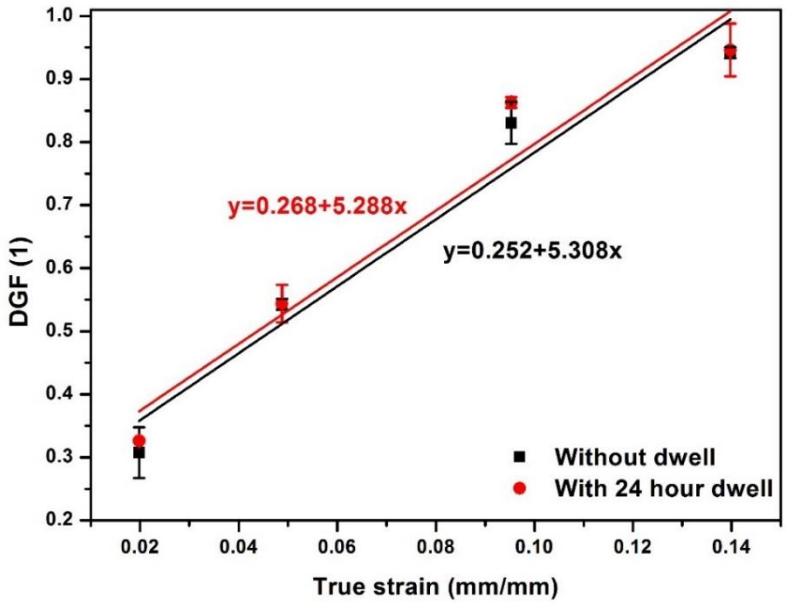

Figure 5.15 Variations of DGF(1), with strain for ex-service Type 316H stainless steel deformed to different strains followed by constant total strain hold for 24 hour. (temperature=550°C, strain rate= 0.025%/s). There are no theoretical assumptions behind using a linear fit.

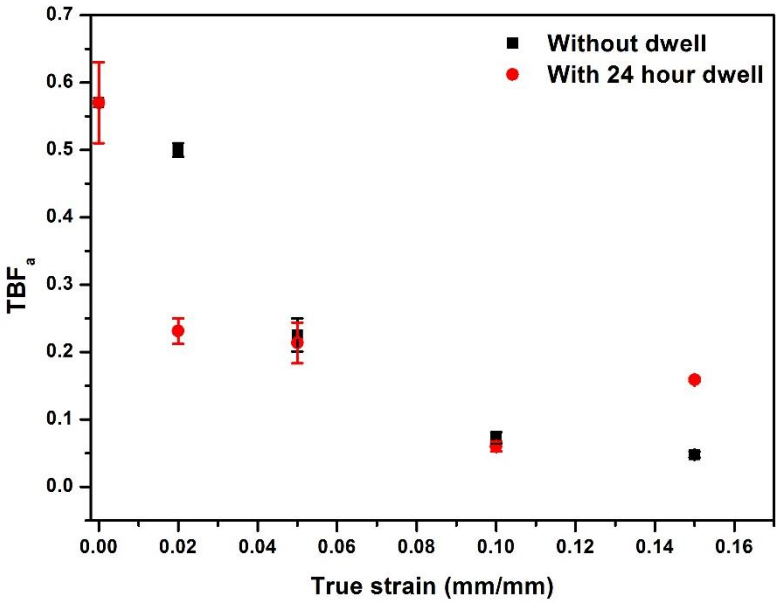

Figure 5.16 TBF$_a$ with strain for ex-service Type 316H stainless steel deformed to different strains followed by constant total strain hold for 24 hour. (temperature=550^{o}C, strain rate= 0.025%/s).

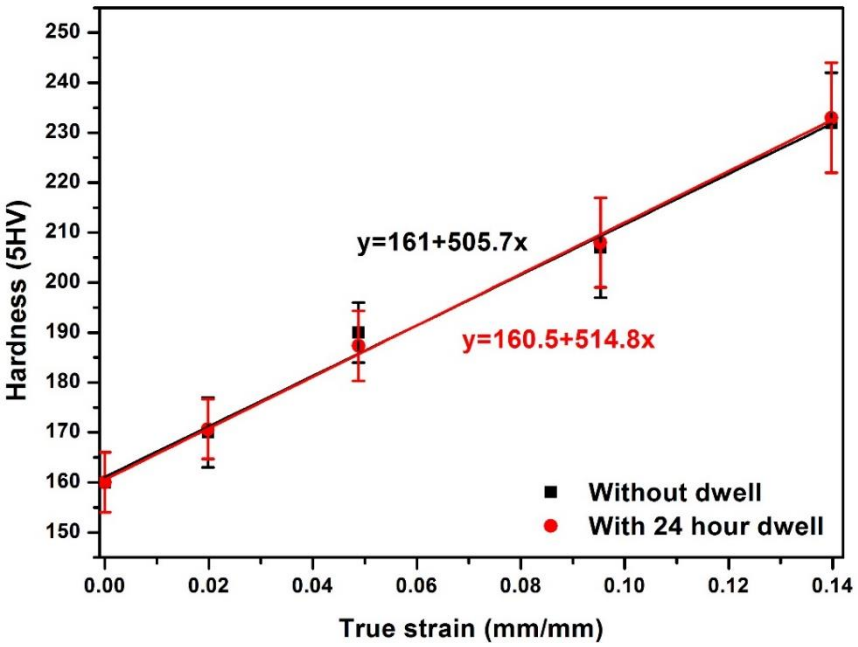

Figure 5.17 Variations of hardness with strain for ex-service Type 316H stainless steel deformed to different strains followed by constant total strain hold for 24 hour. (temperature=550^{o}C, strain rate= 0.025%/s). There are no theoretical assumptions behind using a linear fit.

For the high temperature tensile tests, KAM_a lognormal, GOS_a, DGF(1), DGF(0.5) and LABFA increased with plastic strain (see Figure 5.11, Figure 5.12, Figure 5.13, Figure 5.15). For the same strain the KAM_a lognormal and GOS_a metrics were lower in ex-service 316H material (material B) studied compared to tensile test results[2] of Githinji et al [11]. After plastic deformation (550^{o}C) to a true strain of 0.14 (see Figure 5.12), KAM_a lognormal in this study was found to be approximately 0.42^o whereas Githinji et al [11] reported KAM_a lognormal as 0.56^o. This could be due to property variation across the ex-service material. Also, the KAM data was binned using a 0.01^o class in this study whereas Githinji used a binning of 0.1^o. The variation of KAM_a lognormal fitting with binning has already been shown in chapter 3 where a smaller bin was demonstrated to give a good a lognormal distribution. KAM_a lognormal, GOS_a and DGF(1) showed a good linear fit with true strain. The effect of stress relaxation in GOS_a and KAM_a lognormal was evident with higher strains.

TBF_a was found to decrease with increasing strain (see Figure 5.16) as previously reported for this material [11]. LABFA increased with strain (see Figure 5.14). But a good linear fit could not be established relating TBFa, and LABFA metrics to true strain. Average Vickers hardness measurements also increased linearly with increasing plastic strain (see Figure 5.17). But the hardness measurements didn't clearly detect the inelastic strain accumulated due to stress relaxation.

[2] Githinji et al recorded EBSD data from an area of 700x700µm^2 with ach maps having atleast 100 grains. The step size used was 1µm. The binning with for KAM frequency distribution used was 0.1^o where as in this study a binning width of 0.01^o was used. Also the material was from a different location of the ex-service component. All other SEM operating conditions of this study and Githinji et al remains the same.

However, GOS_a, DGF(0.5) and KAM_a lognormal appeared to show a measurable change after constant strain tensile hold for 24 hours. Looking at the stress relaxation drop (see Table 5.3), the greater the stress relaxation, the more elastic strain is converted to inelastic strain and which appears to register as an increase in KAM_a lognormal and GOS_a metrics.

The SEM microstructures of ex-service test specimen material B (550B15%0.025H24, see Figure 5.18(b)) showed more cavities at the grain boundaries than inside the grains. The cavities were found around intergranular precipitates. There were notably more cavities in the test specimen after 24h relaxation (550B15%0.025H24) than with no relaxation (550B15%0.025), although it is interesting to note the presence of some intergranular cavities, which appear to have been caused by fracture of the intergranular carbides. However, there was no evidence of cavitation in the 550B2%0.025H24 samples (see Figure 5.19) strained to 2%. This reveals the potential significance of creep strain development owing to stress relaxation in grain boundary cavitation. The KAM was concentrated along grain boundaries and around intra-granular precipitates (See Figure 5.20). The SEM images and EDS analysis reveal that it is $M_{23}C_6$ carbides in the grain boundaries that are potential cavity nucleation sites. Similar results were reported by Pommier et al [194] on AISI 316L steels and Burnett et al [195] on AISI 316H steels.

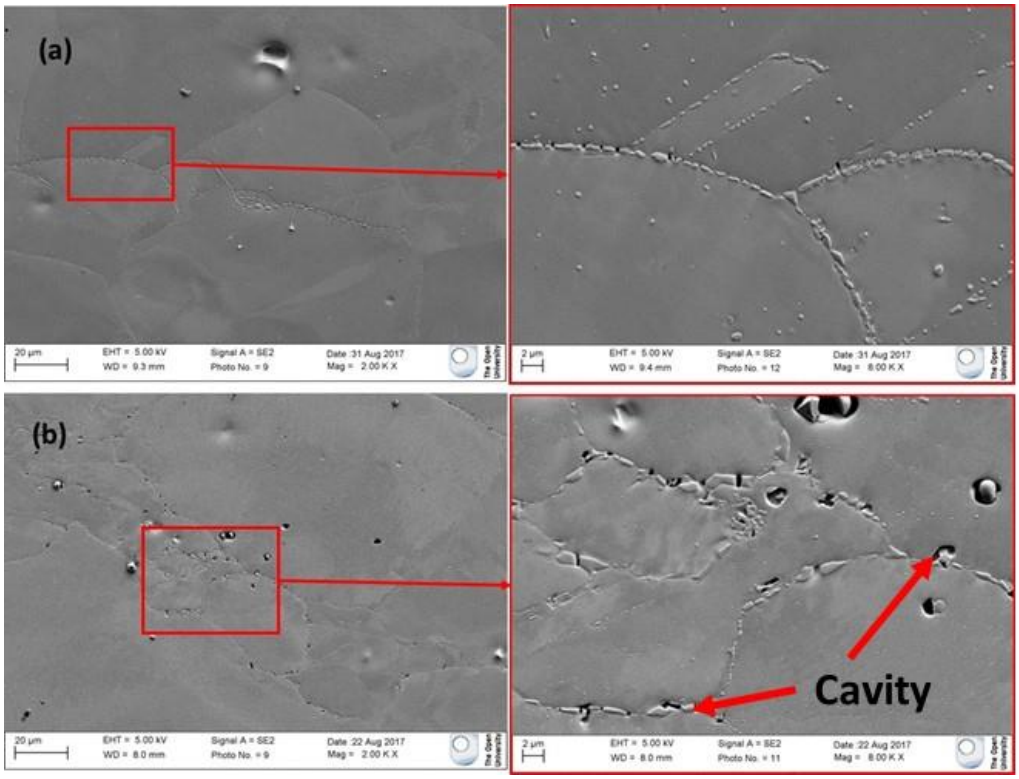

Figure 5.18. SEM micrographs showing grain boundary cavitation in the ex-service Type 316H steel deformed to (a)15% and (b) deformed to 15% followed by 24hour constant total strain dwell. Cavitation is predominant after 24 hour dwell.

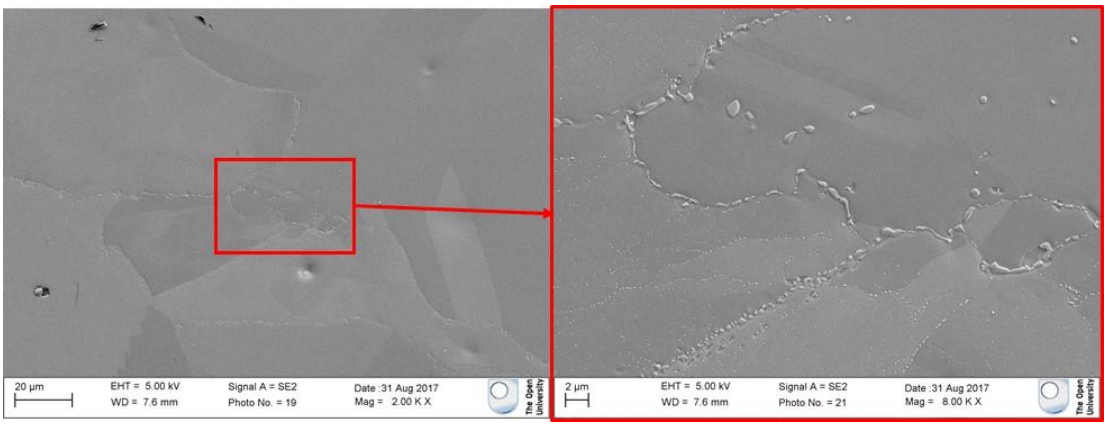

Figure 5.19. SEM micrographs showing grain boundaries in the ex-service Type 316H steel deformed to 2% followed by 24 hour constant total strain dwell. No cavities are visible after 24 hour dwell.

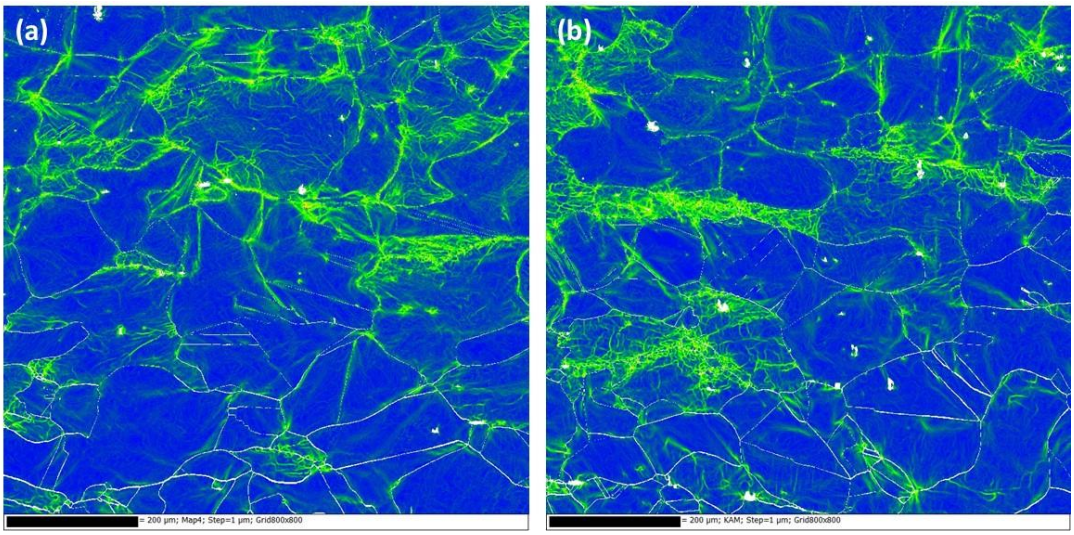

Figure 5.20. KAM maps of the ex-service Type 316H stainless steel: (a) deformed to 15%, and (b) deformed to 15% followed by 24 hour constant total strain dwell. Rainbow colours from blue to red shows minimum to maximum inelastic strain. Scale bar is 200µm.

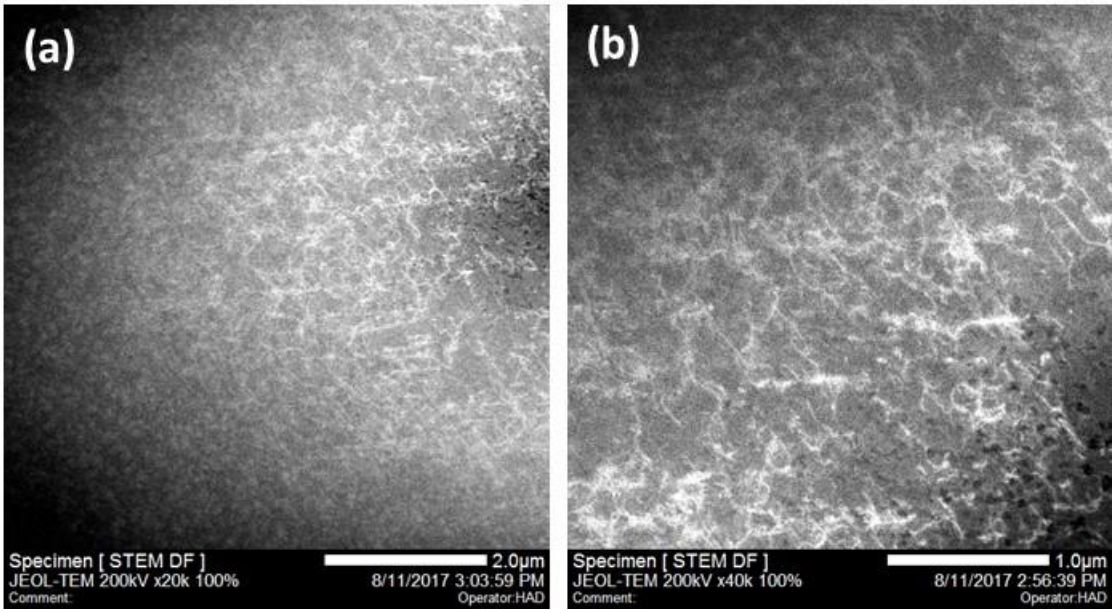

Figure 5.21. STEM HAADF micrographs showing relatively homogeneous dislocations in ex-service Type 316H steel deformed to 0.0198 true strain.

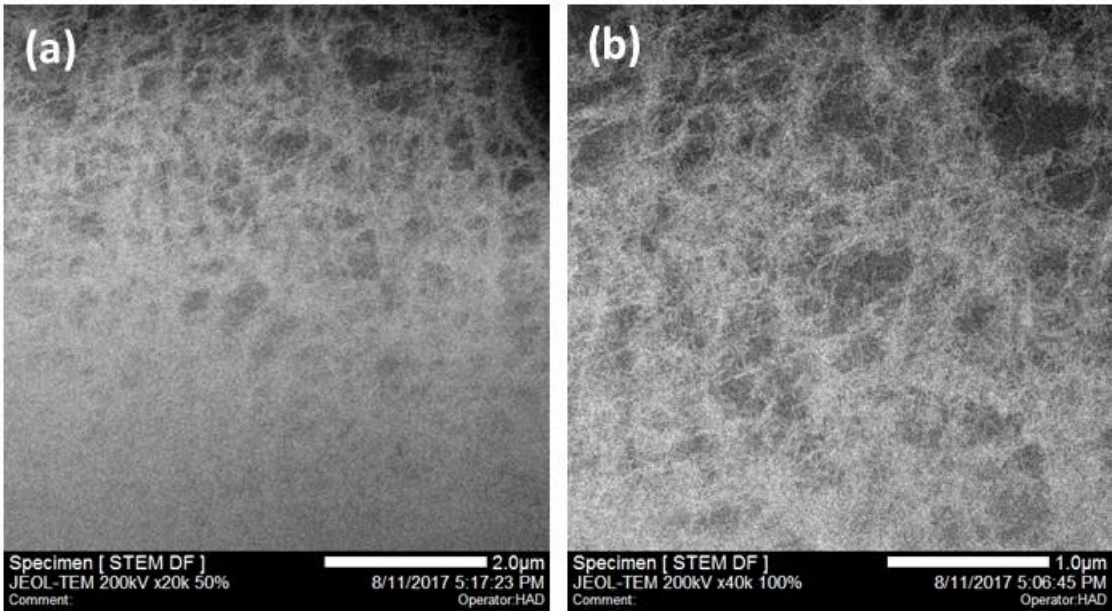

Figure 5.22. STEM HAADF micrographs showing dense dislocation forests with some diffuse cell structures in ex-service Type 316H steel deformed to 0.13976 true strain.

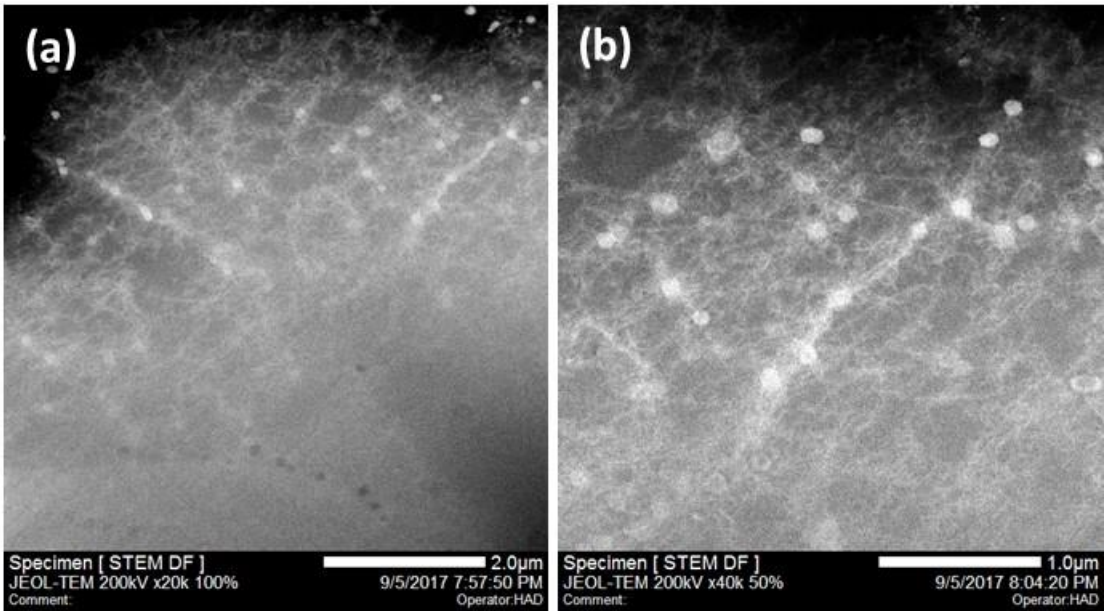

Figure 5.23. STEM HAADF micrographs showing dislocations forming diffuse cell structures in ex-service Type 316H steel deformed to 0.0198 true strain followed by 24 hour dwell.

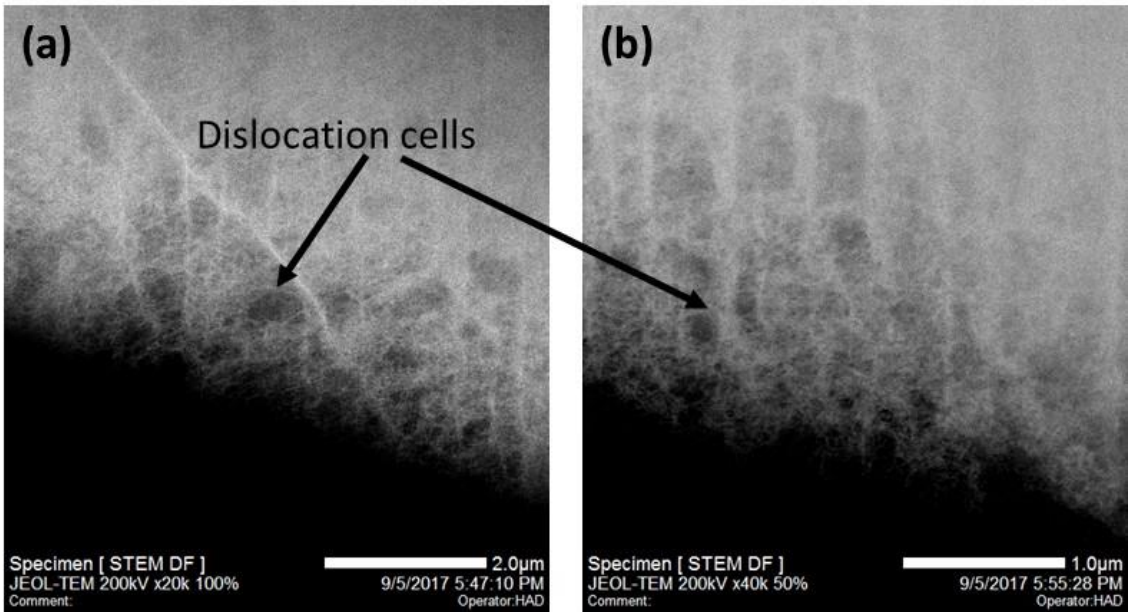

Figure 5.24 STEM HAADF micrographs showing dislocations in ex-service Type 316H steel deformed to 0.13976 true strain followed by 24 h dwell.

STEM characterization was carried out on samples deformed to 0.02 and 0.14 true strain (550B2%0.025, 550B15%0.025, 550B2%0.025H24 and 550B15%0.025H24). STEM clearly showed higher dislocation densities (dense dislocation forests with some diffuse cell structures) at higher strains (see Figure 5.21 and Figure 5.22). The dislocation precipitate interactions were evident in the microstructures. Homogeneous distributions of dislocations were found in samples deformed to 0.0198 true strain. There was some evidence of diffuse cell structures for plastic deformation to 0.13976 true strain (see Figure 5.22). The dislocations formed fairly random diffuse cell-like structures after 24 hour dwell (see Figure 5.23). The sample deformed at 550^{o}C to a true strain of 0.13976 generally had a high dislocation density (see Figure 5.22), but there were some areas free of dislocations. After 24 hour dwell, a more highly organized diffuse cell wall structure (see Figure 5.24) was visible. Evidence of diffuse cell formations were observed after stress relaxation at lower strain (0.0198) also (see Figure 5.23).

5.3.5. Discussion

EBSD and inelastic strains

The degrees of correlation between the accumulated inelastic strain and different EBSD metrics were studied along with the sensitivity of these EBSD metrics to strain rate and temperature. GOS_a, KAM_a lognormal, DGF(1) and DGF(0.5) (see Figure 5.11, Figure 5.12, Figure 5.13, Figure 5.15) showed a monotonic increase with plastic strain. The area under the low angle boundary (2-15^o) fraction curve was also found to increase with plastic strain (see Figure 5.14). KAM considers only misorientation between 0.15^o to 2^o whereas LABF considers misorientation from 2^o to 15^o. LABFA was not found to be sensitive to stress relaxation. This may indicate that stress relaxation involves development of misorientations less than 2^o. But several other studies have suggested grain average misorientation (GAM), which is KAM averaged for a grain, is a useful parameter for quantifying plastic and/or creep damage [21], [29], [32]. Average values of KAM and GAM for an EBSD map would show the same behaviour so GAM was not calculated separately for this thesis.

GOS_a/AMIS is a measure of grain scale deformation in the material. Many studies on 316 steel have shown a linear dependence of GOS_a with plastic strain [11][137][29]. GOS_a is found to be more sensitive to higher strains than KAM or LABF [137]. Githinji et al [11] found that GOS/AMIS and DGF metrics were not sensitive to grain size whereas LABFA can only be used to measure strain in materials with a comparable grain size. TBF was found to decrease with plastic strain in tensile tests (see Figure 5.16). The reduction of the proportion of twins with dislocation accumulation was explained in section 5.2.5, but in this study no good linear relationship was found between TBF and plastic strain, unlike that reported by Githinji et al [11].

Hardness is sometimes used as a tool for creep damage assessment of structural components. But Yoda et al [32] found that creep damage estimation using hardness was unreliable, especially during secondary creep which is the most important behaviour for real structural components. The major reason for this unreliability was that hardness measurements cannot distinguish hardening by plastic deformation from that by precipitation. Whereas hardness gives near-surface information dependent on local microstructural variations along the depth of indent, EBSD is a surface measurement technique (that simultaneously reveals details of the microstructure).

Inelastic strains during stress relaxation

During stress relaxation, the elastic strain (ε_e) is transformed into inelastic strain (ε_p); the total strain (ε_T) remains constant.

$$\varepsilon_T = \varepsilon_e + \varepsilon_p = C \quad (5.1)$$

As the test proceeds, elastic stresses relax and inelastic strain replaces elastic strain, through a creep deformation process which depends on the applied stress. The major mechanism of stress relaxation is the thermal activation of dislocation motion over short-range obstacles generally by climb [196]. More dislocations have to be generated to accommodate the inelastic strain developed during relaxation. As the relaxation time increases, the dislocations may rearrange into energetically favourable cells (observations on 316L steel after stress relaxation at RT [197]). If there are pre-existing cells after plastic deformation, the cell boundaries sharpen and the interiors become cleaner during relaxation [197]. Cell structures were observed after stress relaxation at plastic strain of 0.14 (see Figure 5.24). It is reported that the density of mobile dislocation reduces with time during stress relaxation, which leads over time to a saturation stress drop. Dislocation annihilation was reported in 316L steel after stress relaxation for 30 seconds at room

temperature (after plastic strain of 25%) [197]. However, the thermal activation and creep will be more dominant at 550°C than at room temperature and dislocation generation rather than annihilation might be the major contributor to accumulation of inelastic strains.

Substituting Hooke's law $\sigma = E\varepsilon_e$ (5.2), where E is Young's modulus and σ is the stress, into equation 5.1 and differentiating with respect to time,

$$\frac{d\varepsilon_p}{dt} = -\frac{1}{E}\frac{d\sigma}{dt} \quad (5.3)$$

This relates the rate of change of the stress during the stress relaxation test to the plastic or creep strain rate [69]–[71].

The maximum elastic strain is given by,

$$\varepsilon_{e(max)} = \frac{\sigma_y}{E} \quad (5.4)$$

From the tensile tests described in Chapter 3, the yield strength (σ_y) of 316H steel (Sample B) was 175MPa and Young's modulus (E) was 135GPa at 550°C. Substituting these values, the maximum elastic strain at 550°C is around 0.130%. This gives a maximum possible plastic strain in stress relaxation of 0.130% which is very small.

There was a general trend of GOS_a increasing with stress relaxation from higher initial stress-strain conditions (see Figure 5.11, Figure 5.12). DGF(0.5) was consistently higher after stress relaxation showing the biggest differences after stress relaxation from lower stress-strain conditions, with the difference reducing as stress relaxation was allowed at higher strains (see Figure 5.13).

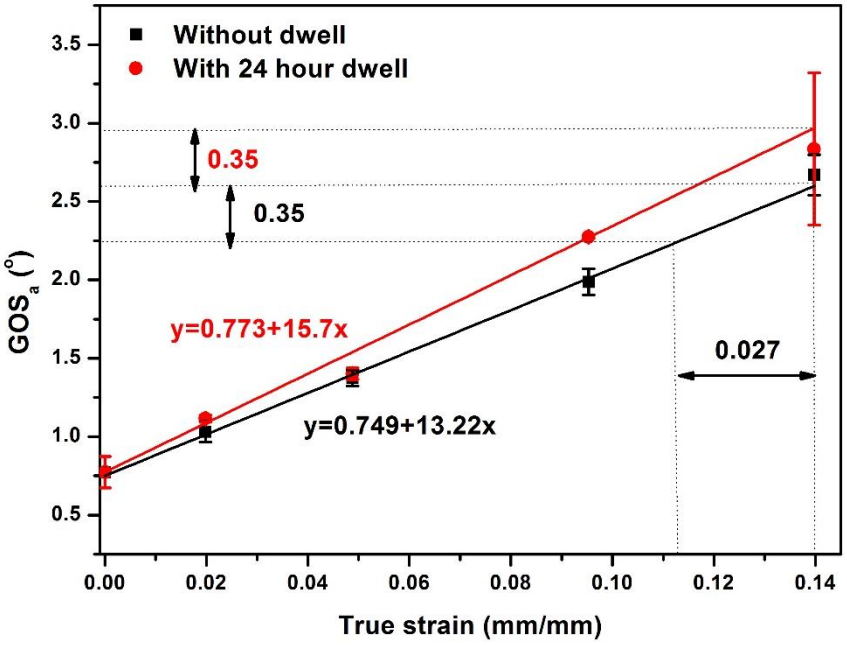

Figure 5.25 Variations of GOS_a, with strain for ex-service Type 316H stainless steel deformed to different strains followed by constant total strain hold for 24 hour. (temperature=550°C, strain rate= 0.025%/s).

Consider the variations of GOS_a, with strain for ex-service Type 316H stainless steel deformed under load control to different strains followed by constant total strain hold for 24 hour (see Figure 5.25 which is a modified version of Figure 5.11). The change in GOS_a at 0.14mm/mm plastic strain after stress relaxation introducing an inelastic strain increment of 0.0026mm/mm was found to be approximately 0.35° (see Figure 5.25). This drop corresponds to a load controlled plastic strain of 0.027mm/mm (see Figure 5.25). These results indicate that stress relaxation introduce far more misorientation (i.e. inelastic damage) than load controlled plastic strain (Almost 35 times i.e. 0.027/0.00076) times more damaging than plastic strain.

At higher strains, the average intragranular misorientation of most of the grains is > 0.5° which makes DGF(0.5) insensitive to inelastic strain accumulation during stress relaxation (see Figure 5.13). The DGF(1) metric was insensitive to stress relaxation at all strain levels (see Figure 5.15). This shows that uniaxial stress relaxation occurs mostly in

grains with an average intragranular misorientations less than 1°. Since grains with higher GOS (>1°) have higher GND density than those with GOS of 0.5°, generation of dislocations to accommodate inelastic strains might be easier in grains with GOS < 1°. However, a grain's deformation might also depend on the deformation behaviour of the neighbouring grains that transfer the stress to it. Hence further detailed investigation is needed (suggested future work) to further understand this. This study has demonstrated a surprising sensitivity of EBSD metrics to small changes in inelastic strain accumulating during stress relaxation. But directly quantifying such minor variations in strains using EBSD metrics is still problematic due to the scatter in results. Far more experimental data are required to arrive at solid conclusions.

The DGF metric which only considers the fraction of grains in an EBSD map with GOS_a values above a certain threshold is already reported to be least sensitive to local deformation associated with precipitate-dislocation interactions [11] and hence can provide a good measure of global macroscopic strain. In this study also, DGF(0.5) gives a better fit with small inelastic strains than DGF(1). The saturation of DGF(0.5) to 1 at higher levels of stress relaxation clearly shows that strain is accommodated in grains with lower misorientations or in other words grains with lower dislocation density. However, the maximum inelastic strain increment developed after stress relaxation in this study was 7.663E-04 which is very small. Even though EBSD metrics seem to detect such strain accumulation during stress relaxation, it is questionable whether the misorientations can be precisely correlated with such small changes in inelastic strains. Nonetheless the apparent measurable increase in GOS_a and KAM_a lognormal are in order of magnitude greater than might be expected based on load controlled creep/plasticity induced levels

of GOS_a and KAM_a lognormal misorientation. This could indicate that displacement controlled creep-stress relaxation is more damaging than load controlled primary creep.

Inelastic damage and cavitation

SEM images (see Figure 5.18(b)) showed that the cavitation was concentrated around areas of intergranular precipitates and triple junctions after plastic strain and stress relaxation. EBSD KAM maps showed higher inelastic strains at grain boundaries. The KAM_a lognormal metric increased more during a 24 hour dwell at a true strain of 0.139762 (550B15%0.025H24) than during a high temperature tensile test up to a true strain of 0.139762 (550B15%0.025). Studies on 316L by Pommier et al [194] suggested that the stress relaxation behaviour and the inelastic strain accumulation at the grain boundary are directly linked to the chemical composition of the steel. For example, the intergranular carbide precipitation which creates a local gradient in chemical composition reduces the grain boundary strength. Phosphorous was found to increase micro cavity nucleation and nitrogen caused lower stress relaxation rates. This maintained high residual stresses at grain boundaries for longer time and so increased the number of nano-cavities. Pommier et al [194] also suggested that temperature influences the local chemical composition and thereby stress relaxation in 316L steel. They suggested that the maximum principal residual stress component is a more important driving force for intragranular damage during stress relaxation than stress triaxiality. The heterogeneous plastic deformation at grain boundaries caused by precipitates increases the local stresses [106]. The behaviour of the EBSD metrics along with the microstructures observed by SEM and STEM suggests that cavity nucleation at grain boundaries and precipitates (see Figure 5.18) can develop following plastic strain and tensile stress relaxation. Reheat cracking described in Chapter 2 is also due to grain boundary cavitation damage in high

temperature components. This all (along with STEM dislocation structures) suggests very different creep damage mechanisms associated with primary creep and creep stress relaxation. This study also suggests that suitable EBSD metrics might be used to monitor inelastic strains developed after uniaxial tensile deformation and stress relaxation in Type 316H steel. The EBSD metrics after stress relaxation showed that creep relaxation misorientations may be an order of magnitude greater than load controlled plastic misorientation development.

5.4. Summary

Misorientation development during uniaxial tensile deformation and stress relaxation has been studied in this chapter. Strain rate (0.025 vs 0.0025%/s) had little effect long range misorientation build-up. Temperature (comparing RT vs 550^{o}C) had a significant effect on misorientation build-up in ex-service material. Less misorientation developed in solution annealed material. KAM_a lognormal, GOS_a, DGF(0.5), DGF(1), LABFA and the average hardness all increased linearly with increasing load controlled strain whereas TBF reduced linearly. The higher the initial strain, the higher the initial stress and the more stress relaxed at constant strain. Diffuse cell wall structures developed from homogeneous dislocation networks during a 24 hour dwell and cavities were observed to develop at grain boundaries in material strained to 14% followed by 24h stress relaxation. Changes in EBSD metrics may be an order of magnitude more sensitive to strain accumulated under displacement conditions compared with strain accumulated under load control.

CHAPTER 6

CYCLIC DEFORMATION: EFFECT OF STRAIN RANGE, DWELL, TEMPERATURE AND PRECIPITATES ON MISORIENTATION DEVELOPMENT

6.1. Introduction

For power plant structural components normally operating at high temperature, the changes of temperature and loading during start-up, the operating period and shut-down can lead to high temperature low cycle fatigue (HTLCF) and creep-fatigue (C-F) damage. Creep damage occurs in these components during the operating period at constant stress/strain (the dwell) whereas the start-up and shut-down operations produce fatigue damage, often leading to fatigue failure by cracking [94]. Creep damage occurring during the dwell time and leading to creep failure is generally manifested as creep voids on the internal grain boundaries that can grow and join to form intergranular cracks [96], [123], [198], [199]. Creep cavitation damage is often found deep within the material while fatigue crack damage is generally observed at the surface. The synergy of these two damage mechanisms often results in accelerated failure [94]. EBSD-based damage assessment methods, quantifying the damage due to the accumulation of inelastic strains, are attracting increasing attention in structural integrity research due to its ability to provide information regarding dislocation density along with microstructure details. In this chapter, the effects of different factors such as dwell time, strain range, temperature, and precipitates on the inelastic strains and misorientations developed during cyclic testing are studied. HTLCF tests were conducted with different strain ranges (ranging from ±0.3% - ±0.75%) to study the effect of the total strain range on the misorientation

development. The effect of dwell was studied by holding the sample at peak tensile strain for different times (180 and 600s). The effect of temperature was studied on samples cyclically deformed at room temperature, 550^{o}C and 640^{o}C. The effect of microstructure was studied on cyclically deformed ex-service material (material B), solution annealed material (material D) and thermally aged material (material E). The effect of strain rate on the misorientation build-up was studied on samples cyclically deformed at 0.025%/s and 0.0025%/s. This chapter first introduces the experimental work carried out, followed by the stress-strain and EBSD results. It ends with a discussion of the results and a summary of the findings.

6.2. Influence of strain range and dwell on misorientation development

6.2.1. Mechanical tests

Strain-controlled high temperature low cycle fatigue tests and creep-fatigue tests were conducted on ex-service material (material A, B and C, see Chapter 4) to study the effect of strain range and dwell on misorientation development. Details of the test conditions are given in Table 6.1. A constant strain dwell was introduced at the peak tensile strain for the creep-fatigue tests. All tests were conducted at 550^{o}C and a strain rate of 0.025%/s for 150 cycles. Some of the tests were repeated on material A, B and C under the same conditions to examine the variability of the results from different parts of the ex-service component (see Chapters 4 and 5 for more details on the tensile properties of the ex-service material).

Table 6.1 Cyclic test conditions for Type 316H stainless steel (Materials A and B, see section 4.2 in Chapter 4) to study the effect of strain range and dwell on misorientation development. The key to the sample ID is given at the foot of the table.

Steels	Total strain range (%)	Dwell time (min)	Sample ID
B	±0.3	10	550B±0.30%0.025H10
B	±0.45	0	550B±0.45%0.025H0
A B	±0.6	0	550A±0.60%0.025H0 550B±0.60%0.025H0
A	±0.6	3	550B±0.60%0.025H03
A B	±0.6	10	550A±0.60%0.025H10 550B±0.60%0.025H10
B	±0.75	0	550B±0.75%0.025H0
B	±0.75	10	550B±0.75%0.025H10

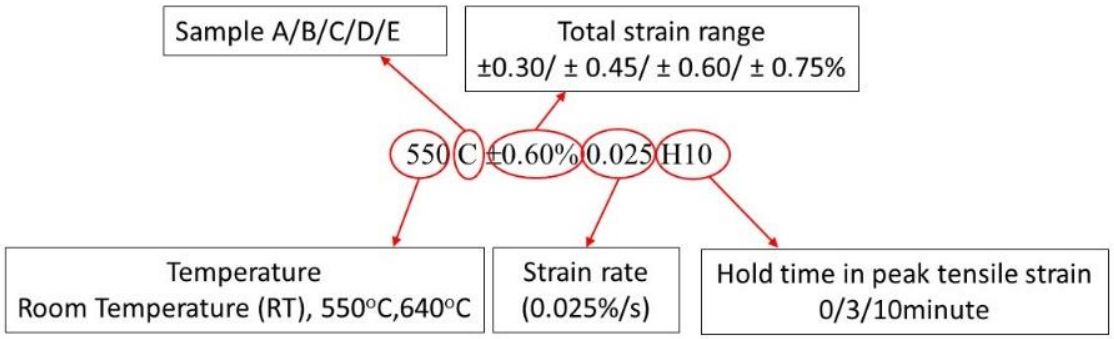

6.2.2. EBSD measurements

The EBSD measurements were carried out on deformed samples as described in Chapter 3. The misorientations developed were studied as a function of inelastic strain using the different EBSD metrics discussed in Chapter 4. The misorientations were assessed both at a local scale (KAM, LABFA) and at longer range (GOS_a, DGF(0.5), DGF(1), TBF).

6.2.3. Quantifying damage in cyclic deformation

The inelastic strain energy density per cycle, Δw, is generally used in the literature for damage calculations in low cycle fatigue (LCF) tests [93], [200]. Δw is calculated as the area inside the stress-strain hysteresis loop (see Figure 6.1). The cumulative strain energy

density was calculated for all cycles as $W = \sum_{n=1}^{N} \Delta w$, where N is the total number of cycles (see section 2.5.2).

Another way of calculating the damage in low cycle fatigue is using the cumulative inelastic strain approach (see Figure 6.1) [140]. The cumulative tensile inelastic strain was calculated for each deformed condition as the sum of the positive strain-intercepts of the stress-strain curve for all the cycles. The cumulative compressive inelastic strain was calculated for each deformed condition as the sum of the negative strain-intercepts of the stress-strain curve for all the cycles. Cumulative inelastic strain is the sum of all strain intercepts (both positive and negative) divided by a factor of 2.

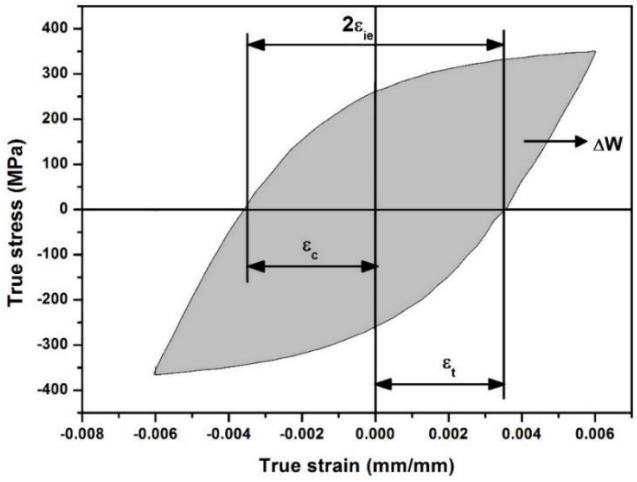

Figure 6.1 Saturated stress-strain hysteresis loop for ex-service material (Material A) cyclically deformed at a total strain range of ±0.6% and strain rate 0.025%/s showing strain energy density (Δw, grey shaded region) total inelastic strain range ($2\varepsilon_{ie}$), tensile inelastic strain (ε_t) and compressive inelastic strain (ε_c).

6.2.4. Results

The cumulative inelastic strain energy densities for all the deformation conditions described in this section are shown in Table 6.2. For a given number of cycles (N=150), the cumulative inelastic strain energy density (column 4 in Table 6.2) increased with the strain range. For materials B and C and a strain range of ±0.6%, the cumulative inelastic strain energy density also increased with the introduction of a 600 s dwell, but there was little difference in the cumulative strain energy densities of material A deformed at ±0.6%

with 0, 180 or 600 seconds holds. For material B at the highest strain range, ±0.75%, the increase in the cumulative inelastic strain energy density with dwell was very small.

The cumulative tensile inelastic strain increased with the introduction of a tensile dwell (see Table 6.2) but in material A there was no significant difference between the cumulative tensile inelastic strains for a dwells of 180 and 600s.

Table 6.2 Cumulative strain energy density and cumulative tensile inelastic strain of ex-service material (Materials A, B and C, see section 4.2.1) cyclically deformed at 550^{o}C and a strain rate of 0.025%/s at different strain ranges and dwell times at the peak tensile strain.

Location of ex-service material (see section 4.2.1)	Total strain range (%)	Dwell time (min)	Cumulative inelastic strain energy density, $W=\sum\Delta w$ (MPa)	Cumulative tensile inelastic strain, $\sum\varepsilon_t$ (mm/mm)	Cumulative compressive inelastic strain, $\sum\varepsilon_c$ (mm/mm)	Cumulative inelastic strain, $\sum\varepsilon_{ie}$ (mm/mm)
B	±0.3	10	183.21	0.29	0.245	0.27
B	±0.45	0	350.38	0.42	0.42	0.412
A	±0.6	0	617.24	0.55	0.55	0.55
B			576.21	0.62	0.63	0.63
C			609.40	0.54	0.54	0.54
A	±0.6	3	629.42	0.62	0.56	0.59
A	±0.6	10	612.30	0.62	0.578	0.60
B			612.92	0.71	0.645	0.68
C			679.48	0.63	0.58	0.61
B	±0.75	0	821.35	0.84	0.84	0.84
B	±0.75	10	829.69	0.93	0.86	0.89

Figure 6.2 shows the stress-strain curve for the 150th cycle of material A cyclically deformed with different dwell times. As mentioned in chapter 3, the effect of backlash is seen in the cyclic curves. The peak stresses after each cycle are shown in Figure 6.4 (peak tensile stress) and Figure 6.5 (peak compressive stress). The peak tensile stress was

reduced by the introduction of a 180s dwell at the peak tensile strain. The peak stress further reduced when the hold time was increased to 600s. During the hold periods, stress-relaxation was observed. The stress relaxation curve for the 150th cycle is shown in Figure 6.3. The peak stresses gradually reduced during the hold but the most significant reduction was during the first 100s of dwell (see Figure 6.3). The effect of strain hardening was visible in the first 80 cycles of the low cycle fatigue tests (see Figure 6.4) but after that the peak stress remained almost constant. The peak stress saturated after approximately 50 cycles for cyclic tests with a hold time of 180s whereas with a 600s dwell, the peak stresses saturated after 35 cycles (see Figure 6.4). The hardening could result from dislocation generation and their mutual interactions and/or interactions between dislocations and precipitates. Little effect of strain hardening due to precipitation would be expected during a short test on ex-service material as the microstructure is very stable.

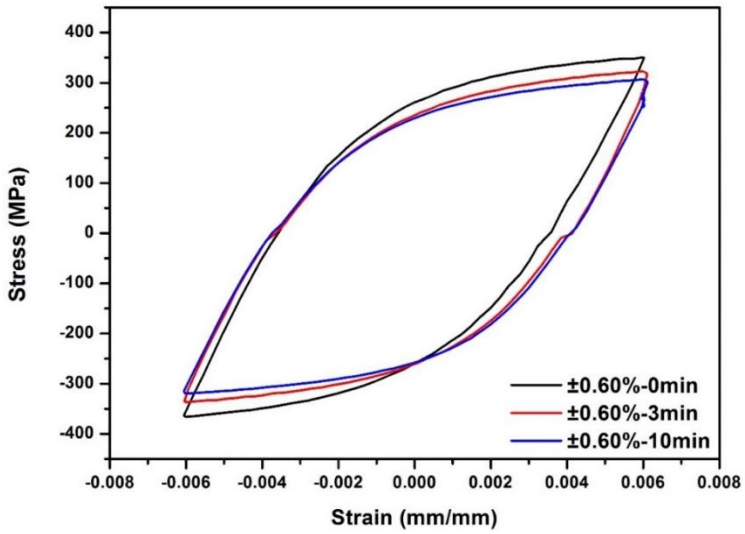

Figure 6.2 Final cycle (150) stress-strain curve for ex-service material (Material A) cyclically deformed at a total strain range of ±0.6% and strain rate 0.025%/s with no dwell, 3 min dwell and 10 minutes dwell at peak tensile strain.

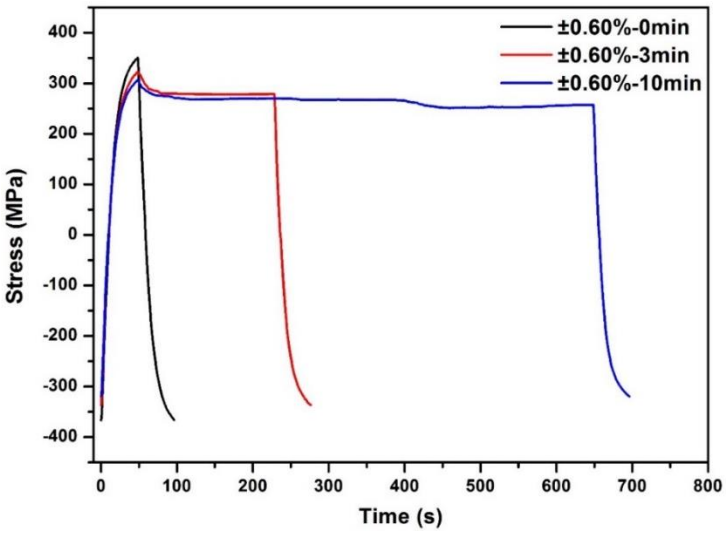

Figure 6.3 Stress vs time curve for the last cycle when ex-service material (Material A) was cyclically deformed at a total strain range of ±0.6% and strain rate of 0.025%/s with no dwell, 3 min dwell and 10 minutes dwell at peak tensile strain.

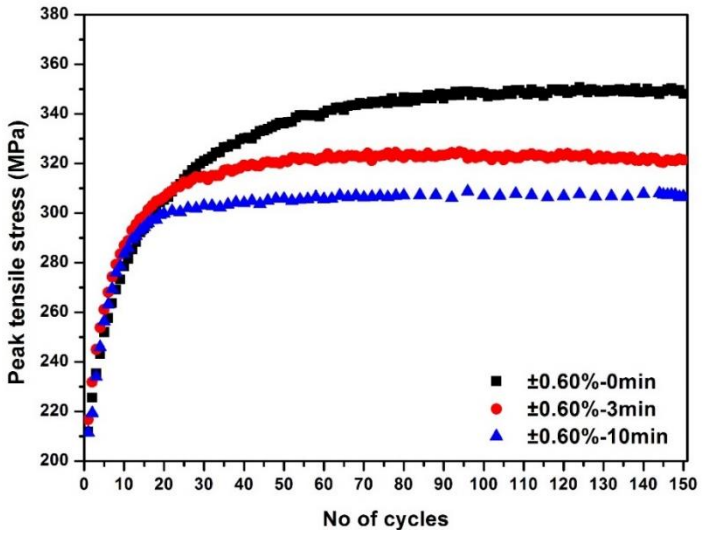

Figure 6.4 Peak tensile stress for ex-service material (Material A) cyclically deformed at a total strain range of ±0.6% and strain rate 0.025%/s with no dwell, 3 min dwell and 10 minutes dwell at the peak tensile strain.

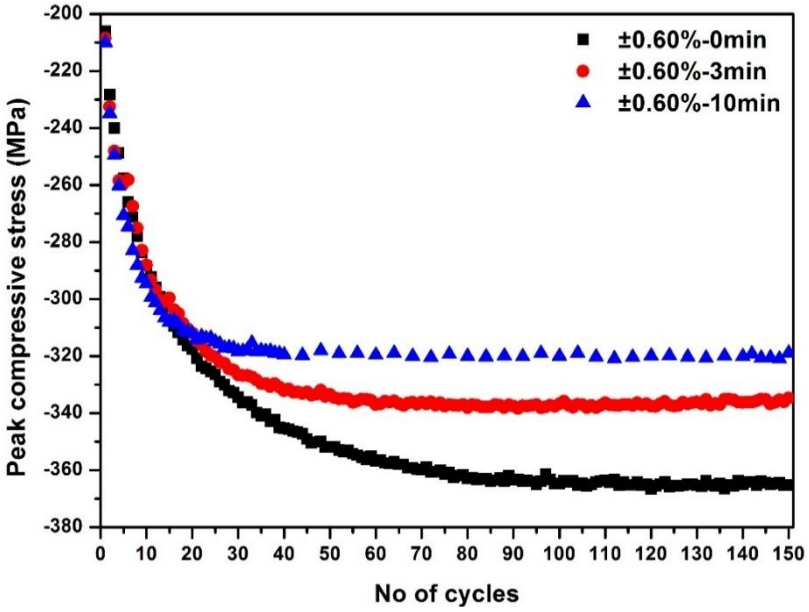

Figure 6.5 Peak compressive stress for ex-service material (Material A) cyclically deformed at a total strain range of ±0.6% and strain rate 0.025%/s with no dwell, 3 min dwell and 10 minutes dwell at peak tensile strain.

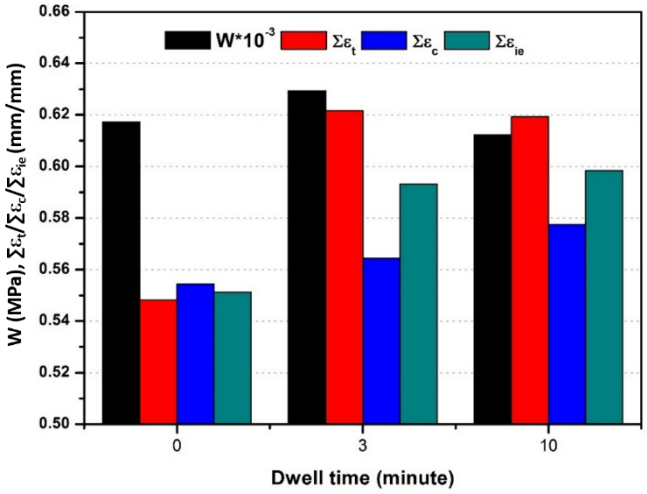

Figure 6.6 Cumulative inelastic strain energy density (W), cumulative tensile inelastic strain ($\sum\varepsilon_t$), cumulative compressive inelastic strain ($\sum\varepsilon_c$) and cumulative inelastic strain ($\sum\varepsilon_{ie}$) for ex-service material (Material A) cyclically deformed at a total strain range of ±0.6% and strain rate 0.025%/s with no dwell, 3 min dwell and 10 minute dwell at peak tensile strain. W is multiplied by 10^{-3}. Please note that Y-axis starts from 0.5.

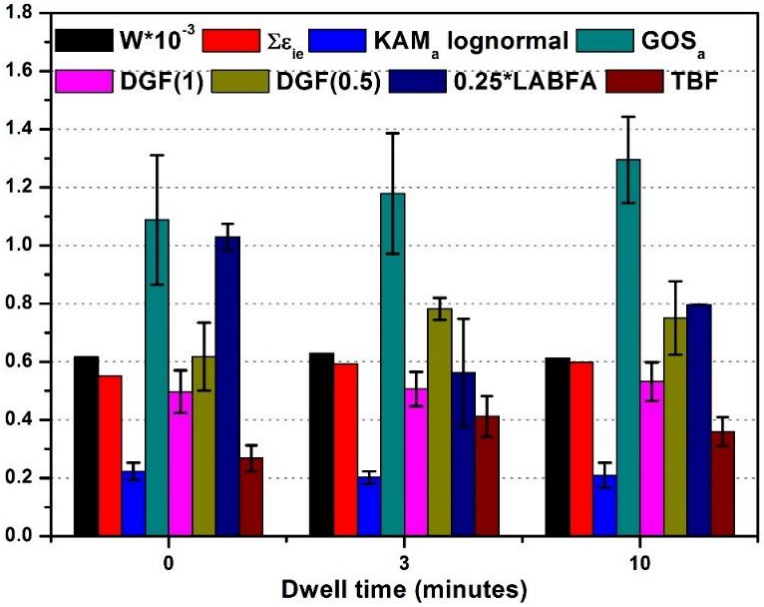

Figure 6.7 Cumulative inelastic strain energy density (W), cumulative inelastic strain ($\sum\varepsilon_{ie}$) and different EBSD metrics for ex-service material (Material A) cyclically deformed at a total strain range of ±0.6% and strain rate 0.025%/s with no dwell, 3 min dwell and 10 minute dwell at peak tensile strain. W is multiplied by 10^{-3} and LABFA by 0.25 to represent the inelastic damage and EBSD metrics in same plot.

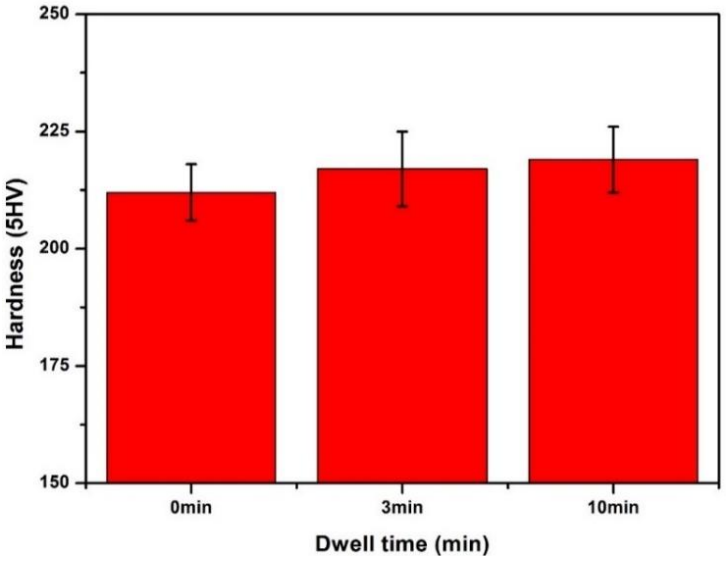

Figure 6.8 Mean hardness values for ex-service material (Material A) cyclically deformed at a total strain range of ±0.6% and strain rate 0.025%/s with no dwell, 3 min dwell and 10 minutes dwell at peak tensile strain.

Figure 6.6 shows the variation of the cumulative inelastic strain energy density (W), cumulative tensile inelastic strain ($\sum\varepsilon_t$), cumulative compressive inelastic strain and cumulative inelastic strain in material A cyclically deformed over a strain range of ±0.6%

(550^{o}C, 0.025%/s, 150 cycles) with tensile dwells of 0, 180 and 600 s. W showed no systematic trend with dwell time but $\sum\varepsilon_c$ and $\sum\varepsilon_{ie}$ increased with increasing dwell time. Figure 6.7 shows the variation in different EBSD metrics with dwell time. There was a slight increase in GOS_a with hold time and DGF(0.5) and DGF(1) too increased with the introduction of dwell. DGF(0.5) seems to be more sensitive to the inelastic strain developed due to 180s dwell than DGF(1). However, the DGF metrics were unchanged when the hold time was increased to 600s. TBF was also found to be higher for samples deformed with a 600s dwell. There was no significant variation in the hardnesses for the three different dwells (see Figure 6.8).

Tests were repeated on Material C (550C±0.60%0.025H0, 550C±0.60%0.025H10) to test the repeatability of the results. The peak tensile and compressive stresses in each cycle are shown in Figure 6.9 and Figure 6.10 respectively. The peak tensile and compressive stresses showed similar behaviour to those of Material A. For saturated cycles, the reduction in the peak tensile stress was more evident than the reduction in the compressive stress.

Figure 6.11 shows the changes in W, $\sum\varepsilon_{t,}$ $\sum\varepsilon_c$ and $\sum\varepsilon_{ie}$ in material C with the introduction of 600s dwells. W, $\sum\varepsilon_{t,}$ $\sum\varepsilon_c$ and $\sum\varepsilon_{ie}$ all increased with introduction of 600s dwell. Figure 6.12 shows the cumulative inelastic strain energy density (W), the cumulative inelastic strain ($\sum\varepsilon_{ie}$) and different EBSD metrics for test specimens 550C±0.60%0.025H0 and 550C±0.60%0.025H10. Both W and $\sum\varepsilon_T$ increased after 600s dwells. DGF(0.5) and DGF(1) also increased slightly after 600s dwells. TBF too was slightly higher on samples deformed with 600s dwells. The EBSD results were consistent with those from Material A (comparing Figure 6.7 and Figure 6.12).

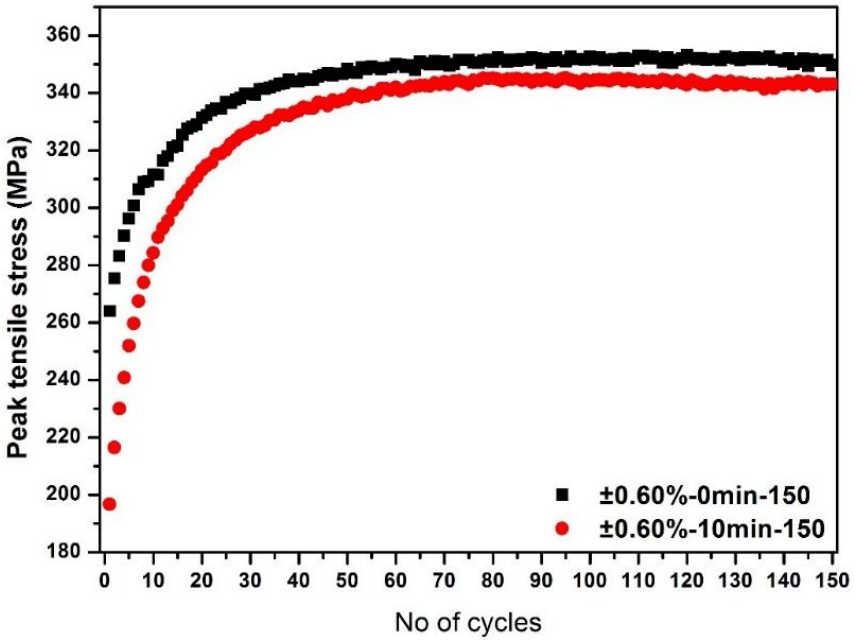

Figure 6.9 Peak Tensile stress for ex-service material (Material C) cyclically deformed at a total strain range of ±0.6% and strain rate 0.025%/s with either no dwell or 10 minute dwells at the peak tensile strain.

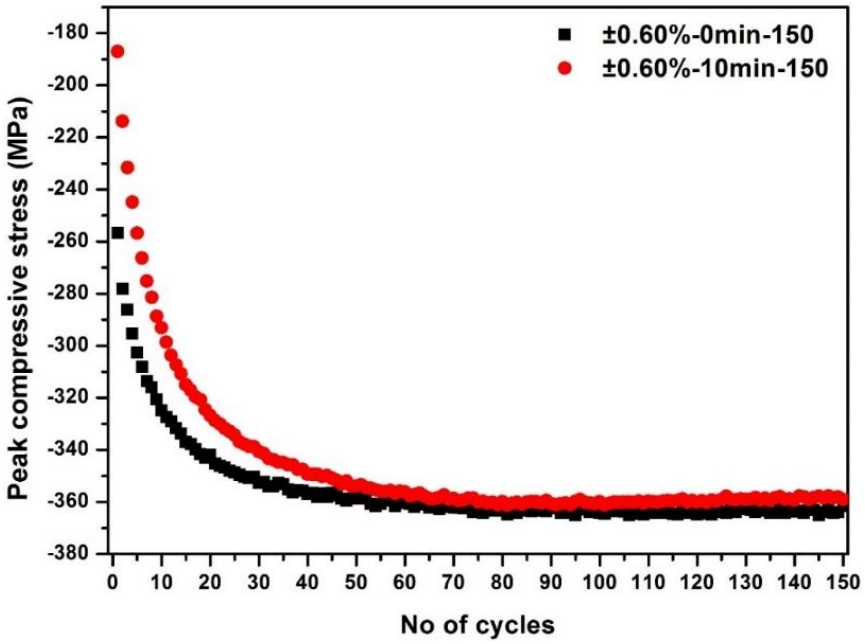

Figure 6.10 Peak compressive stress for ex-service material (Material C) cyclically deformed at a total strain range of ±0.6% and strain rate 0.025%/s with either no dwell or 10 minute dwells at the peak tensile strain.

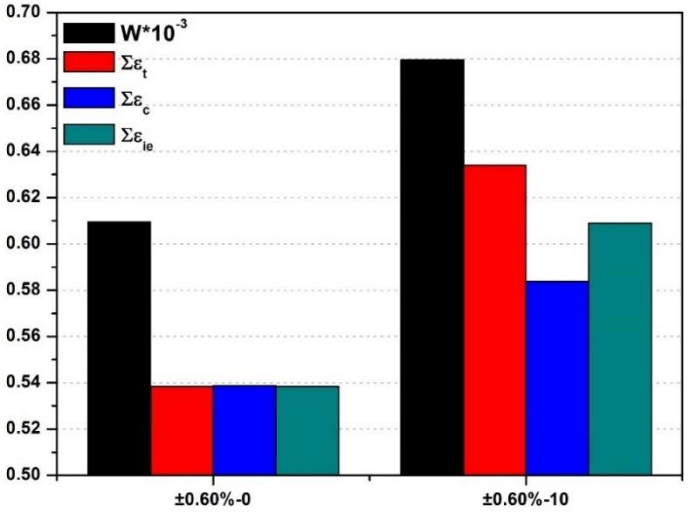

Figure 6.11 Cumulative inelastic strain energy density(W), cumulative tensile inelastic strain ($\sum\varepsilon_t$), cumulative compressive inelastic strain ($\sum\varepsilon_c$) and cumulative inelastic strain ($\sum\varepsilon_{ie}$) for ex-service material (Material C) cyclically deformed over a total strain range of ±0.6% and at a strain rate 0.025%/s with either no dwell or 10 minutes dwells at the peak tensile strain. W is multiplied by 10^{-3} to represent the inelastic damage and EBSD metrics on the same plot.

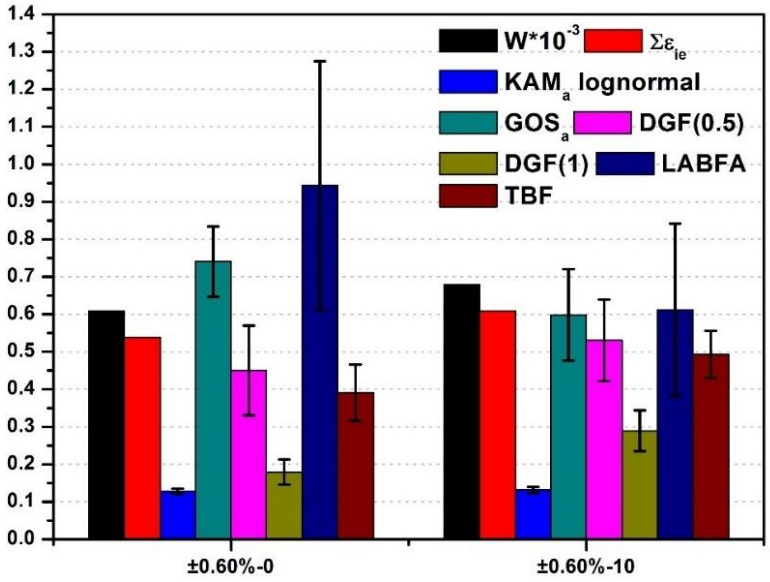

Figure 6.12 Cumulative inelastic strain energy density (W), cumulative inelastic strain ($\sum\varepsilon_{ie}$) and different EBSD metrics for ex-service material (Material C) cyclically deformed over a total strain range of ±0.6% and at strain rate 0.025%/s with either no dwell or 10 minutes dwells at the peak tensile strain. W is multiplied by 10^{-3} to represent the inelastic damage and EBSD metrics on same plot.

Material B was used to study the effects of the total strain range and dwell on low cycle fatigue deformation. All the test conditions of material B are given in Table 6.1. The final

cycle stress-strain curves of material B cyclically deformed under different conditions are shown in Figure 6.13. The peak tensile and compressive stresses for each cycles are shown in Figure 6.14 and Figure 6.15 respectively. The peak stress increased with increasing strain range and reduced with dwell. Figure 6.16 shows the final cycle stress relaxation curve for ex-service material (material B) cyclically deformed at total strain ranges of ±0.30% , ±0.60% and ±0.75% with 600s dwells at the peak tensile strain. The stress relaxation increased at higher strain ranges. The stress relaxation was calculated by taking the difference between stresses at the start and end of the hold period. The stress relaxations were 44.4, 70.6 and 77.7MPa for the total strain ranges of ±0.30% , ±0.60% and ±0.75% respectively.

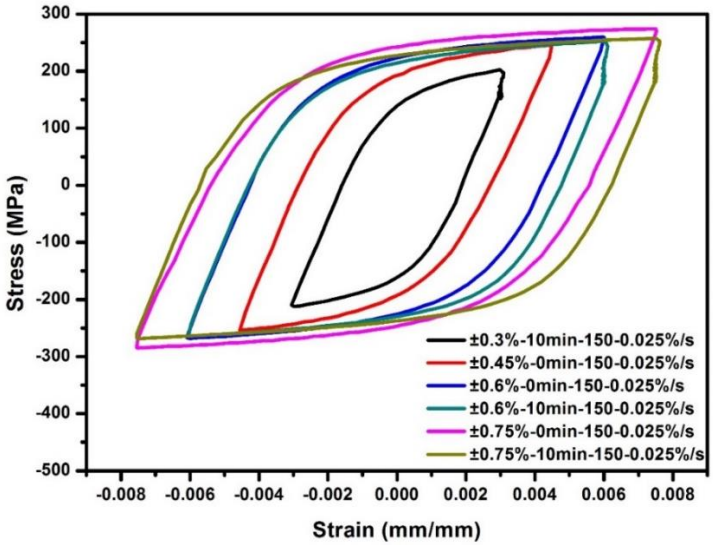

Figure 6.13 Final cycle (150th cycle) stress-strain curves for ex-service material (Material B) cyclically deformed at 550°C and 0.025%/s strain rate at total strain ranges of ±0.45% , ±0.60% and ±0.75% without dwell, and ±0.30%, ±0.60% and ±0.75% with 10 minutes dwells at the peak tensile strains.

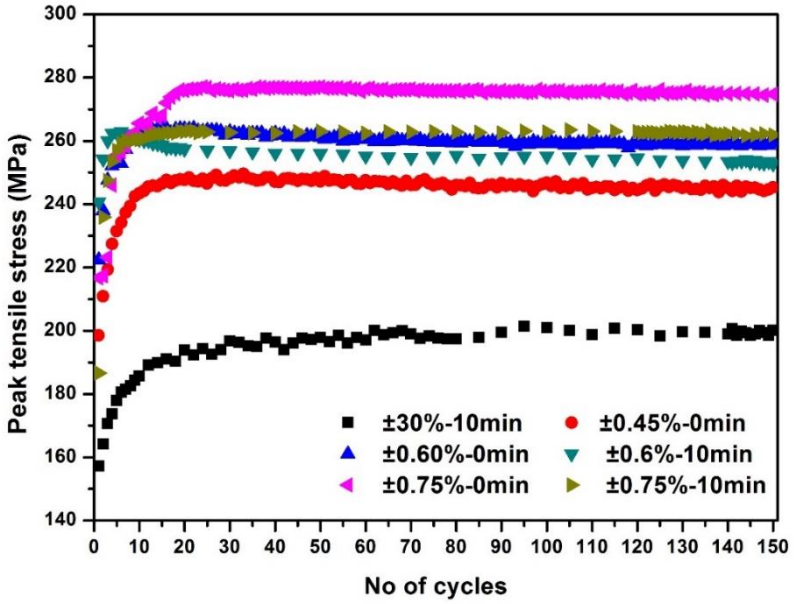

Figure 6.14 Peak tensile stress for ex-service material (Material B) cyclically deformed at 550°C and 0.025%/s strain rate at total strain ranges of ±0.45%, ±0.60% and ±0.75% without dwell, and ±0.30%, ±0.60% and ±0.75% with 10 minute dwells at the peak tensile strains.

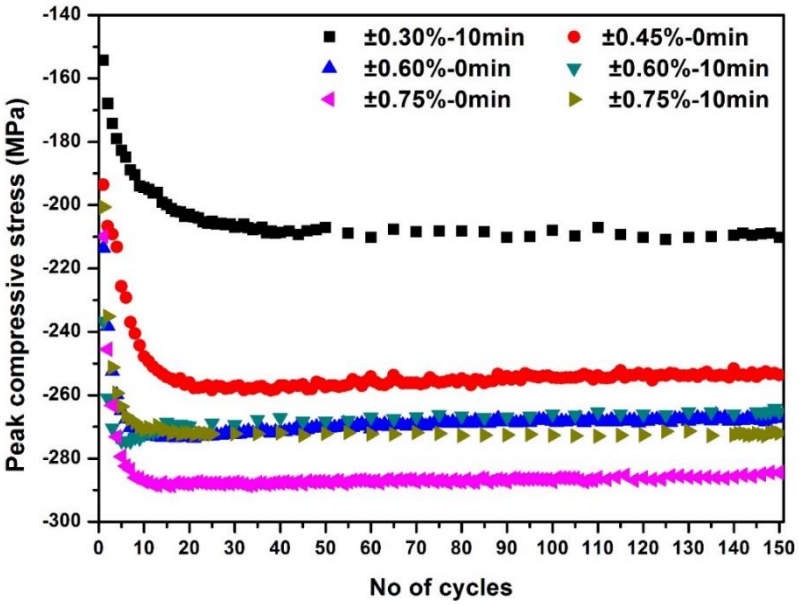

Figure 6.15 Peak compressive stress for ex-service material (Material B) cyclically deformed at 550°C and 0.025%/s strain rate at total strain ranges of ±0.45%, ±0.60% and ±0.75% without dwell, and ±0.30%, ±0.60% and ±0.75% with 10 minute dwells at the peak tensile strains.

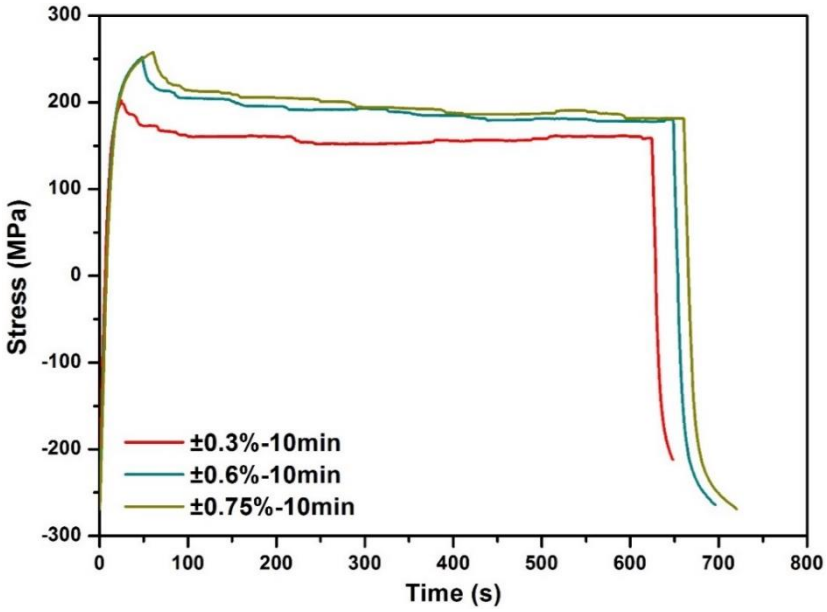

Figure 6.16 Stress vs time curve for last (150th) cycle of ex-service material (Material B) cyclically deformed at 550°C and 0.025%/s strain rate over total strain ranges of ±030%, ±0.60% and ±0.75% with 10 minutes dwells at the peak tensile strain.

Figure 6.17 shows the mean hardness values for ex-service material (material B) cyclically deformed at 550°C over total strain ranges of ±0.45% , ±0.60% and ±0.75% without dwell and ±0.30%, ±0.60% and ±0.75% with 10 min dwells at the peak tensile strain. Even though hardness measurements are not particularly sensitive indicators of strength changes and are subject to local variations, the mean hardness values clearly showed an increasing trend with total strain range. However, as in material A (see Figure 6.8), the hardness measurements did not pick up any damage due to dwell (see Figure 6.17). Figure 6.18 shows the different EBSD metrics for ex-service material (Material B) cyclically deformed over total strain ranges of ±0.45% , ±0.60% and ±0.75% without dwell and ±0.30% with 600s dwells at the peak tensile strain. KAM_a lognormal, GOS_a, DGF(0.5) and DGF(1) all increased with the total strain range. TBF showed a decreasing trend as the strain range increased. There was no significant difference between the EBSD metrics of ex-service material and those of the material deformed over a total strain range of ±0.30%. Figure 6.19 shows the frequency distributions of the KAM values for ex-

service material (material B) deformed over different strain ranges. There is a clear trend of higher KAM values with increasing strain range.

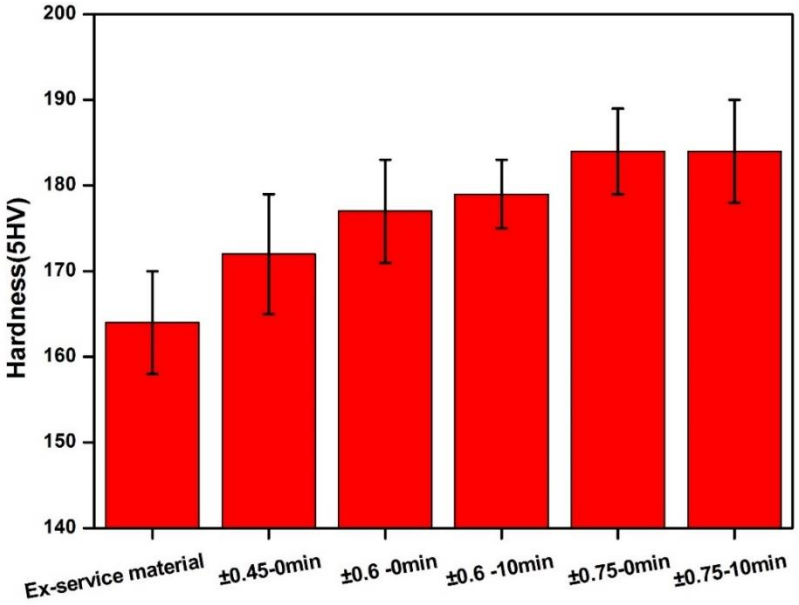

Figure 6.17 Mean hardness values for ex-service material (Material B) cyclically deformed at 550°C and 0.025%/s strain rate over total strain ranges of ±0.45%, ±0.60% and ±0.75% without dwell and ±0.30% with 10 minute dwell at peak tensile strain for 150 cycles.

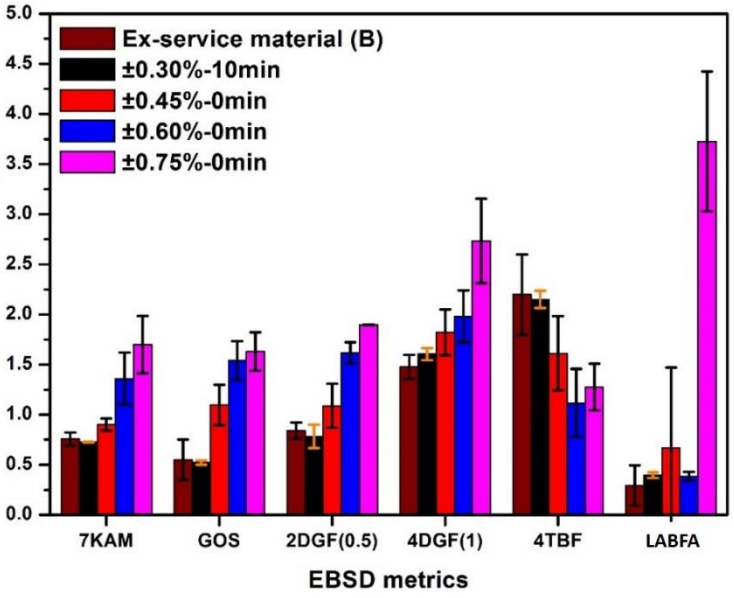

Figure 6.18 EBSD metrics for ex-service material (Material B) cyclically deformed at 550°C and 0.025%/s strain rate over total strain ranges of ±0.45%, ±0.60% and ±0.75% without dwell and ±0.30% with 10 minutes dwell at peak tensile strain for 150 cycles. KAM (KAM_a lognormal) is multiplied by 7, DGF(0.5) by 2, DGF(1) by 4 and TBF by 4 to represent all the EBSD metrics on the same plot.

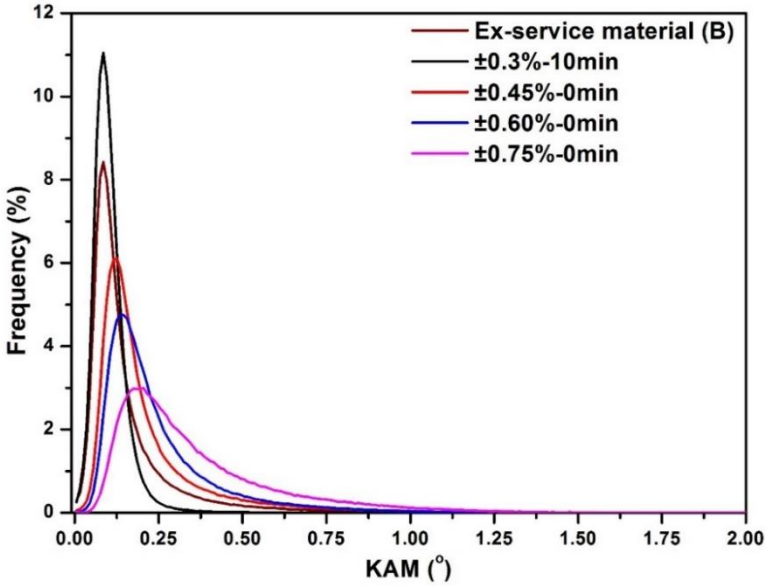

Figure 6.19 KAM distribution for ex-service material (Material B) cyclically deformed at 550°C and 0.025%/s strain rate over total strain ranges of ±0.45%, ±0.60% and ±0.75% without dwell and ±0.30% with 10 minutes dwell at the peak tensile strain for 150 cycles.

Plots of the cumulative strains against the cumulative inelastic strain energy density (W) showed a linear trend (see Figure 6.20). The best linear fits were found for $\sum \varepsilon_{ie}$ and $\sum \varepsilon_{c}$. It is evident that KAM_a lognormal, GOS_a, DGF(0.5) and DGF(1) are the EBSD metrics that gave a good linear fit with low cycle fatigue damage (see Figure 6.21 to Figure 6.26). Figure 6.21 shows, for material B deformed under different conditions, KAM_a lognormal plotted against the cumulative inelastic strain ($\sum \varepsilon_{ie}$) and their relationship fitted by a straight line. Figure 6.21 shows KAM_a lognormal of material B deformed under different conditions plotted against the cumulative inelastic strain energy density (W), again fitted by a straight line. It is clear from the plots that KAM_a lognormal increased almost linearly with inelastic strain and strain energy density. GOS_a also increased with W and $\sum \varepsilon_{ie}$ and could be fitted to linear relationships (see Figure 6.23 and Figure 6.24). DGF was found to be more sensitive to W and $\sum \varepsilon_{ie}$ (see Figure 6.25 and Figure 6.26) and could also fitted

by a linear function. DGF followed a better linear relationship with W than $\sum\varepsilon_{ie}$ and the DGF(0.5) metric was found to give a better linear fit than DGF(1).

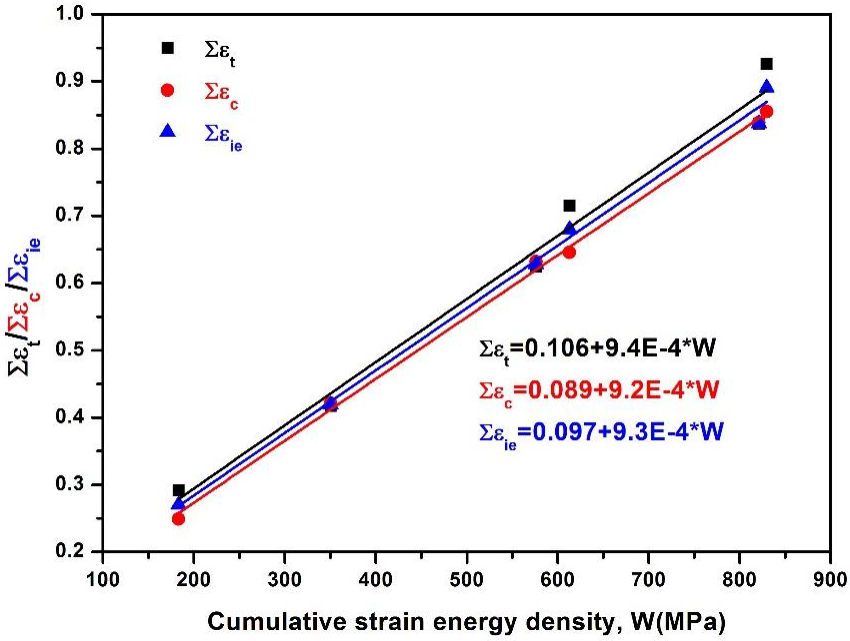

Figure 6.20 Cumulative inelastic strain energy density (W) plotted against cumulative tensile inelastic strain ($\sum\varepsilon_T$), cumulative compressive inelastic strain ($\sum\varepsilon_c$) and cumulative inelastic strain ($\sum\varepsilon_{ie}$) for ex-service material (Material B) cyclically deformed at 550°C and 0.025%/s strain rate over different strain ranges. (Further details regarding experimental conditions are given in Table 6.2). There are no theoretical assumptions behind using a linear fit.

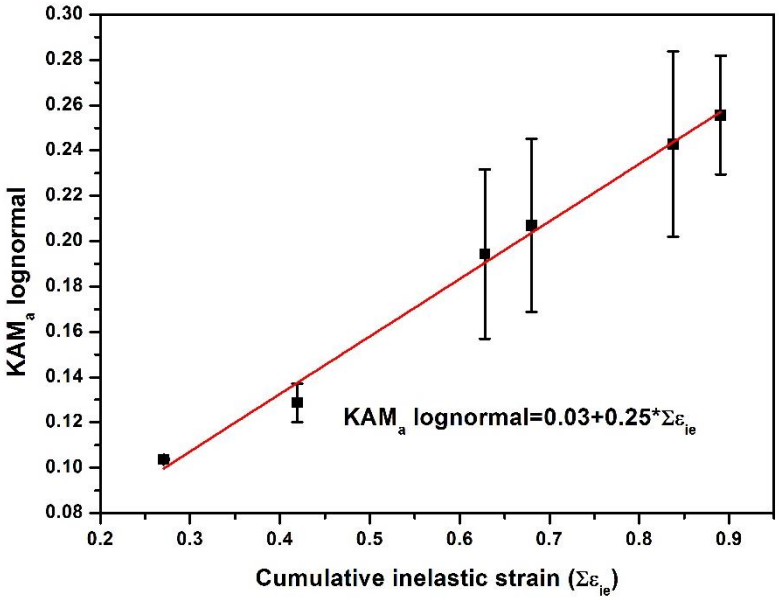

Figure 6.21 Cumulative inelastic strain vs KAM_a lognormal for ex-service material (Material B) cyclically deformed over different strain ranges at 550°C. See Table 6.2 for further details of the experimental conditions. There are no theoretical assumptions behind using a linear fit.

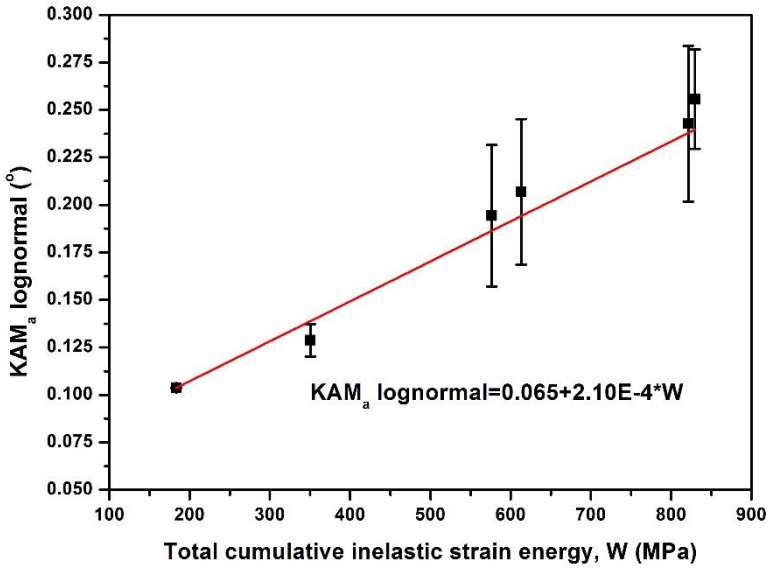

Figure 6. 22 Cumulative inelastic strain energy density vs KAM_a lognormal for ex-service material (Material B) cyclically deformed over different strain ranges at 550°C. See Table 6.2 for further details of the experimental conditions. There are no theoretical assumptions behind using a linear fit.

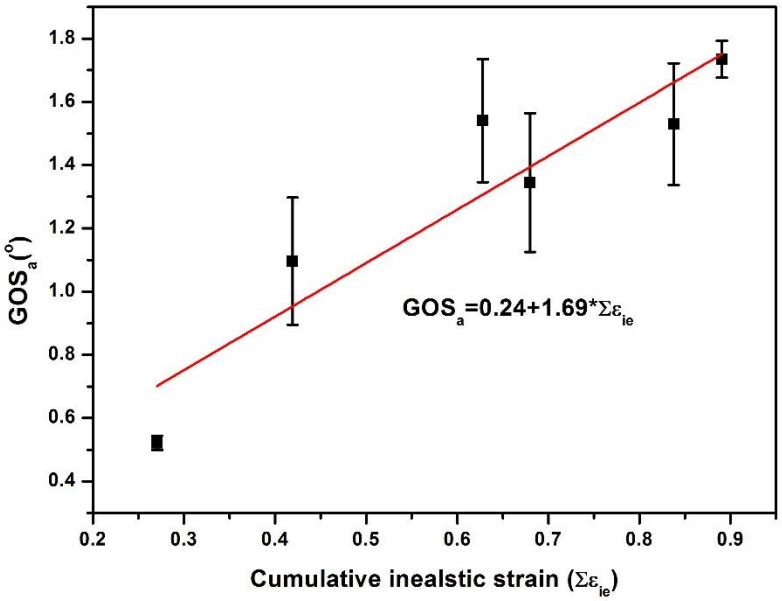

Figure 6.23 Cumulative inelastic strain vs GOS_a for ex-service material (Material B) cyclically deformed over different strain ranges at 550°C. See Table 6.2 for further details of the experimental conditions. There are no theoretical assumptions behind using a linear fit.

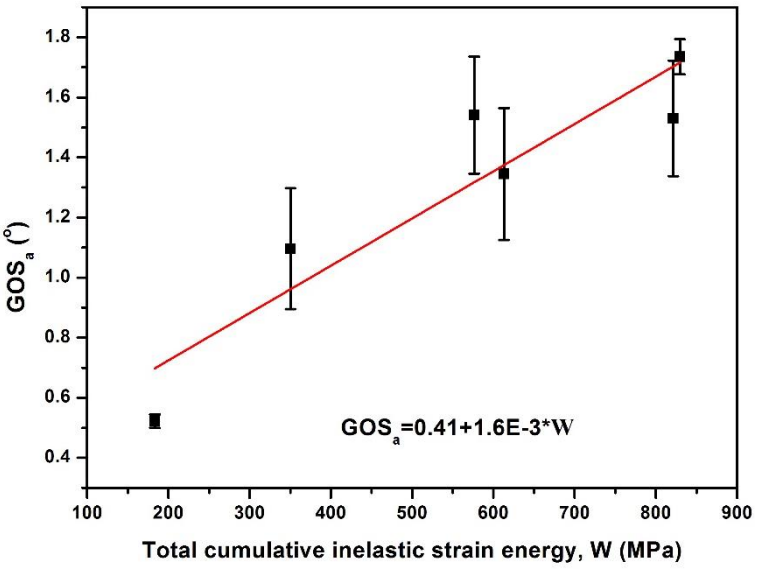

Figure 6.24 Cumulative inelastic strain energy density vs GOS_a for ex-service material (Material B) cyclically deformed over different strain ranges at 550°C. See Table 6.2 for further details of the experimental conditions. There are no theoretical assumptions behind using a linear fit.

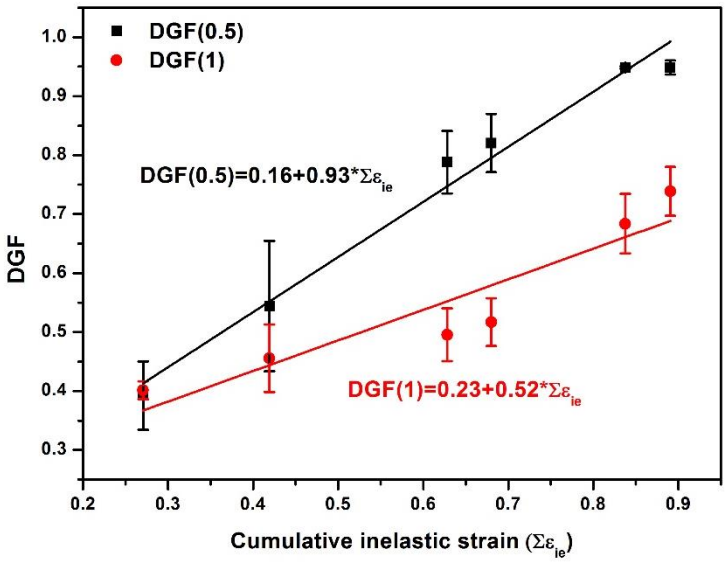

Figure 6.25 Cumulative inelastic strain vs DGF(0.5) and DGF(1) for ex-service material (Material B) cyclically deformed over different strain ranges at 550°C. See Table 6.2 for further details of the experimental conditions. There are no theoretical assumptions behind using a linear fit.

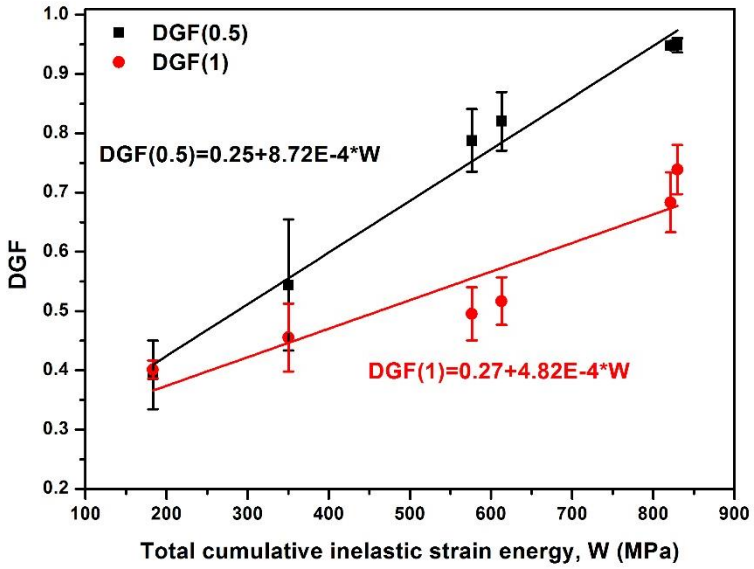

Figure 6.26 Cumulative inelastic strain energy density vs DGF(0.5) and DGF(1) for ex-service material (Material B) cyclically deformed over different strain ranges at550^{o}C. See Table 6.2 for further details of the experimental conditions. There are no theoretical assumptions behind using a linear fit.

The microstructures of material B specimens deformed over different strain ranges, as seen in STEM images, are shown in Figure 6.27. As in Chapter 3, the most commonly occurring dislocation structures in all 3 foils studied for each deformation condition are represented. Little evidence was found of the active slip planes. Tangles of dislocations were frequently observed in material B samples cyclically deformed over a strain range of ±0.3%. The dislocations formed clear cell structures after deformation over strain ranges of ±0.6% and ±0.75%. The precipitates were associated with the dislocation tangles or cell walls. At the higher strain range of ±0.75% (see Figure 6.28) there was evidence of a sub-grain structure and active slip planes (the closely spaced parallel active slip planes might be a part of a persistent slip band). Precipitates were found along the active slip planes and sub grain boundaries (see Figure 6.28).

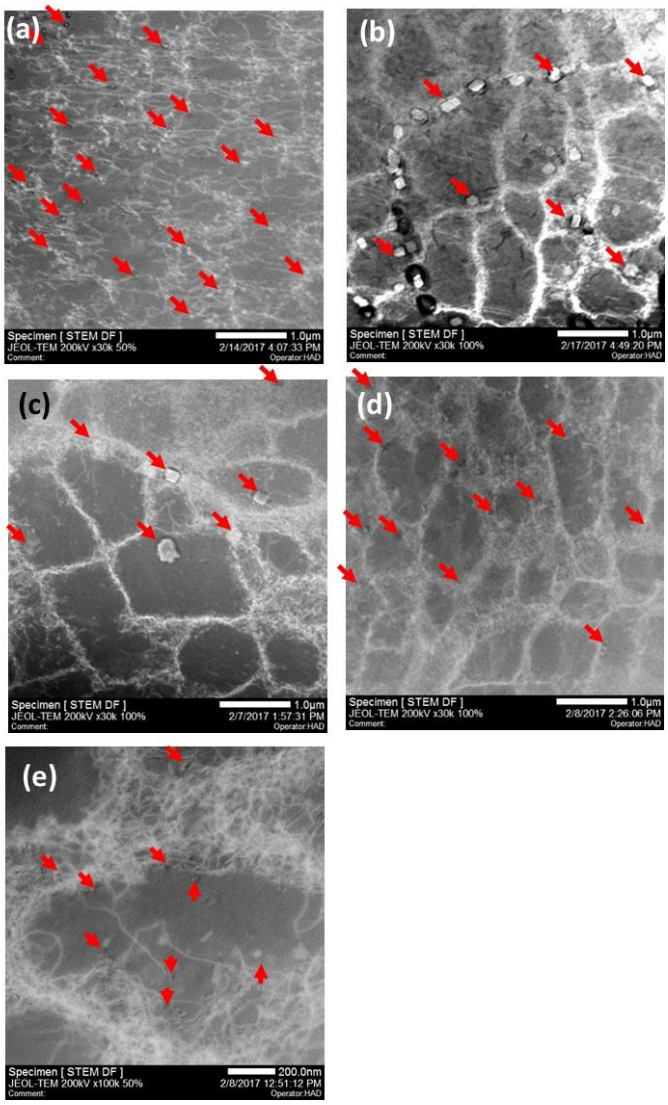

Figure 6.27 STEM DF-HAADF micrographs of service-aged Type 316H austenitic stainless steel (Material B) cyclically deformed at a total strain range of (a) ±0.30% with 10 minute dwell (b) ±0.60% without dwell (c) ±0.75% without dwell (d) ±0.75% with 10 minute dwell and (e) enlarged cell structure of material B deformed at ±0.75% with 10 minute dwell. Intragranular precipitates are marked with red arrows.

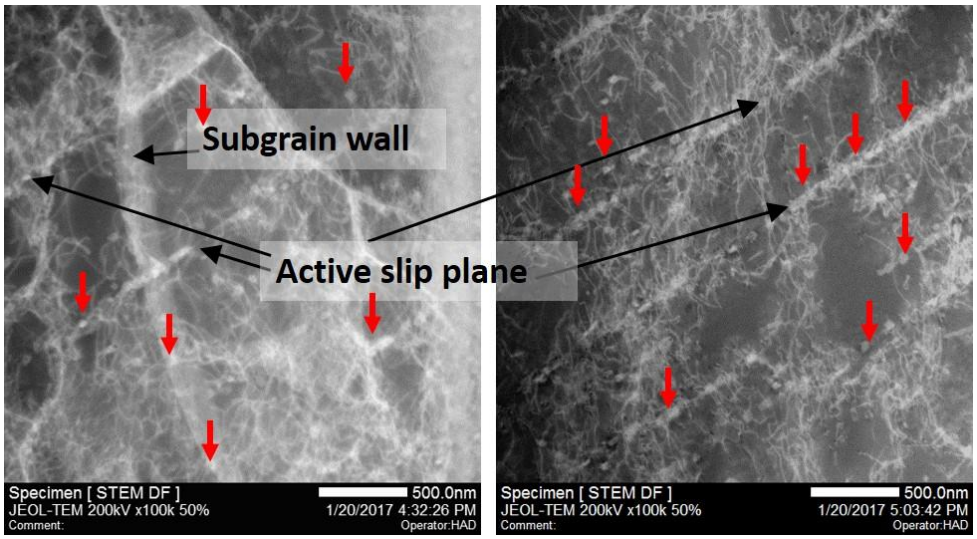

Figure 6.28 STEM DF-HAADF micrographs of service-aged Type 316H austenitic stainless steel (Material B) cyclically deformed at a total strain range of ±0.75% with 10 minute dwell showing sub-grain structure and active slip planes that could together make up a part of persistent slip bands (PSBs). Intragranular precipitates are marked with red arrows.

6.2.5. Discussion

Stress relaxation in cyclic deformation

The cyclic response of ex-service material (material A, B and C) is characterized by an initial hardening followed by a saturation stage (Figure 6.4, Figure 6.9 and Figure 6.14). Figure 6.3 shows the stress relaxation curve for Material A deformed at different dwell times. It is very clear from the figure that there was a significant reduction in stress between pure fatigue loading and creep-fatigue with 180s dwell and a smaller further reduction in stress when the dwell time was increased to 600s. Similar observations were reported for 316 and 316L material where a rapid stress relaxation occurred in the first few minutes of dwell followed by a slower rate of stress relaxation [96], [201][193]. The conversion of elastic strain to plastic strain during stress relaxation was described in Chapters 2 and 5. Tensile inelastic strain build-up leads to the accumulation of grain boundary creep damage in the form of cavities in 316L(N) stainless steels [201]. As the hold time increases the global stress relaxes significantly, leading to an enhanced build-

up of intergranular creep damage [201]. The results reported in Chapter 5 of uniaxial stress relaxation for 24 hour also showed cavitation at the grain boundaries (See Figure 5.18, SEM image). The stress reduction in the tests with dwell periods may be explained by recovery of the dislocation structure [96] and by thermal activation of dislocation motion over short-range obstacles, generally by climb [196].

Microstructure evolution

Figure 6.27 shows the STEM microstructures of material B in selected deformation conditions. At low strain amplitude (±0.3%), the cyclic stress seems to cause less movement of dislocations as evidenced by looser dislocation tangles (see Figure 6.27(a)) compared to the dislocation cell structures at higher strain ranges (±0.6% and ±0.75%, see Figure 6.27(b)-(d)). Similar results were reported from room temperature tests on 316H material for a strain range of ±0.25% and 316L material at ±0.06% [202], [203]. The evolution of the dislocations structures during cyclic deformation at room temperature over different strain ranges has been explained as follows [204]:

Higher strain range

- During cyclic hardening, the dislocation density significantly increases, particularly in regions close to grain boundaries and precipitates
- At the end of cyclic hardening, multiple slip/cross slip occurs, forming a three-dimensional dislocation cell structure [205], as observed after 150 cycles in the high strain range (±0.6, ±0.75%) tests in this study (see Figure 6.27).
- Dislocations then rearrange during the softening stage (after reaching saturation of peak stress) due to the strong activation of secondary slip (cross-slip), finally resulting in the formation of dislocation walls/channels

- Upon further loading, the strong multiple slip at this strain amplitude is responsible for the development of the wall/channel or vein structures into a cellular structure, towards the end of life. Towards the end of fatigue life, the cellular structure becomes more equiaxed.

Lower strain range

- Dislocation densities are lower in both grain boundaries and interiors, resulting in lower rates of the first cyclic hardening response
- Dislocations exhibit a strong tendency to planar arrangements
- This tendency persists to a high life fraction
- Stacking faults are still observed until the middle of life
- Towards the end of fatigue life, a large portion of material is occupied by ill-organised dislocation walls

Similar microstructural features to those described above were observed at 550ºC in this study. The presence of well-developed dislocation tangles at a lower strain range than at room temperature can be attributed to the effects of the higher temperature in making dislocation glide and climb much easier. Subgrains were rarely observed in samples cyclically deformed to the highest strain amplitude (550B±0.75%0.025H10) (see Figure 6.28). The strain hardening in the early cycles can be attributed to the generation of the dislocations which produce the plastic and creep strains and by their mutual interactions. The softening (reduction in the peak tensile stress) can be associated with the rearrangement of these dislocations and with micro-crack generation [96]. The variation of the dislocation structure evolution with strain amplitude will affect the changes in internal stresses during cyclic loading. Type 316 steel is reported to exhibit sub-grain structures under a wide range of strain amplitude loading conditions [206].

Sub-grains and active slip planes that could possibly be part of PSBs were observed here in the tests at the highest strain range (see Figure 6.28). Generally PSBs are less frequent in polycrystals than in single crystals cycled at the same plastic strain amplitude; this can be attributed to the mutually constraining effects of neighbouring grains [207]. However, PSBs have been reported in cyclic deformation of 316 steel in many studies. Stress concentration from dislocations piled up in a neighbouring grain could lead to PSB formation [208][209]. Temperature is reported to be a limiting factor for PSB formation.: PSBs in copper single crystals were found to be unstable at high temperatures (above 250^{o}C), transforming to a cell structure within a few minutes after the cessation of cycling [209]. However, the dislocation structures in type 316H steel might be stabilised by a reduction of the dislocation mobility by interstitial atoms and by dislocation pinning at precipitates. Even though STEM showed more clearly defined cell structures after stress relaxation than after plastic deformation (Figure 5.21-5.24), there was no notable difference between STEM micrographs of low cycle fatigue and creep-fatigue materials.

Nellessen et al [210] studied the influence of grain orientation on the dislocation structures formed during cyclic fatigue. The crystallographic directions of the observed dislocation veins (or elongated ladder structures [211]) were determined using the double pseudo-polygonization (DPP) model proposed by Dickson et al [212].

EBSD and accumulated damage

Creep damage is generated during the tensile part of cyclic deformation whereas the damage is potentially reduced during the compressive part [213]. So, the total damage after cyclic deformation is less than after deformation in tension for the same strain path. Modelling studies by McLean and Pineau on 316 steel showed that at 750^{o}C around 30% of the damage (plastic/creep strains as a function of grain-boundary fissuration generated

by the sliding) generated during the tensile part remains after compression and the model gave good correlation with experimental results [214]. The GOS_a, DGF(0.5), and DGF(1) results in Figure 6.7 show that there is an overall increase in intragranular misorientations with dwell but KAM_a lognormal and GOS_a, were not always sensitive to inelastic strain developed during dwell in cyclic deformation of material C (Figure 6.12). However, the results reported in Chapter 5 (see Figure 5.11, Figure 5.12) showed a clear increase in KAM_a lognormal and GOS_a with dwell for uniaxial stress relaxation. The increase in KAM shows that GNDs are generated during stress relaxation. Stress relaxation in cyclic deformation produced no similar major increase in the EBSD metrics. This may be attributed to the annihilation of some of the dislocations generated during stress relaxation, during the subsequent compressive part of the loading.

As explained in Chapter 2, the overall damage in a creep-fatigue deformation can be decomposed into the individual contributions of creep and fatigue:

$D_t = D_c + D_f = \sum \frac{t_h}{t_r} + \sum \frac{N}{N_f} = \sum \frac{t_h}{t_r} +$ Strain energy density (W or hysteresis loop area) (6.1)

In which D_t, D_c, D_f are the total, creep and fatigue damage respectively. The life fraction term for the fatigue damage $\frac{N}{N_f}$ is the current number of cycles (N) as a fraction of the number of cycles to failure (N_f) for continuous cyclic fatigue tests with hold periods at the same strain amplitude, while the life fraction for the creep damage, is the ratio of the total of the hold times (t_h) in the test up to the N^{th} the cycle to the rupture time (t_r) which would be obtained from a pure creep test at the same stress as that during the hold period.

The fatigue failure of a component can be directly related to the inelastic strain energy [93] but, due to a lack of long term creep data, the creep damage during dwell was not calculated in this study. The cumulative strain approach, which does not require long term

creep data was used, rather than the cumulative strain energy method, to calculate the damage in creep-fatigue deformation for comparison with the EBSD metrics.

Figure 6.6 shows the cumulative inelastic strains for material A cyclically deformed to 150 cycles at 550^{o}C with different tensile dwell times. There was a significant increase in the cumulative tensile inelastic strain with 180s dwell but there was no significant increase for 600s dwell. The cumulative compressive strain and cumulative inelastic strain increased consistently with dwell time but the cumulative strain energy didn't show any trend with dwell. This can be attributed to not considering creep damage during the dwells in the damage calculations. In the literature, strain energy density is only used as a measure to identify failure not to estimate the accumulated damage [96], [200]. The cumulative inelastic strain energy (W) and cumulative inelastic strains of material B deformed at different strain ranges and dwells showed a linear correlation (see Figure 6.20). But a more linear relationship was obtained for cumulative inelastic strain against W.

The variation of different EBSD metrics with dwell time for material A deformed at 550^{o}C is shown in Figure 6.7. GOS_a, DGF(0.5) and DGF(1) increase slightly with dwell time and (as seen in Figure 6.12) DGF(0.5) and DGF(1) showed similar behaviour for Material C. DGF is reported to be the metric least sensitive to local microstructural changes [11]. Though GOS_a has been reported in many studies [11], [29], [132], [138], [145], [215] to increase with inelastic strains or number of cycles to failure, local differences in the precipitate distribution might have affected the GOS_a values in this study giving inconsistent results for Material C (see Figure 6.12). (As described in Chapter 4, Materials A, B and C were all extracted from the same ex-service material but from different locations).

Similar results were obtained for Material B (see Figure 6.21 to Figure 6.26). Most of the EBSD metrics increased with increasing cumulative strain/strain energy and KAM_a lognormal, DGF(0.5) and DGF(1) showed good linear relationships with cumulative strain and strain energy density. The spread in KAM increased with strain range (see Figure 6.19). This could have resulted from a general increase in lattice curvature with increasing GND density. LABFA, which considers misorientations of 2 to $15^{o,}$ was also found to increase with strain range. This shows that there is a general increase in misorientations up to 15^o with strain range in cyclic deformation. Round robin crystal orientation studies on creep damaged 316 stainless steel specimens showed that the area averaged local (KAM) and intra-grain misorientations (AMIS/GOS) correlated well with the degree of the creep damage (inelastic strain) [142]. But the study suggested that KAM measurements might be affected by local inhomogeneity in the microstructure. In this study, both KAM and GOS were found to be slightly affected by local inhomogeneity in the microstructure. Such inhomogeneity might be due to the microstructural changes during the component's manufacturing processes (casting followed by forging [216]) or variations in the local chemical composition associated with precipitates [11]. As described in section 2.2.1. , the precipitation of carbides in austenitic stainless steel can change the local chemical composition. Section 2.2.1 also described the effects of alloying elements on creep and plastic deformation in 316H. The variation in temperature in different parts of the component during its service might have affected the difference in the density and size of precipitates across the thickness (see Figure 4.12 for further information on the precipitate size distributions at different locations in the ex-service material). The metric DGF, which is derived from GOS, was found to be least sensitive to local microstructural changes. This could be due to the fact that looking at GND accumulation over a large area might have reduced the effect of local chemical variations.

The reduction in TBF (see Figure 6.18) with strain range can be attributed to the dislocation accumulation at twin boundaries as explained in section 5.3.5.

6.3. Influence of temperature and precipitates on misorientation development

6.3.1. Mechanical tests

Strain-controlled high temperature low cycle fatigue tests were conducted on ex-service (materials B), solution annealed (material D) and thermally aged (material E) material to study the effects of temperature and precipitates. Details of the test conditions are given in Table 6.3. All tests were conducted over a total strain range of ±0.6% and at a strain rate of 0.025%/s. All samples were cyclically deformed to 150 cycles.

Table 6.3. Cyclic test conditions to study the effect of temperature and precipitation on misorientation development in type 316H stainless steel.

Sample	Total strain range (%)	Temperature	Strain rate	Sample ID
B	±0.6	550	0.025%/s	550B±0.60%0.025H0
B	±0.6	RT	0.025%/s	RTB±0.60%0.025H0
C	±0.6	550	0.025%/s	550B±0.60%0.025H0
D	±0.6	RT	0.025%/s	RTD±0.60%0.025H0
D	±0.6	550	0.025%/s	550D±0.60%0.025H0
D	±0.6	640	0.025%/s	640D±0.60%0.025H0
E	±0.6	550	0.025%/s	550E±0.60%0.025H0

6.3.2. EBSD and Nano-hardness measurements

EBSD measurements followed the same procedures as described in section 6.2.2.

6.3.3. Results

Table 6.4 Cumulative inelastic strain energy density and cumulative tensile inelastic strain of ex-service material (Material B), solution annealed material (Material D) and thermally aged material (Material E) cyclically deformed at different temperatures, all at a strain rate of 0.025%/s, a strain range of ±0.6%, and without dwell .

Sample	Temperature	Cumulative inelastic strain energy density, W	Cumulative tensile inelastic strain ($\sum\varepsilon_T$)
B	550	576.21	0.62
B	RT	679.71	0.60
C	550	609.42	0.5385
D	RT	600.91	0.56
D	550	677.99	0.54
D	640	581.65	0.61
E	550	649.55	0.53

Figure 6.29 and Figure 6.30 show the peak tensile and compressive stresses respectively for ex-service material (Material B) cyclically deformed, at a strain rate of 0.025%/s, over a total strain range of ±0.6% with no dwell at either 550^{o}C or room temperature. The peak stresses were considerably lower for deformation at 550^{o}C. At room temperature softening was observed. For ex-service material (Material B), W was higher and $\sum\varepsilon_t$, $\sum\varepsilon_c$ and $\sum\varepsilon_{ie}$ lower when deformed at room temperature rather than at 550^{o}C (see Figure 6.31). KAM_a lognormal, GOS_a, DGF(0.5) and DGF(1) were also lower when material B was deformed at room temperature rather than at 550^{o}C (see Figure 6.32). LABFA and TBF were higher for materials deformed at room temperature.

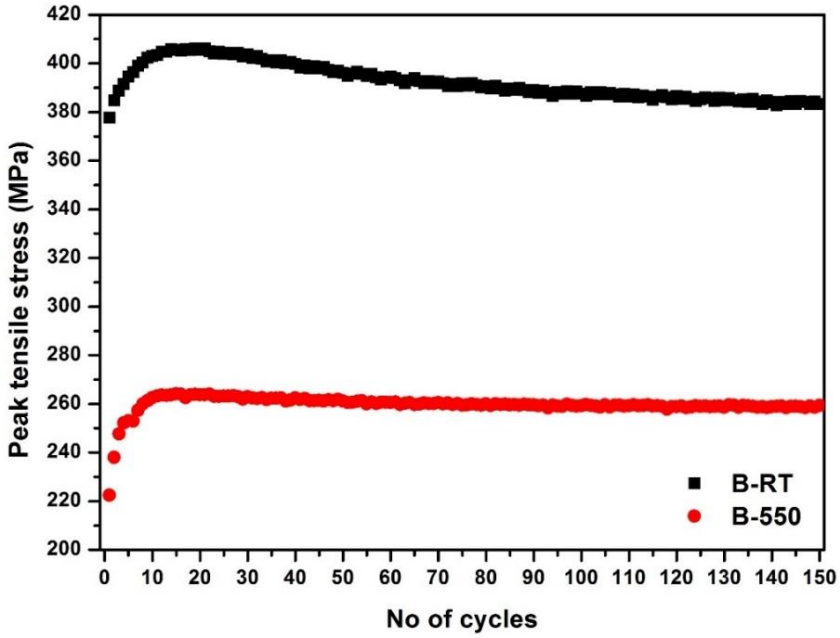

Figure 6.29 Peak Tensile stress for ex-service material (Material B) cyclically deformed at a total strain range of ±0.6% and strain rate 0.025%/s with no dwell at room temperature or 550°C.

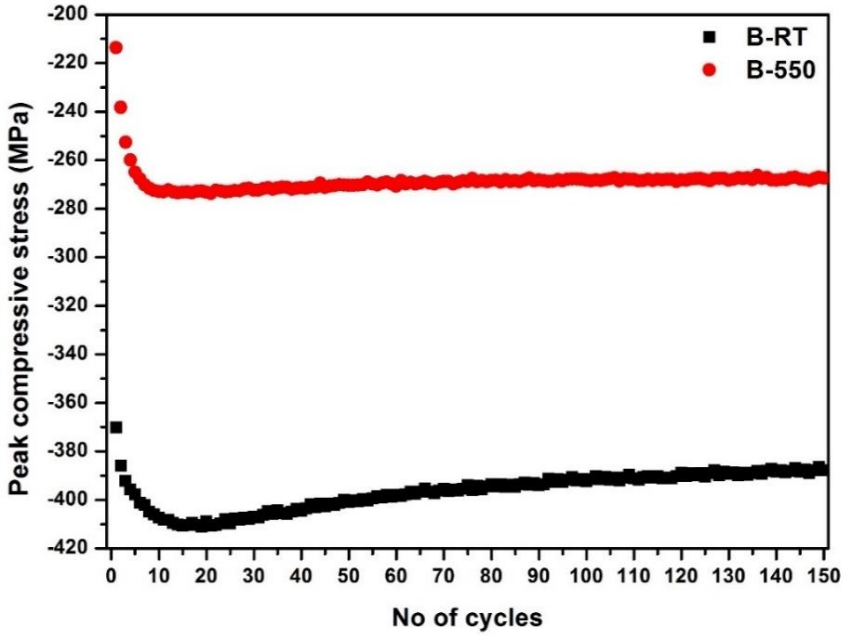

Figure 6.30 Peak compressive stress for ex-service material (Material B) cyclically deformed at a total strain range of ±0.6% and strain rate 0.025%/s with no dwell at room temperature or 550°C.

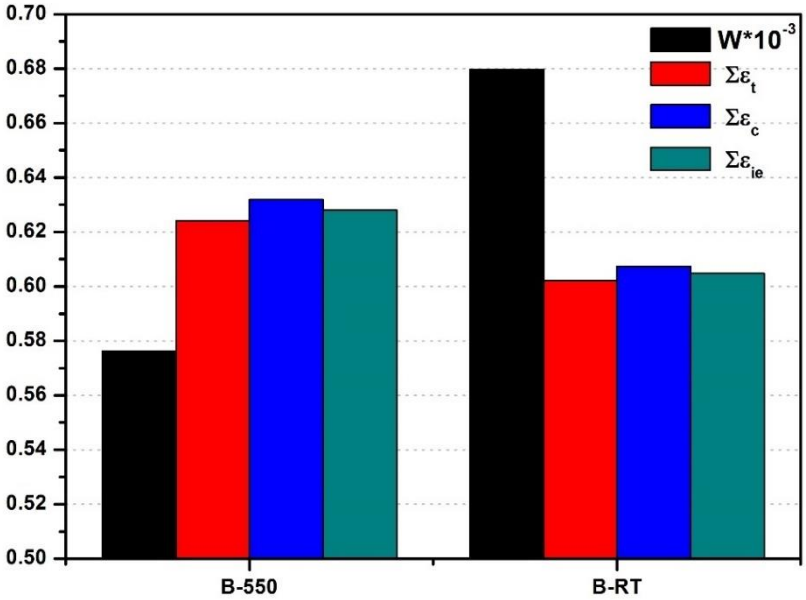

Figure 6.31 Cumulative inelastic strain energy density (W), cumulative tensile inelastic strain ($\sum\varepsilon_t$), cumulative compressive inelastic strain ($\sum\varepsilon_c$) and cumulative inelastic strain ($\sum\varepsilon_{ie}$) for ex-service material (Material B) cyclically deformed over a total strain range of ±0.6% and strain rate 0.025%/s with no dwell at room temperature or 550°C. W is multiplied by 10^{-3} to represent the inelastic strain energy and strains on same plot. Plese note that Y-axis starts from 0.5.

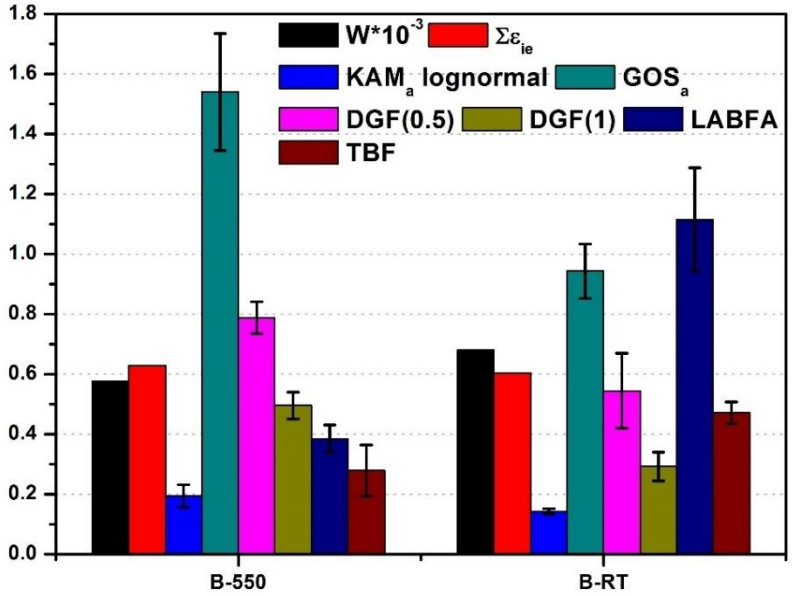

Figure 6.32 Cumulative inelastic strain energy density (W), cumulative tensile inelastic strain ($\sum\varepsilon_t$) and different EBSD metrics for ex-service material (Material B) cyclically deformed at a total strain range of ±0.6% and strain rate 0.025%/s with no dwell at room temperature or 550°C. W is multiplied by 10^{-3} to represent the inelastic damage and EBSD metrics on same plot.

Figure 6.33 shows the final cycle stress-strain curves for ex-service material (Material B) and solution annealed material (Material D) deformed to 150 cycles at room temperature.

The effects of aging on the development of strain-induced misorientations in material D was minimal during the room temperature deformation where no precipitation occurs. The peak tensile and compressive stress for each cycle is shown in Figure 6.34. The peak stresses were higher for ex-service material (Material B) than for solution annealed material (Material D). W, $\sum\varepsilon_t$, $\sum\varepsilon_c$ and $\sum\varepsilon_{ie}$ were all lower for solution-annealed material than for ex-service material (see Figure 6.35). KAM_a lognormal, GOS_a, DGF(0.5), DGF(1) and LABFA were lower for solution-annealed material than for ex-service material (see Figure *6.36*) but TBF was higher for solution-annealed material.

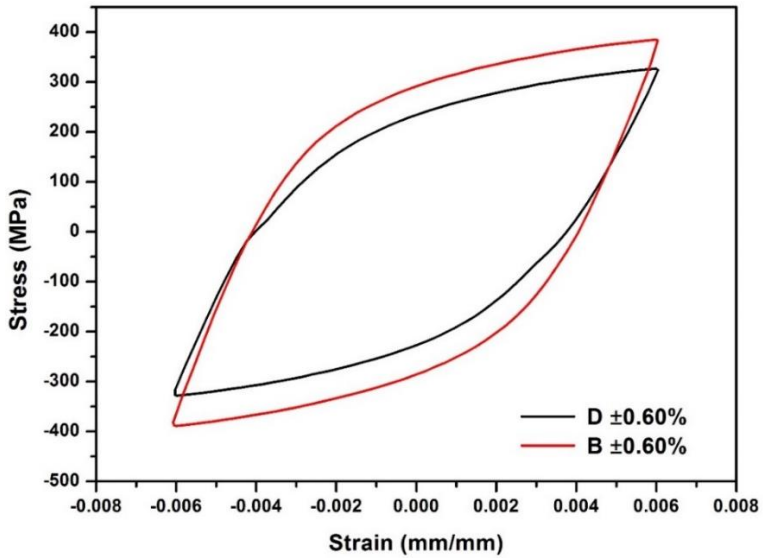

Figure 6.33 Final (150th) cycle stress-strain curves for ex-service material (Material B) and solution annealed material (Material D) cyclically deformed at room temperature, at a strain rate of 0.025%/s over a total strain range of ±0.6% with no dwell.

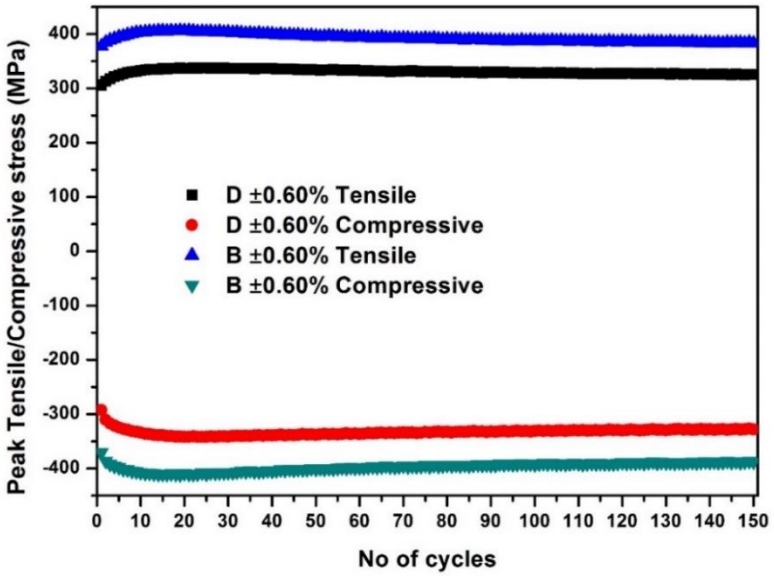

Figure 6.34 Peak Tensile stress and Peak compressive stress for ex-service material (Material B) and solution annealed material (Material D) cyclically deformed over a total strain range of ±0.6% and strain rate 0.025%/s with no dwell at room temperature.

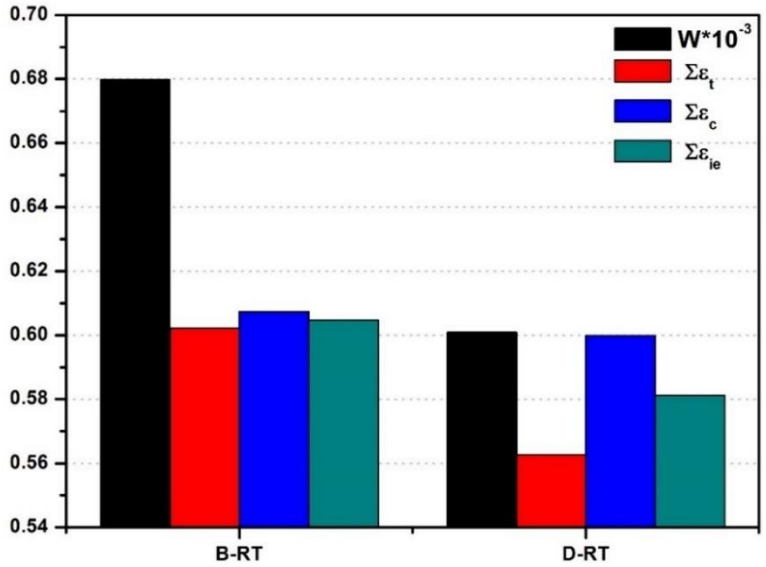

Figure 6.35 Cumulative inelastic strain energy density(W), cumulative tensile inelastic strain ($\sum\varepsilon_t$), cumulative compressive inelastic strain ($\sum\varepsilon_c$) and cumulative inelastic strain ($\sum\varepsilon_{ie}$) for ex-service material (Material B) and solution annealed material (Material D) cyclically deformed over a total strain range of ±0.6% and strain rate 0.025%/s with no dwell at room temperature. W is multiplied by 10^{-3} to represent the inelastic strain energy and strains on same plot. Please note that Y-axis starts from 0.54.

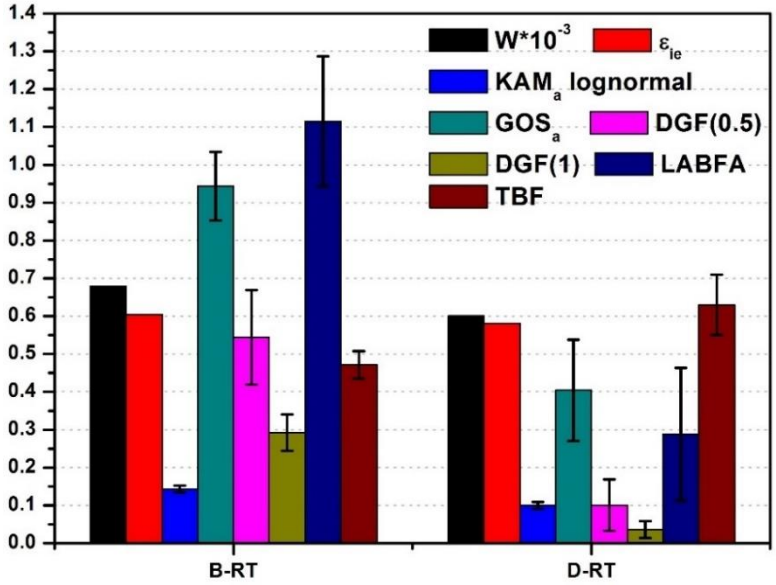

Figure 6.36 Cumulative inelastic strain energy density (W), cumulative inelastic strain ($\sum\varepsilon_{ie}$) and different EBSD metrics for ex-service material (Material B) and solution annealed material (Material D) cyclically deformed at a total strain range of ±0.6% and strain rate 0.025%/s with no dwell at room temperature. W is multiplied by 10^{-3} to represent inelastic damage and EBSD metrics in same plot.

Figure 6.37 shows the final cycle stress-strain curve for solution-annealed material (Material D) cyclically deformed at a total strain range of ±0.6% and strain rate 0.025%/s with no dwell at 550°C and 640°C. Figure 6.38 shows the peak stress values for each cycle. The peak stresses were lower at 640°C. W was lower but $\sum\varepsilon_t$, $\sum\varepsilon_c$ and $\sum\varepsilon_{ie}$ were higher at 640°C than at 550°C (see Figure 6.39). KAM_a lognormal, GOS_a, DGF(0.5) and DGF(1) were also higher after testing at 640°C than after the corresponding tests at 550°C (See Figure 6.40). There was no clear trend in the $LABF_A$ and TBF metrics (See Figure 6.40).

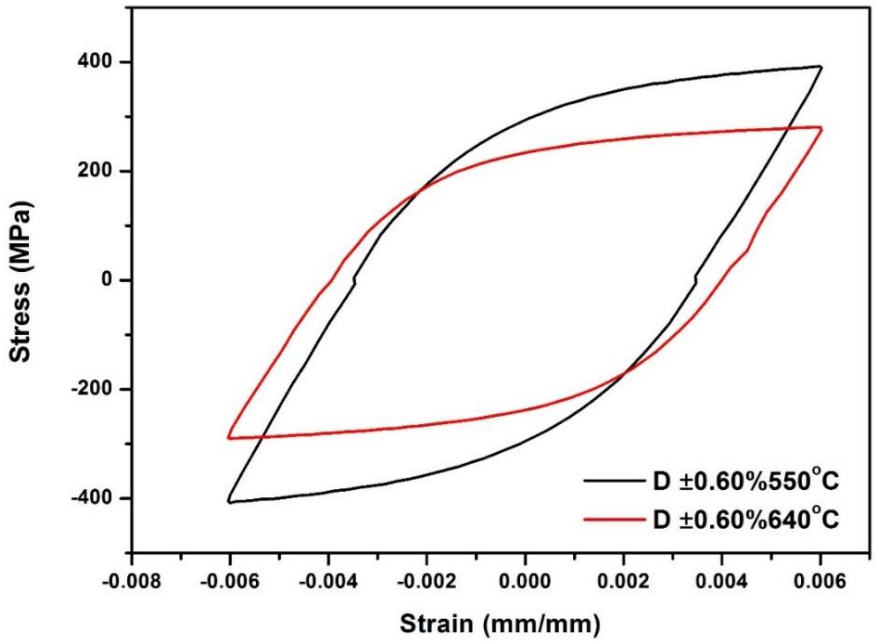

Figure 6.37 Final (150th) cycle stress-strain curve for solution annealed material (Material D) cyclically deformed at a total strain range of ±0.6% and strain rate 0.025%/s with no dwell at 550°C and 640°C.

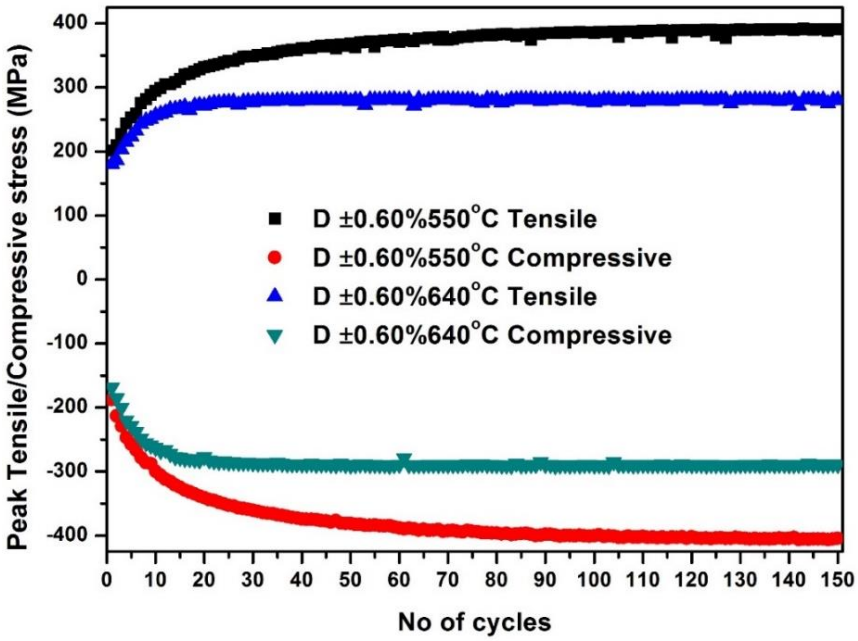

Figure 6.38 Peak tensile and compressive stresses for solution-annealed material (Material D) cyclically deformed at a total strain range of ±0.6% and strain rate 0.025%/s with no dwell at 550°C and 640°C.

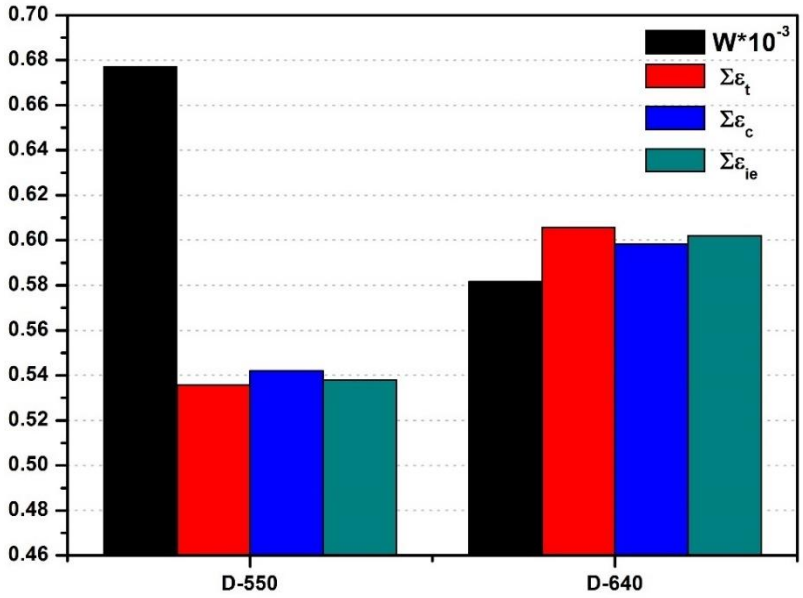

Figure 6.39 Cumulative inelastic strain energy density(W), cumulative tensile inelastic strain ($\sum\varepsilon_T$), cumulative compressive inelastic strain ($\sum\varepsilon_c$) and cumulative inelastic strain ($\sum\varepsilon_{ie}$) for solution-annealed material (Material D) cyclically deformed at a total strain range of ±0.6% and strain rate 0.025%/s with no dwell at 550°C and 640°C. Please note that Y-axis starts from 0.46.

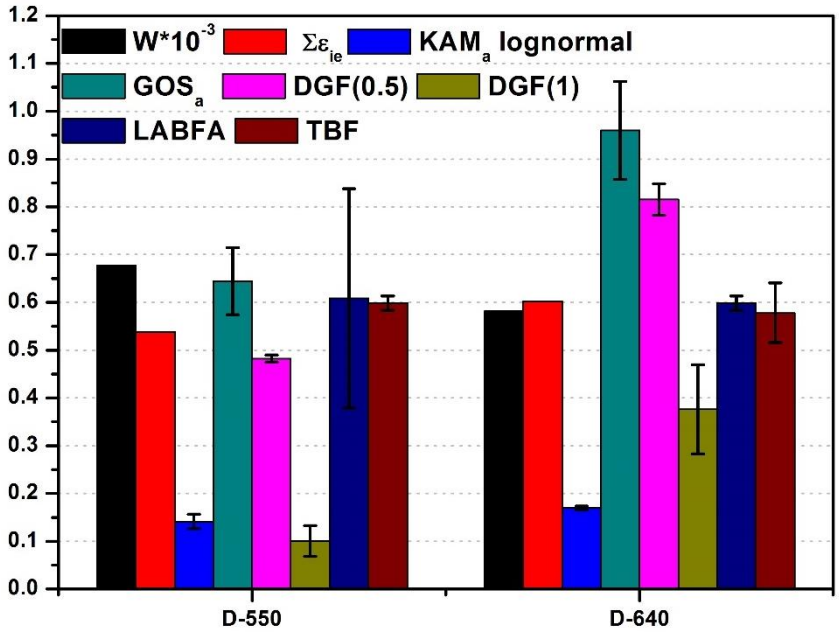

Figure 6.40 Cumulative inelastic strain energy density(W), cumulative tensile inelastic strain ($\sum\varepsilon_T$) and different EBSD metrics for solution-annealed material (Material D) cyclically deformed at a total strain range of ±0.6% and strain rate 0.025%/s with no dwell at 550°C and 640°C.

Figure 6.41 shows the final cycle stress-strain curves for ex-service material (Material C) and thermally-aged material (Material E) cyclically deformed at a total strain range of

±0.6% and strain rate 0.025%/s with no dwell at 550^{o}C. The peak stresses were higher in thermally aged material (E) than in ex-service material (Material C) for stabilised cycles. The peak stresses were higher for ex-service material for approximately the first 15 cycles (See Figure 6.42).

The cumulative inelastic strain energy was higher for thermally-aged material compared to ex-service material but the cumulative inelastic and cumulative compressive strains were lower for thermally-aged material (see Figure 6.43) than ex-service material. GOS_a, DGF(0.5), DGF(1) and $LABF_A$ were lower for thermally-aged material (see Figure 6.44) than ex-service material (Material C) but KAM_a lognormal and TBF was higher for thermally aged material. The combined effect of long thermal ageing and creep deformation on Material C during its service time would have had a significant effect on precipitation. As described in Chapter 4, the precipitates were larger in ex-service material than in the thermally-aged material. The nucleation and growth of intragranular precipitates in Material E might also have led to dislocations piling up around them, thereby increasing local misorientations.

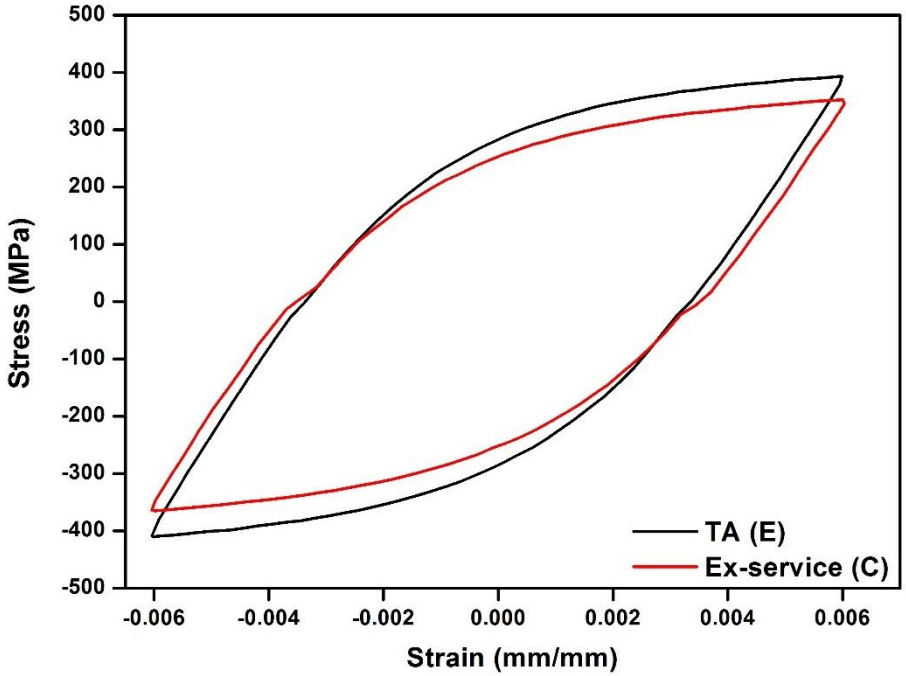

Figure 6.41 Final (150th) cycle stress-strain curve for ex-service material (material C) and thermally-aged material (Material E) cyclically deformed at a total strain range of ±0.6% and strain rate 0.025%/s with no dwell at 550^{o}C.

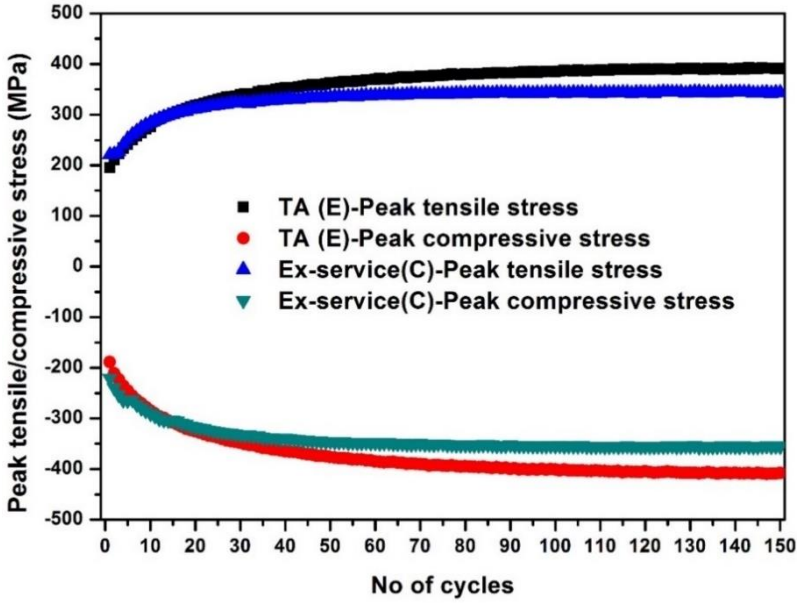

Figure 6.42 Peak tensile and compressive stresses for ex-service (Material C) and thermally-aged (Material E) materials cyclically deformed at a total strain range of ±0.6% and strain rate 0.025%/s with no dwell at 550^{o}C.

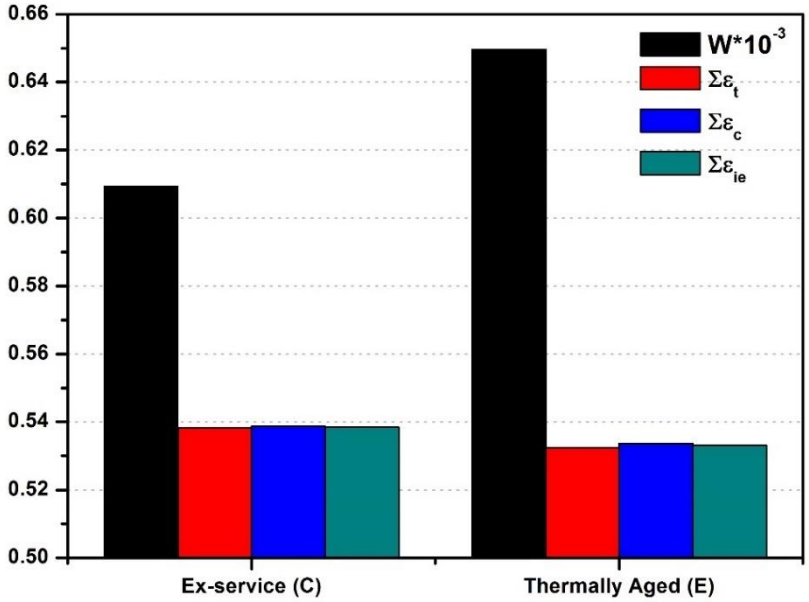

Figure 6.43 Cumulative inelastic strain energy density(W), cumulative tensile inelastic strain ($\sum\varepsilon_t$), cumulative compressive inelastic strain ($\sum\varepsilon_c$) and cumulative inelastic strain ($\sum\varepsilon_{ie}$) for ex-service (Material C) and thermally-aged (Material E) materials cyclically deformed at a total strain range of ±0.6% and strain rate 0.025%/s with no dwell at 550°C.

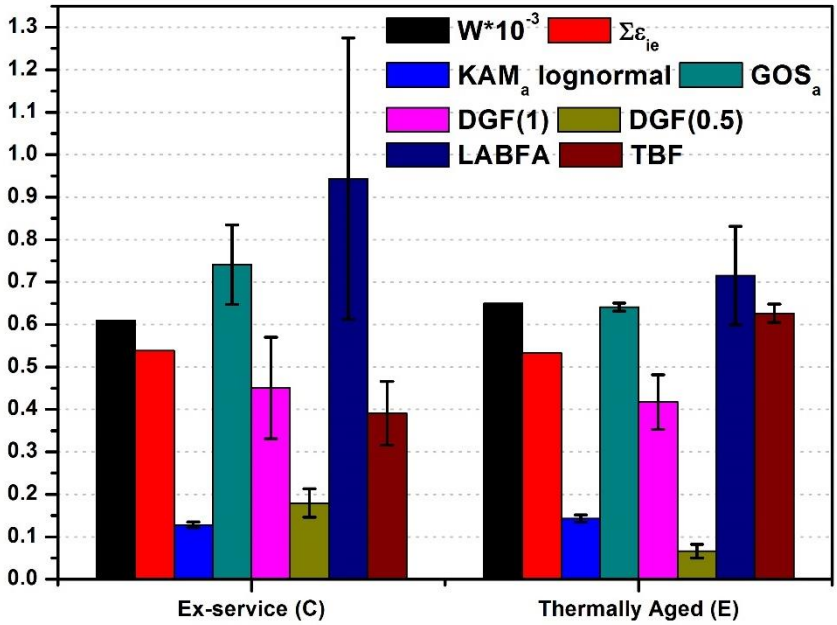

Figure 6.44 Cumulative inelastic strain energy density(W), cumulative tensile inelastic strain ($\sum\varepsilon_T$) and different EBSD metrics for ex-service (Material C) and thermally-aged (Material E) materials cyclically deformed at a total strain range of ±0.6% and strain rate 0.025%/s with no dwell at 550°C.

6.3.4. Discussion

Cyclic stress-strain response

The peak stresses were significantly higher for deformation at room temperature than at 550^{o}C (see Figure 6.29). The increased thermal activation at high temperatures facilitates the processes of dislocation climb over obstacles and of cross- slip. This reduces dislocation pile-ups at barriers and thus the back stresses generated along the slip planes. Thus, the flow stress needed to achieve a given cyclic deformation is lower at 550°C than at room temperature. The increased KAM at 550^{o}C relative to room temperature (see Figure 6.32) can be also attributed to increased thermal activation of dislocation motion at elevated temperature.

The effect of precipitation on misorientation development was studied at room temperature on ex-service (Material B) and solution-annealed materials (Material D) (see Figure *6.36*). The back stresses resulting from dislocations accumulating at precipitates on slip planes may have necessitated higher flow stresses in Material B than in Material D for similar levels of deformation. Grain boundary precipitates are reported to complicate the transfer of slip across grain boundaries and initiate complex slip earlier than clean grain boundaries in service aged 316H material [11]. The service-aged steel in this case exhibits more deformation (demonstrated by the low angle misorientations) along grain boundaries than the solution annealed steel (see Figure 6.45 and Figure 6.46). The KAM of thermally aged steel was found to be higher than ex-service material. This can be attributed to the intragranular precipitates after 1000hours of heat treatment, shown in Figure 4.11. The KAM was higher in some of the grains shown in Figure 6.46 (b).

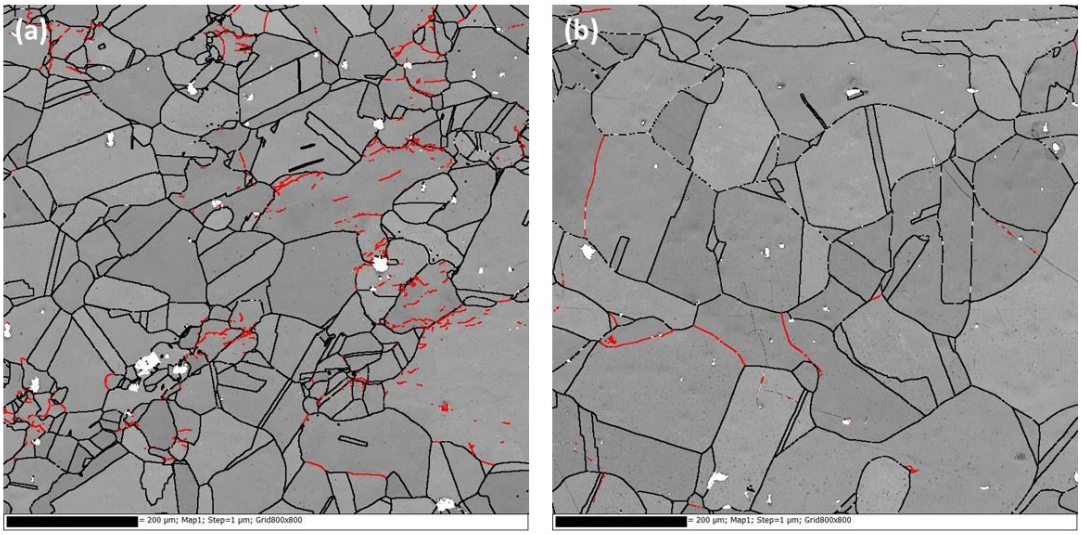

Figure 6.45 Image quality maps of Type 316H stainless steel deformed at a strain range of ±0.6% to 150 cycles at room temperature superimposed with 'low angle grain boundaries' showing dense deformation zones ('red patches') in close proximity to grain boundaries in (a) service-aged steel and (b) solution annealed steel. More deformation near the grain boundaries is evident ex-service material. The scale bar is 200µm.

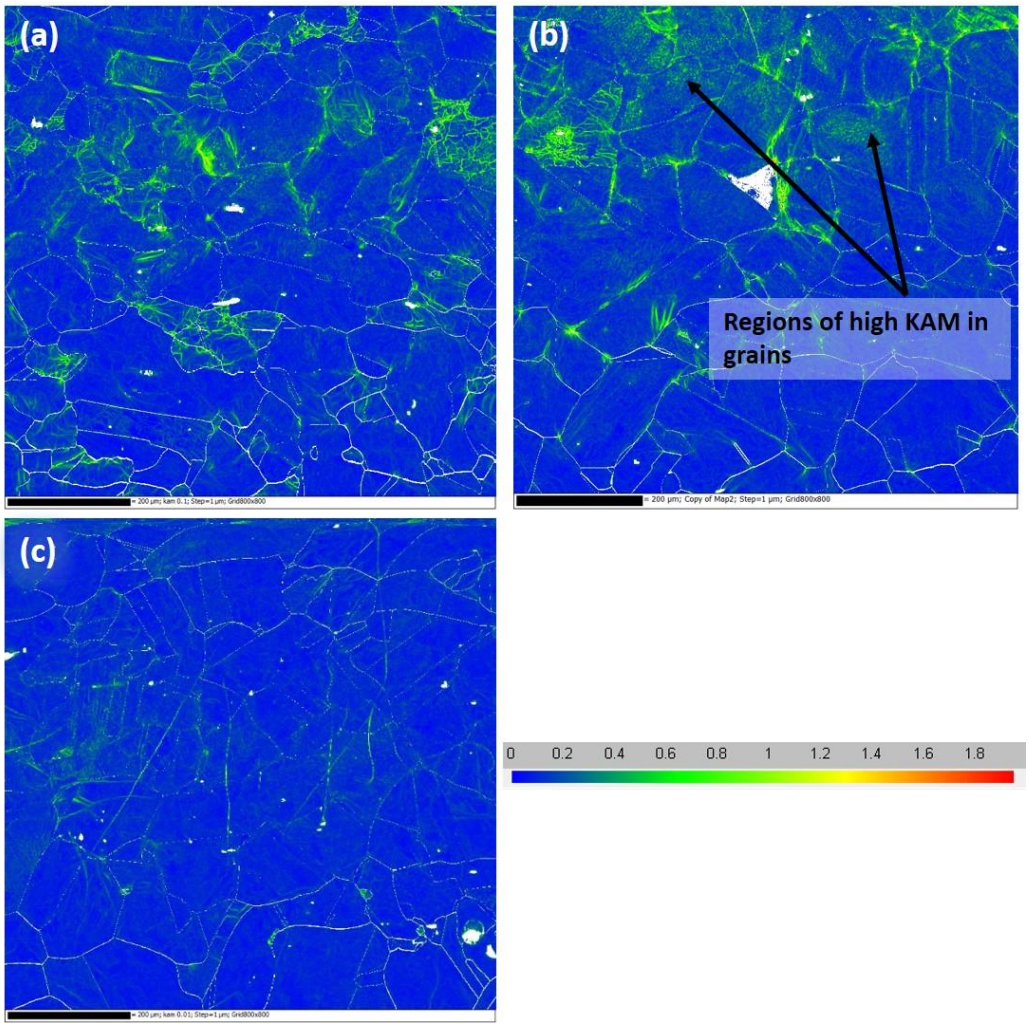

Figure 6.46 KAM maps of Type 316H stainless steel deformed at a strain range of ±0.6% to 150 cycles at 550°C. There is more deformation inside the grains in ex-service (Material C) (a) and thermally-aged (Material D) (b) materials than in solution annealed material (Material E) (c). The scale bar is 200µm.

Sensitivity of the cumulative inelastic strain energy density and cumulative inelastic strains to precipitation

Even though for material deformed under similar conditions of strain rate and temperature the cumulative strain energy density showed a good correlation with damage, as assessed in terms of the cumulative inelastic strains and the EBSD metrics (see section 6.2.4), this section shows the sensitivity of the cumulative inelastic strain energy to precipitation and temperature. The inelastic strain energy density (Δw) is widely used as a damage initiation parameter [63], [93], [96], [103]. Δw is reported to sharply reduce at failure of 316

material and Δw is found to increase when a hold time is introduced [96]. As mentioned in section 6.3.4.1, the increased thermal activation at higher temperature facilitates dislocation climb over obstacles and cross-slip which reduces the dislocation pileups at barriers in ex-service material, thereby reducing the back stress generated on slip planes. Hence the strain energy required to deform a material at 550^{o}C is lower than at room temperature. However, with increasing temperature, the material deforms more and hence the dislocation density also increases. This was evident in comparison of the EBSD metrics of ex-service material deformed at 550^{o}C or room temperature (see Figure 6.32). The cumulative strains also were higher at 550^{o}C (see Figure 6.31).

KAM is more concentrated at grain boundaries up to 150 cycles. Moturu et al [137] also reported similar results on 316L material deformed up to 12 cycles. This was attributed to planar slip mode deformation where activation of secondary slip is very difficult (due to low SFE). In the present study, the STEM images (see Figure 6.27) show clear dislocation cell structures which usually form due to cross slip. KAM accumulation at grain boundaries might be associated with dislocation pinning at grain boundaries especially at locations of intergranular precipitates.

After the same cyclic deformation, KAM_a lognormal, GOS, DGF(0.5) and DGF(1) was higher at 550^{o}C than at room temperature (see Figure 6.32). This can be related to the increased dislocation generation during higher temperature deformation. Since the dislocation density is higher we expect the TBF to be lower at 550^{o}C (see section 5.3.5) than at room temperature and this was found to be so (see Figure 6.32).

Nano-hardness was mapped on test specimen RTB±0.60%0.025H0 (see Table 6.3) over the same area where the EBSD measurements were made. The nano-hardness

measurement followed the procedures given in section 3.5. Two maps each of 400 indents in a square matrix (20x20micron spacing) were constructed and compared to misorientation maps.

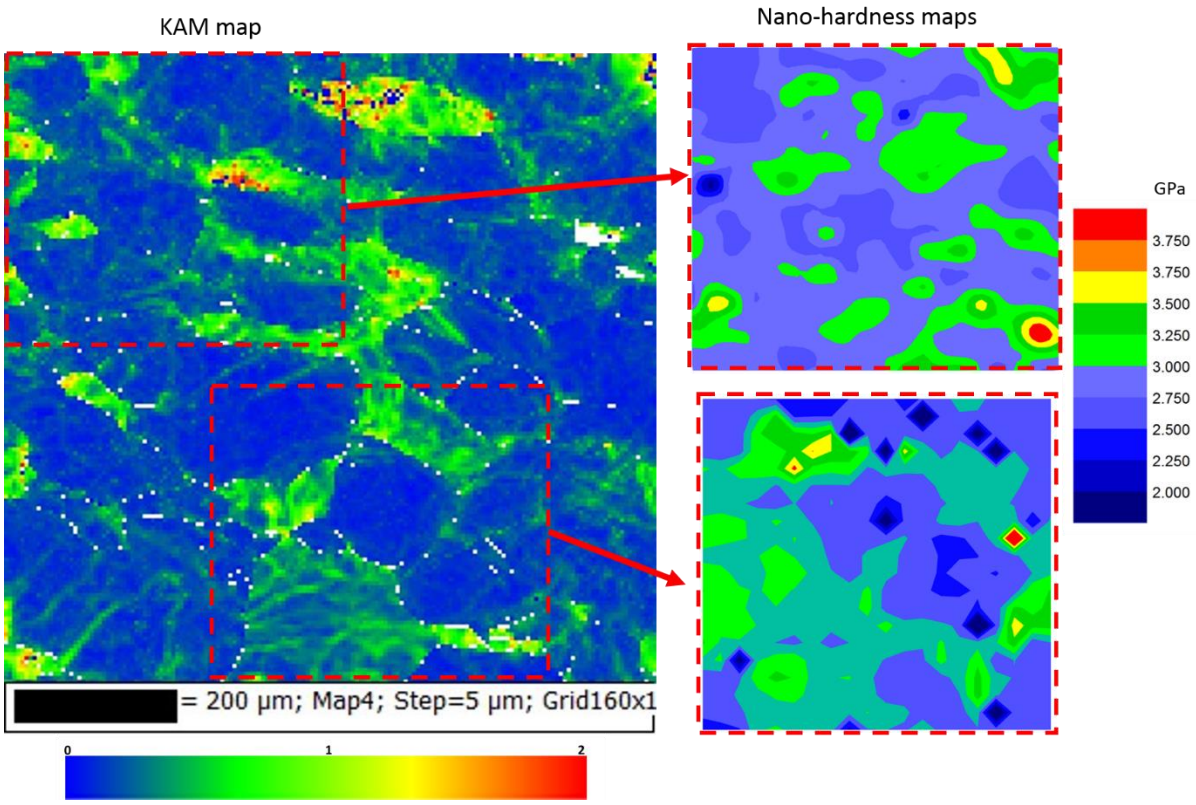

Figure 6.47 KAM maps and nano-hardness maps of ex-service material (Material B) cyclically deformed at a total strain range of ±0.6% and strain rate 0.025%/s with no dwell at room temperature.

Figure 6.47 shows the local misorientation map (KAM) of ex-service material (Material B) cyclically deformed at a total strain range of ±0.6% and strain rate 0.025%/s with no dwell at room temperature. As related in section 2.7.2, the hardness of a material is found to depend on the dislocation density. KAM maps are the misorientation maps that most closely represent the dislocation density of a material [11], [29] and here the KAM maps showed a good correlation with the nano-hardness maps. However no exact point to point correlation could be obtained between the misorientation and hardness maps. This could

be due to the different spatial resolutions of the two techniques, as disussed in section 5.3.5.

6.4. Summary

Over constant strain holds during cyclic deformation, type 316H austenitic stainless steel showed stress relaxation, which depended on the total strain range experienced. DGF(0.5) and DGF(1) were found to increase slightly with increasing dwell time. KAM, GOS and DGF were found to increase linearly with the cumulative inelastic strain energy and the cumulative inelastic strains. Dislocation tangles were observed after cyclic deformation over a lower strain range and a clear cellular dislocation structure was observed after higher strain range cycling, which is consistent with the available literature. KAM and DGF metrics were found to show a similar trend to the cumulative inelastic strains. i.e. material with higher cumulative strains had higher EBSD metrics and vice versa. The damage, as seen in terms of the EBSD metrics, induced by low cycle fatigue was found to be lower at room temperature than at elevated deformation temperatures. The cumulative inelastic strains and EBSD metrics (except TBF) were found to be lower in the absence of precipitates. The local misorientation and nano-hardness showed a good correlation.

CHAPTER 7

EFFECT OF CYCLIC STRAIN ACCUMULATION

7.1. Introduction

In power generating plant, structural components normally operating at elevated temperatures are subjected to varying stresses and strains due to cyclic thermal loading during start-up and shutdown. The cyclic thermal stresses arise when the free expansion/contraction of heated/cooled material within a component is totally or partially restricted by either external or internal constraints. In addition to these, steady state operation at elevated temperature introduces creep dwell loading that promotes creep-fatigue interactions in the components. Nuclear power plants have to be shut down, or the power production has to be significantly reduced, for routine maintenance and refuelling. They may in the future also have to work more flexibly, depending on the variation of energy demand in the power grid. Hence, the effect of load reversals (or of the number of cycles) on low cycle fatigue damage and creep-fatigue damage becomes extremely important. In this chapter, the effect of cumulative cyclic strain (or simply the number of load reversals) on creep-fatigue deformation is studied using EBSD misorientation maps. The dislocation structures were studied using STEM. Low cycle fatigue tests were conducted on ex-service 316H material for different numbers of cycles (150, 300 and 600). Creep-fatigue tests with 600s dwell were also conducted on ex-service material for 150 and 300 cycles. Low cycle fatigue tests were conducted on solution annealed and thermally aged material (Material E) for 150 and 300 cycles to investigate misorientation development in material where the precipitates were smaller and not yet stabilized. This chapter first introduces the experimental work carried out, followed by the stress-strain

and EBSD results. The chapter ends with a discussion of the results and a summary of the experiments' findings.

7.2. Ex-service material (Material C)

7.2.1. Mechanical tests

Strain controlled low cycle fatigue tests and creep fatigue tests were carried out on ex-service 316H material (Material C) under different cycles at 550°C to study the effect of cumulative strains on misorientation development. The details of the test conditions are given in Table 7.1.

Table 7.1 Cyclic test conditions for Type 316H stainless steel (Material C) to study the effect of cumulative cyclic strain. The key to the sample ID is given at the foot of the table.

Total strain range (%)	Dwell time (min)	No of cycles	Sample ID
±0.60	0	150	550C±0.60%0.025H0N150
±0.60	10	150	550C±0.60%0.025H10N150
±0.60	0	300	550C±0.60%0.025H0N300
±0.60	10	300	550C±0.60%0.025H10N300
±0.60	0	600	550C±0.60%0.025H0N600

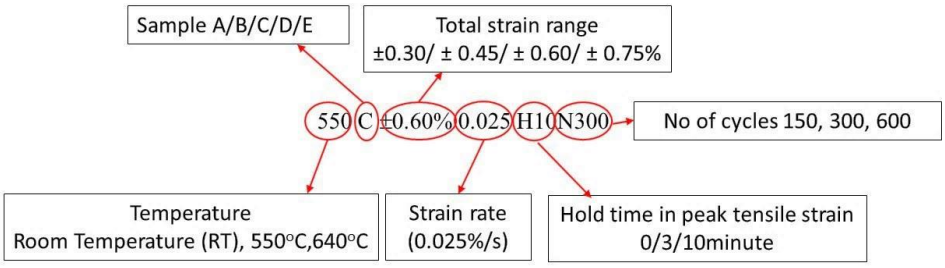

7.2.2. EBSD measurements

The EBSD measurements were carried out on deformed materials as described in Chapter 3. The misorientations developed were studied as a function of the cumulative inelastic strain using the different EBSD metrics described in Chapter 4. The misorientations were

assessed both at a local scale, using KAM and LABFA, and at longer range, using GOS_a, DGF(0.5), DGF(1) and TBF.

7.2.3. Results

The peak tensile and compressive stresses for each cycle of ex-service 316H material (material C) deformed to the different number of cycles given in Table 7.1 are shown in Figure 7.1 and Figure 7.2 respectively. The uniformity in flow behaviour was confirmed by the overlay in the peak stresses shown in Figure 7.1 and Figure 7.2. The slight difference in flow behaviour of 550C±0.60%0.025H0N300 from

550C±0.60%0.025H0N150 and 550C±0.60%0.025H0N300 might be due either to slight temperature variations during testing or to slight variations in the material properties of ex-service material.

The material showed cyclic softening after 150 cycles both in low cycle fatigue and creep-fatigue deformation. The softening was slightly more marked in creep-fatigue deformation than in low cycle fatigue. The calculated cumulative strain energies and strains are shown in Table 7.2 and Figure 7.3. There was little difference between $\sum\varepsilon_{ie}$, $\sum\varepsilon_t$, and $\sum\varepsilon_c$ for each condition.

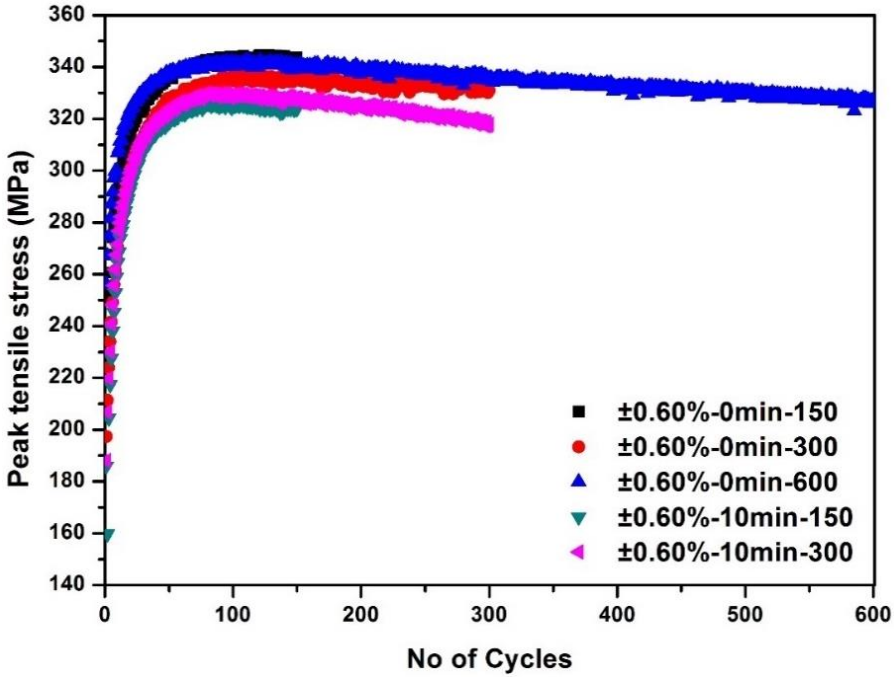

Figure 7.1 Peak tensile stress for ex-service 316H material (Material C) cyclically deformed at 550°C over a total strain range of ±0.6% and at a strain rate of 0.025%/s without dwell for 150, 300 and 600 cycles and with 10 minute dwells at the peak tensile strain for 150 and 300 cycles.

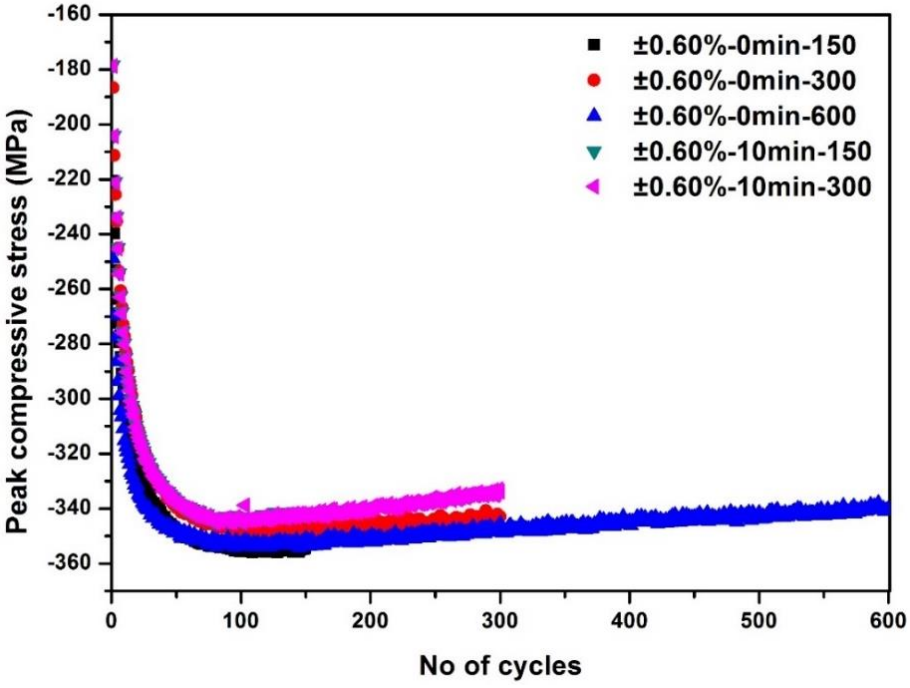

Figure 7.2 Peak compressive stress for ex-service 316H material (Material C) cyclically deformed at 550°C over a total strain range of ±0.6% and at a strain rate of 0.025%/s without dwell for 150, 300 and 600 cycles and with 10 minute dwelsl at peak tensile strain for 150 and 300 cycles.

Table 7.2 Cumulative strain energy density, cumulative tensile inelastic strain, cumulative compressive inelastic strain and cumulative inelastic strain of ex-service material (Material C described in Chapter 4) cyclically deformed at 550°C and a strain rate of 0.025%/s over a strain range of ±0.6% without dwell and with a dwell of 10min at the peak tensile strain to 150, 300 and 600 cycles.

Total strain range (%)	Dwell time (sec)	No of cycles	Cumulative strain energy density W	Cumulative tensile inelastic strain $\sum\varepsilon_t$	Cumulative compressive inelastic strain $\sum\varepsilon_c$	Cumulative inelastic strain $\sum\varepsilon_{ie}$
±0.60	0	150	609.40	0.54	0.54	0.54
±0.60	600	150	648.21	0.63	0.58	0.61
±0.60	0	300	1117.3	1.11	1.13	1.12
±0.60	600	300	1295.2	1.27	1.16	1.21
±0.60	0	600	2396.6	2.14	2.14	2.14

The variation of W, $\sum\varepsilon_{ie}$, $\sum\varepsilon_c$, and $\sum\varepsilon_t$ with number of cycle is shown in Figure 7.3. The EBSD metrics measured for samples cyclically deformed through different numbers of cycles are shown in Figure 7.4. KAM_a lognormal, GOS_a, DGF(0.5), DGF(1) and LAMFA were found to increase with increasing number of cycles and the TBF metric decreased with the number of cycles. The KAM distributions of the deformed samples after 150, 300 and 600 cycles are shown in Figure 7.5 (see Chapter 3 for lognormal fitting of KAM). It is evident from the KAM distributions that KAM values increase with the number of cycles. LABFA also increased with the number of cycles (see Figure 7.4) but the scatter in LABFA was very large. Plotting the EBSD metrics KAM_a lognormal, GOS_a, DGF(0.5), DGF(1) and TBF_a against the cumulative inelastic strains gave good linear fits

(see Figure 7.6-Figure 7.9). EBSD metrics also increased with W (Compare Figure 7.3 and Figure 7.4).

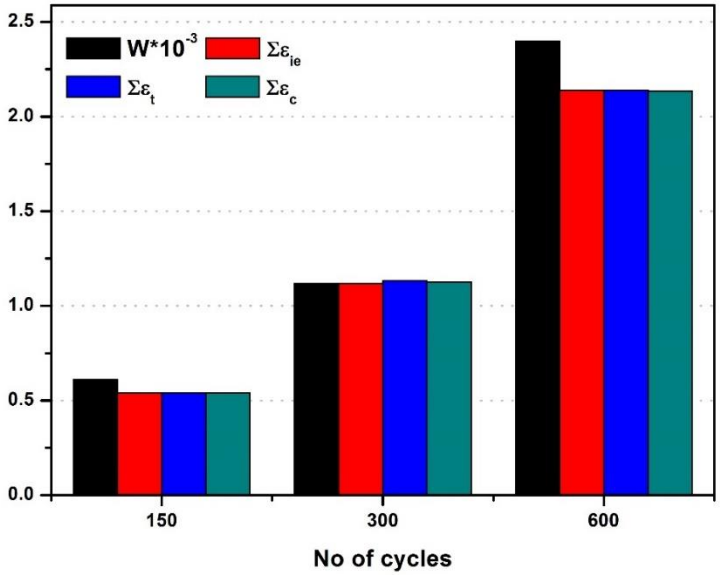

Figure 7.3 Cumulative inelastic strain energy density (W), cumulative inelastic strain($\sum\varepsilon_{ie}$), cumulative tensile inelastic strain ($\sum\varepsilon_t$), cumulative compressive inelastic strain($\sum\varepsilon_c$), for ex-service 316H material (Material C) cyclically deformed at a total strain range of ±0.6% and strain rate of 0.025%/s without dwell to 150, 300 and 600 cycles. W is multiplied by 10^{-3}.

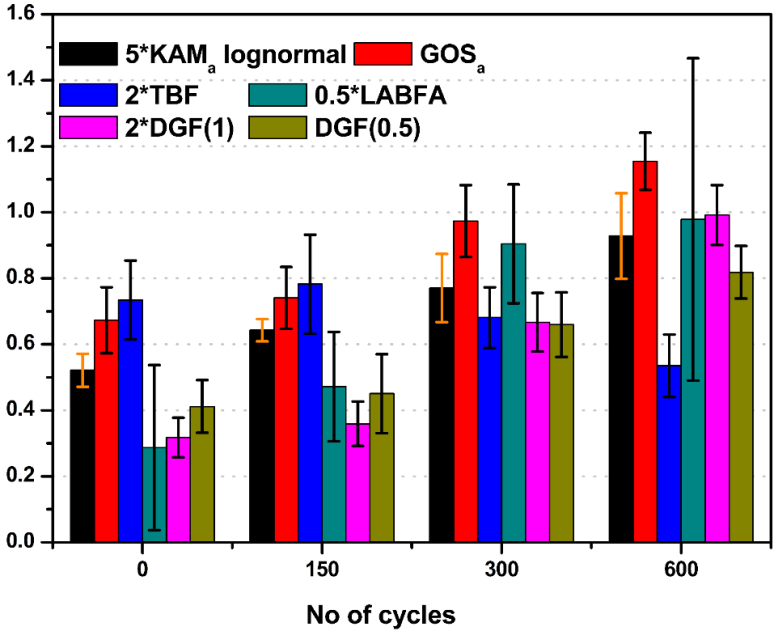

Figure 7.4 Different EBSD metrics for ex-service 316H material (Material C) cyclically deformed at a total strain range of ±0.6% and strain rate of 0.025%/s without dwell to

150, 300 and 600 cycles. KAM_a lognormal is multiplied by 5, TBF by 2, DGF(1) by 2 and LABFA by 2 to represent all EBSD metrics in same plot.

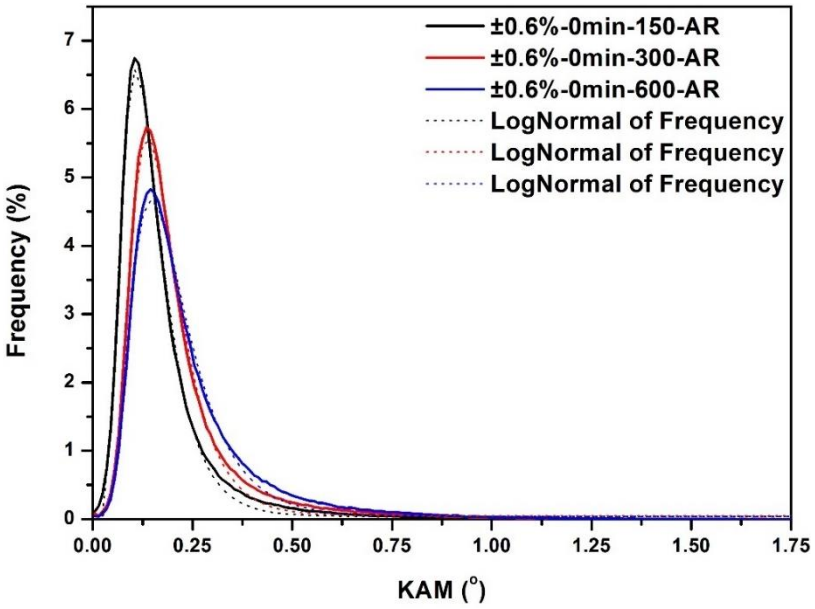

Figure 7.5 KAM distribution for ex-service 316H material (Material C) cyclically deformed at a total strain range of ±0.6% and strain rate of 0.025%/s without dwell to 150, 300 and 600 cycles.

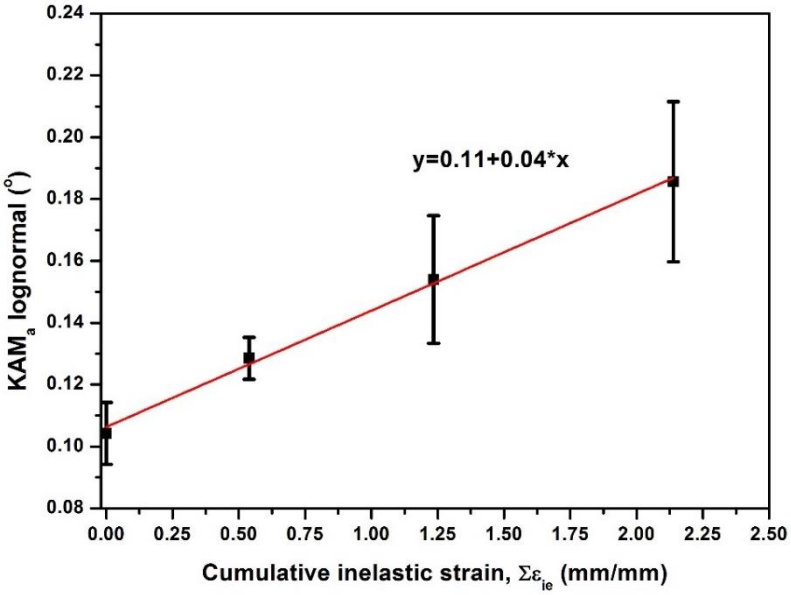

Figure 7.6 Cumulative inelastic strain vs KAM_a lognormal for ex-service 316H material (Material C) cyclically deformed at a total strain range of ±0.6% and strain rate of 0.025%/s without dwell to 150, 300 and 600 cycles.

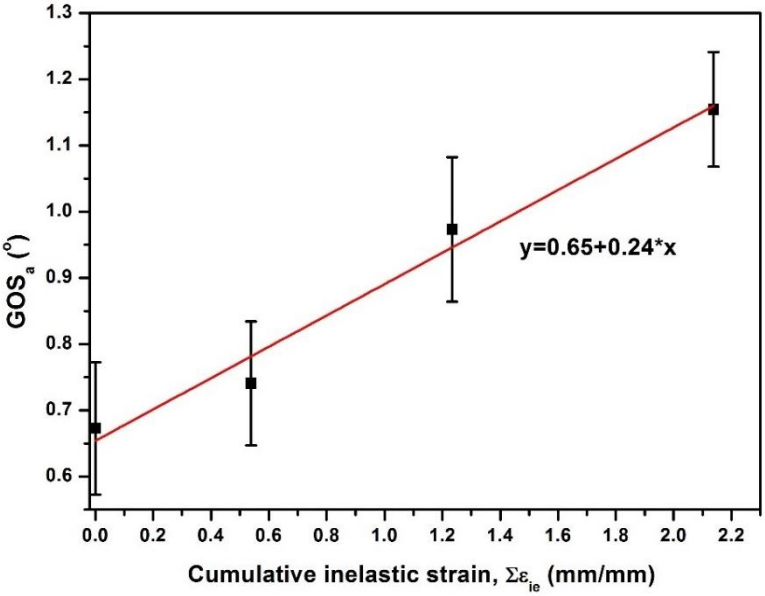

Figure 7.7 Cumulative inelastic strain vs GOS_a for ex-service 316H material (Material C) cyclically deformed at a total strain range of ±0.6% and strain rate of 0.025%/s without dwell to (as received ex-service material, material C), 150, 300 and 600 cycles.

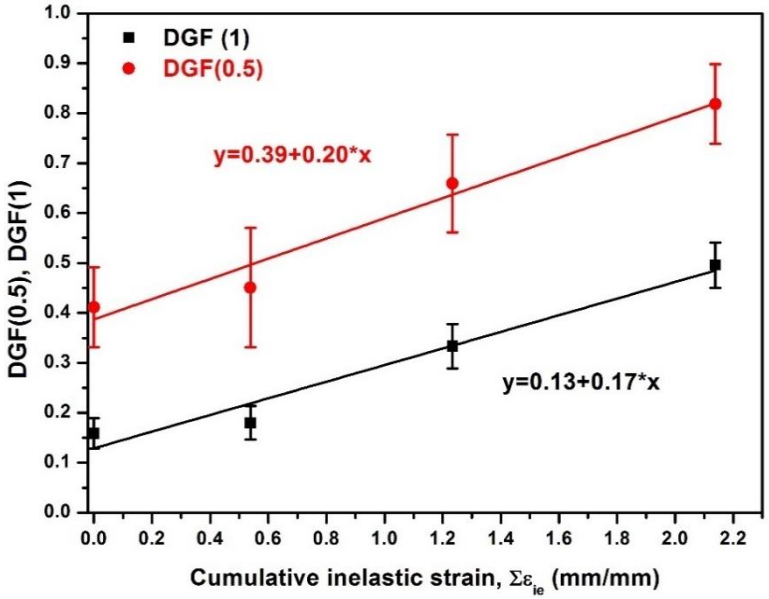

Figure 7.8 Cumulative inelastic strain vs DGF(0.5) and DGF(1) for ex-service 316H material (Material C) cyclically deformed at a total strain range of ±0.6% and strain rate of 0.025%/s without dwell to 0 (as received ex-service material, material C), 150, 300 and 600 cycles.

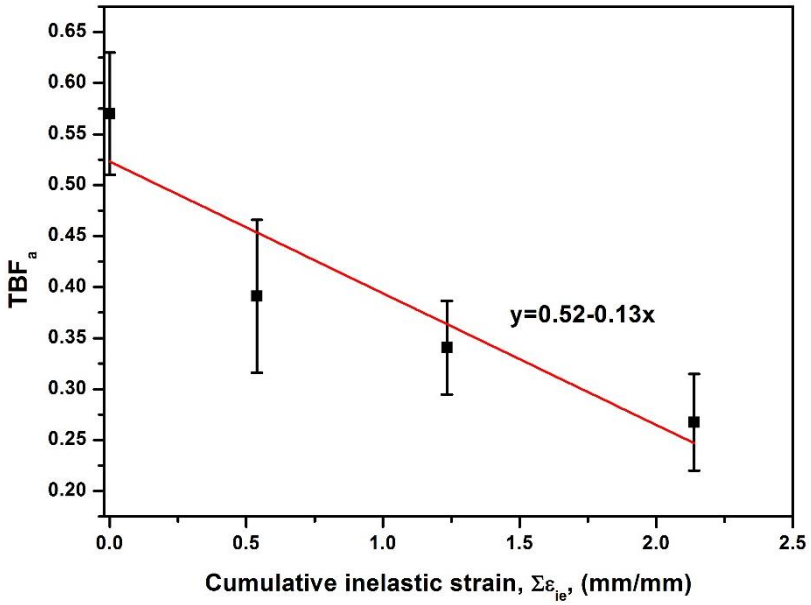

Figure 7.9 Cumulative inelastic strain vs TBF_a for ex-service 316H material (Material C) cyclically deformed at a total strain range of ±0.6% and strain rate of 0.025%/s without dwell to (as received ex-service material, material C), 150, 300 and 600 cycles.

The microstructures of low cycle fatigue deformed ex-service 316H material (Material C) as seen using HAADF-STEM are shown in Figure 7.10. Figure 7.10(a) shows a representative image of dislocations observed by STEM in ex-service 316H (Material C). A detailed study of dislocation structures in ex-service 316H material has already been given in Chapter 4. After 150 cycles, dislocation cell structures were predominantly observed in Material C. The dislocation cell walls were thick and dislocations were present in the cell interiors. The mean cell size (or cell width, *d*) was calculated as approximately 0.6±0.1μm (see Figure 7.10(b)). During the softening stage (after 300 cycles), a wall-channel structure or veins were observed with a width (*d*) of 0.27±0.07μm (see Figure 7.10(c)) along with diffuse dislocation cell structures (see Figure 7.11). After 600 cycles the width of veins were around 0.24±0.09μm (see Figure 7.10(d)). Diffuse cell structures were also observed after 600 cycles along with vein structures (see Figure 7.12).

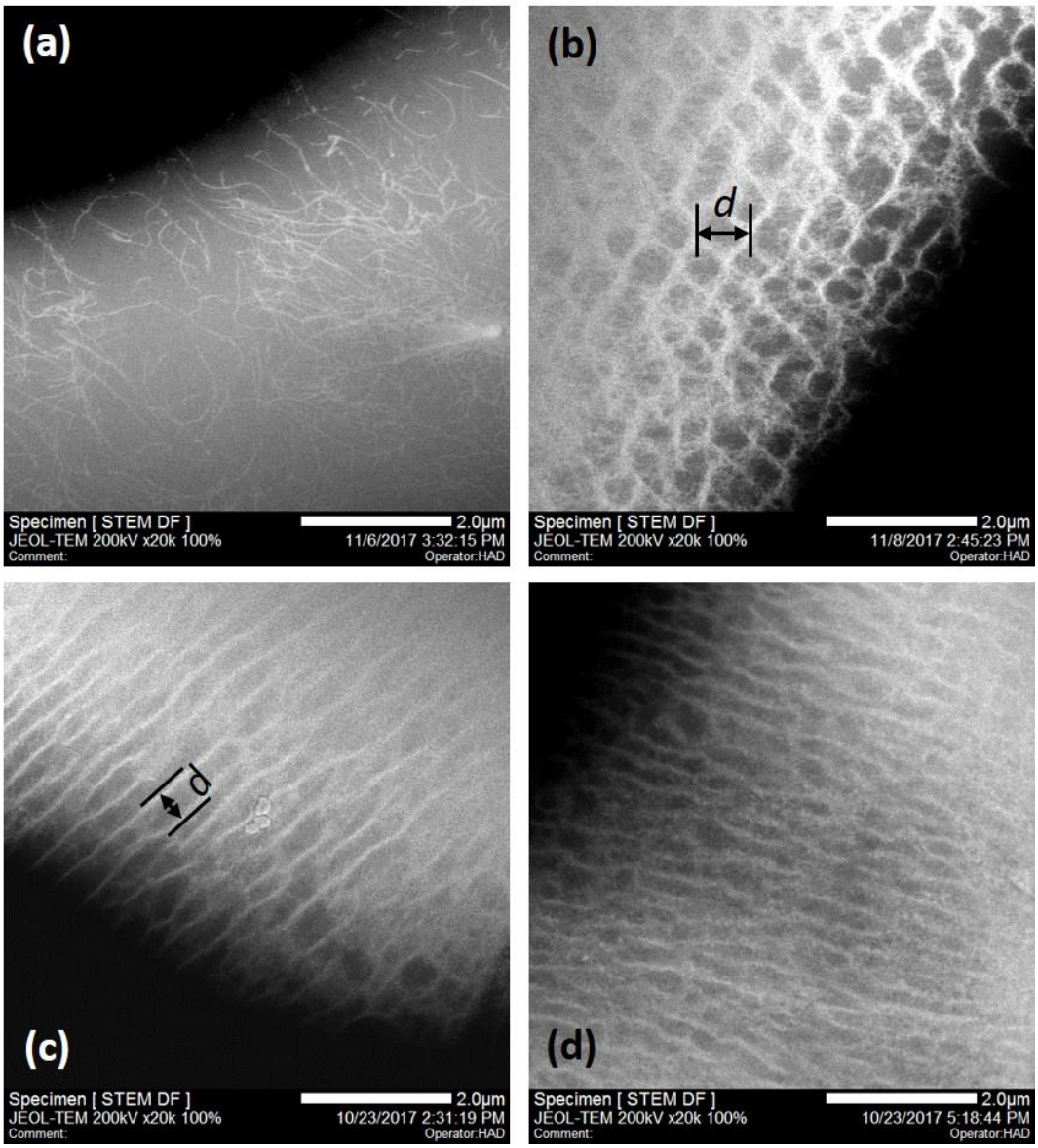

Figure 7.10 STEM-HAADF image of ex-service material (a) before cyclic deformation and after cyclic deformation at a total strain range of ±0.6% and strain rate of 0.025%/s without dwell to (b) 150, (c) 300 and (d) 600 cycles.

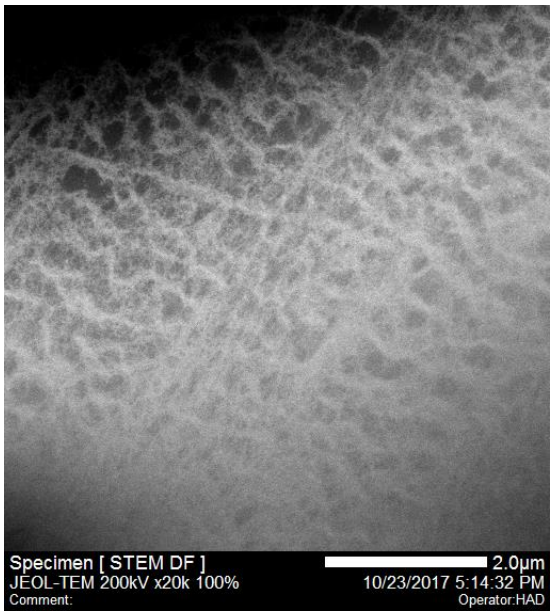

Figure 7.11 Diffuse dislocation cell structures observed in ex-service 316H material (Material C) after cyclic deformation at a total strain range of ±0.6% and strain rate of 0.025%/s without dwell to 300 cycles.

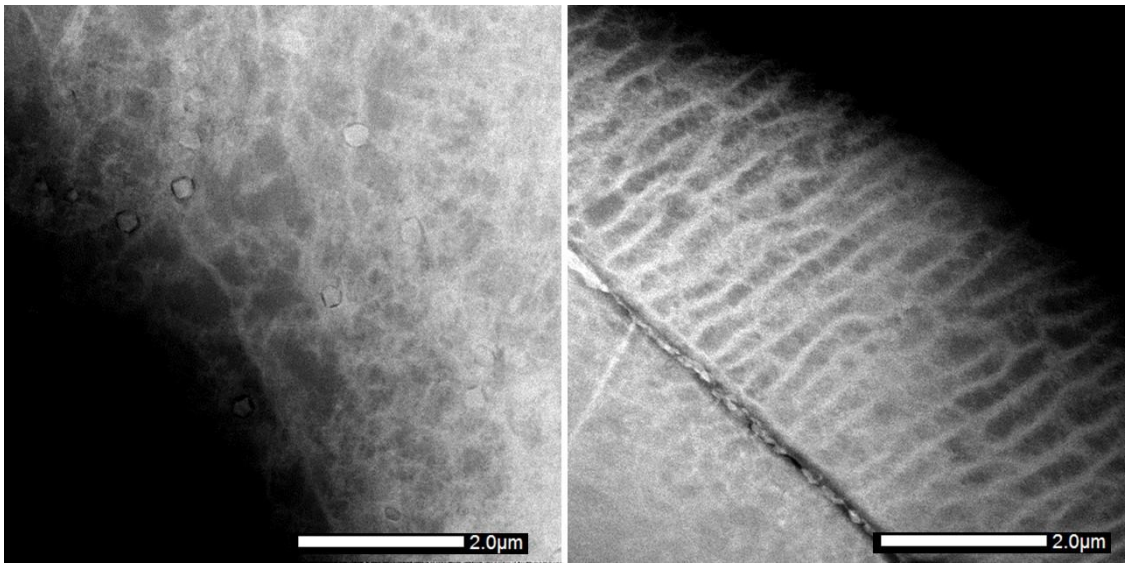

Figure 7.12 Diffuse dislocation cell structures (left) and elongated veins (right) observed in ex-service 316H material (Material C) after cyclic deformation at a total strain range of ±0.6% and strain rate of 0.025%/s without dwell to 600 cycles.

The cumulative strain energy densities and inelastic strains of low cycle fatigue and creep-fatigue samples deformed to 150 and 300 cycles are shown in Table 7.2 and Figure 7.13. There was a slight increase in strain energy density and inelastic strains for creep-fatigue samples compared to low cycle fatigue samples. The effect of dwell on the EBSD metrics

has been studied already in Chapter 6 (see Figure 6.11) for deformation up to 150 cycles. The same trend in the EBSD metrics was observed after 300 cycles, where KAM_a lognormal, DGF(0.5) and DGF(1) increased with 600 second (10min) dwell (see Figure 7.14).

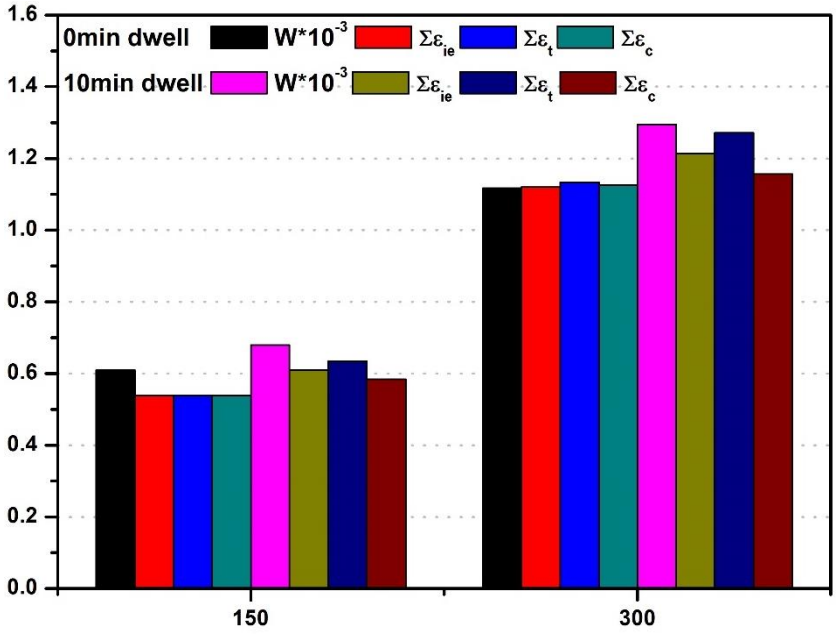

Figure 7.13 Cumulative inelastic strain energy density (W), cumulative inelastic strain ($\sum\varepsilon_{ie}$), cumulative tensile inelastic strain ($\sum\varepsilon_T$), cumulative compressive inelastic strain ($\sum\varepsilon_c$), for ex-service 316H (Material C) cyclically deformed at a total strain range of ±0.6% and strain rate of 0.025%/s without dwell and after 10 minute dwell at peak tensile strain to 150 and 300 cycles. W is multiplied by 10^{-3}.

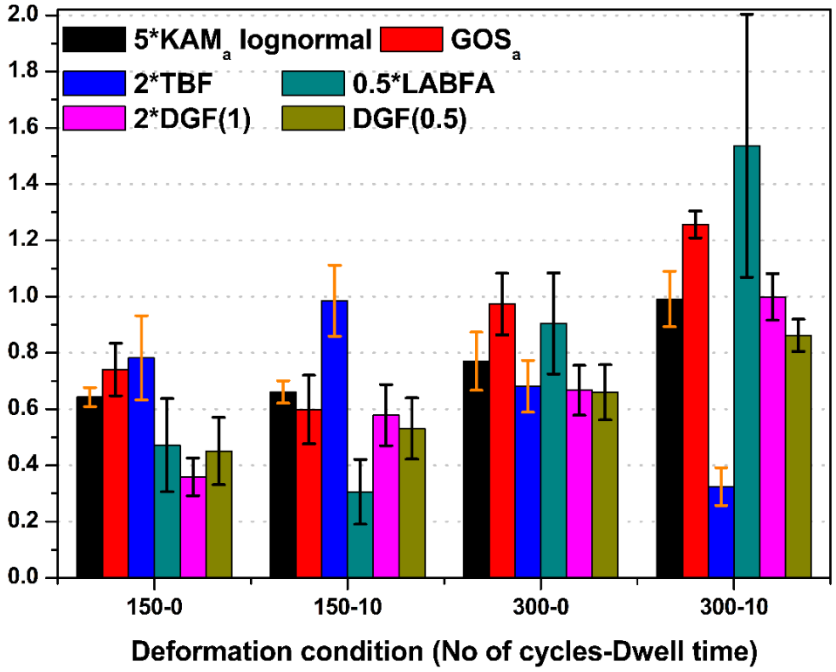

Figure 7.14 Different EBSD metrics for ex-service 316H (Material C) cyclically deformed at a total strain range of ±0.6% and strain rate of 0.025%/s without dwell and after 10 minute dwell at peak tensile strain to 150 and 300 cycles. KAM_a lognormal is multiplied by 5, TBF by 2, DGF(1) by 2 and LABFA by 2 to represent all EBSD metrics in same plot.

The HAADF-STEM microstructure of ex-service material (Material C), creep-fatigue deformed to 150 and 300 cycles with 600s dwells at the peak tensile strain, is shown in Figure 7.15. Like low cycle fatigue deformed samples (550C±0.60%0.025H0N150, see Figure 7.10(b)), diffuse dislocation cell structures were predominant after 150 cycles. The width of cell was around 0.6±0.1µm (see Figure 7.15(a)). Dislocation veins were dominant structures after 300 cycles with a vein spacing of approximately 0.32±0.07µm (see Figure 7.15(b)). Figure 7.16 shows mean hardness values of all the deformed conditions (see Table 7.1). Though hardness did not clearly pick up the inelastic strain accumulation due to dwell, its arguable that there is a slight increase in the hardness values with an increasing number of cycles.

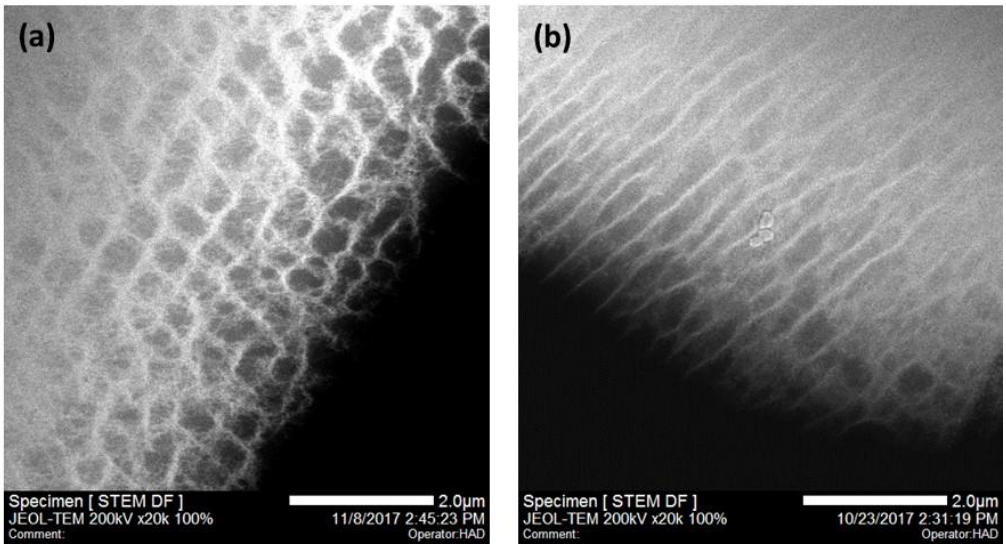

Figure 7.15 STEM-HAADF image of ex-service 316H (Material C) cyclically deformed at a total strain range of ±0.6% and strain rate of 0.025%/s with 10 minute dwells at peak tensile strain to (a) 150 and (b) 300 cycles.

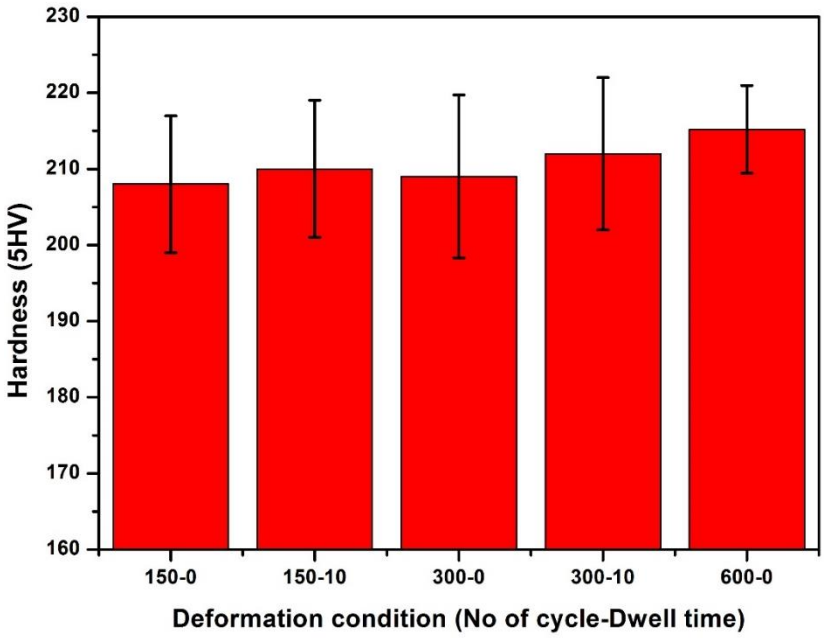

Figure 7.16 Mean hardness values fo——r ex-service material (Material C) cyclically deformed at a total strain range of ±0.6% and strain rate 0.025%/s with no dwell, and 10 minute dwell at peak tensile strain to 150, 300 and 600 cycles.

7.3. Solution annealed and thermally aged material (Material E)

7.3.1. Mechanical tests

Strain-controlled low cycle fatigue tests were carried out on Material E (which is ex-service Material C, solution annealed at 1050^{o}C for 1 hour followed by thermal aging at 550^{o}C for 1000 hours) to study the effect of cumulative cyclic strain on a material with smaller and less stable precipitates than ex-service material. All the tests were conducted for a strain range of ±0.6%, at a strain rate of 0.025%/s and at 550^{o}C. The tests were conducted up to 150 (550E±0.60%0.025H0N150) and 300 (550E±0.60%0.025H0N300) cycles.

7.3.2. EBSD measurements

EBSD measurements followed the same procedures described in section 7.2.2.

7.3.3. Results

The peak tensile and compressive stresses were found to be higher in Material E (see Figure 7.17 and Figure 7.18) than in Material C (Figure 7.1 and Figure 7.2), as reported in Chapter 6. Again, the overlay of the peak stresses for different cycles shows the uniformity in flow. Slight differences in the peak stresses can be attributed to a small temperature difference in the testing conditions. Temperature differences can arise either due to temperature variations in the testing laboratory during day and night in winter and also due to the effect of cooling of the upper cross head to protect the load cell (see Figure 3.1). The peak stresses were found to increase (strain hardening) up to around 120 cycles followed by saturation up to 300 cycles. The strain hardening up to 120 cycles can be attributed to the precipitate-dislocation interaction and dislocation multiplication. In this material there might also be additional precipitates nucleating at dislocations during

deformation which would not occur in ex-service material, as the distribution of precipitates would have stabilised during exposure to service conditions. The cumulative strain energy density and inelastic strains are shown in Table 7.3 and Figure 7.19.There were only minor variations in $\sum\varepsilon_{ie}$, $\sum\varepsilon_t$ and $\sum\varepsilon_c$.

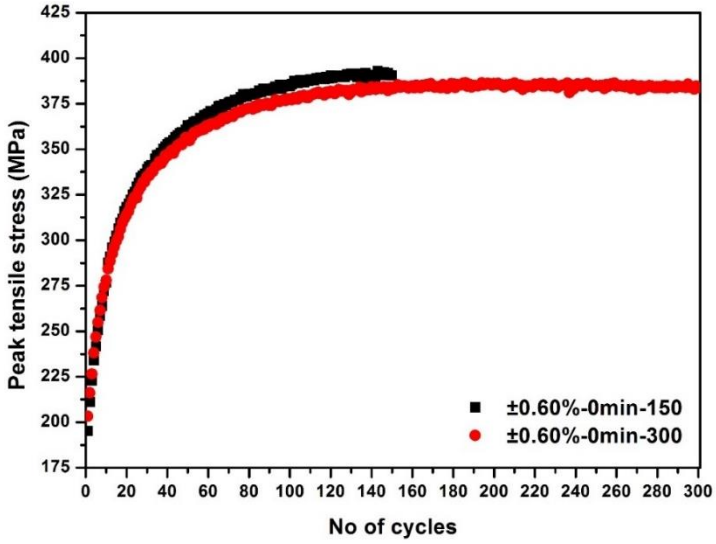

Figure 7.17 Peak tensile stress for thermally aged 316H (Material E) cyclically deformed at a total strain range of ±0.6% and strain rate of 0.025%/s without dwell to 150 and 300 cycles.

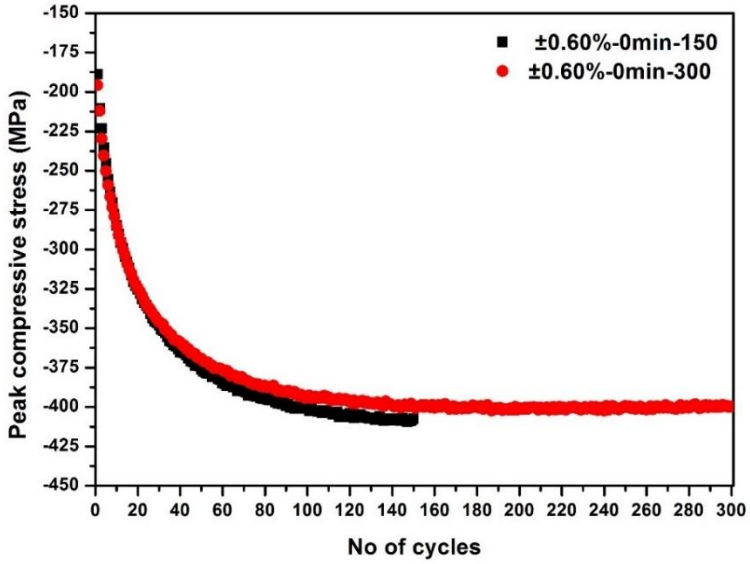

Figure 7.18 Peak compressive stress for thermally aged 316H (Material E) cyclically deformed at a total strain range of ±0.6% and strain rate of 0.025%/s without dwell to 150 and 300 cycles.

Table 7.3 Cumulative strain energy density, cumulative inelastic strain, cumulative tensile inelastic strain and cumulative compressive inelastic strain of thermally aged 316H (Material E mentioned in Chapter 4) cyclically deformed at 550°C and a strain rate of 0.025%/s at a strain range of ±0.6% without dwell to 150 and 300 cycles.

Total strain range (%)	Dwell time (min)	No of cycles	Cumulative strain energy density W	Cumulative inelastic strain $\sum\varepsilon_{ie}$	Cumulative tensile inelastic strain $\sum\varepsilon_t$	Cumulative compressive inelastic strain $\sum\varepsilon_c$
±0.60	0	150	649.5541	0.5331	0.5325	0.5337
±0.60	0	300	1248.2	1.0134	1.0067	1.0201

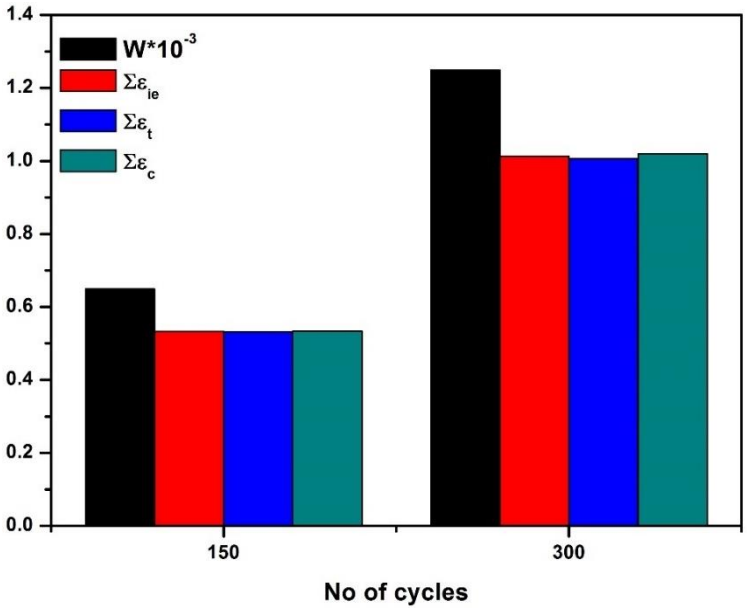

Figure 7.19 Cumulative inelastic strain energy density (W), cumulative inelastic strain($\sum\varepsilon_{ie}$), cumulative tensile inelastic strain ($\sum\varepsilon_t$), cumulative compressive inelastic strain($\sum\varepsilon_c$), for thermally aged 316H (Material E) cyclically deformed at a total strain range of ±0.6% and strain rate of 0.025%/s without dwell to 150 and 300 cycles. W is multiplied by 10^{-3}.

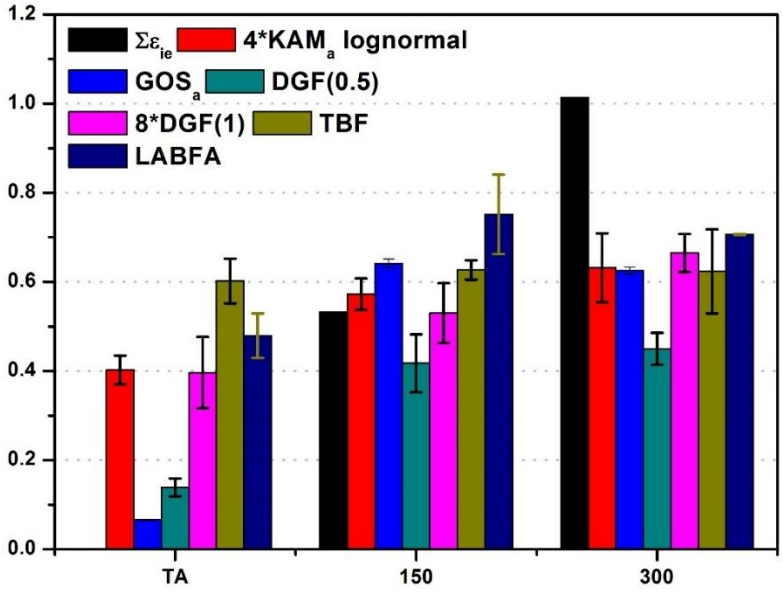

Figure 7.20 Cumulative inelastic strain ($\sum \varepsilon_{ie}$) and different EBSD metrics for thermally aged 316H (Material E) cyclically deformed at a total strain range of ±0.6% and strain rate of 0.025%/s without dwell to 150 and 300 cycles. KAM_a lognormal is multiplied by 4 and DGF(1) by 8 to represent all EBSD metrics in same plot.

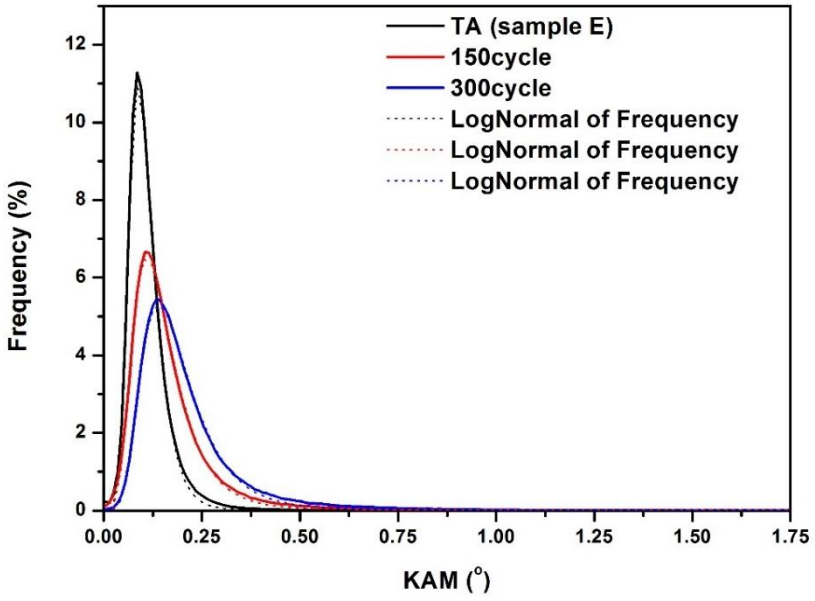

Figure 7.21 KAM distribution for thermally aged (TA) 316H (Material E) cyclically deformed at a total strain range of ±0.6% and strain rate of 0.025%/s without dwell to 150 and 300 cycles.

Figure 7.20 shows the variation in the cumulative inelastic strain and different EBSD metrics with the number of cycles for thermally aged material (Material E). KAM_a lognormal, DGF(0.5) and DGF(1) increased with the number of cycles. There was a

slight reduction in TBF with the number of cycles. Although GOS_a and LABFA increased after deformation to 150 cycles, there was then a slight reduction in these metrics measured up to 300 cycles. This can be attributed to the heterogeneous distribution of precipitates in the thermally aged material, as explained in Chapter 4. The higher precipitation in some grains would result in higher GOS_a and LABFA values, due to dislocation pile-up at precipitates. The higher scatter in KAM_a lognormal values at 300 cycles can be also associated with this. However, looking at the KAM frequency distribution of the deformed material E (see Figure 7.21), its evident that, as for Material C (see Figure 7.5), there is a general trend of KAM increasing with the number of cycles. Also, the decreasing cell size/vein width (from STEM image) can be related to the increasing dislocation density and misorientation and they all seems to be consistent.

7.4. Discussion

7.4.1. Cumulative inelastic strains and EBSD metrics

The quantification of the accumulated fatigue and creep-fatigue damage is a subject that has been explored for many decades now. This chapter has investigated the degree of correlation between the cumulative inelastic strains and different EBSD metrics. An overall increasing trend has been observed in the EBSD metrics KAM_a lognormal, GOS_a and DGF with cumulative strains. In contrast the TBF, which is the only metric concerned with intergranular misorientations rather than intragranular ones, reduces with cumulative inelastic strains (see Figure 7.9 and Figure 7.20), as has already been explained in Chapter 5 (section 5.2.5. Discussion), due to accumulation of dislocations at twin boundaries.

The lognormal mean of the local misorientation, measured by KAM_a, increased with cumulative inelastic strain for both service aged (see Figure 7.6) and thermally aged (see Figure 7.20) materials. This shows that there is a net increase in GND density with the

number of cycles. As in uniaxial creep deformation [11], in cyclic deformation the inelastic strains have a significant effect in developing misorientations < 2°. Fujiyama et al [140] reported a more extensive change in KAM with time fraction to failure[3] in creep-fatigue deformation (strain range of ±0.5% at 650°C) of 304 austenitic steel than in uniaxial creep deformation[4]. The comparison shown in Figure 7.22, of the KAM_a lognormal data from this study with that from uniaxial creep tests on other ex-service material from the same component [11] shows KAM_a lognormal to be much lower in creep-fatigue deformation up to 600 cycles. The Youngs modulus of material studied by Githinji et al [11] was 158 GPa whereas the Youngs modulus of the material (Material C) used in this study was around 142 GPa. Also, the grain size by MLI method in Githinji et al [11] material was around 98μm and the grain size of Material C was around 76μm. But Githinji et al [11] used parallel lines to calculate grain size whereas grain size in ASTM standards suggest random lines. The measured KAM_a lognormal before uniaxial creep deformation of ex-service material used by Githinji et al [11] was around 0.3° whereas the KAM_a lognormal of service aged material measured before cyclic deformation was around 0.1° (the difference between EBSD measurement and analysis in this thesis with Githinji et al is given in foot note 1, page 156). But all these differences in EBSD measurement settings, data analysis and material property were far too small to explain the difference in KAM slopes. This clearly shows that even though KAM_a lognormal increases with the number of cycles, at high temperatures, the KAM_a

[3] Failure being defined as 25% reduction in the peak tensile stress after saturation
[4] The time fraction to failure in uniaxial creep deformation was calculated as the fraction of time to reach given creep strain to total time to failure and time fraction in cyclic deformation was calculated as total number of cycles to number of cycle to failure

lognormal developed for an equivalent cumulative strain is much lower in cyclic deformation than in uniaxial deformation.

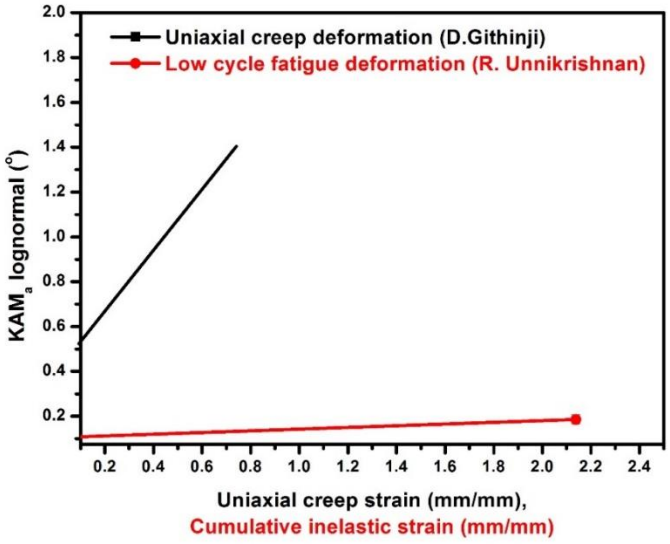

Figure 7.22 Variations of KAM$_a$ lognormal (a) in cyclic deformation (Figure 7.6) with cumulative inelastic strain and (b) in creep deformation with uniaxial creep strain [11] *for service-aged Type 316H stainless steel at 550°C.*

Cavity growth at the grain boundaries during high temperature deformation can be attributed to vacancy diffusion [217] and stress relaxation (see Chapter 5). Cavities might be formed by the condensation of the vacancies produced during cyclic loading. For example, cavities can be produced by the motion of dislocation jogs or by the annihilation of close edge dislocation dipoles. The same processes occur during monotonic loading as well, but to a smaller extent since the cumulative strain is much smaller in uniaxial deformation [218]. Creep-fatigue studies on the fine grained heat affected zone of high chromium heat resistant steel found higher values of KAM around creep voids, which was attributed to inelastic strain accumulation at voids [152]. KAM values higher than 0.5^o were also reported in the grain interiors close to triple junctions, after fatigue tests on Fe-3Si steel [145]. Similar results were found in this study with KAM values greater than 1.2^o at the grain boundaries especially at the triple junctions (see Figure 7.23). This is direct evidence of intergranular damage. The KAM concentration at triple junctions

suggests that grain boundary sliding might be a significant contributor to deformation in low cycle fatigue loading of 316H steel. The process of grain boundary sliding can be explained as movement of dislocations along the grain boundaries, which could lead to lattice mismatch at those boundaries. Grain boundary sliding can also lead to stress concentration at triple points [219]. This stress might ultimately be relieved by cavity nucleation at the grain junctions and boundaries.

Higher levels of KAM were also found in the interiors of some grains after 300 (see Figure 7.24) and 600 cycles (see Figure 7.23). This can be attributed to activation of secondary slip (including cross slip) increasing the dislocation density in some grain interiors.

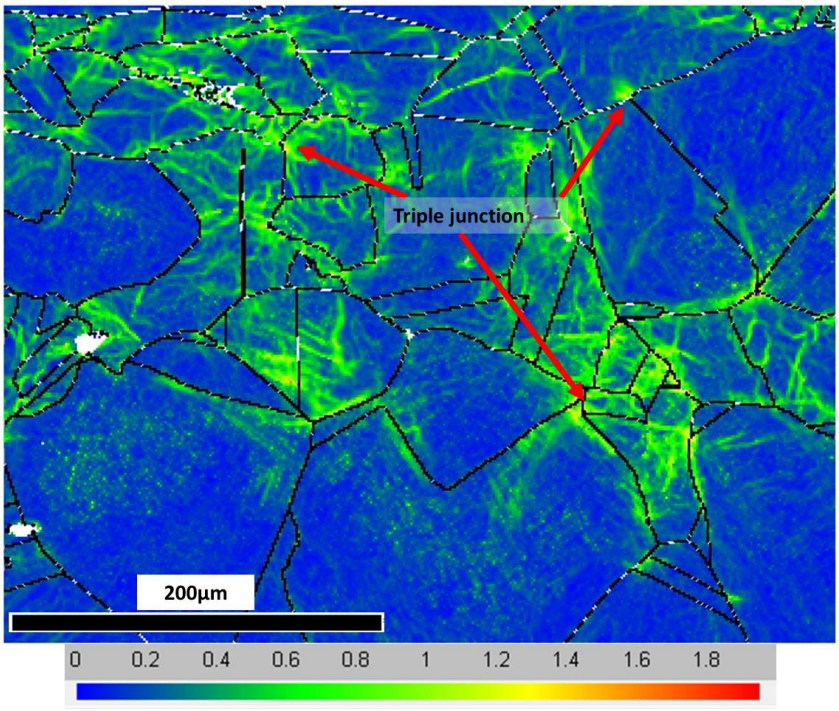

Figure 7.23 Ex-service 316 H fatigue deformed to 600 cycles: KAM map super imposed with high angle (>15^o) grain boundaries. KAM scale follows a rainbow, where blue indicates the lowest and red the highest (2^o) KAM value. The highest KAM values are evident at triple junctions.

From the KAM maps (e.g. see Figure 7.24(a)), it is evident that there is a wide variation in the local misorientations of different grains in the gauge lengths of deformed specimens

and there are some grains with areas of low local misorientation even after a deformation up to 300 cycles. Even though a direct relation between KAM and Schmidt factor maps were not observed, most of the reddest areas in the Schmid factor map (Figure 7.24c) are those that are blue in the KAM map (Figure 7.24a), a direct relation between these two maps was not found. The misorientation maps did not show any show any obvious relationship with IPF maps (see Figure 7.24).

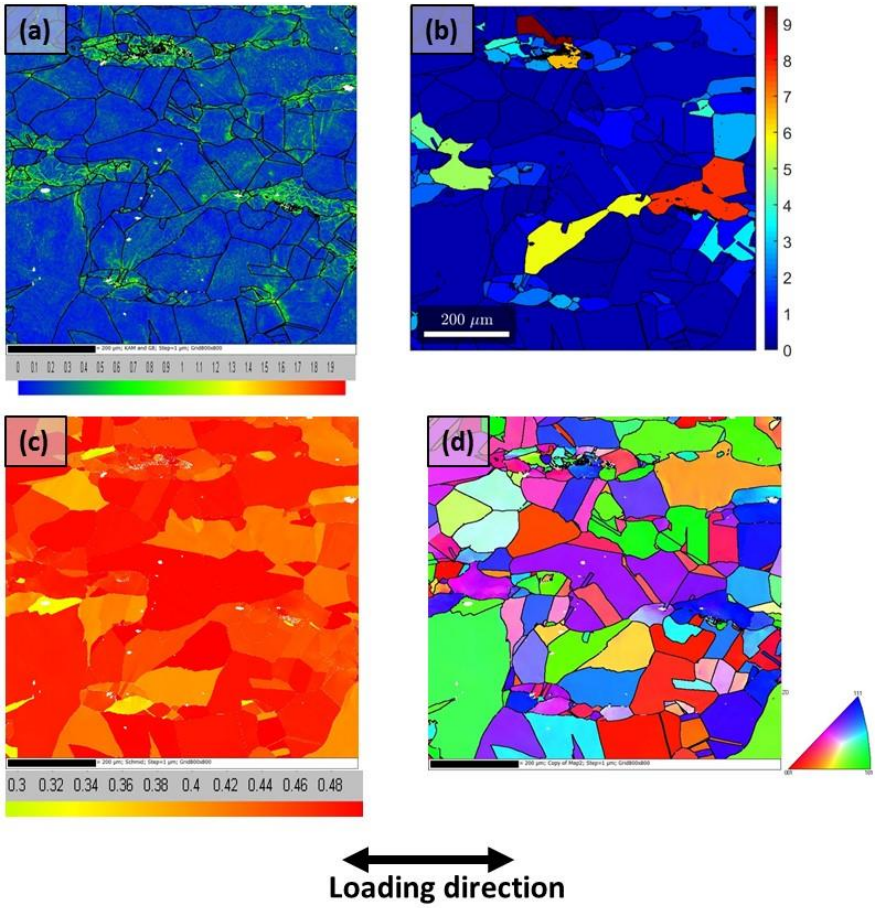

Figure 7.24 (a) Kernel average misorientation (KAM) map, (b) Grain orientation spread (GOS) map, (c) Schmidt factor maps and (d) IPF map of ex-service 316 H, fatigue deformed (Material C) to 300 cycles without dwell.

Although there was a clear increasing trend in GOS_a for Material C with cumulative cyclic strain (see Figure 7.7), the GOS_a of Material E deformed to 300 cycles was slightly lower than that deformed at 150 cycles (see Figure 7.20). Similar results were reported in

Chapter 6. GOS_a and local misorientation in terms of KAM can be subject to two major effects:

1) The orientation of the grain with respect to the loading direction which was not observed in this study. But studies by Nellesson et al [206] showed the orientation dependence of dislocation structures in 316 austenitic steels, which can affect KAM values. This needs further investigation.
2) The distribution of intergranular and intragranular precipitates which changes the local chemical composition, the local mechanical/creep properties and the extent of dislocation pinning at precipitates.

Since GOS and KAM are both influenced by local microstructural features, an EBSD metric considering a much larger scale is required to be representative of cumulative inelastic strain in the material. DGF which gives the fraction of grains above a particular GOS value is found to be the metric least sensitive to local microstructural features in this study. DGF has already been reported to be a good metric for measuring the global macroscopic strain after uniaxial creep deformation in ex-service 316H material [11]. GOS and DGF were also reported to be relatively insensitive to EBSD measurement set-up parameters, such as step size, as they are derived from spatially uncorrelated misorientations [11].

The decay in TBF with cumulative inelastic strain was found to be higher in service aged material (Material C, see Figure 7.9) than in thermally aged material (material E, see Figure 7.20). The higher density of precipitates in ex-service material would be expected to promote multiple slip in the austenite matrix, leading to complex deformation which might have more rapidly reduced TBF with strain [220]. Similar results were observed in uniaxial creep deformation of ex-service 316H austenitic stainless steel [11]. It has been

shown by Varin et al [221] that the twinning frequency in Type 316 stainless steel is virtually independent of the grain size in the range of 1.5μm to 100μm. The grain sizes of the steels used in this study (~70-90μm) lie within these limits, which would allow TBF's use as a measure of cumulative cyclic strains in 316H steel but no direct relationship was found in this study between the strain developed during stress relaxation and TBF.

The flow stress for the inelastic deformation of crystalline metals generally depends on the generation, motion, and interactions of dislocations. In single crystals, the self-organisation of dislocations, to lower their energy, leads to a patterning of high and low dislocation density regions throughout the material, often as cell structures of few micros size [222]. In polycrystalline materials, interactions between grains arise from the need to satisfy both equilibrium and compatibility conditions of stress and strain during deformation, despite abrupt changes in the slip system orientations at grain boundaries [222]. Wang et al [223] studied experimentally the effect of boundary conditions (constant load, constant strain) on the creep behaviour of Type 316H austenitic stainless steel. This study showed maximum relaxation of lattice strains in {200} planes during constant strain dwell; {111} planes relaxed the least. In order to satisfy strain compatibility conditions, the relaxation of elastic strains in {200} planes might be accommodated either by plastic deformation of grains with <200> along the loading direction or by plastic deformation of grains around <200>//loading direction grains which needs further investigation.

7.4.2. Evolution of the dislocation structures

The evolution of dislocation structures is often explained as a result of interactions between a huge number of dislocations [224]. In polycrystalline materials, the dislocation structures are generally organized heterogeneously due to the different crystallographic

orientation of individual grains. The different orientations result in different activations of slip systems, and significantly different amounts of shear slip may be accumulated [224]. Apart from the orientation, the precipitate density in grains might also affect the evolution of dislocation structures.

The representative dislocation structures of ex-service material cyclically deformed to different cycles is shown in Figure 7.10. It is evident from peak stress plots that material started softening at 300 and 600 cycles (Figure 7.1 and Figure 7.2). The dislocation structure evolution during cyclic deformation was explained in Chapter 6 (Section 6.2.4.2). As explained in this section, the dislocation wall or vein structure can be attributed to the strong activation of secondary slip (or cross-slip) during softening. Upon deformation from 300 to 600 cycles, the dislocation walls/veins were found to become more equiaxed (see Figure 7.10). No sub-grain boundaries were observed in the TEM foils studied for deformation up to 600 cycles (Figure 7.10). The dense precipitation of $M_{23}C_6$ carbides in the austenite matrix might have prevented sub-grain development by preventing recovery [225].

Nellessen et al [206] formulated a dislocation structure map for 316 austenitic steel (Figure 7.25). This map was plotted as a function of cycle number, strain amplitude and crystallographic orientation in loading direction. This map showed a general trend of increasing complexity in the dislocation structures with increasing cumulative strain. Nellessen et al [206] also reported that the dislocation structures depend more on the local strain amplitude in the test specimen than the global strain amplitude. Such a change in dislocation structure was not noticed in this study since the TEM foils studied were from different locations of the specimen gauge length. Nellessen et al [206] also reported

pronounced pre-veins with dislocations in between, or dislocation free areas, in grains of all orientations studied after 100 cycles for a local strain amplitude of 0.95%.

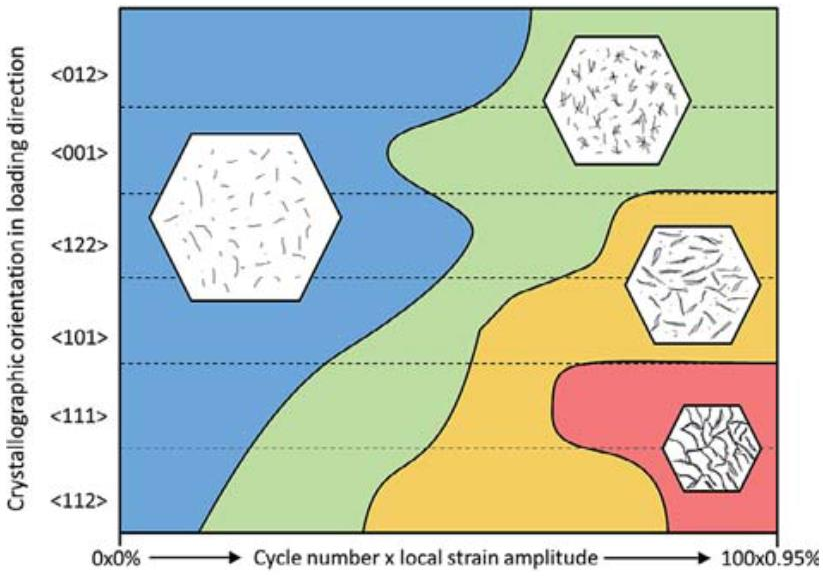

Figure 7.25 Dislocation structure formation map as a function of the combination of cycle number and strain amplitude and crystallographic orientation in loading direction [206].

Even though the EBSD maps and STEM images have different spatial resolution, STEM is generally used to complement EBSD results. As described in chapter 3, individual dislocations are not observed in EBSD maps, but rather the misorientations between pixels that arises due to the lattice rotations caused by dislocation accumulation. For example, the step size used in the EBSD measurement was a 1μm which is many times larger than the Burger's vector of a dislocation. Jiang et al [222] mapped and calculated GND density in copper sample plastically deformed to 2% using the high resolution EBSD cross-correlation method (directly from the EBSD Kikuchi patterns). Dislocation cell structures were seen as patterns within the grain interiors for the large central grains in the GND maps. Jiang et al [222] assumed that GNDs are either pure screw dislocations with line and Burgers vectors along <110> (six types) or pure edge with <110> Burgers vectors and <1-12> line directions (12 types). A step size of 0.5μm was used for EBSD

measurements in that study whereas 1µm was used in this thesis research. Even though GND maps and KAM maps cannot be directly compared, studies by Jiang et al [222] showed that GND maps pick up the dislocation structures observed in TEM images. Also, ECCI (a technique based on SEM/EBSD)[145] can be used to image dislocation structures directly this needs a higher beam current than the SEM available for use in this thesis work.

7.4.3. EBSD Vs DPPA

DPPA (see Chapter 4) is receiving increasing attention as a method for measuring plastic strains from X-ray peak broadening associated with dislocations. The principle of diffraction peak profile analysis was covered in Chapter 3 and the X-ray measurements here followed the procedure given in Chapter 3.

The diffraction peaks from {111} and {200} planes of ex-service 316H (Material C) were studied qualitatively (see Figure 7.26 and Figure 7.27). From the plots, there was no systematic trend, with the number of cycles, shown by the observed full width half maximum (FWHM) of the 111 and 200 peaks. The coarse grain size of the material might have affected the results of the laboratory X-ray diffraction. The interaction volume of laboratory X-rays is very small and only a few diffracting planes may have been sampled from the coarse grains. Similar issues were reported by Claire et al [145] on Fe-3Si steel. This problem could probably be resolved using neutron or synchrotron diffraction. X-ray diffraction was also conducted to study the peak broadening of creep-fatigue samples (not presented in this thesis) but, again, due to insufficient diffracting grains, the data could not be processed properly.

Apart from the large grain size, the following factors might have also affected the X-ray measurements on ex-service 316H material:

- The variation in precipitate density across a grain might affect the X-ray scattering.
- Asymmetric broadening of peaks was reported in Grade 100 micro alloyed steel due to presence of nano-size precipitates [226]. TEM microstructures shown in Chapter 4 also shows nano-size precipitates in ex-service 316H material.
- If there is a slight change in texture in the material (which can be expected on an ex-service material due to its manufacturing process), the diffraction intensity can be biased towards specific peaks.

Thus, due to the microstructural complexity of the material being studied, EBSD has been observed to be a better technique than X-ray peak profile broadening to study inelastic strain accumulation in 316H material.

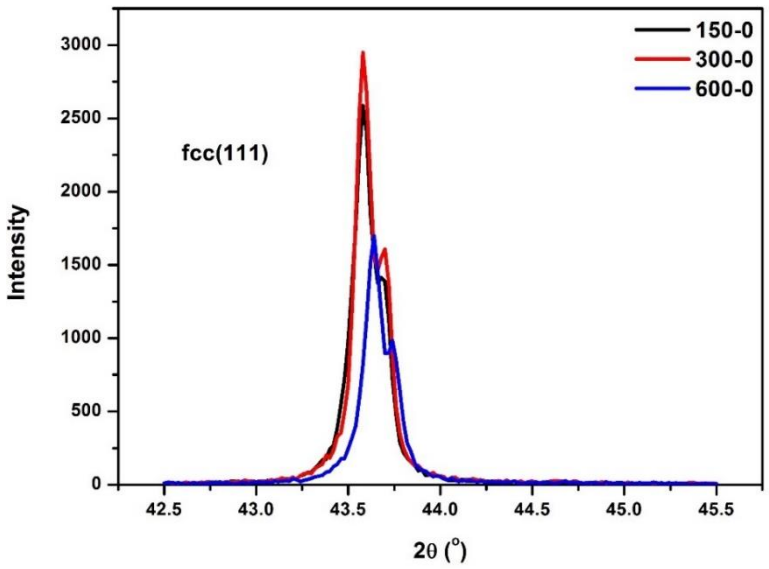

Figure 7.26 XRD raw data of 111 peak for ex-service 316H (Material C) cyclically deformed at a total strain range of ±0.6% and strain rate of 0.025%/s without dwell to 150, 300 and 600 cycles.

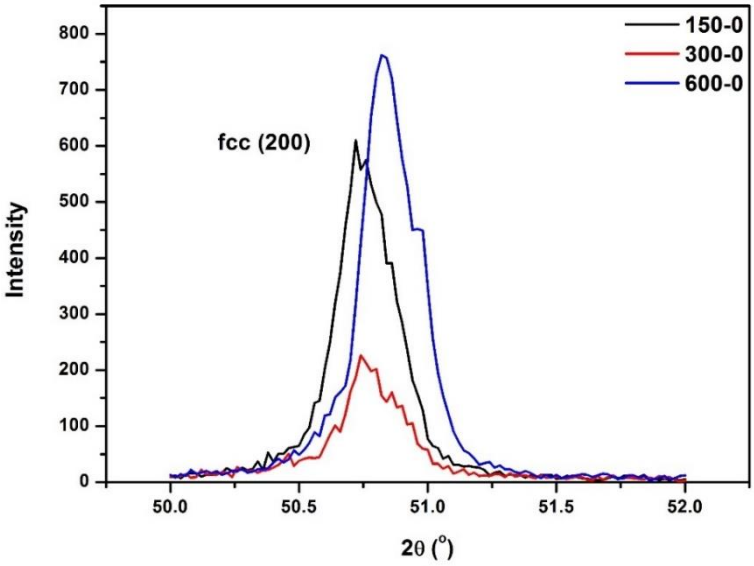

Figure 7.27 XRD raw data of 200 peak for ex-service 316H (Material C) cyclically deformed at a total strain range of ±0.6% and strain rate of 0.025%/s without dwell to 150, 300 and 600 cycles.

7.5. Summary

The misorientation development resulting from cumulative cyclic strain accumulation has been studied on ex-service and thermally aged 316H material. The materials both showed cyclic softening after 150 cycles. In ex-service material the cyclic softening was more dominant with 600s dwell while thermally aged material was still in its saturation stage. KAM_a lognormal, GOS_a, DGF(0.5) and DGF(1) metrics were found to increase linearly with cumulative inelastic strain up to 600 cycles. Higher KAM values were found at grain interiors close to triple junctions. TBF was found to reduce linearly with the cumulative inelastic strain. Dislocation cellular walls or vein structures were observed after 300 cycles. This was attributed to secondary slip activation. The limitations of using laboratory X-ray diffraction peak broadening to estimate inelastic strain were discussed.

CHAPTER 8

GENERAL DISCUSSION

8.1. Introduction

The aim of this PhD project was to explore the possibilities of using a misorientation-based EBSD method to quantify the inelastic strains developed during uniaxial stress relaxation, low cycle fatigue and creep-fatigue deformation of 316H austenitic stainless steels used in high temperature structural components.

This chapter first reviews creep-fatigue damage evaluation in pressure vessels and then summarises key results from this research relating to the potential of EBSD to characterise inelastic strains developed during uniaxial deformation and cyclic loading at high temperatures. It then explores the possibilities of using EBSD metrics to study the accumulation of inelastic strain around creep cavities adjacent to a service induced reheat crack. The EBSD metric results are compared with Small Angle Neutron Scattering (SANS) cavity studies already reported on a failed structural component.

8.2. Creep-fatigue damage evaluation in structural components

As described in Chapter 3, the material studied in this thesis has been extracted from an ex-service steam header. Steam headers are important components in power generating plants which operate under harsh conditions (variable temperature and pressures) during their service period. The structural integrity of these components in nuclear systems can be critical, as they are very expensive and difficult to replace [182], the prospect of being able to monitor/map inelastic strain accumulation in safety-critical components is of high interest to plant owner/operators. Generally steady state operational stresses are a maximum at the outer surface of these components allowing ready inspection [182].

Chapter 2 discussed various methods of detecting creep damage in structural components. Other than the NDT techniques explained in Chapter 2, direct observation, replication and material sampling are the general options available for damage assessment by microstructural observations (optical or SEM). Finite element models [227][228], using the loading history and material properties as inputs, are generally used to predict both the regions expected to experience maximum damage and to access the amount of sample material that can be removed from those locations without compromising the component's life. Scoop techniques are sometimes used for extracting a small amount of material for examination without compromising the integrity of the component. These methods are directed mainly at plant condition monitoring rather than creep damage assessment and, due to their relatively poor spatial resolutions, direct estimation of dislocation densities is impossible (unless TEM/STEM is used).

Methods of creep damage evaluation can be classified by the ranges of component length that can be assessed by their respective measurement probes, sensors or gauges, as shown in Figure 8.1 [104]. Generally, the greater the assessable length, the lower the ability to detect the earlier stages of creep. Three possible creep condition-monitoring strategies (A, B and C) using the available techniques are shown in Figure 8.1 [104]. Most of the metallurgical-based methods would be classified as short range. Usually the temperature and pressure data are used to get a rough estimate of the creep damage in a component followed by metallurgical investigations [104].

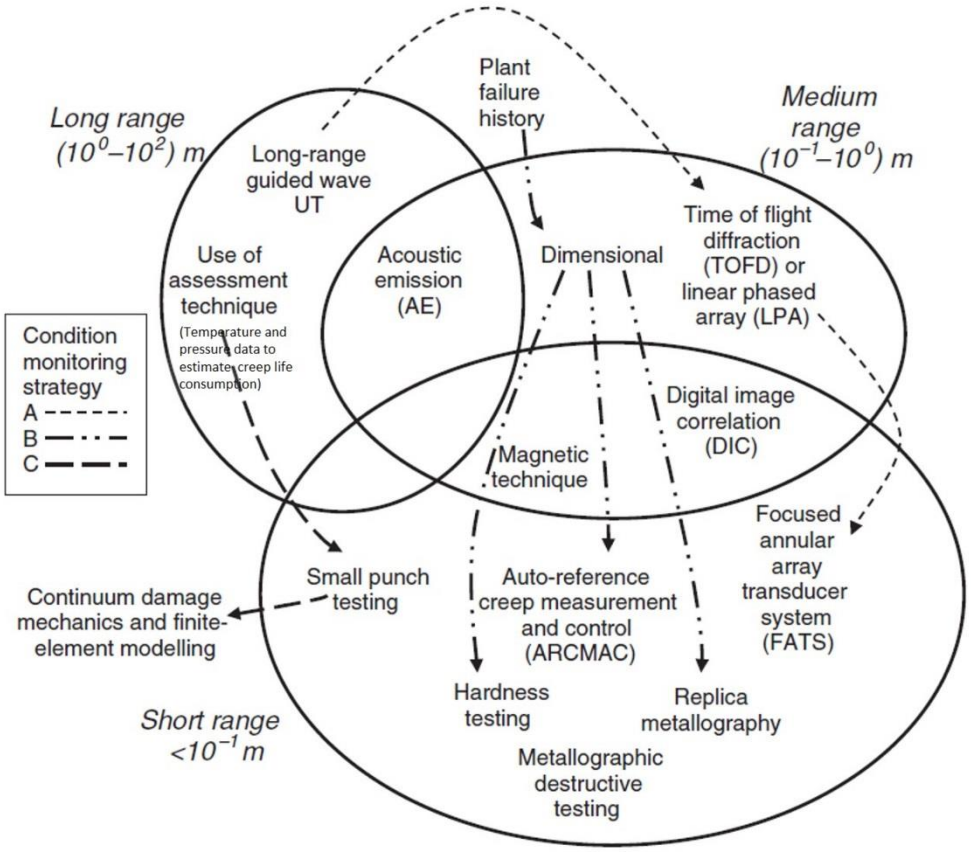

Figure 8.1 Creep damage estimation methods classified according to the length of component that can be assessed. Three possible condition-monitoring strategies are shown [104].

As mentioned in the literature [40], [53], [229]–[234], [59], [62], [68], [87], [103], [131], [152], [194], the evaluation of low cycle fatigue and creep-fatigue strains is vital for these components during varying plant operating conditions. The deformation is much more complex in cyclic deformation than in uniaxial creep because slip can be partially/completely reversed when the load changes from tensile to compressive. The deformation mechanism map (see Figure 2.6, Figure 2.8) clearly shows that in 316 steel deformation at around 550^{o}C is mostly dislocation dominated. Thus, a damage assessment method incorporating the dislocation density accumulated in the material will give more reliable information regarding the inelastic strains in the material.

8.3. Discussion of key findings

8.3.1. An EBSD-based misorientation method to quantify inelastic strains

In the published literature [32], [142], [194], EBSD metrics have been used to quantify the inelastic strains developed in uniaxial plastic and creep deformation of 316H austenitic stainless steel. However, to date, there have been no publications focussing on using EBSD metrics to evaluate creep strains due to stress relaxation in 316H, nor on the effect of different cyclic loading parameters on the measured EBSD metrics. Chapters 5, 6 and 7 all concerned the behaviour of the different EBSD metrics. Chapter 5 presented results comparing the effects of uniaxial plastic deformation and stress relaxation on them, Chapter 6 presented the effects of precipitates, temperature and different cyclic loading parameters and Chapter 7 presented the effects of cumulative inelastic cyclic strain. The EBSD results were compared with micro/nano hardness measurements and STEM was used to study the dislocation structures in selected samples.

The EBSD metrics (GOS, KAM, DGF and LABF) were found to increase linearly with plastic strain (results reported in Chapter 5, Figure 5.11, 5.12, 5.13, 5.14, 5.16) which was in agreement with most of the studies comparing EBSD metrics and plastic strain such as [11], [32], [135], [137] in the literature. TBF was found to reduce with strain (Figure 5.15). The general opinion about stress relaxation in the literature is that elastic strain tends to relax with time by creep deformation at high temperatures though some studies suggest an orientation dependence of stress relaxation which will be discussed later in this section [223]. Some of the finite element models assumed relaxation of the dislocations, forming cell structures during stress relaxation [96]. Room temperature uniaxial stress relaxation on 316L material for time up to 60s also showed dislocation annihilation and cell structure formation [197] which was attributed to the immobilization

of mobile dislocations, as evidenced by the formation of sharp walls and low angle grain boundaries, leading to a change in the internal stress [235]. However, this study neglected variations in the internal stress. Results in Chapter 5 show that there is a similar trend in 316H austenitic stainless steel where dislocations form a diffuse cell structure after stress relaxation for 24 hours (see Figure 5.23, Figure 5.24). There was a general trend of increasing local misorientation and average intragrain misorientation with dwell; the difference being more significant at higher strains. Local misorientation was concentrated at grain boundaries and precipitates.

Austenitic stainless steels have low stacking fault energies. This impedes the cross-slip of dislocations during the early cycles of deformation. As a result, high dislocation densities are formed at the grain boundaries, whilst in middles of the grains there are fewer dislocations [204], [236], [237]. This was the general trend observed in uniaxial tensile/stress relaxation and low cycle fatigue/creep-fatigue samples where higher local misorientations were observed near grain boundaries (see Figure 5.18) but there were also some dislocation pile ups within the austenite matrix around intra-granular precipitates. The results in Chapter 5 show higher KAM near grain boundaries in all samples deformed at either room or high temperature and this was more marked at higher strains (see Figure 5.20).

DGF metrics increased with plastic strain (see Figure 5.13, Figure 5.15). At high strains the DGF metric saturated to 1 (see Figure 5.13, Figure 5.15). The sensitivity of EBSD metrics to deformation conditions was also discussed in chapter 5. The values of the EBSD metrics at a particular strain were found to be sensitive to the deformation mechanisms (see Figure 5.4Figure 5.6, Figure 6.32,Figure *6.36*).

Githinji et al [11] observed in uniaxial creep deformation that GOS values were frequently higher for grains with higher overall Schmid factors, in which deformation would be expected to occur first, ("creep weak grains") during the primary and secondary creep. These grains have their slip systems favourably oriented with the respect to the applied stresses. The ease of creep deformation in these grains during service could have resulted in the intragranular precipitation variations amongst the grains as discussed in section 4.3.3.1. This Schmid factor dependence could lead to the high rate of DGF development with respect to the accumulated strain, but as the overall deformation increases the rate of DGF increase reduces as the deformation progresses to grains with relatively low overall Schmid factors, leading to the observed saturation [11]. After tensile deformation to large strain or cyclic deformation to large strain ranges, the intragranular misorientation (GOS) of all grains are mostly above 1^{o} which leads to saturation of DGF(1) to 1. This also explains the DGF saturation at high plastic strains. Any dependence of creep on the Schmid factor would suggest that the evolution of DGF with creep strain would be a function of the existing texture in the material. However, texture studies of the different 316H materials used in this study showed there was no evident strong texture in them (Chapter 4, section 4.3.5). Hence further studies would have to be conducted on a material with a strong texture to examine this hypothesis. This is a suggestion for future work.

The STEM images in Chapter 7 (see Figure 7.10) shows that the cell size/vein width reduces with the increasing dislocation density. These results are consistent with EBSD results where the misorientations increase with number of cycles. The dislocation densities generated in cyclic deformation are reported to be much lower than after an equivalent cumulative strain in uniaxial deformation. During the reverse phase of the

cyclic loading, some of the dislocations developed in the previous cycle will annihilate by interacting with opposite sign dislocations, due to their reversible movement. As deformation proceeds, planar tangled structures are increasingly formed. This obstructs further dislocation movement and cross slip is activated. This in turn enhances the dislocation annihilation mechanisms [137][237].

As observed throughout Chapters 5, 6 and 7, the true localized inelastic strain at any position does not exactly correspond to the true global plastic strain. The plastic strain at a microstructural level should be defined carefully. Local deformation at high temperatures is usually achieved by crystallographic slip or by diffusion. During cyclic deformation the local crystal orientation fluctuates, which affects the average local misorientation significantly [79]. As a result, the EBSD metrics based on the misorientations between neighbouring points, KAM and LABFA, are unable to provide reliable measures of the total accumulated plastic strain. In the fatigue of austenitic stainless steels, it is the orientation gradients caused by the crystallographic slip, rather than the global strain, that is relevant to the cracking behaviour [206]. In general, the orientation gradients increased with the macroscopic plastic strain induced in 316 austenitic stainless steels [131]. So, by identifying the local gradients or misorientations by EBSD measurements, the degree of local deformation can be assessed quantitatively.

Valsan et al [201] studied low cycle fatigue behaviour of 316L(N) steels in constant strain hold tests. Rapid stress relaxation was reported in the first few seconds of the strain hold, followed by a slower rate of stress relaxation during the rest of the hold period [201]. Similar results were obtained in this study for uniaxial stress relaxation (see Figure 5.10) and relaxation during the tensile holds in cyclic deformation (see Figure 6.3). As already mentioned in Chapters 2 and 5, during stress relaxation, conversion of elastic to plastic

strain takes place and the strain rates are reported typically of the order of $10^{-4}s^{-1}$ to $10^{-8}s^{1}$ during the slow relaxation period [201]. The build-up of tensile inelastic strain leads to the accumulation of grain boundary creep damage in the form of cavities (see Figure 5.19, 5.20). With increasing strain and/or duration of the hold time, a significant amount of stress relaxation takes place, leading to an enhanced build-up of intergranular creep damage [201]. It is possible that the increased local misorientation (KAM) after dwell at large strains (15% strain) (see Figure 5.12) assists cavitation at grain boundaries to accommodate the large inelastic strains developed during stress relaxation because dislocations generated might give a high diffusivity path for vacancies. The cavities found in SEM secondary images supported this suggestion (see Figure 5.18. SEM micrographs showing grain boundary cavitation in the ex-service Type 316H steel deformed to (a)15% and (b) deformed to 15% followed by 24hour constant total strain dwell. Cavitation is predominant after 24 hour dwell.

The general concept of stress relaxation in metals, that elastic strain converts to creep strain, was explained in chapter 2. However, recent neutron diffraction studies of 316H suggest an orientation dependence of elastic strains in the material [192], [223], [238]–[240]. Uniaxial stress relaxation of 316H material by Wang et al [223] showed maximum stress relaxation on {200} grain families (200 planes aligned with longitudinal direction of applied stress) and minimum on {111} grain families (111 planes aligned with longitudinal direction of applied stress) after 12 hours. Studies by Rao et al [240] also reported maximum creep strain developed in {200} grains after 12 hour. The higher KAM values with higher values of stress relaxation can be attributed to the accommodation of inelastic strain at the grain boundaries (See Chapter 5).

Comparing the uniaxial stress relaxation tests for 24 hour with the creep-fatigue tests with 10min dwell (550B±0.60%0.025H10, Chapter 6), the total dwell time for 150 cycles is approximately 25 hour. Calculating the inelastic strain generated for each cycle (ie. stress relaxed for 10 minute divided by Youngs modulus, i.e. stress relaxed/135), the total strain developed during the stress relaxations of 25 hour is approximately 0.822 which is almost 1000 times more than that generated after the single 24 hour dwell after plastic deformation to 15% engineering strain (550B15%0.025H24, Chapter 5) which is approximately $7.66*10^{-4}$). For a saturated cycle for deformation condition 550B±0.60%0.025H10, the stress relaxed is approximately 74MPa (for 100th cycle). The calculated inelastic strain for a stress relaxation of 74MPa is approximately $0.55*10^{-3}$. The results in Chapter 5 shows that the KAM and GOS are sensitive to inelastic strains developed due to stress relaxation after high plastic strain (see Figure 5.11and Figure 5.12). But the increase in KAM and GOS was much smaller in creep-fatigue tests with 10 min dwell compared to low cycle fatigue tests (see Figure 6.7, Figure 6.12). Even though the total inelastic strain developed over 150 cycles is much higher than that for the uniaxial deformed and stress relaxed sample, some of the dislocations generated during stress relaxation at each peak tensile hold might be reversed/ annihilated during the compressive part of the next cyclic loading, resulting in lower KAM values than after uniaxial stress relaxation.

The effects of strain rate on cyclic deformation was not investigated in this thesis due to the limited material available. However, low cycle fatigue and creep-fatigue studies by Hormozi et al [96] at 650^{o}C on 316H at two different strain rates (1 and 0.1%/s) showed a higher peak tensile stress, after cyclic saturation, at the lower strain rate. Similar results were reported by Shan et al [137] on 316L(N) material. This is due to DSA where the

strong interaction of solute atoms with mobile dislocations reduces the number of available mobile dislocations to accommodate inelastic strain. In austenitic alloys, the ductility of materials decreases at slow strain rates due to formation of precipitates in the grain boundaries and dislocation interaction with precipitates. Hormozi et al [96] reported transgranular fatigue cracking at higher strain rates and intergranular creep-fatigue cracking mechanism governing low strain rate deformation. During deformation, the stresses are concentrated around precipitates so cavitation and fracture can be expected around the precipitates. In this study, TBF was the only EBSD metric to show variation with strain rate (comparing 0.025%/s and 0.0025%/s) for uniaxial deformation at 550ºC (Figure 5.3). Previously KAM_a has been reported to increase with both increasing strain and strain rate in ex-service material plastically deformed at 550ºC while DGF was found insensitive to strain rate down to 10^{-3}%/s [11].

Another factor that was not investigated here was the effect of pre-strain (either tensile or compressive) on misorientation development. Pre-straining increases the material's dislocation density which in turn increases strain hardening thereby reducing the creep ductility. Githinji et al [11] studied the effect of pre-straining on creep deformation. After pre-strain, the development of long-range misorientations due to creep strain added to the existing misorientation [11]. For the same creep strain, the misorientations were lower in the absence of pre-strain than with pre-strain. No literature was available on the development of misorientation during creep deformation after cyclic pre-strain. However, modelling and experimental studies by Erinosho et al [241] demonstrated that creep strain accumulation in 316H austenitic stainless steel is slower following prior cyclic plasticity because dislocation structures develop during the cyclic pre-strain phase, which cause hardening.

8.3.2. Choice of EBSD metrics

The results reported in chapters 5, 6 and 7 along with published literature [11], [21], [137], [145], [242], [243] demonstrate that the choice of EBSD metrics is very important in studying inelastic strain accumulation over different length scales. Different EBSD metrics reveal misorientation information over a small scale (within grains/kernels) and over a larger scale (across grains). As mentioned in Chapter 2, the Society of Material Science, Japan (JSMS) has already issued an EBSD-based strain measurement standard for measuring creep strain in uniaxial creep deformation[5] [142] This suggested that average intragrain misorientation (GOS) and local misorientation (KAM) are good measures of creep damage in terms of inelastic strain, and that the experimental scatter observed in KAM values was assumed to be due to material inhomogeneity [142]. Although the orientation dependence of lattice strains in 316H material were reported in the literature [223], [240], [244] this study could neither confirm nor disapprove it. This section discusses the selection of appropriate EBSD metrics to study different aspects of deformation.

KAM: As explained in Chapter 2, KAM measures the average local misorientation within a kernel and is a good measure of GND density [11], [145] in the observed area and hence has been used as a measure of inelastic strain in many studies [11], [21], [25], [141], [144], [146], [215], [245], [246]. Some of the studies around cavities and cracks reported higher KAM values around them, possibly due to the inelastic strain accommodated during deformation [152]. This suggests the possibility of using KAM to study creep cavities in metals. However, this study suggests that, KAM is influenced by the material's inhomogeneity, especially in ex-service 316H material due to the presence of precipitates

[5] The step size of EBSD measurement was 0.5µm.

(see results in chapters 5 and 6, Figure 5.7, Figure 6.46). A similar scatter in KAM was reported in the literature [142]. KAM is affected by the step size used in the EBSD measurements [11]. A smaller step size scan can reveal more information regarding GNDs but the time required to collect orientation data from a statistically significant area will increase correspondingly. Even though recent studies using high resolution EBSD (HR-EBSD) demonstrated an improved calculation of the density of GNDs with new algorithms compared to GND calculations using conventional Hough transformations, the measurement area using HR-EBSD is far smaller due to the time constraints mentioned above [247][248]. Hence conventional EBSD data analysis using Hough transformation remains the preferred method of studying inelastic strain accumulation in a structural component made of material with a large grain size, even though collecting EBSD data from a large grain material using a small step size takes a long time.

GOS: Average intragrain misorientation (GOS) is another major EBSD metric shown in many studies [11], [29], [132], [136], [137], [140], [142], [215], [245] to be directly related to inelastic strain. JSMS guidelines prefer GOS for measuring inelastic (creep) strains [142]. However, the results in Chapter 7, shows that GOS_a values may not always increase with cumulative strain (e.g. results on Material E) possibly due to the orientation of the grains relative to the loading direction or the presence of intragranular precipitates (see Figure 7.20). These factors might affect the scatter in the GOS_a values. The results in Chapter 6 (see Figure 6.12) show that GOS is also affected by local material inhomogeneities.

DGF: Deformed grain fraction, which is fraction of grains with GOS values above a particular threshold, has also been reported in a few publications as the metric which gives the smallest scatter when used as a measure of inelastic strain [11][145]. This metric is also reported to be the least sensitive to deformation temperature, grain size, strain rate

and EBSD step size [11]. Githinji et al [11] reported DGF as the preferred EBSD metric to estimate creep strain in 316H due to its insensitivity to microstructural changes which may occur during service. In this study too, DGF was found to be insensitive to local inhomogeneity (see Figure 6.12).

TBF: TBF is the only EBSD metric that showed a reducing trend with inelastic cyclic strain in this thesis work, both for uniaxial and low cycle fatigue deformation. TBF cannot be directly compared with other EBSD metrics since TBF is the only metric based on intergranular misorientations rather than intragranular misorientation. Similar results were reported for uniaxial creep deformation by Githinji et al [11] who also reported a greater reduction in TBF under creep than in plastic deformation to the same total strain [11]. The use of this metric is based on the observation that the fraction of HAGB which are twins will be maximum in undeformed austenitic stainless steels due to their tendency to develop annealing twins [188]. However, during deformation the twin boundaries may be effective barriers to dislocation motion [189], [190] resulting in dislocation pile-ups and/or absorptions. These interactions may introduce lattice rotation at the twin boundaries such that their near-twin orientation is progressively lost.

LABFA: Even though LABF considers all misorientations between 2 to 15^{o}, the scatter in the LABFA metric makes it least preferred choice among all the EBSD metrics used in this thesis. The scatter might be due to local changes in the precipitate density which affects dislocation density but the major reason is probably that LAMF does not consider misorientations <2^{o}, whereas KAM shows that almost all the misorientations developed during cyclic deformation are < 2^{o} (see Figure 6.19).

8.3.3. Comparison of EBSD metrics with other methods to quantify dislocation density

This thesis has compared EBSD results with other characterization methods like NDT, micro/nano hardness, STEM and X-ray peak profiling. The deformation mechanisms and maps in section 2.7.5 show that the deformation expected of 316H material in actual service conditions at around 550^{o}C is dislocation assisted creep. Hence a creep damage/strain assessment technique measuring the dislocation density in the material should be a good tool.

The mean micro-hardness value increased with strain range, as reported in Chapter 6 (see Figure 6.16). However, hardness measurements were unable to detect the changes in cumulative inelastic strain after deformation at 150, 300 and 600 cycles (see Figure 7.16). It has already been discussed in Chapter 2 that hardness measurements are not an ideal metallurgical technique for industrial environments because of their scatter. However, this technique remains popular in industry because hardness measurements are quick and simple. Although both micro-hardness and the EBSD metrics (except TBF) clearly increased with increasing cyclic strain range, the area or volume studied by the two techniques and their spatial distribution are very different. Despite this, much published literature has shown a direct correlation between hardness and dislocation density [11], [152] and a comparison was undertaken (as presented in Chapter 6) between nano-hardness and KAM maps of a sample cyclically deformed at room temperature. The EBSD step size used was 5 microns and hardness measurements (400 indents) were made in the same area on a square grid pattern with 20*20 micron spacing. The hardness maps showed a good correlation with KAM maps of the same region but a 100% one to one correlation couldn't be achieved perhaps due to:

- The different step sizes used for EBSD and hardness measurements

- The sampling depth of EBSD is only of the order of 100 nm, whereas the nano-hardness data contains information from much greater depths.

The use of smaller nano-indent loads to acquire information from closer to the surface is limited by the indentation size effect where a very small indentation depth can lead to an increase in the measured hardness [249]. This occurs due to smaller indents activating fewer dislocation sources, thereby reducing the plastic response around the indent [250].

The fundamentals of using X-ray peak profile analysis to estimate the dislocation density in a material were explained in Chapter 3 and this project's exploration of the potential application of laboratory based X-ray diffraction to estimating the dislocation density in 316H steel is described in Chapter 7. The large grain size of the material led to insufficient diffracting planes in the interaction volume (see section 7.4.3. EBSD Vs DPPA), introducing large errors in the calculations, exacerbated, as also explained in Chapter 7, by possible asymmetric peak broadening due to the precipitates.

Even though TEM is still considered one of the best characterization tools from which to calculate accurate dislocation densities, getting statistically significant information from TEM is extremely slow, due to its very low sampling volume and difficult sample preparation. In contrast, the sample preparation for EBSD is much easier and crystallographic information can be obtained from a much larger area by this method. Recently electron channel contrast imaging (ECCI) is gaining attention for studying dislocations [145], [210], [251], [252]. Electron channelling offers the ability to execute diffraction contrast imaging from a solid specimen inside a scanning electron microscope, removing many of the difficulties of conventional TEM [252]. Claire et al [145] suggested

that an EBSD misorientation method along with ECCI could be a good method of indicating strain in low cycle fatigue of Fe-3Si steel.

Chapter 2 reviewed the literature on studying inelastic strains using EBSD. As explained in that chapter, the lattice misorientations associated with the accumulation of GNDs has been found in many studies to be closely associated with creep or inelastic strains. Section 8.3.2 discussed the selection of suitable EBSD metrics to estimate inelastic strain under different deformation conditions. In the work of this thesis, linear relationships were obtained between EBSD metrics and inelastic strains in both uniaxial tensile deformation and cyclic deformation.

8.4. Using EBSD for creep cavitation studies around a reheat crack and comparison with Vickers hardness and SANS cavitation measurements

Creep cavitation theories [217] propose cavity nucleation by (a) grain boundary sliding leading to voids at grain boundaries especially at triple points (b) vacancy condensation at grain boundaries where there is high stress concentration and (c) cavity formation at the head of a dislocation pile-up or hard phased second particles. Stress relaxation by creep or diffusional flow is proposed to be a major cause of the reheat cracking found during post weld heat treatment or high temperature service of the heat affected zones of high temperature structural weldments (as reviewed in Chapter 2). The conversion of elastic strain to creep strain during stress relaxation results in larger inelastic strain accumulations than the material can accommodate and thereby cavities are formed. The cavities then join together to form micro-cracks [16].

The relationships between the EBSD metrics and inelastic strain has been established in Chapter 5,6 and 7, the final part of this discussion focusses on using these relationships on a reheat crack found in the ex-service header adjacent to a nozzle weld. Study 1

compares the local misorientations around the crack with micro-hardness maps while study 2 compares the pattern of local misorientations with cavitation studies using SANS. Even though both cracked samples were from same component, their lengths were found to be different (because they were extracted from different positions around the nozzle).

8.4.1. Study 1: EBSD and microhardness studies around a reheat crack

Optical examination revealed the crack to be intergranular (see Figure 8.2) and around 16.8mm long. It started from grain boundaries in the heat affected zone near the weld. The crack was not continuous but branched and fragmented (see Figure 8.2). EBSD measurements were made at three locations on the crack; (1) at the crack mouth, near the weld, (2) mid-way along the crack, around 8mm from its mouth and (3) at the crack tip. EBSD measurements of deformation were also made on an area far from the crack for comparison. A minimum of 600,000 data points covering an area of at least 1.4mm^2 was recorded in each EBSD scan. The outcome of this study has already been published [253].

SEM images in the region of the crack near the weld and near the crack tip are shown in Figure 8.3 and Figure 8.5 respectively. Cavities can be seen around intergranular precipitates along the grain boundaries, as previously reported for this component [122], [254]. EBSD orientation maps (IPF colouring) suggest that the grains around the crack are randomly orientated (see Figure 8.4).

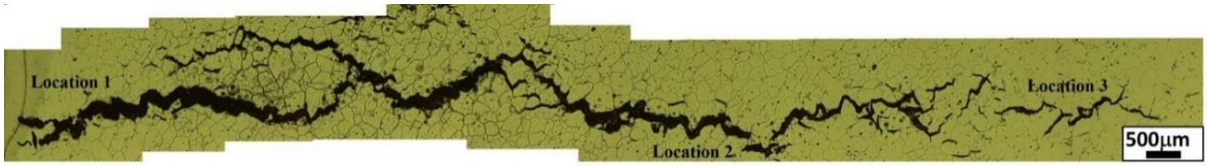

Figure 8.2 Optical microstructure of the reheat crack 16.8mm long

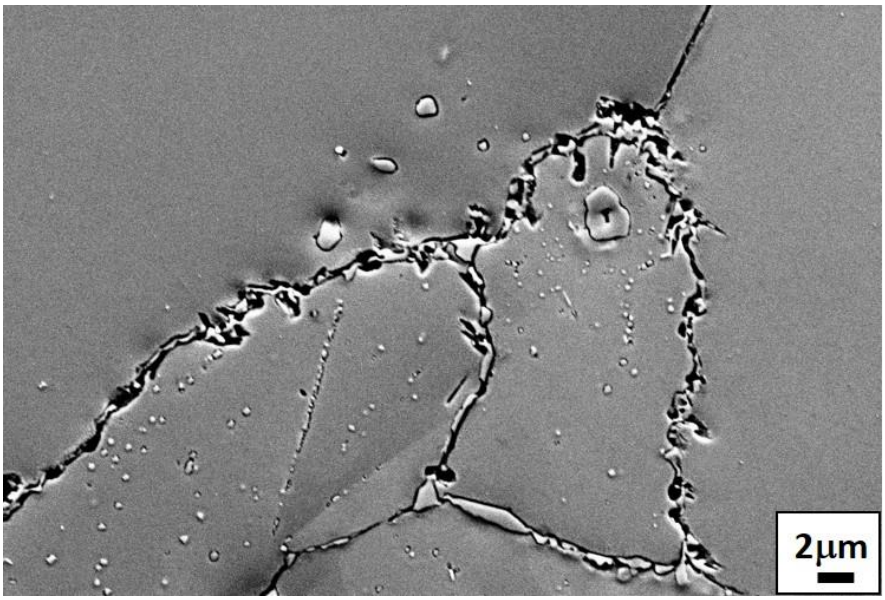

Figure 8.3 Secondary electron image of grains near the crack tip at location of high KAM.

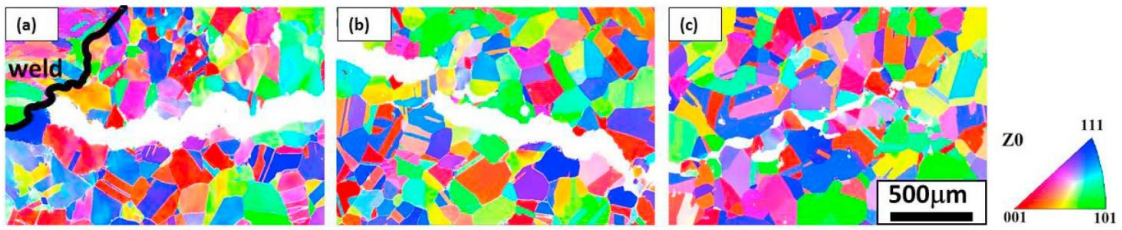

Figure 8.4 Orientation maps of reheat crack at (a) location 1(at the crack mouth, near the weld), (b) location 2 (mid-way along the crack around 8mm from its mouth) and (c) location 3 (at the crack tip). Scale bar applies to all images.

Figure 8.5 shows point to point misorientations >2°, those in the range $2 < \theta < 15°$ being identified by the EBSD software as 'low angle grain boundaries' + (LAGBs) and those >15° as high angle grain boundaries' (HAGBs). Regions with a high concentrations of 'LAGB's correspond to areas of high dislocation density [255]. From Figure 8.5(a) and (c) it's evident that highly dislocated regions are present in the crack path and especially near the weld, in the region where the crack is believed to have initiated.

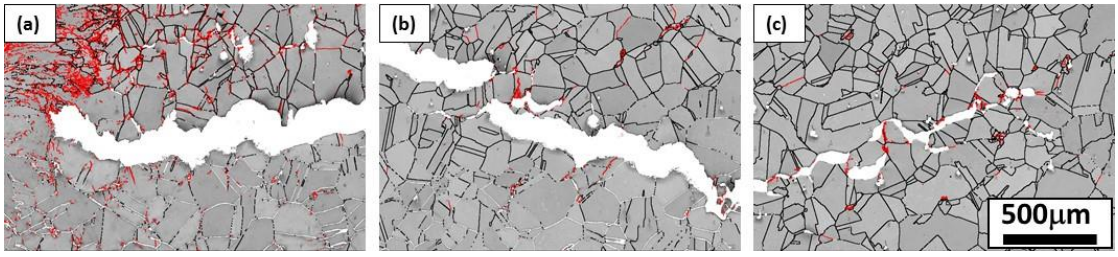

Figure 8.5 . 'Grain boundary' maps of the reheat crack at ((a) location 1(at the crack mouth, near the weld), (b) location 2 (mid-way along the crack around 8mm from its mouth) and (c) location 3 (at the crack tip). (black lines are high angle boundaries [$\theta > 15^o$] and red lines are 'low angle boundaries' [$2° < \theta < 15°$]). The scale bar applies to all images.

Figure 8.6 shows KAM (local misorientation) at three locations along the reheat crack. KAM values are high at location 1 (the region of crack initiation) implying a high dislocation density in this area. As mentioned earlier in this chapter and in Chapter 3, KAM values are not an absolute measure of dislocation density as they depend on the step-size of the EBSD data acquisition. The frequency of low KAM values (< 0.2°) is highest in the areas of the crack remote from the weld, whereas high KAM values (up to 1.2°) are evident near the weld (see Figure 8.7). Both grain boundary and KAM maps show the accumulation of dislocations along grain boundaries far from the crack [124]. As mentioned earlier in this chapter and in Chapter 2, in many studies KAM maps have revealed complex strain localization around voids [163]. Here, unsurprisingly, both 'grain boundary' (see Figure 8.5) and KAM (see Figure 8.6) maps show more intense deformation at the grain boundaries near the crack. This study and studies by Fujiyama et al [152] have demonstrated a strong association between cavities and areas of high KAM. Both KAM and 'grain boundary' maps showed more intense deformation at the grain boundaries near the crack. Higher resolution (0.1µm step size) KAM maps (for example, see Figure 8.8) in the region of micro-cracking show localised regions of large misorientations but cannot be compared quantitatively with the lower magnification maps presented in Figure 8.6 because of the difference in the step size.

An appropriate colour coding in the misorientation maps can help to reveal the extent of plastic deformation within each grain [110]. Misorientation maps may also be helpful in predicting the direction of crack propagation but this needs further investigation. EBSD and micro-hardness are simple representation methods to illustrate the local dislocation density around reheat cracks, but it is difficult to quantify the degree of deformation present as a reference unstrained condition must be defined [128].

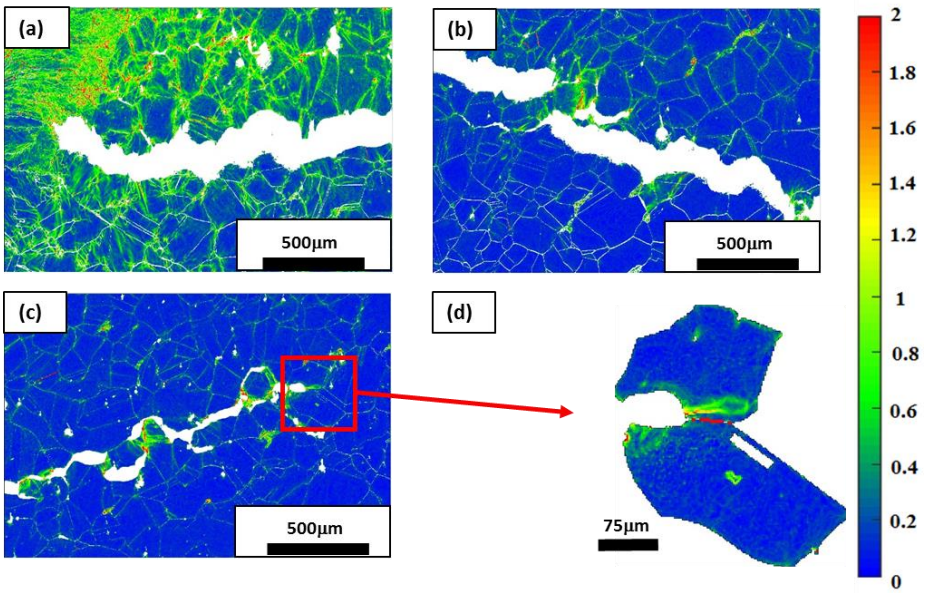

Figure 8.6 Kernel average misorientation (KAM) maps of the reheat crack at (a) location 1, (b) location 2, (c) location 3 and (d) magnified map of grains at the crack tip.

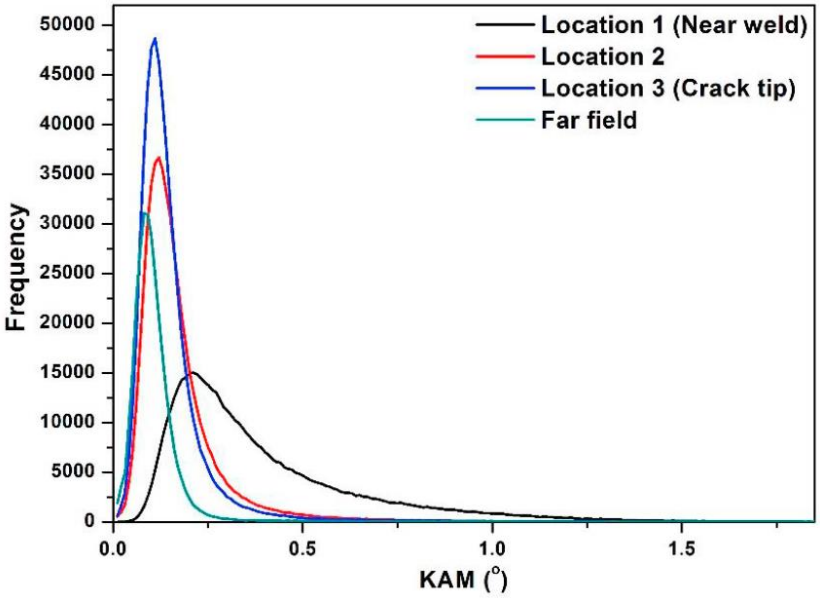

Figure 8.7 Frequency distribution of Kernel Average Misorientation (KAM) values at different locations.

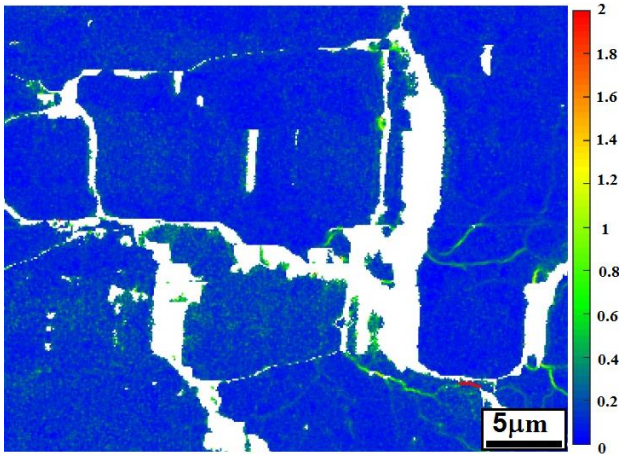

Figure 8.8 Kernel average misorientation (KAM) maps around intergranular cavities at higher magnification.

The local deformation around the crack was also characterized by measuring Vickers hardness (HV). The micro-hardness contour maps (see Figure *8.9*) also showed higher hardness values near the weld near the crack initiation position. The misorientation and hardness maps are qualitatively similar (compare Figure 8.5, Figure 8.6 and Figure *8.9*). Like some EBSD metrics, hardness values have been shown to be proportional to the square root of the dislocation density [152] but a direct correspondence between the two

methods is limited by the difference in their spatial resolutions and the different extent of the strain fields they sample.

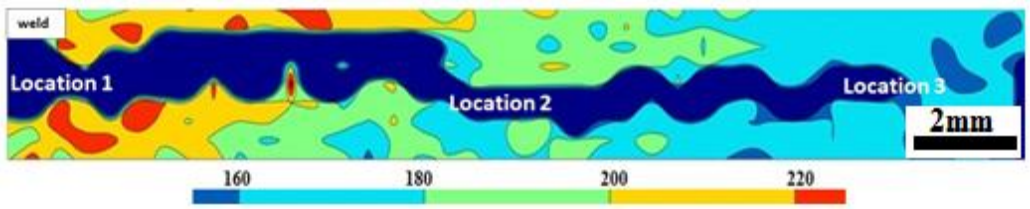

Figure 8.9 Hardness map around the reheat crack [253].

8.4.2. Study 2: EBSD and SANS studies around a reheat crack

Jazaeri et al [256] used small angle neutron scattering (SANS) to study creep cavitation around reheat cracks in a 316H austenitic stainless steel header. The volumes studied were at different locations around the crack, as shown in Figure 8.10. Measurements were carried out at 3, 5, 7, 9, 11 and 13mm away from the crack face (B1-1 to B1-6) along the line B1 normal to the crack and 6mm away from crack mouth. Another set of measurements were made along line B2 which is drawn along the crack tip and measurements were made at 5, 7, 9, 11 and 13mm away from crack tip (B2-1 to B2-5). Three measurements were also made in the 'far field' region, along line B3 which is 41mm away from the crack and 6, 16 and 26mm away from the crack mouth.

The overall size of the all defects (i.e cavities and precipitates) increased as the SANS measurement location approached the crack along line B1 (see Figure 8.11). The mode cavity size was 100 to 300nm at location B1-1 which was the closest to crack. In contrast, there was little variation in the number density distributions of cavities measured at positions along line B2, i.e. moving away from the crack tip along the crack direction (see Figure 8. 12).

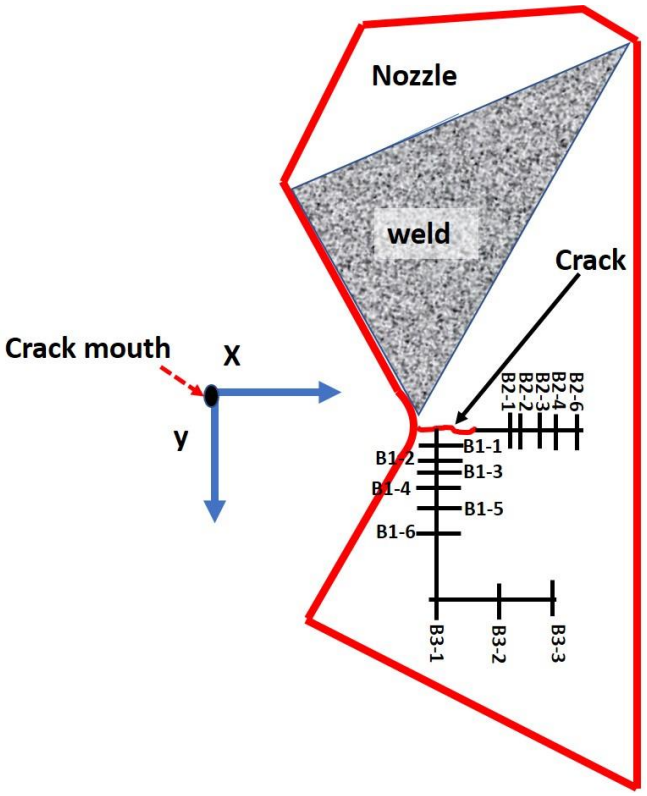

Figure 8.10 Schematic view showing SANS measurement positions around a reheat crack.

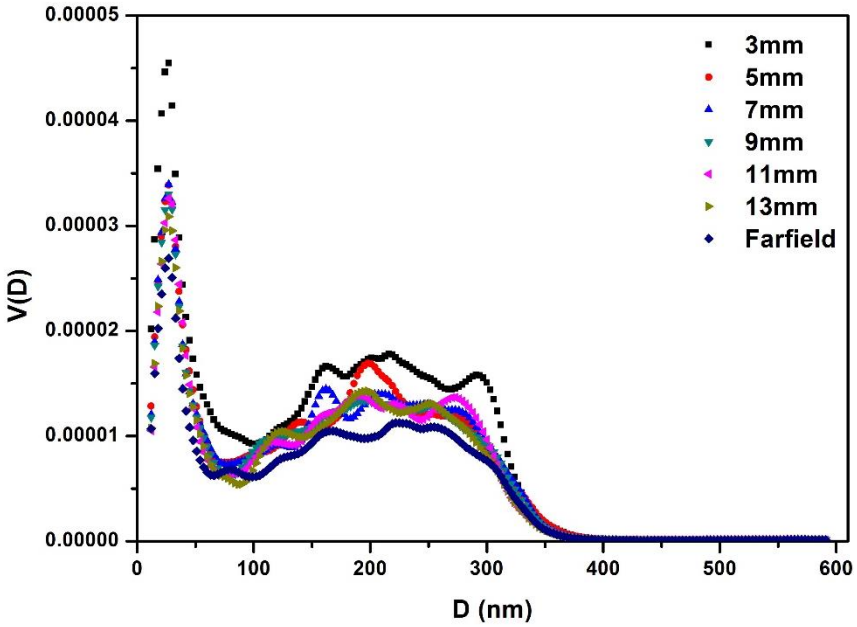

Figure 8.11 SANS data showing increase in volume fraction, V(D) of all defects approaching crack face along line B1 and comparison with farfield location (mean of B2-3 and B3-3).

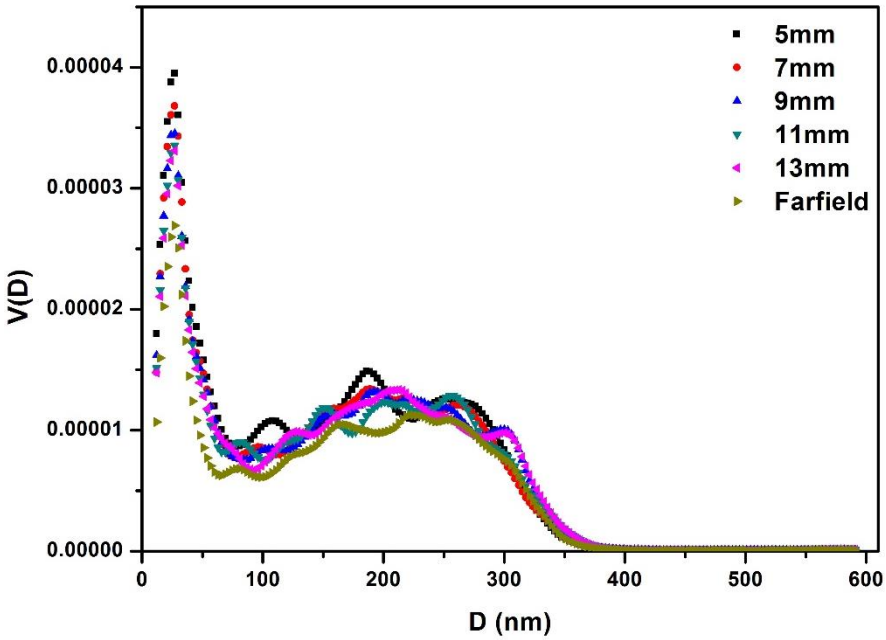

Figure 8. 12 SANS data showing volume fraction V(D) of all defects approaching crack tip along line B2 and comparison with far field location (mean of B2-3 and B3-3).

As suggested in this thesis, intragranular misorientations are found to be concentrated around creep voids due to the accumulation of inelastic strain during plastic/creep deformation at high temperatures. EBSD measurements were made at the same locations where the SANS studies were conducted. EBSD measurements were carried out on an area $1.8\times1.7mm^2$ with a step size of 2μm. A bigger step size was used in this study than in the other EBSD measurements reported in earlier chapters, to get information from a larger area while minimising the thermal drift in the positioning of the electron beam.

Figure 8.13 shows the KAM map at location B1-1 in Figure 8.10. Similar to the results in section 8.4.1, KAM accumulation was more pronounced at grain boundaries. The KAM_a lognormal values of areas along line B1 are shown in Figure 8.14. The KAM_a lognormal values were higher when the measured areas were closer to the crack, in agreement with the observations of Jazaeri et al [256] using SANS. Again in agreement with the SANS results, the KAM_a lognormal values of areas along line B2 (see Figure

8.14) were lower than that along line B1 and the KAM_a lognormal values were much lower along line B3 (i.e. in the far field region).

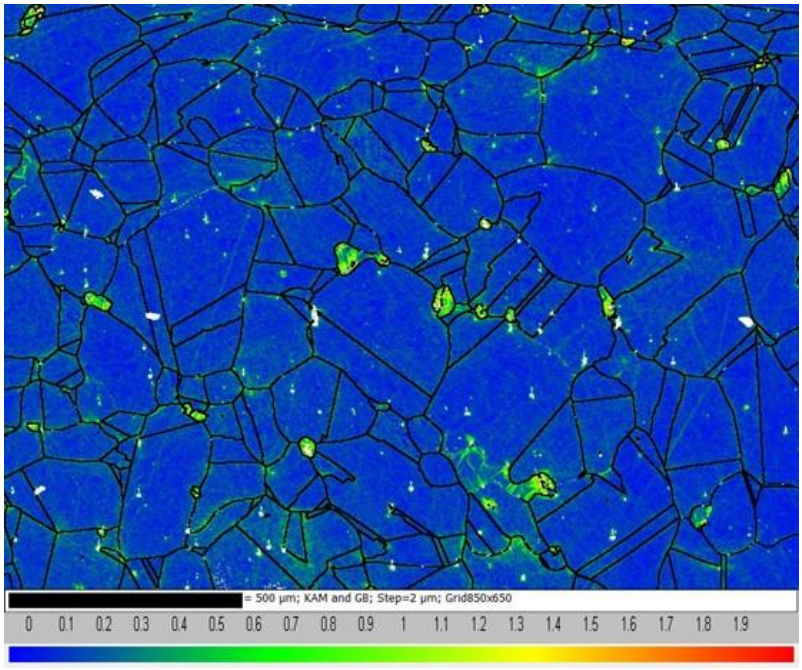

Figure 8.13 KAM map at location B1-1 (3mm away from crack face) in Figure 8.10. Scale bar is 500µm.

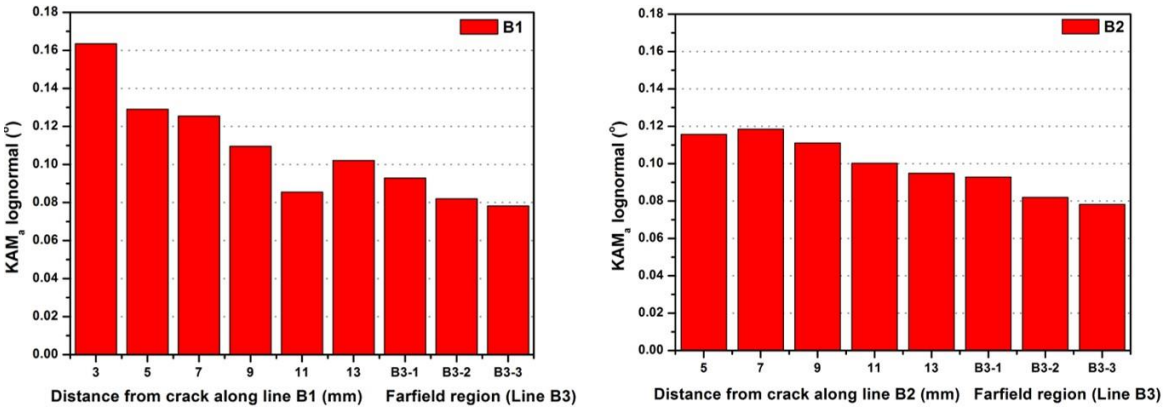

Figure 8.14 KAM_a lognormal showing higher values approaching the crack face along line B1 (3, 5, 7, 9, 11 and 13mm away from the crack face), B2 (5, 7, 9, 11 and 13mm away from crack tip) and B3 (far field locations, 41mm away from the crack and 6,16 and 26mm away from the crack mouth)

The lognormal KAM_a values and the SANS results showed similar trends along line B1 and B2 even though the SANS studies only considered cavities up to 600nm diameter. However, studies by Bouchard et al [257] reported the development of cavities 500-

1200nm in diameter in tertiary creep, due to necking. The SEM image in Figure 8.3 (in Case 1) also shows evidence of large cavities around intergranular precipitates at grain boundaries.

8.4.3. Conclusion

Both the EBSD studies of reheat cracks showed higher local misorientation in areas closer to the crack. The KAM maps revealed higher levels of lattice misorientation towards the weld region, where the crack initiated, with strain particularly concentrated at the grain boundaries. However it's still not directly clear from this study whether the misorientation accumulation led to crack or the crack led to misorientation or it's a combination of both. But results from Chapter 5, 6 and 7 clearly shows misorientations more concentrated near grain boundaries with strain. Hence it's more likely that the misorientations lead to cavitation which ultimately lead to cracking. The pattern of deformation shown by the EBSD measurements was confirmed by the hardness survey. KAM was higher in areas with a high density of cavities. This study demonstrates that the areas with high cavity densities have large strain accumulations as well. However it's still not directly clear from this study whether the misorientation accumulation lead to crack or the crack lead to misorientation or it's a combination of both. As already explained earlier in section 8.4, the major mechanism of reheat cracking is creep straining during post weld heat treatments[18] and it's evident from results in chapter 5, and 6 that creep deformation during stress relaxation leads to higher KAM values near grain boundaries. So, it is possible that the misorientation build-up at grain boundaries is associated with cracking. As the header undergoes many load reversals during its service, there might be an influence of creep-fatigue deformation in the formation and growth of reheat crack. But this study did not separately consider the effect of creep-fatigue loading on crack growth.

Another factor that has not been considered in this study is the effect of multi-axial stress components in reheat crack formation and growth. During multi-axial loading, dislocation pile ups in multiple slip planes are possible which could result in step damage in grain boundaries [105]. This study on the reheat crack only revealed the total misorientation accumulation in the component and did not separate misorientation accumulation from different factors mentioned above. However this study demonstrates the potential of EBSD misorientation methods to understand deformation in actual structural components and that the trends observed are similar with other characterization techniques. But further studies will have to be conducted to separate the effect of creep-fatigue loading and multi axial stress components on misorientation build-up.

8.5. Limitation of the high temperature test equipment available

A major limitation of the experiments reported in the thesis was the limited availability of a strain-controlled high temperature mechanical test rig. Because of this, the uniaxial stress relaxation and creep-fatigue tests had to be limited to shorter dwells and a lower number of cycles. The short creep dwells may not well represent the creep dwells experienced in actual operating power generating plants, where structures are exposed to high-temperature constant strain conditions for hours or days and experience thousands of complex load and/or temperature cycles. The strain range experienced in actual conditions is also much lower than that used in this thesis. For practical reasons, in order to get measureable results in limited time, test acceleration methods had to be applied where high stresses were used. However, the temperature and stress regimes used in this study lie in the same areas of the deformation map as real plant conditions so the mechanisms operating in the material should be the same as in real plant.

CHAPTER 9

OVERALL CONCLUSION AND FUTURE WORK

9.1. Overall conclusions

The main objective of the work presented in this thesis was to explore the potential of EBSD to characterize inelastic strains in austenitic stainless steel structural components operating at high temperature. This method works on the principle that the dislocations associated with inelastic deformation lead to local changes in misorientation which can be measured. The material used in the study was type 316H austenitic stainless steel. Although many studies had been conducted on the development of misorientations in plastic and creep deformation, there was nothing in the literature on the effect of stress relaxation and creep-fatigue deformation in this material. The spatial and size distributions of the misorientations developed have been examined and characterised in terms of the metrics KAM, GOS, DGF(0.5), DGF(1), LABFA and TBF.

The major conclusions derived from this thesis are:

1. The misorientations (measured by KAM, GOS, DGF(0.5), DGF(1), and LABFA) and the average hardness increased linearly with increasing plastic strain whereas TBF reduced linearly with plastic strain. Strain rate (comparing 0.025 and 0.0025%/s) and temperature (comparing RT, 550 and 640^0C) had little effect on the long range misorientation build-up during tensile deformation. Lower misorientations were developed in solution annealed material than in ex-service material.
2. DGF(0.5) was more sensitive to the strains developed during stress relaxation from low initial plastic strains whereas KAM and GOS were more sensitive to the

strains developed during stress relaxation from higher plastic strains. A notable finding was that stress relaxation appeared to introduce more misorientations (~30x) than an equivalent plastic strain. Cavities were observed at the grain boundaries after 24 h relaxation from high initial plastic strain (14%).

3. The stress relaxation during each constant strain hold during cyclic deformation depended on the total strain. DGF(0.5) and DGF(1) in cyclically deformed material increased slightly with increasing dwell time (180s to 600s). KAM, GOS and DGF increased linearly with the cumulative inelastic strains. The misorientations induced by low cycle fatigue at room temperature were lower than at 550^{o}C. As for tensile deformation, after the same cyclic loading history the misorientations developed in solution annealed material were lower than in ex-service material.
4. The misorientations (as measured by KAM, GOS and DGF) increased linearly with cumulative inelastic strain up to 600 cycles and TBF decreased linearly with cumulative inelastic strain.
5. The decreasing length scale of the dislocation structures observed with increasing cyclic deformation was consistent with the observed increases in misorientation.
6. EBSD was found to be a better technique for detecting inelastic strains that DPPA using laboratory X-rays or hardness for 316H stainless steel.
7. EBSD studies of reheat cracks showed higher local misorientation in areas closer to the crack with higher levels of lattice misorientation towards the weld region, where the crack initiated.
8. KAM was higher in areas with a high density of cavities. This study demonstrates that the areas with high cavity densities have large strain accumulations as well.

9.2. Suggested future work

The work reported in this thesis has laid a foundation for assessing inelastic strain in service-aged Type 316H stainless steel using EBSD. Due to the limited availability of material and the limited time some important issues could not be fully addressed which suggests the following further work to build on that in this thesis.

1. The uniaxial stress relaxation tests were carried out for a dwell period of 24 hour (Chapter 5) whereas the actual dwell periods in power plants are much longer. Longer dwell tests should be conducted to study the longer term misorientation development in uniaxial stress relaxation.
2. Even though SEM images after stress relaxation at 15% strain showed cavitation around precipitates (Chapter 5), a detailed study of cavitation has yet to be done. A detailed SEM study with SANS can reveal more details about the cavitation.
3. No cyclic tests were performed beyond 600 cycles. The EBSD metrics changed linearly with the cumulative strain up to 600 cycles. Cyclic tests up to failure should be carried out to see whether the linear trend continues up to failure. High KAM was found around cavities: creep tests should be continued into the tertiary region to see whether the KAM around voids increases or remains constant.
4. A detailed TEM investigation with selected area diffraction would reveal the orientation dependence of dislocation structures if specimens could be extracted using FIB to maintain a known relationship between the stress axis and the sample. Alternatively ECCI would allow study of this relationship on a solid specimen.

REFERENCES

[1] "Nuclear Power and Climate Change," *International Atomic Energy Agency*, 2017. [Online]. Available: https://www.iaea.org/topics/nuclear-power-and-climate-change.

[2] G. Evans, "EDF extends life of two nuclear power stations," *The Independent*, 04-Dec-2012.

[3] "Doosan Babcock signs EDF deal to extend nuclear plants," *BBC NEWS*, 19-Feb-2014.

[4] "Hartlepool power station to stay open until 2024," *BBC NEWS*, 05-Nov-2013.

[5] J. Lillington, *The Future of Nuclear Power*. Amsterdam: Elsevier, 2004.

[6] T. Mckeen, "'Advanced gas cooled reactors,' Nuclear energy material and reactors vol. II.," *Nuclear energy material and reactors*, vol. 2. .

[7] H. Hongo, M. Yamazaki, T. Watanabe, M. Tabuchi, and T. Tanabe, "Evaluation for creep properties of 316FR weld metal with miniature weld metal and full-thickness welded joint specimens," *Soc. Mater. Sci. Japan*, vol. 53, no. 5, pp. 566–571, 2004.

[8] Y. Sakanashi, "Measurement of creep deformation in weldments," The Open University, 2013.

[9] D. R. Hayhurst, F. Vakili-Tahami, and J. Q. Zhou, "Constitutive equation for time independent plasticity and creep of 316 stainless steel at 550 °C," *Int. J. Press. Vessel. Pip.*, vol. 80, pp. 97–109, 2003.

[10] B. Chen, P. E. J. Flewitt, D. J. Smith, and C. P. Jones, "An improved method to identify grain boundary creep cavitation in 316H austenitic stainless steel,"

Ultramicroscopy, vol. 111, no. 5, pp. 309–313, 2011.

[11] D. N. Githinji, "Characterisation of Plastic and Creep Strains From Lattice Orientation Measurements, PhD Thesis," The Open University, 2013.

[12] A. Mehmanparast, C. M. Davies, D. W. Dean, and K. M. Nikbin, "The influence of pre-compression on the creep deformation and failure behaviour of Type 316H stainless steel," *Eng. Fract. Mech.*, vol. 110, pp. 52–67, 2013.

[13] A. Mehmanparast, C. M. Davies, D. W. Dean, and K. Nikbin, "Material pre-conditioning effects on the creep behaviour of 316H stainless steel," *Int. J. Press. Vessel. Pip.*, vol. 108–109, pp. 88–93, Aug. 2013.

[14] D. . Hayhurst, F. Vakili-Tahami, and J. . Zhou, "Constitutive equations for time independent plasticity and creep of 316 stainless steel at 550°C," *Int. J. Press. Vessel. Pip.*, vol. 80, no. 2, pp. 97–109, Feb. 2003.

[15] B. Chen, P. E. J. Flewitt, and D. J. Smith, "Microstructural sensitivity of 316H austenitic stainless steel: Residual stress relaxation and grain boundary fracture," *Mater. Sci. Eng. A*, vol. 527, no. 27–28, pp. 7387–7399, Oct. 2010.

[16] P. J. Bouchard, P. J. Withers, S. A. McDonald, and R. K. Heenan, "Quantification of creep cavitation damage around a crack in a stainless steel pressure vessel," *Acta Mater.*, vol. 52, no. 1, pp. 23–34, Jan. 2004.

[17] A. Mehmanparast, C. M. Davies, D. W. Dean, and K. M. Nikbin, "Plastic pre-compression and creep damage effects on the fracture toughness behaviour of Type 316H stainless steel," *Eng. Fract. Mech.*, vol. 131, pp. 26–37, Nov. 2014.

[18] S. Hossain, C. E. Truman, D. J. Smith, R. L. Peng, and U. Stuhr, "A study of the generation and creep relaxation of triaxial residual stresses in stainless steel," *Int. J. Solids Struct.*, vol. 44, no. 9, pp. 3004–3020, May 2007.

[19] P. J. Withers, M. Turski, L. Edwards, P. J. Bouchard, and D. J. Buttle, "Recent

advances in residual stress measurement," *Int. J. Press. Vessel. Pip.*, vol. 85, no. 3, pp. 118–127, Mar. 2008.

[20] A. N. Mehmanparast and M. Ardakani, "A microstructural study of compressive plastic pre-strain effects on creep damage behaviour of type 316H stainless steel," *PVP2011-57268*, pp. 1–6, 2011.

[21] K. Fujiyama and H. Ogawa, Akihiro, Harada, Kazuma, Kimachi, "EBSD Analysis of Grain Strain Distribution for Creep Damaged Modified 9Cr Steel," *J. Soc. Mater. Sci. Japan*, vol. 64, no. 2, pp. 94–99, 2015.

[22] D. J. Dingley, A. J. Wilkinson, G. Meaden, and P. S. Karamched, "Elastic strain tensor measurement using electron backscatter diffraction in the SEM.," *J. Electron Microsc. (Tokyo).*, vol. 59 Suppl 1, pp. S155-63, 2010.

[23] T. B. Britton, J. Jiang, R. Clough, E. Tarleton, a. I. Kirkland, and a. J. Wilkinson, "Assessing the precision of strain measurements using electron backscatter diffraction - part 1: Detector assessment," *Ultramicroscopy*, vol. 135, no. December, pp. 126–135, 2013.

[24] D. Dingley and A. Wilkinson, "Elastic strain tensor measurement using electron backscatter diffraction in the SEM," *J. Electron Microsc. (Tokyo).*, vol. 59 Suppl 1, pp. S155-63, 2010.

[25] K. Fujiyama, K. Harada, A. Ogawa, and H. Kimachi, "EBSD analysis of Grain strain distribution for creep damaged SUS304HTB," *J. Soc. Mater. Sci. Japan*, vol. 64, no. 2, pp. 88–93, 2015.

[26] K. Fujiyama, A. Ogawa, K. Harada, and H. Kimachi, "EBSD analysis of grain strain distribution for creep damaged modified 9Cr steel," *J. Soc. Mater. Sci. Japan*, vol. 64, no. 2, pp. 94–99, 2015.

[27] D. N. Githinji, S. M. Northover, P. J. Bouchard, and M. A. Rist, "An EBSD Study

of the Deformation of Service-Aged 316 Austenitic Steel," *Metall. Mater. Trans. A*, vol. 44A, pp. 4150–4167, May 2013.

[28] M. Kamaya, A. J. Wilkinson, and J. M. Titchmarsh, "Quantification of plastic strain of stainless steel and nickel alloy by electron backscatter diffraction," *Acta Mater.*, vol. 54, no. 2, pp. 539–548, Jan. 2006.

[29] K. Kubushiro, Y. Sakakibara, and T. Ohtani, "Creep strain analysis of austenitic stainless steel by SEM/EBSD," *J. Soc. Mater. Sci. Japan*, vol. 64, no. 2, pp. 106–112, 2015.

[30] S. Subedi, R. Pokharel, and A. D. Rollett, "Orientation Gradients in relation to grain boundaries at varying strain level and spatial resolution," *Mater. Sci. Eng. A*, vol. 638, pp. 348–356, 2015.

[31] S. I. Wright, M. M. Nowell, and D. P. Field, "A Review of Strain Analysis Using Electron Backscatter Diffraction," *Microsc. Microanal.*, vol. 17, no. 3, pp. 316–329, 2011.

[32] R. Yoda, T. Yokomaku, and N. Tsuji, "Plastic deformation and creep damage evaluations of type 316 austenitic stainless steels by EBSD," *Mater. Charact.*, vol. 61, no. 10, pp. 913–922, Oct. 2010.

[33] *Steel products manual: Stainless steels*. Iron & Steel Society, 1999.

[34] H. Bhadeshia and R. Honeycombe, *Steels: Microstructure and Properties*. 2006.

[35] J. C.M.Farrar, *The alloy tree: A guide to low-alloy steels, stailess steels and nickel-base alloys*. Woodhead Publishing Limited.

[36] M.McGuire, *Stainless Steels For Design Engineers*. ASM International®, 2008.

[37] T. Sourmail, "Precipitation in creep resistant austenitic stainless steels," *Mater. Sci. Technol.*, vol. 17, no. 1, pp. 1–14, 2001.

[38] B. Weiss and S. R, "Phase instabilities during high temperature exposure of 316

austenitic stainless steel," *Metall. Mater. Trans. B*, vol. 3, no. 4, pp. 851–866, 1972.

[39] S. Briks, S. Roberts, and R. Leese, *Advances in Materials Technology for Fossil Power Plants 2007*, no. 1016250. 2007.

[40] K. H. Lo, C. H. Shek, and J. K. L. Lai, "Recent developments in stainless steels," *Mater. Sci. Eng. R Reports*, vol. 65, no. 4–6, pp. 39–104, 2009.

[41] J. C. Lippold, W. A. B. III, and I. Varol, "Heat-affected zone liquation cracking in austenitic and duplex stainless steels," *Weld. Res. Suppl.*, no. January, pp. 1–14, 1992.

[42] J. O. Nilsson, "Effect of Nitrogen on Creep-Fatigue Interaction in Austenitic Stainless Steels at 600°C," in *ASTM STP 492 symposium on Low Cycle Fatigue*, 1988, pp. 543–557.

[43] D. W. Kim, J. H. Chang, and W. S. Ryu, "Evaluation of the creep-fatigue damage mechanism of Type 316L and Type 316LN stainless steel," *Int. J. Press. Vessel. Pip.*, vol. 85, no. 6, pp. 378–384, 2008.

[44] H. Berns, V. Gavriljuk, and S. Riedner, *High Interstitial Stainless Austenitic Steels*. Springer.

[45] T.-U. K. and R. V. Fujio Abe, Ed., *Creep-resistant Steels*. Woodhead Publishing Ltd, 2008.

[46] L. P. Stoter, "Thermal ageing effects in AISI type 316 stainless steel," *J. Mater. Sci.*, vol. 16, no. 4, pp. 1039–1051, 1981.

[47] N. Terao and B. Sasmal, "Precipitation of M ~ 8C6 Type Carbide on Twin Boundaries in Austenitic Stainless Steels," vol. 133, pp. 117–133, 1980.

[48] F. Zhu, R. G. Faulkner, R. L. Higginson, S. Spindler, A. Baker, and C. D. Hamm, "Prediction of microstructural evolution in austenitic stainless steels for extended life power plant applications," in *Advances in Materials Technology for Fossil*

Power Plants: Proceedings of the 7th International Coference, pp. 949–969.

[49] F. R. N. Nabarro, *Dislocations in Solids*, vol. 12. 2004.

[50] D. Hull and D. J. Bacon, “Introduction to Dislocations,” 2001.

[51] B. Verlinden, J. Driver, I. Samajdar, and R. Doherty, *Thermo-mechanical processing of metallic materials*, 2007th ed. Elsevier Ltd, 2007.

[52] *Component reliability under creep-fatigue conditions*. Springer-Verlag Wein GmbH, 1998.

[53] G. E. Dieter and D. Bacon, *Mechanical Metallurgy*. McGraw-Hill Book Company, 1988.

[54] J. A. Venables, “Deformation twinning in face-centred cubic metals,” *Philos. Mag.*, vol. 6, no. 63, pp. 379–396, 1961.

[55] M. A. Meyers and K. K. Chawla, *Mechanical Behavior of Materials*. 2009.

[56] D. J. Bowden, “Assessment of Cobalt-Free Hardfacing Stainless Steel Alloys for Nuclear,” 2016.

[57] W. F. Hosford, *The mechanics of crystals and textured polycrystals*. Oxford University Press(USA), 1993.

[58] V. Randle, “Twinning-related grain boundary engineering,” *Acta Mater.*, vol. 52, no. 14, pp. 4067–4081, 2004.

[59] A. Heinz and P. Neumann, “Crack initiation during high cycle fatigue of an austenitic steel,” *Acta Metall. Mater.*, vol. 38, no. 10, pp. 1933–1940, 1990.

[60] S. Kobayashi, M. Hirata, S. Tsurekawa, and T. Watanabe, “Grain boundary engineering for control of fatigue crack propagation in austenitic stainless steel,” *Procedia Eng.*, vol. 10, pp. 112–117, 2011.

[61] A. H. Cook, W. B. Harland, N. F. Hughes, A. Putnis, J. G. Sclater, and M. R. A. Thomson, *Creep of crystals*. 1985.

[62] R. T. Tenchev, *High temperature component life assessment*, vol. 32, no. 1–2. 1995.

[63] J. Lemaitre and R. Desmorat, *Engineering Damage Mechanics*. 2005.

[64] M. Ashby and H. Frost, *Deformation-Mechanism Maps: The Plasticity and Creep of Metals and Ceramics*. Oxford:Pergamon Press, 1982.

[65] K. D. Challenger and J. Moteff, "Quantitative characterization of the substructure of AISI 316 stainless steel resulting from creep," *Metall. Trans.*, vol. 4, no. 3, pp. 749–755, 1973.

[66] C. C. Bampton, I. P. Jones, and M. H. Loretto, "Stacking fault energy measurements in some austenitic stainless steels," *Acta Metall.*, vol. 26, pp. 39–51, 1978.

[67] H. T. Yao, F. Z. Xuan, Z. Wang, and S. T. Tu, "A review of creep analysis and design under multi-axial stress states," *Nucl. Eng. Des.*, vol. 237, no. 18, pp. 1969–1986, Oct. 2007.

[68] H. Riedel, *Fracture at High Temperatures*, vol. 53. Springer-Verlag Berlin GmbH, 1987.

[69] A. Pagliarello and J. Beddoes, "The stress relaxation and creep behaviour of a manganese-stabilized austenitic stainless steel," *J. Strain Anal. Eng. Des.*, vol. 44, no. 3, pp. 201–209, 2009.

[70] J. Beddoes, "Prediction of creep properties for two nickel-base superalloys from stress relaxation testing," *J. Strain Anal. Eng. Des.*, vol. 46, no. 6, pp. 416–427, 2011.

[71] D. A. Woodford, "Advances in the use of stress relaxation data for design and life assessment in combustion turbines," *JSME international Journal*, vol. 45, no. 1. pp. 98–103, 202AD.

[72] J. F. Chen, J. T. Jiang, L. Zhen, and W. Z. Shao, “Stress relaxation behavior of an Al-Zn-Mg-Cu alloy in simulated age-forming process,” *J. Mater. Process. Technol.*, vol. 214, no. 4, pp. 775–783, 2014.

[73] M. Ivanchenko, “Dynamic Strain Aging of Austenitic Stainless Steels and Ni Base Alloys,” School of Science and Technology, 2010.

[74] C. Cornet *et al.*, “Effects of temperature and hold time on dynamic strain aging in a nickel based superalloy,” *Mater. High Temp.*, vol. 31, no. 3, pp. 226–232, 2014.

[75] A. Yilmaz, “The Portevin – Le Chatelier effect: a review of experimental findings,” *Sci. Technol. Adv. Mater.*, vol. 12, no. March, pp. 1–16, 2011.

[76] K. Peng, K. Qian, and W. Chen, “Effect of dynamic strain aging on high temperature properties of austenitic stainless steel,” *Mater. Sci. Eng. A*, vol. 379, no. 1–2, pp. 372–377, 2004.

[77] M. Calmunger, G. Chai, and S. Johansson, “Influence of dynamic strain ageing on damage in austenitic stainless steels.”

[78] S. Kumar, J. Kró, and E. Pink, “Mechanism of serrated flow in binary Al-Li alloys,” *Scr. Mater.*, vol. 35, no. 6, pp. 775–780, 1996.

[79] F. R. N. Nabarro, “Distribution of solute atoms round a moving dislocation,” *Mater. Sci. Eng. A*, vol. 400–401, no. 1–2 SUPPL., pp. 22–24, 2005.

[80] J. Lepinoux, D. Maziere, V. Pontikis, and G. Saada, Eds., *Multiscale Phenomena in Plasticity: from experiment to phenomenology, modelling and materials engineering*. Springer-Science+Business Media, B.V, 2000.

[81] M. T. Nogueira and M. A. Fortes, “Conditions for periodic serrations in tensile curves,” *Scr. Metall.*, vol. 18, no. c, pp. 505–508, 1984.

[82] K. Prewo, J. C. M. Li, and M. Gensamer, “Lüders band motion in iron,” *Metall. Trans.*, vol. 3, no. 8, pp. 2261–2269, 1972.

[83] C. E. Feltner and C. Laird, “Cyclic stress-strain response of F.C.C. metals and alloys—I Phenomenological experiments,” *Acta Metall.*, vol. 15, no. l, pp. 1621–1632, 1967.

[84] U. Essmann and H. Mughrabi, “Annihilation of dislocations during tensile and cyclic deformation and limits of dislocation densities,” *Philos. Mag. A*, vol. 40, no. 6, pp. 731–756, 1979.

[85] B. J, “On the change of the position of the elastic limit of iron and steel under cyclic variations of stress,” Munich, 1886.

[86] C. E. Feltner and C. Laird, “Cyclic stress-strain response of F.C.C. metals and alloys—II Dislocation structures and mechanisms,” *Acta Metall.*, vol. 15, pp. 1633–1653, 1967.

[87] H. Mughrabi, “Fatigue, an everlasting materials problem - Still en vogue,” *Procedia Eng.*, vol. 2, no. 1, pp. 3–26, 2010.

[88] J. Grosskreutz, “Fatigue mechanisms in the sub-creep range,” in *Metal Fatigue Damage: Mechanism, Detection , Avoidance and Repair: With Special Reference to Gas Turbine Components*, 1971, vol. STP495.

[89] M. Bílý, Ed., *Cyclic deformation and fatigue of metals*. Elsevier, 1993.

[90] J. Schijve, Ed., *Fatigue of Structures and Materials*. Springer, 2001.

[91] T. Magnin, C. Ramade, J. Lepinoux, and L. P. Kubin, “Low-cycle fatigue damage mechanisms of f.c.c. and b.c.c. polycrystals: Homologous behaviour?,” *Mater. Sci. Eng. A*, vol. 118, no. C, pp. 41–51, 1989.

[92] A. F. Armas, O. R. Bettin, I. Alvarez-Armas, and G. H. Rubiolo, “Strain aging effects on the cyclic behavior of austenitic stainless steels,” *J. Nucl. Mater.*, vol. 155–157, no. 1988, pp. 644–649, 1988.

[93] R. Hormozi, F. Biglari, and K. Nikbin, “Experimental and numerical creep-fatigue

study of Type 316 stainless steel failure under high temperature LCF loading condition with different hold time," *Eng. Fract. Mech.*, vol. 141, pp. 19–43, 2015.

[94] X.-L. Yan, X.-C. Zhang, S.-T. Tu, S.-L. Mannan, F.-Z. Xuan, and Y.-C. Lin, "Review of creep–fatigue endurance and life prediction of 316 stainless steels," *Int. J. Press. Vessel. Pip.*, vol. 126–127, pp. 17–28, 2015.

[95] J. Wareing, "Creep-fatigue interaction in austenitic stainless steels," *Metall. Trans. A*, vol. 8, no. 5, pp. 711–721, 1977.

[96] R. Hormozi, F. Biglari, and K. Nikbin, "Experimental study of type 316 stainless steel failure under LCF/TMF loading conditions," *Int. J. Fatigue*, vol. 75, pp. 153–169, 2015.

[97] K. Yamaguchi and K. Kanazawa, "Effect of strain wave shape on high temperature fatigue life of a type 316 steel and application of the strain range partitioning method," *Metall. Trans. A*, vol. 11, no. 12, pp. 2019–2027, 1980.

[98] M. Willis, A. Mcdonaugh-smith, and R. Hales, "Prestrain effects on creep ductility of a 316 stainless steel light forging," vol. 76, pp. 355–359, 1999.

[99] D. F. Li, N. P. O'Dowd, C. M. Davies, and K. M. Nikbin, "A review of the effect of prior inelastic deformation on high temperature mechanical response of engineering alloys," *Int. J. Press. Vessel. Pip.*, vol. 87, no. 10, pp. 531–542, 2010.

[100] S. Sivaprasad, S. K. Paul, A. Das, N. Narasaiah, and S. Tarafder, "Cyclic plastic behaviour of primary heat transport piping materials: Influence of loading schemes on hysteresis loop," *Mater. Sci. Eng. A*, vol. 527, no. 26, pp. 6858–6869, 2010.

[101] "R5, Assessment Procedure for the High Temperature Response of Structures, Issue 3.," 2003.

[102] D. M. Knowles, "R5 High Temperature Creep-Fatigue Life Assessment for Austenitic Weldments," *Procedia Eng.*, vol. 86, pp. 315–326, 2014.

[103] J. Jelwan, M. Chowdhury, and G. Pearce, “Design for creep: A critical examination of some methods,” *Eng. Fail. Anal.*, vol. 27, pp. 350–372, 2013.

[104] C. Maharaj, J. P. Dear, and A. Morris, “A review of methods to estimate creep damage in low-alloy steel power station steam pipes,” *Strain*, vol. 45, pp. 316–331, 2009.

[105] R. P. Skelton, I. W. Goodall, G. A. Webster, and M. W. Spindler, “Factors affecting reheat cracking in the HAZ of austenitic steel weldments,” *Int. J. Press. Vessel. Pip.*, vol. 80, no. 7–8, pp. 441–451, Jul. 2003.

[106] Q. Auzoux, L. Allais, C. Caës, I. Monnet, a. F. Gourgues, and a. Pineau, “Effect of pre-strain on creep of three AISI 316 austenitic stainless steels in relation to reheat cracking of weld-affected zones,” *J. Nucl. Mater.*, vol. 400, no. 2, pp. 127–137, May 2010.

[107] Q. Auzoux, L. Allias, A. Pineau, and A. F. Gourgeus, “Reheat cracking in austenitic stainless steels,” in *Proceedings of the 14th Biennal European Conference on Fracture*, 2000, pp. 137–144.

[108] N. Sakaguchi, Y. Ohguchi, T. Shibayama, S. Watanabe, and H. Kinoshita, “Surface cracking on Σ3, Σ9 CSL and random grain boundaries in helium implanted 316L austenitic stainless steel,” *J. Nucl. Mater.*, vol. 432, no. 1–3, pp. 23–27, 2013.

[109] D. N. Wasnik, V. Kain, I. Samajdar, B. Verlinden, and P. K. De, “Resistance to sensitization and intergranular corrosion through extreme randomization of grain boundaries,” *Acta Mater.*, vol. 50, no. 18, pp. 4587–4601, 2002.

[110] Y. J. Jin, H. Lu, C. Yu, and J. J. Xu, “Study on grain boundary character and strain distribution of intergranular cracking in the CGHAZ of T23 steel,” *Mater. Charact.*, vol. 84, pp. 216–224, 2013.

[111] F. Ueno, K. Aoto, and Y. Wada, “Study on metallographic damage parameter in creep-damage-dominant condition under creep-fatigue loading,” *Nucl. Eng. Des.*, vol. 162, no. 1, pp. 85–95, 1996.

[112] G. Sposito, C. Ward, P. Cawley, P. B. Nagy, and C. Scruby, “A review of non-destructive techniques for the detection of creep damage in power plant steels,” *NDT E Int.*, vol. 43, no. 7, pp. 555–567, 2010.

[113] C. Maharaj, “Creep analysis of Incoloy 800H reformer outlet pigtail tubes,” 2001.

[114] H. Altenbach and J. J. Skrzypek, Eds., *Creep and damage in materials and structures*. Springer-Verlag Wein GmbH.

[115] E. J. Wightman, *Instrumentation in Process Control*. London Butterworths, 1972.

[116] S. Shibli and G. Merckling, “Creep and Fracture in High Temperature Components: Design and Life Assessment Issues,” in *ECCC Creep Conference*, 2005.

[117] K. Fujiyama, T. Iseki, A. Komatsu, and N. Okabe, “Creep life assessment of 2.25Cr-1Mo piping steel and of its simulated HAZ material,” *Mater. Sci. Res. Int.*, vol. 3, no. 4, pp. 237–243, 1997.

[118] K. Fujiyama *et al.*, “Creep damage assessment of 10Cr-1Mo-1W-VNbN steel forging through EBSD observation,” *Int. J. Press. Vessel. Pip.*, vol. 86, pp. 570–577, Sep. 2009.

[119] B. R. Cardoso, C. F. T. Matt, H. C. Furtado, and L. H. de Almeida, “Creep Damage Evaluation in High-Pressure Rotor Based on Hardness Measurement,” *J. Mater. Eng. Perform.*, vol. 24, no. Ref 1, pp. 2784–2791, 2015.

[120] A. Tomor and E. Verstrynge, “A joint fatigue-creep deterioration model for masonry with acoustic emission based damage assessment,” *Constr. Build. Mater.*, vol. 43, pp. 575–588, 2013.

[121] T. H. Simm, “The use of diffraction peak profile analysis in studying the plastic deformation of metals, PhD Thesis,” University of Manchester, 2012.

[122] P. J. Bouchard, P. J. Withers, S. a. McDonald, and R. K. Heenan, “Quantification of creep cavitation damage around a crack in a stainless steel pressure vessel,” *Acta Mater.*, vol. 52, no. 1, pp. 23–34, Jan. 2004.

[123] H. Jazaeri, P. J. Bouchard, M. T. Hutchings, A. A. Mamun, and R. K. Heenan, “Application of small angle neutron scattering to study creep cavitation in stainless steel weldments,” *Mater. Sci. Technol.*, vol. 31, no. 5, pp. 535–539, 2015.

[124] O. Engler and V. Randle, *Macrotexture Analysis*, 2nd ed. Taylor & Francis Group, LLC, 2009.

[125] V. Randle, *Microtexture determination and its aplications*, Second. Maney Publishing, 2008.

[126] A. J. Wilkinson, D. J. Dingley, and G. Meaden, “Strain Mapping Using Electron Backscatter Diffraction,” in *Electron Backscatter Diffraction in Materials Science*, A. J. Schwartz, M. Kumar, B. L. Adams, and D. P. Field, Eds. Springer US, 2009, pp. 231–249.

[127] A. Schwartz, M. Kumar, B. Adams, and D. Field, *Electron Backscatter Diffraction in Material Science*. Springer, 2000.

[128] A. J. Wilkinson, E. E. Clarke, T. B. Britton, P. Littlewood, and P. S. Karamched, “High-resolution electron backscatter diffraction: an emerging tool for studying local deformation,” *J. Strain Anal. Eng. Des.*, vol. 45, no. 5, pp. 365–376, Jul. 2010.

[129] F. J. Humphreys, M. Materials, and S. Centre, “Grain and subgrain characterisation by electron backscatter diffraction,” *J. Mater. Sci.*, vol. 36, pp. 3833–3854, 2001.

[130] K. Nomura, K. Keiji, Y. Sakakibara, S. Takahashi, and H. Yoshizawa, “Effect of

Grain Size on Plastic Strain Analysis by EBSD for Austenitic Stainless Steels with Tensile Strain at 650°C," *J. Soc. Mater. Sci. Japan*, vol. 61, no. 4, pp. 371–376, 2012.

[131] M. Kamaya, "Assessment of local deformation using EBSD: quantification of accuracy of measurement and definition of local gradient.," *Ultramicroscopy*, vol. 111, no. 8, pp. 1189–99, Jul. 2011.

[132] A. Sáez-Maderuelo, L. Castro, and G. de Diego, "Plastic strain characterization in austenitic stainless steels and nickel alloys by electron backscatter diffraction," *J. Nucl. Mater.*, vol. 416, no. 1–2, pp. 75–79, Sep. 2011.

[133] R. S. Coelho, a. Kostka, J. dos Santos, and a. R. Pyzalla, "EBSD Technique Visualization of Material Flow in Aluminum to Steel Friction-stir Dissimilar Welding," *Adv. Eng. Mater.*, vol. 10, no. 12, pp. 1127–1133, Dec. 2008.

[134] M. Kamaya, J. Quinta da Fonseca, L. . Li, and M. Preuss, "Local plastic strain measurement by EBSD," *Appl. Mech. Mater.*, vol. 7–8, pp. 173–179, 2007.

[135] M. Kamaya, "Assessment of local deformation using EBSD: Quantification of local damage at grain boundaries," *Mater. Charact.*, vol. 66, pp. 56–67, Apr. 2012.

[136] M. A. Othon and M. M. Morra, "EBSD Characterization of Residual Plastic Strain Across Alloy 182 Weld Joints," *Microsc. Soc. Am.*, vol. 11, no. Suppl 2, pp. 522–523, 2005.

[137] S. R. Moturu, "Characterization of residual stress and plastic strain in austenitic stainless steel 316L(N) weldments, PhD Thesis," The Open University, 2015.

[138] V. D. Vijayanand, V. Ganesan, J. Ganesh Kumar, P. Parameswaran, Naveena, and K. Laha, "Assessment of Creep Strain Distribution Across Base Metal of 316LN Austenitic Stainless Steel Weld Joint by an EBSD-Based Parameter," *Metall. Mater. Trans. A Phys. Metall. Mater. Sci.*, vol. 46, no. 11, pp. 5456–5466, 2015.

[139] M. Shamanian, M. Mohammadnezhad, M. Amini, A. Zabolian, and J. A. Szpunar, "Electron Backscatter Diffraction Analysis of Joints Between AISI 316L Austenitic/UNS S32750 Dual-Phase Stainless Steel," *J. Mater. Eng. Perform.*, 2015.

[140] K. Fujiyama, H. Kimachi, T. Tsuboi, H. Hagiwara, S. Ogino, and Y. Mizutani, "Damage Assessment of Heat Resistant Steels through Electron BackScatter Diffraction Strain Analysis under Creep and Creep-Fatigue Conditions," *J. Solid Mech. Mater. Eng.*, vol. 6, no. 6, pp. 530–544, 2012.

[141] H. Shigeyama, R. Sugiura, T. Matsuzaki, and A. T. Yokobori, "Micro- and macro-creep damage formation for P92 under multiaxial stress related to circular notched specimen," *Mater. Sci. Technol.*, vol. 30, no. 1, pp. 43–49, 2014.

[142] M. Kamaya *et al.*, "Round robin crystal orientation measurement using EBSD for damage assessment," *Bull. JSME Mech. Eng. J.*, vol. 3, no. 3, 2016.

[143] X. Chen, Z. Yang, M. A. Sokolov, D. L. Erdman, K. Mo, and J. F. Stubbins, "Low cycle fatigue and creep-fatigue behavior of Ni-based alloy 230 at 850??C," *Mater. Sci. Eng. A*, vol. 563, pp. 152–162, 2013.

[144] M. Muramatsu, T. Suzuki, and Y. Nakasone, "Effects of Microstructure on Creep-fatigue Properties in Modified 9Cr-1Mo Steel," pp. 1–10, 2013.

[145] C. Schayes, J. Bouquerel, J. B. Vogt, F. Palleschi, and S. Zaefferer, "A comparison of EBSD based strain indicators for the study of Fe-3Si steel subjected to cyclic loading," *Mater. Charact.*, vol. 115, pp. 61–70, 2016.

[146] J. B. Vogt, J. Bouquerel, F. Léaux, and F. Palleschi, "Fatigue damage assessment of alternator fans by EBSD," *Procedia Eng.*, vol. 66, pp. 608–614, 2013.

[147] R. Unnikrishnan *et al.*, "Effect of heat input on the microstructure, residual stresses and corrosion resistance of 304L austenitic stainless steel weldments," *Mater.*

Charact., vol. 93, pp. 10–23, Jul. 2014.

[148] C.-M. Lin, H.-L. Tsai, C.-D. Cheng, and C. Yang, "Effect of repeated weld-repairs on microstructure, texture, impact properties and corrosion properties of AISI 304L stainless steel," *Eng. Fail. Anal.*, vol. 21, pp. 9–20, Apr. 2012.

[149] M. A. Othon and M. M. Morra, "EBSD Characterization of the Deformation Behavior of Alloy 182 Weld Metal," *Microsc. Microanal.*, vol. 14, no. Supplement S2, pp. 934–935, 2008.

[150] L. Lan, C. Qiu, and D. Zhao, "EBSD analysis of HAZ microstructure characteristics of a high strength low welding crack susceptibility steel," *Adv. Mater. Res.*, vol. 152–153, pp. 852–855, 2011.

[151] J. Guo, S. Amira, P. Gougeon, and X. Chen, "Effect of the surface preparation techniques on the EBSD analysis of a friction stir welded AA1100-B 4 C metal matrix composite," *Mater. Charact.*, vol. 62, no. 9, pp. 865–877, 2011.

[152] K. Fujiyama *et al.*, "Creep-damage assessment of high chromium heat resistant steels and weldments," *Mater. Sci. Eng. A*, vol. 510–511, pp. 195–201, 2009.

[153] R. Badji, B. Bacroix, and M. Bouabdallah, "Texture, microstructure and anisotropic properties in annealed 2205 duplex stainless steel welds," *Mater. Charact.*, vol. 62, no. 9, pp. 833–843, Sep. 2011.

[154] J. Kell, J. R. Tyrer, R. L. Higginson, and R. C. Thomson, "Microstructural characterization of autogenous laser welds on 316L stainless steel using EBSD and EDS.," *J. Microsc.*, vol. 217, no. Pt 2, pp. 167–73, Mar. 2005.

[155] J. Hou *et al.*, "Residual strain measurement and grain boundary characterization in the heat-affected zone of a weld joint between Alloy 690TT and Alloy 52," *J. Nucl. Mater.*, vol. 397, no. 1–3, pp. 109–115, Feb. 2010.

[156] M. A. Othon, M. M. Morra, S. Ooki, and R. B. Rebak, "Assessing Residual Strains

in nuclear power reactor internal components weld mockups of nickel alloys using EBSD," *Press. Vessel. Pip. Conf.*, vol. 97350, pp. 1–10, 2013.

[157] E. Ranjbarnodeha, S. Weissb, S. Hankeb, and A. Fischerb, "EBSD Characterization of the effect of welding parameters on HAZ of AISI 409," *J. Min. Metall. Sect. B Metall.*, vol. 48, no. 1, pp. 115–121, 2012.

[158] Z. Lu, T. Shoji, S. Yamazaki, and K. Ogawa, "Characterization of microstructure, local deformation and microchemistry in Alloy 600 heat-affected zone and stress corrosion cracking in high temperature water," *Corros. Sci.*, vol. 58, pp. 211–228, 2012.

[159] L. N. Brewer, M. A. Othon, L. M. Young, and T. M. Angeliu, "Misorientation Mapping for Visualization of Plastic Deformation via Electron Back-Scattered Diffraction," *Microsc. Microanal.*, vol. 12, pp. 85–91, 2006.

[160] V. Gaffard and J. Besson, "High Temperature Creep Flow and Damage Properties of the Weakest Area of 9Cr1Mo – NbV Martensitic Steel Weldments," vol. 45, no. 12, pp. 1915–1924, 2005.

[161] Y. Li, V. Aubin, C. Rey, and P. Bompard, "Polycrystalline numerical simulation of variable amplitude loading effects on cyclic plasticity and microcrack initiation in austenitic steel 304L," *Int. J. Fatigue*, vol. 42, pp. 71–81, Sep. 2012.

[162] F. . Humphreys, "Characterisation of fine-scale microstructures by electron backscatter diffraction (EBSD)," *Scr. Mater.*, vol. 51, no. 8, pp. 771–776, Oct. 2004.

[163] A. J. Schwartz, M. Kumar, B. L. Adams, and D. P. Field, *Electron Backscatter Diffraction in Materials Science*, 2nd Editio. Springer Science+Business Media, LLC, 2010.

[164] A. Glage *et al.*, "Cyclic Deformation of Powder Metallurgy Stainless Steel/Mg-

PSZ Composite Materials," *Steel Res. Int.*, vol. 83, no. 6, pp. 554–564, Jun. 2012.

[165] "BS EN ISO 6892-1:2016 Metallic materials. Tensile testing. Method of test at room temperature," 2016.

[166] "BS EN ISO 6892-2:2011 Metallic materials. Tensile testing. Method of test at elevated temperature," 2011.

[167] "ASTM E1012 - 14 Standard Practice for Verification of Testing Frame and Specimen Alignment Under Tensile and Compressive Axial Force Application."

[168] J. R. Goldstein, J., Newbury, D.E., Joy, D.C., Lyman, C.E., Echlin, P., Lifshin, E., Sawyer, L., Michael, *Scanning Electron Microscopy and X-ray Microanalysis*, Third. Springer, 2003.

[169] D. Aliya, *Metallographic sectioning and specimen extraction.*, vol. 9. 2004.

[170] M. A. Crimp, B. A. Simkin, and B. C. Ng, "Demonstration of the g · b x u = 0 edge dislocation invisibility criterion for electron channelling contrast imaging," *Philos. Mag. Lett.*, vol. 81, no. 12, pp. 833–837, 2001.

[171] N. Tanaka, "Scanning Transmission Electron Microscopy of Nanomaterials: Basics of Imaging and Analysis." 2014.

[172] F. Bachmann, R. Hielscher, and H. Schaeben, "Texture Analysis with MTEX – Free and Open Source Software Toolbox," *Solid State Phenom.*, vol. 160, pp. 63–68, 2010.

[173] S. Mitsche, P. Poelt, and C. Sommitsch, "Recrystallization behaviour of the nickel-based alloy 80 A during hot forming," *J. Microsc.*, vol. 227, no. 3, pp. 267–274, 2007.

[174] "E2627-13 Standard Practice for Determining Average Grain Size Using Electron Backscatter Diffraction (EBSD) in Fully Recrystallized Polycrystalline," 2014.

[175] "OriginLab/Origin Help/ Appendix 3 - Built-in Functions/ Curve Fitting

Functions." [Online]. Available: https://www.originlab.com/doc/Origin-Help/LogNormal-FitFunc.

[176] D. G Brandon, "The structure of high-angle grain boundaries," *Acta Metall.*, vol. 14, pp. 1479–1484, 1966.

[177] K. Fujiyama, T. Iseki, A. Komatsu, and N. Okabe, "Creep life assessment of 2.25Cr-1Mo piping steel and of its simulated HAZ material," *J. Soc. Mater. Sci. Japan*, vol. 46, pp. 237–243, 1997.

[178] "BS EN ISO 6507-1:2005 Metallic materials. Vickers hardness test. Test method," 2006.

[179] "BS EN ISO 14577-1:2015 Metallic materials. Instrumented indentation test for hardness and materials parameters. Test method."

[180] L. Lutterotti and S. Gialanella, "X-ray diffraction characterization of heavily deformed metallic specimens," *Acta Mater.*, vol. 46, no. 1, pp. 101–110, 1998.

[181] Y. Yin, R. G. Faulkner, and F. Starr, "Austenitic steels and alloys for power plants," in *Structural alloys for power plants: Operational challenges and high-temperature materials*, 2014, p. 119.

[182] A. Strang, Ed., *Materials for high temperature power generation and process plant applications*. IOM Communications Ltd, 2000.

[183] "Standard Test Methods for Determining Average Grain Size (ASTM E112-13)," West Conshohocken, PA, 2013.

[184] "ASTM-E2627-10: Standard practice for determining average grain size using electron backscatter diffraction (EBSD) in fully recrystallized polycrystalline materials," 2010.

[185] "Channel 5 Software, HKL Technology." 2017.

[186] J. C. M. Li, "Petch Relation and Grain Boundary Sources," *Trans. Metall. Soc.*

AIME, vol. 227, pp. 239–247, 1963.

[187] C. Fukuoka, K. Morishima, H. Yoshizawa, and K. Mino, "Misorientation development in grains of tensile strained and crept 2.25%Cr-1%Mo steel," *Scr. Mater.*, vol. 46, no. 1, pp. 61–66, 2002.

[188] V. Y. Gertsman and K. Tangri, "A study of grain boundary statistics in 304 and 316L stainless steels," *Philos. Mag. A*, vol. 64, no. 6, pp. 1319–1330, 1991.

[189] K. K. and J. W. Wyrzykowski, "The effect of twin boundaries on the yield stress of a material," *J. Mater. Process. Technol.*, vol. 64, pp. 223–230, 1997.

[190] I. Karaman, H. Sehitoglu, H. J. Maier, and Y. I. Chumlyakov, "Competing mechanisms and modelling of deformation in austenitic stainless steel single crystals with and without nitrogen," *Acta Mater.*, vol. 49, pp. 3919–3933, 2001.

[191] P. R. Howell, J. O. Nilsson, and G. L. Dunlop, "The effect of creep deformation on the structure of twin boundaries," *Philos. Mag. A Phys. Condens. Matter, Struct. Defects Mech. Prop.*, vol. 38, no. 1, pp. 39–47, 1978.

[192] H. Wang, B. Clausen, C. N. Tomé, and P. D. Wu, "Studying the effect of stress relaxation and creep on lattice strain evolution of stainless steel under tension," *Acta Mater.*, vol. 61, pp. 1179–1188, 2013.

[193] Y. Kaji *et al.*, "Evaluation of in-pile and out-of-pile stress relaxation in 316L stainless steel under uniaxial loading," *J. Nucl. Mater.*, vol. 307–311, no. 1 SUPPL., pp. 331–334, 2002.

[194] H. Pommier, E. P. Busso, T. F. Morgeneyer, and A. Pineau, "Intergranular damage during stress relaxation in AISI 316L-type austenitic stainless steels: Effect of carbon, nitrogen and phosphorus contents," *Acta Mater.*, vol. 103, no. June, pp. 893–908, 2016.

[195] T. L. Burnett *et al.*, "Multiscale 3D analysis of creep cavities in AISI type 316

stainless steel," *Mater. Sci. Technol.*, vol. 31, no. 5, pp. 522–534, Mar. 2015.

[196] D. Caillard and J. L. Martin, "Interactions Between Dislocations and Small-size Obstacles," in *Thermally Activated Mechanisms in Crystal Plasticity*, Pergamon, 2003.

[197] A. Varma, A. Gokhale, J. Jain, K. Hariharan, P. Cizek, and M. Barnett, "Investigation of stress relaxation mechanisms for ductility improvement in SS316L," *Philos. Mag.*, vol. 98, no. 3, pp. 165–181, 2018.

[198] Y. Takahashi, "Effect of cyclic loading on subsequent creep behaviour and its implications in creep-fatigue life assessment," *Mater. High Temp.*, vol. 32, no. 5, pp. 492–501, 2015.

[199] Michael E. Kassner and Maria-Teresa Perez-Prado, *Fundamentals of creep in metals and alloys*. ELSEVIER, 2004.

[200] K. Daniel, "Fatigue failure criterion based on strain energy density," *Mechanika Teoretyczna I Stosowana*, vol. 1, no. 27. p. 8, 1989.

[201] M. Valsan and A. Nagesha, "Low cycle fatigue and creep-fatigue interaction behaviour of 316L(N) stainless steel and its welds," *Trans. Indian Inst. Met.*, vol. 63, no. 2–3, pp. 209–215, 2010.

[202] S. Goyal, R. Sandhya, M. Valsan, and K. Bhanu Sankara Rao, "The effect of thermal ageing on low cycle fatigue behaviour of 316 stainless steel welds," *Int. J. Fatigue*, vol. 31, no. 3, pp. 447–454, 2009.

[203] M. Gerland, J. Mendez, P. Violan, and B. Ait Saadi, "Evolution of dislocation structures and cyclic behaviour of a 316L-type austenitic stainless steel cycled in vacuo at room temperature," *Mater. Sci. Eng. A*, vol. 118, no. C, pp. 83–95, 1989.

[204] M. S. Pham, S. R. Holdsworth, K. G. F. Janssens, and E. Mazza, "Cyclic deformation response of AISI 316L at room temperature: Mechanical behaviour,

microstructural evolution, physically-based evolutionary constitutive modelling," *Int. J. Plast.*, vol. 47, pp. 143–164, 2013.

[205] H. Mughrabi, "Dislocation wall and cell structures and long-range internal stresses in deformed metal crystals," *Acta Metall.*, vol. 31, no. 9, pp. 1367–1379, 1983.

[206] J. Nellessen, S. Sandlöbes, and D. Raabe, "Effects of strain amplitude, cycle number and orientation on low cycle fatigue microstructures in austenitic stainless steel studied by electron channelling contrast imaging," *Acta Mater.*, vol. 87, pp. 86–99, 2015.

[207] P. Lukáš and L. Kunz, "Role of persistent slip bands in fatigue," *Philos. Mag.*, vol. 84, no. 3–5, pp. 317–330, 2004.

[208] Y. Kaneko, K. Fukui, and S. Hashimoto, "Electron channeling contrast imaging of dislocation structures in fatigued austenitic stainless steels," *Mater. Sci. Eng. A*, vol. 400–401, no. 1–2 SUPPL., pp. 413–417, 2005.

[209] F. Bochme, K. Hidaka, and J. R. Weertman, "PSB observation in copper fatigued at one half the melting temperature," *Scr. Metall.*, vol. 24, pp. 2341–2346, 1990.

[210] J. Nellessen, S. Sandlobes, and D. Raabe, "Effects of strain amplitude , cycle number and orientation on low cycle fatigue microstructures in austenitic stainless steel studied by electron channelling contrast imaging," vol. 87, pp. 86–99, 2015.

[211] M. S. Pham and S. R. Holdsworth, "Change of stress-strain hysteresis loop and its links with microstructural evolution in AISI 316L during cyclic loading," *Procedia Eng.*, vol. 10, pp. 1069–1074, 2011.

[212] J. I. Dickson, J. Boutin, and G. L'Espérance, "An explanation of labyrinth walls in fatigued f.c.c. metals," *Acta Metall.*, vol. 34, no. 8, pp. 1505–1514, 1986.

[213] R. Sandstrom, J. Engstrom, J. O. Nilsson, and A. Nordgren, "Elevated temperature low-cycle fatigue of the austenitic stainless steels type 316 and 253MA. Influence

of microstructure and damage mechanisms," *High Temp. Technol.*, vol. 7, no. 1, pp. 2–10, 1989.

[214] D. McLean and A. Pineau, "Grain-boundary sliding as a correlating concept for fatigue hold-times," *Met. Sci.*, vol. 12, no. November, pp. 313–316, 1978.

[215] K. Fujiyama, H. Kimachi, Y. Watanabe, K. Hijikuro, and T. Tsuboi, "The concept of 'eBSD strain analysis' and its application to creep and creep-fatigue damage assessment of ferritic and austenitic heat resistant steels," *Strength, Fract. Complex.*, vol. 7, no. 2, pp. 123–135, 2011.

[216] M. Turski, P. J. Bouchard, a. Steuwer, and P. J. Withers, "Residual stress driven creep cracking in AISI Type 316 stainless steel," *Acta Mater.*, vol. 56, no. 14, pp. 3598–3612, Aug. 2008.

[217] M. E. Kassner and T. A. Hayes, "Creep cavitation in metals," *Int. J. Plast.*, vol. 19, no. 10, pp. 1715–1748, 2003.

[218] H. Riedel, "Grain boundary cavitation under creep-fatigue conditions," in *Fracture at high temperatures*, Springer-Verlag Berlin GmbH, 1987, pp. 247–262.

[219] Y. Xun, M. J. Tan, and K. M. Liew, "EBSD characterization of cavitation during superplastic deformation of Al-Li alloy," *J. Mater. Process. Technol.*, vol. 162–163, no. SPEC. ISS., pp. 429–434, 2005.

[220] A. Rohatgi, K. S. Vecchio, and G. T. Gray, "The influence of stacking fault energy on the mechanical behavior of Cu and Cu-Al alloys: Deformation twinning, work hardening, and dynamic recovery," *Metall. Mater. Trans. A*, vol. 32, no. 1, pp. 135–145, 2001.

[221] R. A. Varin and J. Kruszynska, "Control of annealing twins in type 316 austenitic stainless steel," *Acta Metall.*, vol. 35, no. 7, pp. 1767–1774, 1987.

[222] J. Jiang, T. Ben Britton, and A. J. Wilkinson, "Accumulation of geometrically

necessary dislocations near grain boundaries in deformed copper," *Philos. Mag. Lett.*, vol. 92, no. 11, pp. 580–588, 2012.

[223] Y. Q. Wang, S. Hossain, S. Kabra, S. Y. Zhang, D. J. Smith, and C. E. Truman, "Effect of boundary conditions on the evolution of lattice strains in a polycrystalline austenitic stainless steel," *J. Mater. Sci.*, vol. 52, no. 13, pp. 7929–7936, 2017.

[224] T. Mayama, K. Sasaki, and M. Kuroda, "Quantitative evaluations for strain amplitude dependent organization of dislocation structures due to cyclic plasticity in austenitic stainless steel 316L," *Acta Mater.*, vol. 56, no. 12, pp. 2735–2743, 2008.

[225] J. M. Kenneth D. Challenger, "Quantitative characterization of the substructure of AISI 316 stainless steel resulting from creep," *Metall. Trans.*, vol. 4, no. 3, pp. 749–755, 1973.

[226] J. Wiskel, J. Lu, O. Omotoso, D. Ivey, and H. Henein, "Characterization of Precipitates in a Microalloyed Steel Using Quantitative X-ray Diffraction," *Metals (Basel).*, vol. 6, no. 4, p. 90, 2016.

[227] A. Le Guellaut, M. Houari, and C. Leneve, "Remaining life study of a 2.25Cr-1Mo catalytic reforming reactor," in *4th International ECCC Conference*, pp. 1–13.

[228] M. K. Samal, B. K. Dutta, H. S. Kushwaha, R. Daga, and G. Bandyopadhyay, "Creep damage evaluation of a power plant header using combined FEM analysis and quantitative metallography," *Trans. Indian Inst. Met.*, vol. 63, no. June, pp. 411–416, 2010.

[229] S. Wright, "Applications of EBSD in Materials Research for Nuclear Energy," 2008.

[230] D. A. Wigley, *Mechanical Properties of Materials at Low Temperatures*. 1971.

[231] F. Walther and D. Eifler, “Cyclic deformation behavior of steels and light-metal alloys,” *Mater. Sci. Eng. A*, vol. 468–470, no. SPEC. ISS., pp. 259–266, 2007.

[232] D. W. Dean and D. N. Gladwin, “Creep crack growth behaviour of Type 316H steels and proposed modifications to standard testing and analysis methods,” *Int. J. Press. Vessel. Pip.*, vol. 84, no. 6, pp. 378–395, Jun. 2007.

[233] J. Polák, “Cyclic Deformation, Crack initiation, and Low-cycle Fatigue,” *Compr. Struct. Integr. Fract. Mater. from Nano to Macro*, pp. 1–39, 2003.

[234] S. Holmström, R. Pohja, A. Nurmela, P. Moilanen, and P. Auerkari, “Creep and creep-fatigue behaviour of 316 stainless steel,” in *Procedia Engineering*, 2013, vol. 55, pp. 160–164.

[235] A. Varma, A. Gokhale, J. Jain, K. Hariharan, P. Cizek, and M. Barnett, “Investigation of stress relaxation mechanisms for ductility improvement in SS316L,” *Philos. Mag.*, no. October, pp. 1–17, 2017.

[236] M. S. Pham and S. R. Holdsworth, “Role of microstructural condition on fatigue damage development of AISI 316L at 20 and 300°C,” *Int. J. Fatigue*, vol. 51, pp. 36–48, Jun. 2013.

[237] M. S. Pham, C. Solenthaler, K. G. F. Janssens, and S. R. Holdsworth, “Dislocation structure evolution and its effects on cyclic deformation response of AISI 316L stainless steel,” *Mater. Sci. Eng. A*, vol. 528, no. 7–8, pp. 3261–3269, 2011.

[238] B. Chen *et al.*, “Role of the misfit stress between grains in the Bauschinger effect for a polycrystalline material,” *Acta Mater.*, vol. 85, pp. 229–242, Feb. 2015.

[239] A. A. Mamun, R. J. Moat, J. Kelleher, and P. J. Bouchard, “Origin of the Bauschinger effect in a polycrystalline material,” *Mater. Sci. Eng. A*, vol. 707, no. September, pp. 576–584, 2017.

[240] A. Rao, P. John Bouchard, S. M. Northover, and M. E. Fitzpatrick, “Anelasticity

in austenitic stainless steel," *Acta Mater.*, vol. 60, no. 19, pp. 6851–6861, Nov. 2012.

[241] T. O. Erinosho, K. A. Venkata, M. Mostafavi, D. M. Knowles, and C. E. Truman, "Influence of Prior Cyclic Plasticity on Creep Deformation using Crystal Plasticity Modelling," *Under Rev.*, no. February, 2017.

[242] M. Kamaya, "Measurement of local plastic strain distribution of stainless steel by electron backscatter diffraction," *Mater. Charact.*, vol. 60, no. 2, pp. 125–132, Feb. 2009.

[243] K. FUJIYAMA, Y. Mizutani, Y. Taniguchi, and H. Kimachi, "EBSD Analysis of creep damage process in SUS304HTB steel," *J. Soc. Mater. Sci. Japan*, vol. 62, no. 5, pp. 305–310, 2013.

[244] H. Wang, B. Clausen, C. N. Tomé, and P. D. Wu, "Studying the effect of stress relaxation and creep on lattice strain evolution of stainless steel under tension," *Acta Mater.*, vol. 61, pp. 1179–1188, 2013.

[245] F. Engineering, "EBSD Strain Analysis of CuZn10 Alloy in As-cast State and After Plastic Working and Annealing During Cavitational Wear," vol. 1, no. 2, pp. 53–60, 2013.

[246] J. Hou, Q. J. Peng, T. Shoji, J. Q. Wang, E. H. Han, and W. Ke, "Effects of cold working path on strain concentration, grain boundary microstructure and stress corrosion cracking in Alloy 600," *Corros. Sci.*, vol. 53, no. 9, pp. 2956–2962, 2011.

[247] J. Jiang, T. B. Britton, and a. J. Wilkinson, "Measurement of geometrically necessary dislocation density with high resolution electron backscatter diffraction: Effects of detector binning and step size," *Ultramicroscopy*, vol. 125, pp. 1–9, 2013.

[248] T. J. Ruggles and D. T. Fullwood, "Ultramicroscopy Estimations of bulk

geometrically necessary dislocation density using high resolution EBSD," *Ultramicroscopy*, vol. 133, pp. 8–15, 2013.

[249] J. Swadener, "The correlation of the indentation size effect measured with indenters of various shapes," *J. Mech. Phys. Solids*, vol. 50, no. 2002, pp. 681–694, 2002.

[250] A. Barnoush, "Correlation between dislocation density and nanomechanical response during nanoindentation," *Acta Mater.*, vol. 60, no. 3, pp. 1268–1277, 2012.

[251] A. J. Wilkinson and P. B. Hirsch, "Electron diffraction based techniques in scanning electron microscopy of bulk materials," *Micron*, vol. 28, no. 4, pp. 279–308, Aug. 1997.

[252] R. J. Kamaladasa and Y. N. Picard, "Basic Principles and Application of Electron Channeling in a Scanning Electron Microscope for Dislocation Analysis," pp. 1583–1590, 2010.

[253] R. Unnikrishnan, S. M. Northover, H. Jazaeri, and P. J. Bouchard, "Investigating plastic deformation around a reheat-crack in a 316H austenitic stainless steel weldment by misorientation mapping," *21st Eur. Conf. Fract.*, vol. 2, pp. 3501–3507, 2016.

[254] H. Jazaeri, P. J. Bouchard, M. T. Hutchings, and P. Linder, "Study of creep cavitation in a stainless steel weldment using small angle neutron scattering and Scanning electron microscopy," in *Proceedings of ASME 2014 Pressure Vessels & Piping Conference*, 2014, p. V06AT06A037 1-6.

[255] G. Gottstein and L. S. Shvindlerman, *Grain Boundary Migration Metals*, 2nd Editio. Taylor and Francis Group, LLC, 2010.

[256] H. Jazaeri, P. J. Bouchard, M. T. Hutchings, A. A. Mamun, and R. K. Heenan,

"Application of small angle neutron scattering to study creep cavitation in stainless steel weldments," *Mater. Sci. Technol.*, vol. 31, no. 5, pp. 535–539, 2015.

[257] P. J. Bouchard, F. Fiori, and W. Treimer, "Characterisation of creep cavitation damage in a stainless steel pressure vessel using small angle neutron scattering," *Appl. Phys. A Mater. Sci. Process.*, vol. 74, no. SUPPL.II, pp. 1689–1691, 2002.